



MONASH University

Kinetic Study of Reactive Flash Volatilization of Biomass

Tigabwa Yosef Ahmed
M.Sc. Chemical Engineering

A thesis submitted for the degree of *Doctor of Philosophy* at
Monash University in 2018
Department of Chemical Engineering
Faculty of Engineering

Copyright notice

© Tigabwa Yosef Ahmed (2018).

Abstract

Syngas that can be produced from lignocellulosic biomass via gasification has a potential for use in green chemicals synthesis. Reactive flash volatilization (RFV) is a promising emerging gasification technology for a tar-free syngas production. This process integrates pyrolysis, tar cleaning, and water-gas shift reactions in a single millisecond residence time reactor. Solid feedstock is converted into bio-oil via fast pyrolysis on or above the surface of catalyst bed, followed by gasification of char, reforming of bio-oil and water-gas shift reaction in the catalytic bed. This prevents the secondary tar formation by converting the primary tar compounds *in-situ*. This study aims to understand the conversion behaviour of primary tar compounds (bio-oil) from cellulose and lignin pyrolysis (acetol and guaiacol, respectively) under the conditions of reactive flash volatilization using a nickel-based Rh-Ni/ γ -Al₂O₃ catalyst. A freeboard design of the reactor along with the use of oxygen as additional oxidant prevents the formation of secondary tar and char in the reforming process. The influence of the main reaction conditions: temperature, steam-to-carbon (S/C) molar ratio, carbon-to-oxygen (C/O) molar ratio, gas hourly space velocity (GHSV), and catalyst weight on the H₂/CO molar ratio in the product gas were examined by applying a fractional factorial experimental design method. The nature and extent of primary tar (acetol) conversion in the reactor freeboard has also been investigated for the first time. Thermal decomposition and partial oxidation of acetol precedes the catalytic reactions involving steam. At 650°C more than 60% of the carbon in the acetol feed was converted to permanent gases before reaching the catalytic bed. For acetol reforming a minimum reaction temperature of at least 500°C should be maintained to avoid char and tar formation and the optimal operating conditions were identified as 650°C, C/O ratio of 1.7, and S/C ratio of 1.2. A possible reaction scheme for the tar conversion in the freeboard has also been proposed. For the reforming of guaiacol, a minimum operating temperature of 600°C was required to eliminate the formation of carbonaceous deposits. The kinetic model developed for autothermal reforming of acetol allows to evaluate the effect of process conditions such as the time-temperature history of the tar compound, the mode of reactor operation, and the influence of the catalytic reactions on molar ratio of H₂ and CO in the product gas. The findings from this work will help to improve direct processing of biomass in short contact time through the advancements in the understanding of the reactive flash volatilization process.

Declaration

This thesis contains no material which has been accepted for the award of any other degree or diploma at any university or equivalent institution and that, to the best of my knowledge and belief, this thesis contains no material previously published or written by another person, except where due reference is made in the text of the thesis.

Signature:

A solid black rectangular box used to redact the signature of the author.

Print Name: Tigabwa Yosef Ahmed

Date: 10/19/2018

Publications during enrolment

Conference Publication

Ahmed, T. Y., Hoadley, A. & Tanksale, A. Investigation of Reactive Flash Volatilization of Cellulose for Syngas Production using the Aspen Plus Simulator. *CHEMECA 2015*, pp. 55-63.

Acknowledgements

First and foremost, I am indebted to my advisors, A/Prof Andrew Hoadley and Dr. Akshat Tanksale, for their unreserved guidance and support throughout the study period. I have greatly benefited from their insightful comments and suggestions.

It wouldn't have been possible to conduct this research without the scholarships I received from Monash University (Monash International Postgraduate Research Scholarship and Monash Graduate Scholarship).

I would also like to express my gratitude to A/Prof Kentaro Umeka from the Luleå University of Technology (LTU), Sweden, who gave me the opportunity to join his research group as a visiting scholar.

I would like to thank my labmates here at Monash University: Pratik Gholkar, Dr. Frank Chan, and Waqar Ahmed for the valuable discussions we have had. A special thanks to my friend Meipeng Jian for his help with the acquisition of the TEM images. I am absolutely grateful to Angé David García Llamas and Gustav Häggström for the assistance they provided when I was building my experimental setup at LTU.

I am thankful for the help provided by the staff of Chemical Engineering Department of Monash University: Harry Bouwmeester, Ross Ellingham, Kim Phu, Lilyanne Price, and Jill Chrisfield.

I owe a debt of gratitude to my husband, Dr. Tamiru Alemu, for the support and patience throughout the years. I thank you for being a mentor and a best friend.

Last but not least, I owe my deepest gratitude to my parents, Yeshe Abebe and Yosef Ahmed, and my sisters, Muluwork Yosef and Fasika Yosef, for their help to raise my son, Matthias Tamiru, in my absence. I would also like to thank my brother, Wondifraw Yosef, and my sisters, Fantaneshi Yosef and Eskedar Yosef, for encouraging me through the years.

Dedication

This thesis is dedicated to the memory of my loving sister, Alemtsehay Yosef, who always believed in me.

Table of Contents

Chapter 1	Introduction.....	1
1.1	Lignocellulosic Biomass as an Alternative Carbon Source.....	3
1.2	Conventional Biomass Gasification Technologies	5
1.3	A New Integrated Catalytic Biomass Gasification	9
1.4	Scope of the Study	11
1.4.1	Research Aims.....	12
1.5	Thesis Structure and Chapter Outline	12
	References	15
Chapter 2	Literature Review.....	18
2.1	Reactive Flash Volatilization	18
2.2	Syngas Production from Bio-oil.....	20
2.2.1	Catalytic Steam Reforming of Bio-oil.....	21
2.2.2	Air-Steam Gasification (Autothermal Reforming) of Bio-oil.....	26
2.3	Kinetics of Catalytic Steam Reforming of Bio-oil.....	30
2.3.1	Reaction Schemes	30
2.3.2	Kinetic Models.....	32
2.4	Kinetics of Air-Steam Reforming of Bio-Oil.....	33
2.4.1	Reaction Schemes	33
2.4.2	Kinetic Models	35
2.5	Simulation Models	36
2.6	Summary and Research Gaps.....	38
	References	41
Chapter 3	Thermodynamic Equilibrium Model for Reactive Flash Volatilization of Cellulose using Aspen Plus	47

3.1	Introduction	47
3.2	Model Data	49
3.2.1	Feedstock Conditions.....	49
3.2.2	Cellulose Decomposition.....	50
3.3	Modelling Approach	52
3.3.1	Cellulose Decomposition Submodel.....	52
3.3.2	Aspen Plus Simulation Model.....	53
3.4	Result and Discussion	56
3.4.1	Calculated Yield of the Tar Compounds	56
3.4.2	Mass Balance.....	56
3.4.3	Effect of Reaction Conditions	57
3.4.4	Energy Balance	61
3.5	Conclusions	64
	References	65
Chapter 4	Experiment Methods.....	68
4.1	Introduction	68
4.2	Experimental Setup	69
4.3	Materials	72
4.4	Calibrations.....	72
4.5	Catalyst Preparation	72
4.6	Catalyst Characterization.....	73
4.7	Experimental Procedures	75
4.7.1	Experimental Design.....	75
4.7.2	Reactor Operating Procedures.....	77
4.7.3	Gas Sampling and Analysis.....	77
4.7.4	Liquid Condensate Sampling and Analysis.....	79
4.7.5	Gas Composition Analysis from the Reactor Freeboard	79

References	82
Chapter 5 Air-Steam Reforming of Acetol and Guaiacol under Reactive Flash	
Volatilization Conditions.....	84
5.1 Introduction	84
5.2 Acetol Conversion.....	84
5.2.1 Reactor Freeboard Gas Composition Analysis	84
5.2.2 Catalyst Bed Temperature Measurements.....	89
5.2.3 Experimental Matrix Results for Acetol Conversion	90
5.3 Guaiacol Conversion.....	104
5.3.1 Catalyst Bed Temperature Measurements.....	106
5.3.2 Experimental Matrix Results for Guaiacol Conversion.....	106
5.4 Conclusions	113
References	114
Chapter 6 Kinetic Model of Air-Steam Reforming of Acetol.....	115
6.1 Introduction	115
6.2 Model Development.....	115
6.3 Results and Discussion	121
6.4 Conclusions	127
References	128
Chapter 7 Conclusions and Recommendations	130
7.1 Conclusions	130
7.2 Contribution to Knowledge	131
7.3 Recommendations	133
Appendices.....	134

List of Figures

Chapter 1

Figure 1.1: Pathways for chemical production from syngas adapted from Spath and Dayton (2003)	1
Figure 1.2: Global syngas outlook by feedstock: the data is taken from Gasification Technologies Council (GSTC, 2018)	3
Figure 1.3: Chemical structures of the basic units (monomers) of a) cellulose b) hemicellulose and, c) lignin: adapted from Chen (2014) and Anderson (1982).....	4
Figure 1.4: Van Krevelen's diagram for atomic O/C- and H/C-ratio of various feedstocks: adapted from Suriapparao et al. (2015).....	5
Figure 1.5: A reaction scheme for biomass pyrolysis (Koufopoulos et al., 1991).....	6
Figure 1.6: Classifications of gaseous products from biomass gasification (Boerrigter and Rauch, 2005).....	8
Figure 1.7: Reaction zones in a downdraft fixed bed biomass gasifier.....	9
Figure 1.8: Schematic of the reactive flash volatilization gasifier (Colby et al., 2008).....	10
Figure 1.9: Operation performance of the various processes involved in syngas production grouped by process type despite utilizing different catalysts: dolomite (▲), Ni (■), Rh (◆), and Ru (●) adapted and redrawn from (Colby et al., 2008).....	11

Chapter 2

Figure 2.1: Photograph of the front face of a catalyst used in reactive flash volatilization of cellulose particles (230mm) adapted from Dauenhauer et al. (2007) with permission from the publisher	18
Figure 2.2: Decomposition characteristic of cellulose by reactive flash volatilization using a thermogravimetric analyser at 700°C with catalysts: ■ Re-Ni, ● Rh-Ni, ▲ Ru-Ni adapted from Chan et al. (2015).	19
Figure 2.3: Possible routes for bio-oil conversion to syngas	21

Figure 2.4: The influence of oxygen on the distribution of products a) pyrolysis and b) partial oxidation (Marda et al., 2009).....	28
Figure 2.5: The configuration of a bench scale bio-oil reforming reactor system used by Czernik and French (2014).....	30
Figure 2.6: C:O ratio for different bio-oil and bio-oil model compounds	40

Chapter 3

Figure 3.1: Numerical and analytical solutions for particle temperature with constant and variable <i>h_{rad}</i>	47
Figure 3.2: Pyrolysis product distribution at a reaction temperature of 700°C	48
Figure 3.3: Optimization framework for calculating the yields of tar compounds	53
Figure 3.4: Aspen Plus simulation model for reactive flash volatilization of cellulose.....	54
Figure 3.5: The conversion of cellulose by partial oxidation at C/O = 0.7, 0.8, and 0.9 with no steam.....	58
Figure 3.6: The conversion of cellulose to equilibrium products with steam at C/O = 0.8 for three different S/C ratios.....	59
Figure 3.7: The selectivity of H ₂ (■), H ₂ O (▲), CO (●), CO ₂ (▼), and CH ₄ (◆): the dash lines represent simulation results while the bullet points are experimental data from Colby et al. (2008)	60
Figure 3.8: Comparison between simulated results and experimental data from Colby et al. (2008) at T = 730°C, C/O = 0.9, and S/C = 0.55: ■ simulated data and ▣ experimental data.....	61
Figure 4.1: the formation path of acetol (Wang and Luo, 2017).....	68

Chapter 4

Figure 4.2: Chemical structure of guaiacol.....	69
Figure 4.3: Schematic of the experimental system used for kinetic analysis of primary tar model compounds	70
Figure 4.4: Dimensions of the reactor used for the kinetic analysis	71
Figure 4.5: Adsorption isotherm for the Rh-Ni/Al ₂ O ₃ catalyst	74

Figure 4.6: Reduction temperature profile for the Rh-Ni/Al ₂ O ₃ catalyst.....	75
Figure 4.7: Gas sampling arrangement.....	78
Figure 4.8: The working principle of RGA. Redrawn and slightly modified from (Brillson, 2016) and reproduced with permission from the publisher.	79
Figure 4.9: The instrument used for the gas analysis from the reactor freeboard	80
Figure 4.10: Fragment ions from acetol sample analysis using the RGA at 61°C.....	81

Chapter 5

Figure 5.1: The gas composition from the reactor freeboard (dry and argon free basis): acetol=0.089 ml/min, GHSV=15500h ⁻¹ , C/O=1.7, and S/C=1.2.....	85
Figure 5.2: The conversion of acetol to C ₁ products: 0.089 ml/min acetol, GHSV=15500h ⁻¹ , C/O=1.7, and S/C=1.2	86
Figure 5.3: Product gas composition from the reactor outlet: acetol=0.089 ml/min, 0.345 g of Rh-Ni/γAl ₂ O ₃ catalyst and 0.05 g quartz wool, GHSV=15500h ⁻¹ , C/O=1.7, and S/C=1.2.....	87
Figure 5.4: Comparison of the gas composition between the present study at 650°C (0.345 g Rh-Ni/γAl ₂ O ₃ catalyst, GHSV=15500h ⁻¹ , C/O=1.7, and S/C=1.2) with the work of Ramos et al. (2007) at 650°C (0.8 g Ni-Al catalyst, G _{C1} HSV=22323h ⁻¹ , C/O=0, and S/C=4.6).....	88
Figure 5.5: Arrhenius plot for rate of acetol decomposition.....	89
Figure 5.6: Catalyst bed temperature for acetol conversion: acetol=0.115 ml/min, 0.5 g catalyst, GHSV=17000h ⁻¹ , S/C=1.2, and C/O=1.3.....	90
Figure 5.7: Product gas distribution on dry and N ₂ free basis: acetol=0.085 ml/min, 0.5 g Rh-Ni/γAl ₂ O ₃ catalyst, T=800°C, GHSV=14000h ⁻¹ , C/O=1.3, and S/C=1.2	92
Figure 5.8: Acetol concentration in the liquid sample using HPLC.....	93
Figure 5.9: Effect of temperature on product gas composition: acetol=0.085 ml/min, 0.5 g catalyst, GHSV=15500 h ⁻¹ , C/O=1.5, and S/C=1.8	94
Figure 5.10: Effect of S/C ratio on product gas composition: acetol=0.085 ml/min, 0.65 g catalyst, T=750°C, GHSV=15500h ⁻¹ , and C/O=1.5.....	95

Figure 5.11: Effect of GHSV on product gas composition: acetol=0.085ml/min, 0.65 g catalyst, T=750°C, C/O=1.5, and S/C=1.8	96
Figure 5.12: Effect of C/O ratio on product gas composition: acetol=0.085ml/min, 0.65g catalyst, T=750°C, GHSV=15500 h ⁻¹ , and S/C=1.8	97
Figure 5.13: Effect of C/O ratio on product gas composition at acetol=0.085 ml/min, 0.5 g catalyst, T=650°C, GHSV=17000h ⁻¹ , and S/C=1.2	97
Figure 5.14: Effect of S/C ratio on the molar ratio of H ₂ /CO: 0.65 g catalyst, T=750°C, GHSV=15500 h ⁻¹ , and C/O=0.75	99
Figure 5.15: Effect of temperature, S/C ratio, C/O ratio and GHSV on CO/CO ₂ molar ratio.....	99
Figure 5.16: TEM images of Rh-Ni/Al ₂ O ₃ catalyst surface (a) fresh (b) spent catalyst after 4 hours reaction from acetol conversion: T=700°C, C/O=1.3, and S/C= 2.4	100
Figure 5.17: Picture of the reactor after reaction: T=500°C, 0.5 g of Rh-Ni/γAl ₂ O ₃ , C/O=1.3, and S/C=0	101
Figure 5.18: TEM images of (a) fresh sample of Rh-Ni/Al ₂ O ₃ catalyst (b) spent catalyst after 4 hours reaction at temperature of 500°C, S/C=0, and C/O=1.3	102
Figure 5.19: Carbon forming region for acetol conversion from an equilibrium model	103
Figure 5.20: Guaiacol conversion: guaiacol=0.06 ml/min, 0.5 g of Rh-Ni/γAl ₂ O ₃ catalyst, T=700°C, GHSV=17000h ⁻¹ , C/O=0.85, and S/C=1.2	104
Figure 5.21: Guaiacol conversion: guaiacol=0.0575 ml/min, 0.5 g catalyst, T=700°C, GHSV=17000h ⁻¹ , C/O=1.15, and S/C=1.2	105
Figure 5.22: Guaiacol conversion a) without a catalyst and b) in the presence of catalyst	105
Figure 5.23: Catalyst bed temperature of guaiacol conversion: 0.1 ml/min guaiacol, GHSV=17000h ⁻¹ , C/O=1.15, and S/C=1.2	106
Figure 5.24: Effect of temperature on product gas composition: 0.0575 ml/min guaiacol, 0.5 g catalyst, GHSV=15500 h ⁻¹ , C/O=1, and S/C=1.8.....	108
Figure 5.25: Effect of S/C ratio on product gas composition: guaiacol=0.0575 ml/min, 0.5 g catalyst, T=750°C, GHSV=15500 h ⁻¹ , and C/O=1	109

Figure 5.26: Interactive effect of (a) S/C ratio and temperature on methane yield: GHSV=15500 h ⁻¹ and C/O=1 (b) S/C ratio and C/O ratio on H ₂ yield: T=750°C and GHSV=15500 h ⁻¹	110
Figure 5.27: Effect of temperature on gas product composition: guaiacol=0.0575 ml/min, 0.5 g catalyst, C/O=1, and S/C=1.8	110
Figure 5.28: Effect of temperature on gas product composition: guaiacol=0.0575 ml/min, 0.5 g catalyst, GHSV=15500 h ⁻¹ , C/O=1, and S/C=1.8	111
Figure 5.29: Effect temperature and S/C ratio on molar ratio of H ₂ /CO and CO/CO ₂	112
Figure 5.30: TEM images of Rh-Ni/Al ₂ O ₃ catalyst surface (a) fresh catalyst (b) spent catalyst after 4 hours reaction time for guaiacol conversion: T=700°C, C/O=0.85, and S/C=1.2	113

Chapter 6

Figure 6.1: Aspen Plus simulation setup for autothermal reforming of acetol	119
Figure 6.2: Effect of reaction temperature on acetol conversion in the freeboard: the dotted line represents experimental data and the solid lines for the model predictions	122
Figure 6.3: Dependence of composition of the product gas (dry and argon free basis) on operating temperature for Case 1: dotted lines represent experimental data and the solid lines are modelling results	123
Figure 6.4: Mole fraction of the reactants and products along the catalytic bed length at operating temperature of 650°C on argon free basis	124
Figure 6.5: Comparison of the gas composition between kinetic and equilibrium conditions at 650°C	125
Figure 6.6: Dependence of composition of the product gas (dry and argon free basis) on operating temperature for Case 2: dotted lines represent experimental data and solid lines denote modelling results	126
Figure 6.7: Mole fraction of the reactants and products along the catalytic bed length at 650°C on argon free basis	126
Figure 6.8: Catalytic bed temperature change for Case 1 and 2	127

Chapter 7

Figure 7.1: Aspen Plus simulation setup for autothermal reforming of acetol.....	133
--	-----

List of Appendix Figures

Chapter 3

Figure A.1: The numerical and analytical solutions for particle temperature with constant and variable h_{rad}	136
Figure A.2: Velocity profile of the particle.....	138
Figure A.3: Temperature of the fluid and the particle over the reactor length with the constant fluid velocity.....	142
Figure A.4: Temperature of the fluid and the particle over the reactor length with variable fluid velocity.....	142
Figure A.5: A two-stage semi-global reaction scheme (Koufopoulos et al., 1991)	143
Figure A.6: Pyrolysis products distribution at temperature of 700°C.....	144
Figure B.1: Catalyst bed temperature adapted from Colby et al. (2008)	146

Chapter 4

Figure A.1: Calibration curve for Ar feed rate.....	147
Figure B.1: Calibration curve for acetol feed rate using the syringe pump.....	149
Figure B.2: Calibration curve for the guaiacol feed rate using the syringe pump.....	150
Figure C.1: Calibration curve for the water feed rate using the HPLC pump.....	151
Figure D.1: Calibration plot for H ₂ analysis using GC.....	152
Figure D.2: Calibration curve for CO analysis using GC.....	153
Figure D.3: Calibration curve for CO ₂ analysis using GC.....	154
Figure D.4: Calibration plot for CH ₄ analysis using GC.....	155
Figure D.5: Calibration curve for N ₂ analysis using GC.....	156
Figure D.6: Calibration curve for O ₂ analysis using GC.....	157
Figure E.1: Calibration curve for acetol concentration in liquid samples using HPLC.....	159

Figure F.1: Sample result from acetol conversion using 1%Ru-10%Ni/Al ₂ O ₃ (T=700°C, S/C=1.2, C/O=1.13)	160
Figure H.1: Calibration curve for H ₂ analysis using RGA.....	162
Figure H.2: Calibration curve for CO analysis using RGA.....	163
Figure H.3: Calibration plot for CO ₂ analysis using RGA.....	164
Figure H.5: Calibration curve Ar analysis using RGA.....	166

Chapter 5

Figure A.1: Ion spectra for gas sample taken from the reactor freeboard at 650°C.....	167
Figure C.1: A sample chromatogram from the flame ionization detector (FID)	174
Figure C.2: A sample chromatogram from the thermal conductivity detector (TCD)	174

Chapter 6

Figure A.1: Mass spectra from acetol conversion in the freeboard: T=650°C, C/O=1.7, and S/C=1.2	182
---	-----

List of Tables

Chapter 1

Table 1.1: Syngas composition specifications (vol%) for selected applications (Hofbauer et al., 2007).....	2
Table 1.2: Modes of pyrolysis and typical major products from wood pyrolysis (Balat et al., 2009, De Wild, 2015).....	6
Table 1.3: Classification of tar compounds (Morf et al., 2002).....	7

Chapter 2

Table 2.1: A typical composition of crude bio-oil derived from pyrolysis of rice husk (Wang et al., 2013).....	20
Table 2.2: Cracking reactions that can lead to carbon deposition	24
Table 2.3: Possible reactions during steam reforming of acetic acid (Yang et al., 2016).....	31
Table 2.4: Possible reactions during steam reforming of ethanol (Wu et al., 2014).....	32
Table 2.5: Proposed reaction steps for bio-oil steam reforming over Ni/La ₂ O ₃ - α -Al ₂ O ₃ catalyst al. (Gayubo et al., 2018).....	33
Table 2.6: Possible reaction in steam reforming of ethanol in the presence of oxygen (Klouz et al., 2002).....	34
Table 2.7: Proposed key chemical reactions in autothermal glycerol reforming	35
Table 2.8: Simulated steam reforming reactions for steam reforming of bio-oil	37
Table 2.9: Relative yield of tar cracking product (Kaushal and Tyagi, 2017).....	38

Chapter 3

Table 3.1: Proximate and ultimate analysis of cellulose on a dry basis (Wang et al., 2012).....	50
Table 3.2: The product yield from fast pyrolysis of cellulose at 550°C (Piskorz et al., 1986)	50
Table 3.3: Chemical structure of the primary tar model compounds used to represent pyrolysis oil from cellulose.....	51

Table 3.4: Example of composition of the streams from the partial oxidation and stream reforming steps of the process at 700°C, S/C=1.2, and C/O=0.9.....	54
Table 3.5: Calculated yield for selected tar compounds from flash pyrolysis of cellulose	56
Table 3.6: An example mass balance table	57
Table 3.7: Possible reactions in the partial oxidation and steam reforming steps of the process..	57
Table 3.8: Experimental data from reactive flash volatilization of cellulose (Colby et al., 2008)	62
Table 3.9: Energy balance comparison between experimental and model results with cellulose 30 g/hr, C/O=0.9, S/C=0.55, and temperature 730°C.....	64

Chapter 4

Table 4.1: Physical properties of acetol and guaiacol	72
Table 4.2: Surface area and pore size analysis of fresh Rh-Ni/Al ₂ O ₃ catalyst	74
Table 4.3: Experimental design matrix for acetol experiments	76
Table 4.4: Experimental design matrix for guaiacol experiments	77

Chapter 5

Table 5.1: Signal ratios of m/z=29 to m/z=27	86
Table 5.2: Composition of the product gas (dry and N ₂ free basis) from acetol conversion	91
Table 5.3: An example TOC analysis result for a liquid sample.....	92
Table 5.4: Comparison between gas yield at 700°C from Figure 5.3 and the gas yield from the design of experiments method: T=700°C, GHSV=15500h ⁻¹ , C/O=1.7, and S/C=1.2	98
Table 5.5: CHN analysis results of Rh-Ni/γAl ₂ O ₃ spent catalyst from the acetol experiments ..	101
Table 5.6: Catalyst weight before and after the reaction.....	102
Table 5.7: Product gas composition on nitrogen free basis: acetol=0.085 ml/min, 0.5 g of catalyst, T=650°C, GHSV=17000h ⁻¹ , C/O=2, and S/C=1.2	103
Table 5.8: Results from guaiacol conversion experiments	107
Table 5.9: An example TOC analysis result for a liquid sample.....	107

Chapter 6

Table 6.1: Possible major reactions in the reactor freeboard.....	117
Table 6.2: Proposed major reactions for acetol conversion in the reactor freeboard.....	118
Table 6.3: Values of the kinetic parameters for uncatalyzed water-gas shift reaction.....	119
Table 6.4: Rate equations for the reactions used to simulate the PFR	120
Table 6.5: Values of the Arrhenius parameters for reactions in the PFR.....	120
Table 6.6: Simulation conditions for the PFR	121
Table 6.7: Comparison of the composition of the gaseous product exiting the CSTR: model (Mod.) and experimental (Exp.) values	122

Chapter 7

Table 7.1: Possible major reactions in the reactor freeboard.....	132
---	-----

List of Appendix Tables

Chapter 3

Table A.1: Values of the parameters used in the heat transfer model.....	137
Table A.2: Values of the parameters used in the momentum transfer model	139
Table A.3: Values of the parameters used in the coupled model.....	141
Table A.4: Pyrolysis kinetic parameters used for in the kinetic model.....	143

Chapter 4

Table A.1: Measured Ar flow rate from the mass flow controller for different setpoints.....	147
Table A.2: Measured O ₂ outlet flow rates from the mass flow controller for different setpoints	148
Table B.1: Measured acetol feed rate using the syringe pump for different set-points	149
Table B.2: Measured guaiacol feed rates using the syringe pump.....	150
Table C.1: Measured water outlet flow rate from the for HPLC pump for different set-points..	151
Table D.1: GC peak areas for known concentrations of H ₂	152
Table D.2: GC peak areas for known concentrations of CO.....	153
Table D.3: GC peak areas for known concentrations of CO ₂	154
Table D.4: GC peak areas for known concentrations of CH ₄	155
Table D.5: GC peak areas for known concentrations of N ₂	156
Table D.6: GC peak areas for O ₂ analysis using GC.....	157
Table E.1: HPLC peak areas for known concentration of acetol.....	158
Table G.1: An element mass balance for the tail gas.....	161
Table H.1: Calibration data for H ₂ analysis using RGA.....	162
Table H.2: Calibration data for CO analysis using RG.....	163
Table H.3: Calibration data for CO ₂ analysis using RGA.....	164

Table H.4: Calibration data for CH ₄ analysis using RGA.....	165
---	-----

Table H.5: Calibration data for Ar analysis using RGA.....	166
--	-----

Chapter 5

Table B.1: Moles of compounds in the feed.....	168
--	-----

Table B.3: Composition and molar flow rate of the gases in the freeboard (dry basis)	169
--	-----

Table B.4: Mass balance for the reaction temperature of 650°C.....	170
--	-----

Table B.5: Mass balance for the reaction temperature of 700°C.....	171
--	-----

Table B.6: Mass balance for the reaction temperature of 750°C	172
---	-----

Table B.7: Mass balance for the reaction temperature of 850°C.....	173
--	-----

Table D.1: Summary of analysis of variance for H ₂ (mol%) for acetol conversion	175
--	-----

Table D.2: Summary of analysis of variance for CO (mol%).....	176
---	-----

Table D.3: Summary of analysis of variance for CH ₄ (mol%)	176
---	-----

Table D.4: Summary of analysis of variance for CO ₂ (mol%)	177
---	-----

Table D.5: Summary of analysis of H ₂ /CO (mol%)	177
---	-----

Table D.6: Summary of analysis of variance for CO/CO ₂ (mol%).....	178
---	-----

Table E.1: Summary of analysis of variance for H ₂ (mol%)	179
--	-----

Table E.2: Summary of analysis of variance for CO (mol%).....	180
---	-----

Table E.3: Summary of analysis of variance for CH ₄ (mol%).....	180
--	-----

Table E.4: Summary of analysis of variance for CO ₂ (mol%).....	181
--	-----

Abbreviations

BET	Brunauer-Emmett-Teller
GC	Gas Chromatography
HPLC	High Performance Liquid Chromatography
ID	Inside Diameter
MFC	Mass Flow Controller
MS	Mass Spectrometer
OD	Outside Diameter
PG	Pressure Gauge
RFV	Reactive Flash Volatilization
RGA	Residual Gas Analyzer
TI	Temperature Indicator

Symbols

A	m^2	Area
C_D	-	Drag coefficient
c_p	$\text{J g}^{-1} \text{K}^{-1}$	Particle specific heat capacity
f	-	Fluid
h_{cov}	$\text{W m}^{-2} \text{K}^{-1}$	Convective heat transfer coefficient
h_{rad}	$\text{W m}^{-2} \text{K}^{-1}$	Radiation heat transfer coefficient
k	$\text{W m}^{-1} \text{K}^{-1}$	Thermal conductivity
m	g	Mass
$\text{mol}\%$		Mole percent
N	mol s^{-1}	Molar flow rate
N_u	-	Nusselt number
p	-	Particle
Pr	-	Prandtl number
Re	-	Reynolds number
t	s	Time
T	$^{\circ}\text{C}$ or K	Temperature
u	m s^{-1}	Velocity

vol%	-	Volume percent
wt%	-	Weight percent
y	-	Mole fraction
ρ	kg m^{-3}	Density
ε	-	Emissivity of a surface
σ	$\text{W m}^{-2} \text{K}^{-4}$	Stephen-Boltzmann constant
μ	N s m^{-2}	Dynamic viscosity of the fluid

Chapter 1

Introduction

Synthesis gas (syngas) is a mixture of hydrogen and carbon monoxide with low levels of carbon dioxide and methane (Matar et al., 1989). It is an important platform chemical for the production of several higher-value chemicals such as hydrogen, methanol, ammonia, and oxo-alcohols, Figure 1.1.

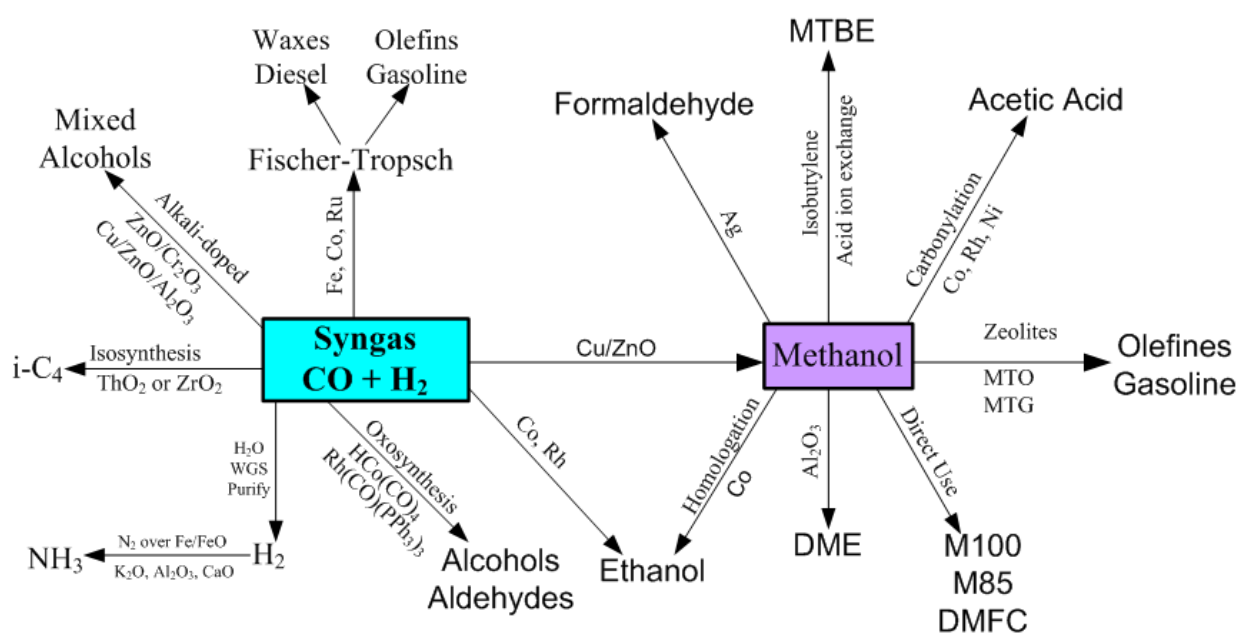


Figure 1.1: Pathways for chemical production from syngas adapted from Spath and Dayton (2003)

The requirements for the stoichiometric ratio of H_2 and CO in syngas differs among the various applications as shown in Table 1.1. Generally, the amount of inert gases such as N_2 or Ar and the CO_2 and CH_4 content need to be kept to lowest levels possible because, for instance, in some application areas the presence of CO_2 and CH_4 might lead to catalyst poisoning.

Table 1.1: Syngas composition specifications (vol%) for selected applications (Hofbauer et al., 2007)

Synthesis	H₂ for refinery	Methanol	Ammonia	Oxo-alcohols	Fisher-Tropsch
H ₂	>98%	71%	75%	75%	60%
CO	<10-50 ppmv	19%	*CO + CO ₂ (<20 ppmv)	25%	30%
CO ₂	<10-50 ppmv	4-8%		-	-
N ₂	-	-	25%	-	-
Inert	N ₂ , Ar, CH ₄ balance	N ₂ , Ar, CH ₄ as low as possible	Ar, CH ₄ as low as possible	-	CO ₂ , N ₂ , Ar, CH ₄ low
H ₂ /CO	-	1.0-4.0	-	1.0-1.5	0.6-2

*CO + CO₂ is the combined composition of CO and CO₂ in syngas by volume.

Globally, coal, heavy petroleum residues, and natural gas are the primary sources of syngas (Mondal et al., 2011), Figure 1.2. Concerns with the rapid depletion of these fossil fuel-based resources and the related environmental issues have, however, prompted the intensified research activities directed to investigating renewable and clean carbon sources (such as biomass) for chemicals. Biomass utilization may result in much lower CO₂ emission since the plants fix the emitted carbon dioxide via photosynthesis during growth. This, therefore, directly entails the need to increase the share of biomass for syngas production to a more significant level than is currently the case i.e., only 0.68% (GSTC, 2018).

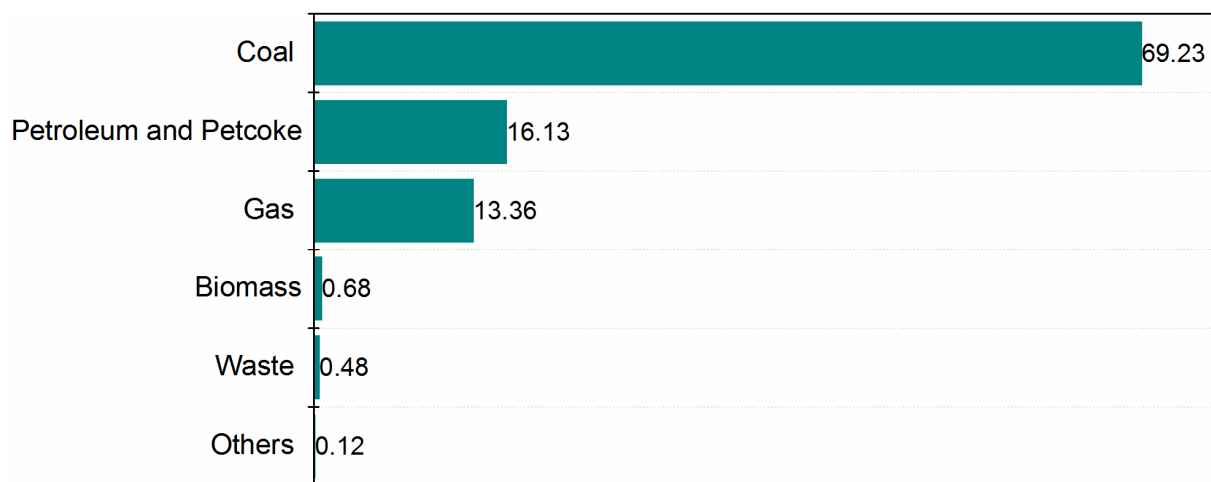


Figure 1.2: Global syngas outlook by feedstock: the data is taken from Gasification Technologies Council (GSTC, 2018)

Over the years, conversion of lignocellulosic biomass to syngas through gasification (a thermochemical conversion) has received much attention. A much-reduced processing time (a few seconds) and its ability to convert the whole biomass in an environmentally benign manner makes gasification superior over biological conversion routes. In the presence of oxidants (steam, oxygen, air, CO₂, or a combination thereof) gasification generates gaseous products containing permanent (H₂, CO, CO₂, CH₄, and C_xH_y) and condensable (tar) gases alongside coke/soot (Moneti et al., 2016). Throughout this thesis, unless stated otherwise, product gas refers to the gaseous products from gasification. This chapter discusses lignocellulosic biomass as a potential alternative carbon source followed by a discussion on the conventional biomass gasification technologies. Finally, the scope of this thesis is highlighted.

1.1 Lignocellulosic Biomass as an Alternative Carbon Source

Plant and plant-derived materials that are mainly composed of cellulose, hemicellulose, and lignin are collectively referred to as lignocellulosic biomass. Chemical structures of the building blocks of the three polymers of biomass are shown in Figure 1.3.

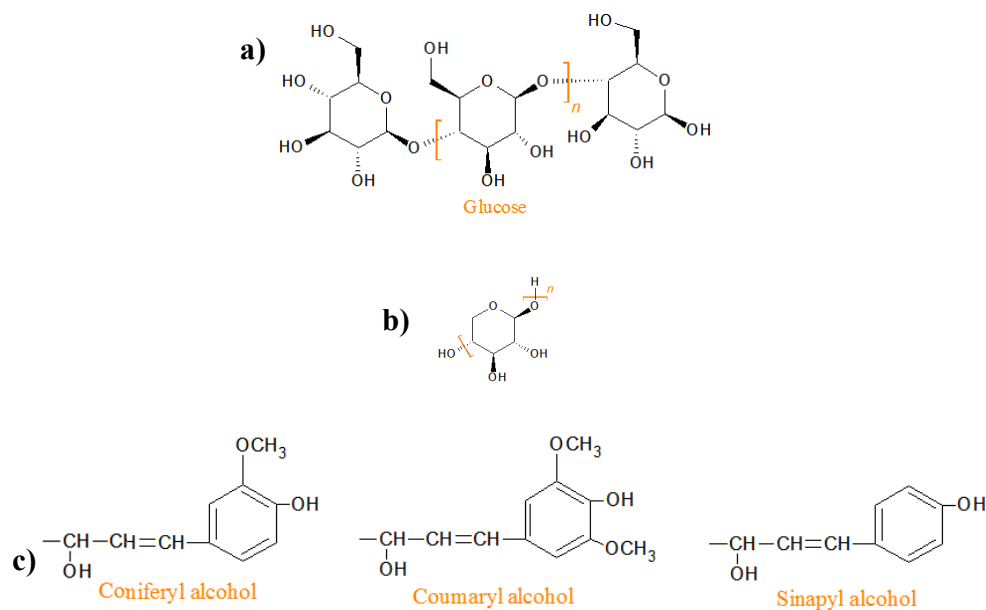


Figure 1.3: Chemical structures of the basic units (monomers) of a) cellulose b) hemicellulose and, c) lignin: adapted from Chen (2014) and Anderson (1982)

A higher oxygen content (i.e., higher O/C) is found in biomass compared with coal (Figure 1.4). This lowers the heating value of biomass and also makes its conversion behaviour different from coal and other hydrocarbons. The other notable difference between coal and biomass is the higher volatiles content of the latter (Anderson, 1982). In Australia, agricultural and forestry wastes have the potential to meet the demand for biomass. As these biomass resources are, however, scattered a decentralized processing facility can bring economic benefits by cutting down the transportation cost. The transportation cost of biomass is the key component of the overall cost since biomass has high moisture content and low volumetric energy density (Searcy et al., 2007).

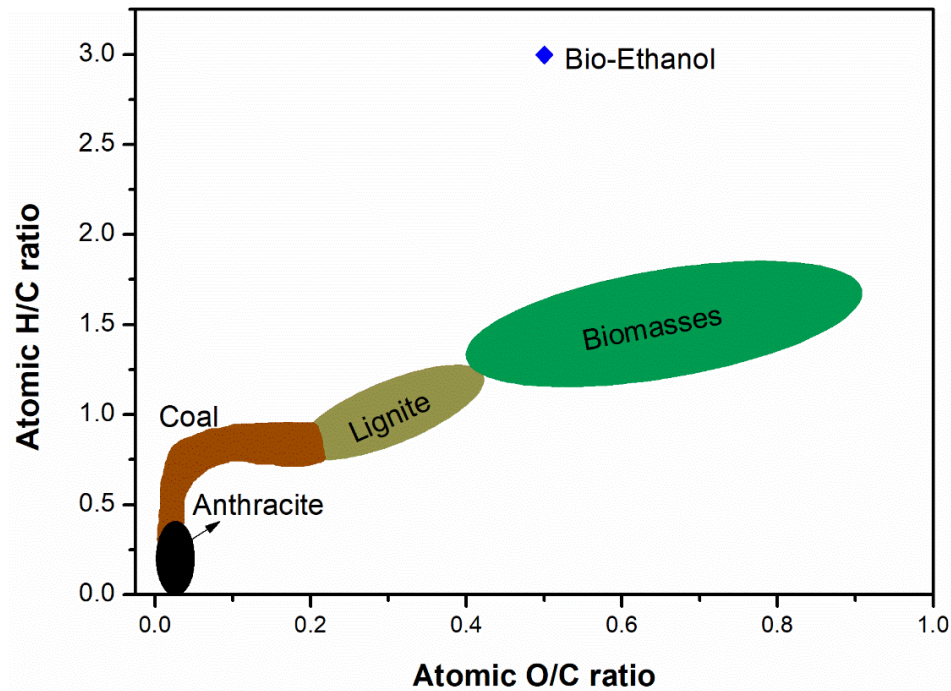


Figure 1.4: Van Krevelen's diagram for atomic O/C- and H/C-ratio of various feedstocks: adapted from Suriapparao et al. (2015)

1.2 Conventional Biomass Gasification Technologies

During gasification, initially the biomass particles thermally decompose into bio-oil (primary tar compounds), gas (H_2 , CO , CO_2 , CH_4 , and traces of C_2 species) and char, and this step of the process is called pyrolysis. Subsequently, in gasification, the pyrolysis products react with the oxidant in use and among each other to produce the final form of the product gas (Corella and Sanz, 2005). Depending on the operating conditions employed in pyrolysis, not only as a subset of gasification but also as an independent process, can be classified as flash, fast, and slow (Table 1.2).

Table 1.2: Modes of pyrolysis and typical major products from wood pyrolysis (Balat et al., 2009, De Wild, 2015)

Mode	Reaction conditions	Typical product distribution (wt%) from wood pyrolysis		
		Oil	Gas	Char
Flash	Reactor temperature >1050 K High heating rate >1000 K/s Solid residence time < 0.5s Particle size < 0.2 mm	75	12	13
Fast	Reactor temperature 850-1250 K Heating rate 10-200 K/s Solid residence time 0.5-10 s Particle size <1 mm	50	30	20
Slow	Reactor temperature 550-950 K Heating rate 0.1-1 K/s Solid residence time 450-550 s Particle size 5-50 mm	30	35	35

One of the major hurdles in biomass gasification is the formation of an undesirable by-product i.e., tar. Tar is a complex mixture of condensable hydrocarbons including, oxygen-containing 1- to 6-ring aromatic, and complex polyaromatic hydrocarbons (PAH) (Devi et al., 2003). Since tar condenses at reduced temperatures it poses operational issues in downstream equipment causing blockage and fouling. Unless the primary tar compounds produced during pyrolysis are converted *in-situ* into permanent gases, the cracking and/or polymerisation of these compounds can lead to the formation of secondary tar and char as illustrated in Figure 1.5 (Koufopoulos et al., 1991).

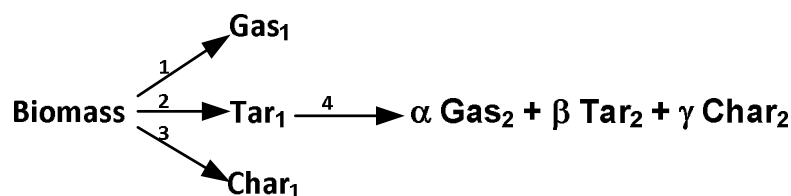


Figure 1.5: A reaction scheme for biomass pyrolysis (Koufopoulos et al., 1991)

Table 1.3 shows the classifications of tar and some examples for each category. Oxygenated hydrocarbons constitute the primary tar compounds and are found in a reactor temperature range of 400-700°C (Morf et al., 2002). In the temperature range of 700-850°C, the secondary tar products are formed and are characterized by phenolics and olefins (Morf et al., 2002). Aromatics make up the tertiary tar products and appear between 850-1000°C (Morf et al., 2002).

Table 1.3: Classification of tar compounds (Morf et al., 2002)

Tar compound class	Compound type	Compound name
Primary tar compounds	Acids	Acetic acid, Propionic acid, Butyric acid
	Ketones	Hydroxyacetone (Acetol)
	Phenols	Phenol, 2,3-Dimethylphenol, 2,4/2,5-Dimethylphenol, 2,6-Dimethylphenol, 3,4-Dimethylphenol, 3,5-Dimethylphenol
	Guaiacol	Guaiacol, 4-Methylguaiacol
	Furans	Furfural, Furfural alcohol, 5-Methylfurfural
Secondary tar compounds	Phenols	Phenol, <i>o</i> -Cresol, <i>p</i> -Cresol, <i>m</i> -Cresol
	Monoaromatic hydrocarbons	<i>p/m</i> -Xylene, <i>o</i> -Xylene
Secondary/Tertiary tar	Monoaromatic hydrocarbons	Benzene, Ethylbenzene, <i>a</i> -Methylstyrene, 3&2-Methylstyrene, 4-Methylstyrene, 3-Ethyltoluene, 4-Ethyltoluene, 2-Ethyltoluene
	Miscellaneous hydrocarbons	2,3-Benzofuran, Dibenzofuran, Biphenyl,
	Methyl derivative aromatics	Toluene, 2-Methylnaphthalene, 1-Methylnaphthalene,
Tertiary tar compounds	PAH:2-ring	Naphthalene, Acenaphthylene, Acenaphthene, Fluorene,
	3-ring	Phenanthrene, Anthracene, Fluoranthene, Pyrene,
	4-ring	Benz[a]anthracene, Chrysene, Benz[e]acephenanthrylene, Benzo[k]fluoranthene

Tar compound class	Compound type	Compound name
	5-ring	Benzo[a]pyrene, Perylene, Dibenzo[ah]anthracene, Indeno[1,2,3-cd]pyrene
	6-ring	Benzo[ghi]perylene

Conventionally, biomass can be directly converted to syngas through high-temperature (1200-1400°C) gasification as depicted in Figure 1.6. Conversion in entrained flow gasifiers is an example of the high-temperature gasification. The need to operate at very high temperatures and pressures, however, deters a wider use of entrained flow gasifier for biomass conversion (Mckendry, 2002). The product gas from the low-temperature gasification ($T < 1000^\circ\text{C}$), on the other hand, still contains higher hydrocarbons (C_xH_y) and tar. Hence, downstream vapour/gas conversion step involving thermal cracking and/or reforming is required to generate a clean syngas (Van Rossum et al., 2009). Conversion in fixed and fluidized bed gasifiers are good examples of the low-temperature gasification.

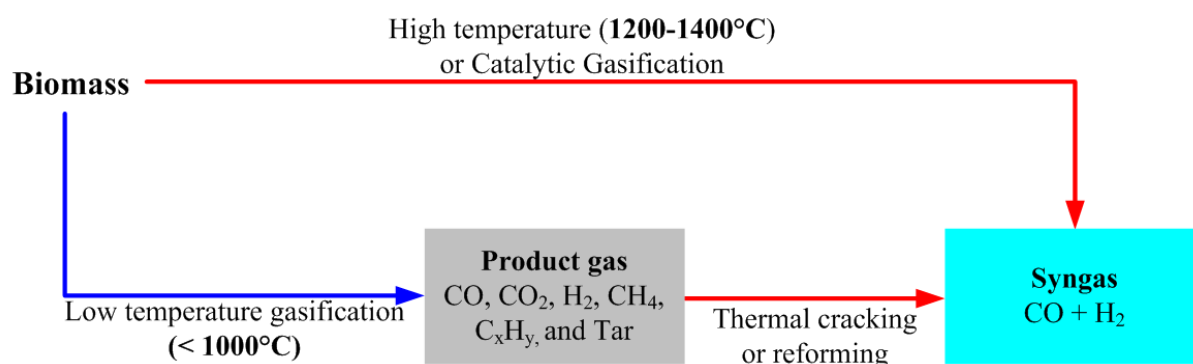


Figure 1.6: Classifications of gaseous products from biomass gasification (Boerrigter and Rauch, 2005)

In fixed bed gasifiers, a bed of solid biomass particles moves slowly down the reactor while being continually converted. Fixed bed gasifiers are usually employed for small-scale applications largely attributed to their construction and operation simplicity. Figure 1.7 illustrates the reaction zones unique to one of the possible configurations of fixed bed gasifiers i.e., a downdraft gasifier.

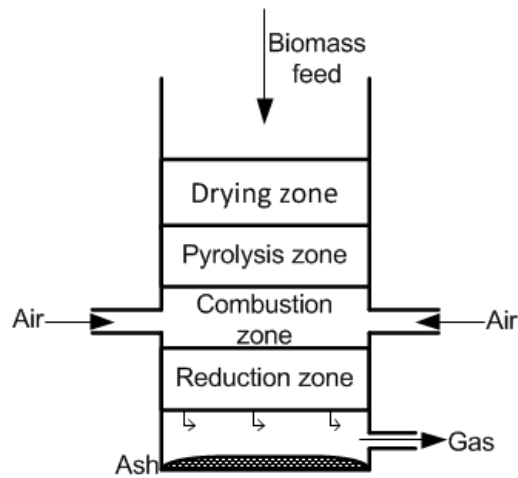


Figure 1.7: Reaction zones in a downdraft fixed bed biomass gasifier

On the other hand, in fluidized bed gasifiers the oxidant is blown through a bed of solid biomass particles at an adequate velocity to keep the particles in a state of suspension (Puig-Arnavat et al., 2010). In the case of *in-situ* catalytic fluidized bed gasifier (through mixing the catalyst with the biomass feedstock) the catalyst efficiency is low as coke deposits rapidly plug the active sites and prevent surface reactions (Richardson et al., 2012). Some advantages of fluidized bed gasifier over fixed bed gasifiers include the uniform and controllable temperature distribution and ability to accommodate a flexible feed rate and composition (Cui and Grace, 2007). Nonetheless, these gasifiers are not economical for small-scale applications and also hard to scale down (Kaushal et al., 2010).

In entrained flow gasifiers, the biomass particles and the oxidant move in the same direction and the reaction occur in a dense cloud of fine particles (0.1-0.4mm) at high temperatures ($T > 1000^{\circ}\text{C}$) and pressures (19.7-69.1atm) (Zhang et al., 2010). Entrained flow gasifiers are instead commonly employed for coal processing as they can be slurry-fed that makes solid fuel feeding at high pressures inexpensive (Gómez-Barea and Leckner, 2010).

1.3 A New Integrated Catalytic Biomass Gasification

In recent years, to improve the quality of the product gas from biomass gasification the integration of pyrolysis and catalysis has gained research interest. Schmidt and co-workers have applied

integrated flash pyrolysis and catalysis in a single reactor with short contact times (millisecond time scales) for various applications (Skinner et al., 2011, Sun and Schmidt, 2011). Colby et al. (2008) applied the same method for converting cellulose into a clean syngas via a process termed as reactive flash volatilization (RFV). In the process, as depicted in Figure 1.8, the cellulose particles came into a direct contact with the top surface of a pre-heated fixed-bed of catalyst (Rh-Ce/ γ -Al₂O₃) that led to a complete conversion to syngas into a single autothermal millisecond gasifier. Therefore, as a whole, the process circumvented the need for downstream cleaning requirements of the product gas since it combines gasification, tar removal, and water-gas shift steps in the same reactor. The process is “autothermal” in that the endothermic reforming reactions proceed with the assistance of *in-situ* oxidation (or partial oxidation) of a portion of the feed hydrocarbons.

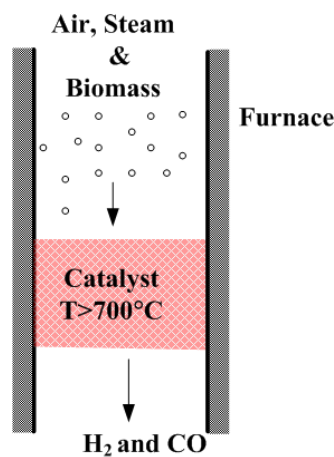


Figure 1.8: Schematic of the reactive flash volatilization gasifier (Colby et al., 2008)

Dauenhauer et al. (2007) and Colby et al. (2008) highlighted that reactive flash volatilization gasifier has a simple design and is smaller by at least an order of magnitude than the conventional gasifiers as it requires a much shorter residence time as shown in Figure 1.9.

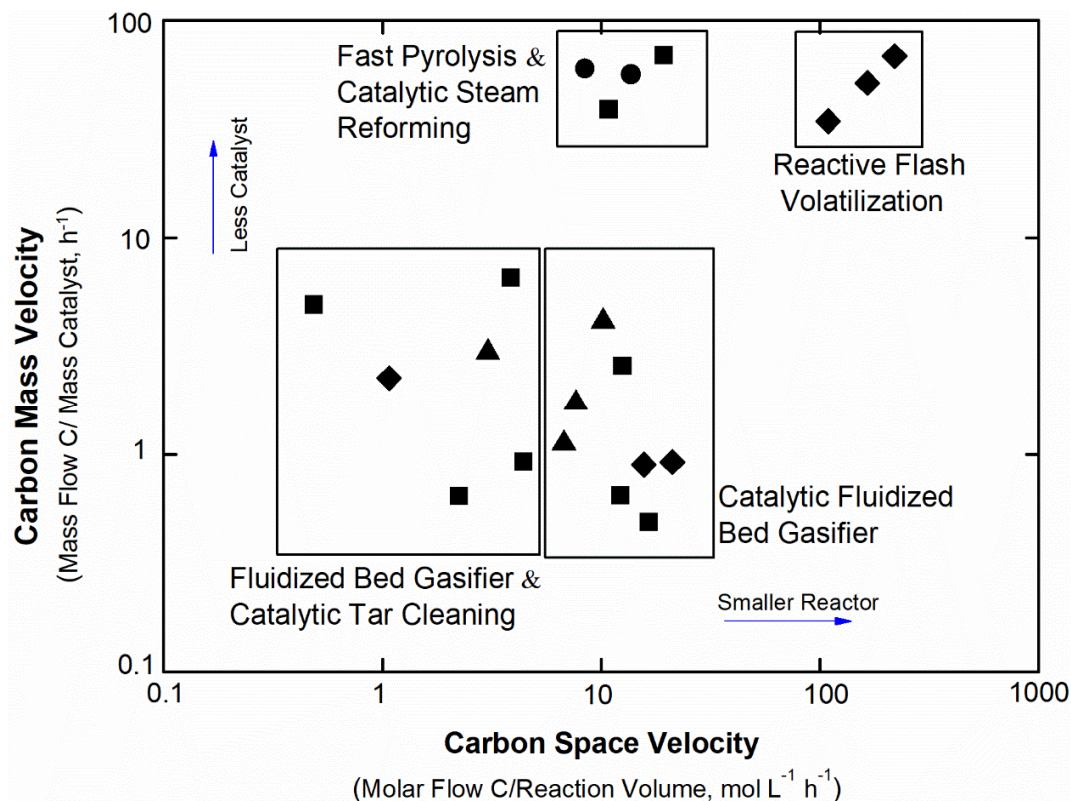


Figure 1.9: Operation performance of the various processes involved in syngas production grouped by process type despite utilizing different catalysts: dolomite (▲), Ni (■), Rh (◆), and Ru (●) adapted and redrawn from (Colby et al., 2008)

1.4 Scope of the Study

As discussed, one of the major challenges facing biomass utilization is the high cost associated with its collection and transportation. A more direct solution is to install an efficient compact reactor near to the sources of biomass, which has minimal tar or char production. This research is directed to the design of such a reactor. The present study aims to evaluate the kinetics of reactive flash volatilization using primary tar compounds derived from the cellulose and lignin fraction of lignocellulosic biomass in order to obtain valuable information towards the understanding of the reaction behaviour.

1.4.1 Research Aims

The specific aims of this project are:

- To develop a one-dimensional flow model to investigate the influence of two-phase flow on the heating rate of a cellulose particle before it reaches the catalytic bed.
- To develop a thermodynamic equilibrium model using the Aspen Plus simulation package to represent reactive flash volatilization of cellulose. This will allow to obtain preliminary information about the nature of the process and to identify any limitations of the modelling approach.
- To conduct experimental analysis of air-steam reforming of primary tar compounds derived from cellulose and lignin pyrolysis (acetol and guaiacol, respectively). This will allow to identify optimal operating conditions for a clean syngas, free of tar and char, production.
- To conduct kinetic analysis of primary tar conversion in the reactor freeboard
- To develop a kinetic model of the autothermal reforming of primary tar (acetol) using Aspen Plus considering reactions that occur both in the reactor freeboard and in the catalytic bed. The model can then be used to evaluate the influence of the reactions on the molar ratio of H₂ and CO in the product gas.

1.5 Thesis Structure and Chapter Outline

This thesis is presented in seven chapters:

Chapter 1: Introduction

This chapter provides the overall motivation of the research conducted in this thesis. The research aims and the thesis outlines are also presented.

Chapter 2: Literature Review

This chapter provides a critical review of the recent advances in *in-situ* catalytic tar conversion, in particular reactive flash volatilization. The use of a limited oxygen supply in catalytic steam reforming of bio-oil is reported to have suppressed carbon formation and hence improved catalyst

stability. However, in the published literature, there are only a few studies on catalytic air-steam reforming of bio-oil or bio-oil model compounds. The kinetic and reaction mechanism of this process is also not well established. An upstream freeboard design has been indicated to lessen carbon formation as well. The nature and extent of the bio-oil conversion in the freeboard has however not been studied.

Chapter 3: Thermodynamic Equilibrium Model for Reactive Flash Volatilization of Cellulose using Aspen Plus

This chapter discusses an equilibrium model of reactive flash volatilization of cellulose developed using the Aspen Plus simulation package. The work aimed to obtain preliminary information about the process by modelling it as three distinct process steps in the gasifier: pyrolysis of cellulose, partial oxidation of volatiles, and steam reforming of products from the partial oxidation. When compared to experimental product distribution data from the literature, some deviations from equilibrium were observed which form the research questions addressed in this thesis.

Chapter 4: Experimental Methods

This chapter discusses the experimental methods for kinetic study of air-steam reforming of the bio-oil model compounds: acetol and guaiacol. Acetol has the second highest content in the aqueous fraction of bio-oil. The methoxy (CH_3O) group found in guaiacol can easily polymerise to carbonaceous deposits. Hence, this study aimed to examine the extent of conversion, catalyst stability, and potential carbon forming reaction conditions for the conversion of these important model compounds into syngas. Such information regarding the process cannot merely be captured by an equilibrium model. A quartz reactor with a freeboard (25mm OD) that was designed to be a well-mixed zone and a catalyst bed of 10mm OD was used for the study. A low-cost nickel-based catalyst with a 1 wt% rhodium promoter ($1\%\text{Rh}-10\%\text{Ni}/\gamma\text{-Al}_2\text{O}_3$) was used.

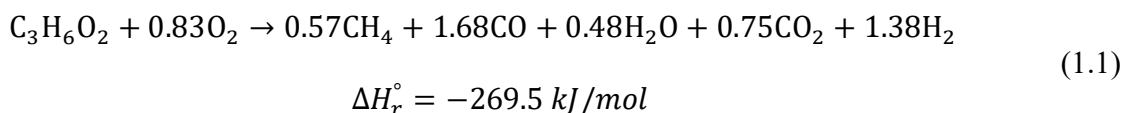
Chapter 5: Experimental Results

This chapter presents experimental findings from the kinetic study of air-steam reforming of the bio-oil model compounds. In contradiction to our initial hypothesis that most of the bio-oil could reach the catalyst bed, it was found that at 650°C more than 60 percent of the carbon in the acetol

feed was converted to C₁ compounds in the reactor freeboard. The gas leaving the catalyst bed was rich in H₂ and CO unlike the equilibrium distribution (rich in H₂ and CO₂). To avoid secondary tar and char formation, a minimum reaction temperature of 500°C was required for acetol and 600°C for guaiacol. The partial pressure of steam in the feed stream was also a key operating parameter that influenced the H₂/CO ratio in the final product gas.

Chapter 6: Kinetic Model of Air-Steam Reforming of Acetol

This chapter presents findings from a kinetic-based simulation model of air-steam reforming of acetol. By fitting experimental gas composition data to a proposed global reaction scheme, a stoichiometric overall reaction for acetol conversion in the freeboard was obtained, Equation 1.1.



Two reactor models in series: a CSTR followed by a PFR, represented the acetol conversion process well. The catalytic reforming reactions involving steam were modelled in the PFR. Depending on the final application of the syngas, the catalyst bed height can be varied as it influences the final gas composition via the water-gas shift reaction.

Chapter 7: Conclusions and Recommendations

This chapter draws conclusions from the thesis and gives suggestions for future experiments to extend the work. The air-steam reforming of volatiles in reactive flash volatilization of biomass occurs in two parts: partial oxidation followed by steam reforming within the catalyst bed. The conversion of the volatiles into intermediates that can easily be reformed catalytically avoids carbon deposition on the catalyst bed. The experimental and modelling kinetic studies assist the understanding of the conversion behaviour of the primary tar model compounds. Thus, findings from the current study can help to improve direct processing of biomass in short contact time reactors through the advancements in the understanding of the process. For future studies, it is proposed to test the process using a mixture of acetol and guaiacol and other catalyst promoters to further cut down the cost of the catalyst.

References

- Anderson, L. L. 1982. A Comparison of Biomass and Coal as Feedstocks for Synthetic Fuels. *In*: Sarkanen, K. V., Tillman, D. A. & Jahn, E. C. (eds.) *Progress in Biomass Conversion*. Elsevier.
- Balat, M., Balat, M., Kırtay, E. & Balat, H. 2009. Main routes for the thermo-conversion of biomass into fuels and chemicals. Part 1: Pyrolysis systems. *Energy Conversion and Management*, 50, 3147-3157.
- Chen, H. 2014. *Biotechnology of lignocellulose : theory and practice* Springer, Dordrecht.
- Corella, J. & Sanz, A. 2005. Modeling circulating fluidized bed biomass gasifiers. A pseudo-rigorous model for stationary state. *Fuel Processing Technology*, 86, 1021-1053.
- Cui, H. & Grace, J. R. 2007. Fluidization of biomass particles: A review of experimental multiphase flow aspects. *Chemical Engineering Science*, 62, 45-55.
- Dauenhauer, P. J., Dreyer, B. J., Degenstein, N. J. & Schmidt, L. D. 2007. Millisecond reforming of solid biomass for sustainable fuels. *Angewandte Chemie International Edition*, 46, 5864-5867.
- De Wild, P. J. 2015. Chapter 8 - Biomass Pyrolysis for Hybrid Biorefineries A2 - Pandey, Ashok. *In*: Höfer, R., Taherzadeh, M., Nampoothiri, K. M. & Larroche, C. (eds.) *Industrial Biorefineries & White Biotechnology*. Amsterdam: Elsevier.
- Devi, L., Ptasiński, K. J. & Janssen, F. J. J. G. 2003. A review of the primary measures for tar elimination in biomass gasification processes. *Biomass and Bioenergy*, 24, 125-140.
- Gómez-Barea, A. & Leckner, B. 2010. Modeling of biomass gasification in fluidized bed. *Progress in Energy and Combustion Science*, 36, 444-509.
- Global Syngas Technologies Council (GSTC), website last accessed on 5/23/18: https://www.google.com.au/search?q=global+outlook+of+syngas+Gasification+Technologies+Council&safe=strict&rlz=1C1JZAP_enAU742AU742&source=lnms&tbn=isch&sa=X&ved=0ahUKEwiEtLi8hJrbAhWFn5QKHbUNDPIQ_AUICygC&biw=1280&bih=615#imgcr=565-xNUGEL9d9M:
- Hofbauer, H., Rauch, R. & Ripfel-Nitsche, K. 2007. Report on Gas Cleaning for Synthesis Applications. ThermalNet 2E.3.
- Kaushal, P., Abedi, J. & Mahinpey, N. 2010. A comprehensive mathematical model for biomass gasification in a bubbling fluidized bed reactor. *Fuel*, 89, 3650-3661.

- Koufopoulos, C. A., Papayannakos, N., Maschio, G. & Lucchesi, A. 1991. Modelling of the pyrolysis of biomass particles. Studies on kinetics, thermal and heat transfer effects. *The Canadian Journal of Chemical Engineering*, 69, 907-915.
- Matar, S., Mirbach, M. J. & Tayim, H. A. 1989. Production and Uses of Synthesis Gas. In: Matar, S., Mirbach, M. J. & Tayim, H. A. (eds.) *Catalysis in Petrochemical Processes*. Dordrecht: Springer Netherlands.
- Mckendry, P. 2002. Energy production from biomass (part 3): conversion technologies. *Bioresource Technology*, 83, 47-54.
- Mondal, P., Dang, G. S. & Garg, M. O. 2011. Syngas production through gasification and cleanup for downstream applications — Recent developments. *Fuel Processing Technology*, 92, 1395-1410.
- Moneti, M., Di Carlo, A., Bocci, E., Foscolo, P. U., Villarini, M. & Carlini, M. 2016. Influence of the main gasifier parameters on a real system for hydrogen production from biomass. *International Journal of Hydrogen Energy*, 41, 11965-11973.
- Morf, P., Hasler, P. & Nussbaumer, T. 2002. Mechanisms and kinetics of homogeneous secondary reactions of tar from continuous pyrolysis of wood chips. *Fuel*, 81, 843-853.
- Puig-Arnavat, M., Bruno, J. C. & Coronas, A. 2010. Review and analysis of biomass gasification models. *Renewable and Sustainable Energy Reviews*, 14, 2841-2851.
- Richardson, Y., Blin, J. & Julbe, A. 2012. A short overview on purification and conditioning of syngas produced by biomass gasification: Catalytic strategies, process intensification and new concepts. *Progress in Energy and Combustion Science*, 38, 765-781.
- Searcy, E., Flynn, P., Ghafoori, E. & Kumar, A. 2007. The relative cost of biomass energy transport. *Applied Biochemistry and Biotechnology*, 137, 639-652.
- Skinner, M. J., Michor, E. L., Fan, W., Tsapatsis, M., Bhan, A. & Schmidt, L. D. 2011. Ethanol dehydration to ethylene in a stratified autothermal millisecond reactor. *ChemSusChem*, 4, 1151-1156.
- Spath, P. L. & Dayton, D. C. 2003. Preliminary Screening - Technical and Economic Assessment of Synthesis Gas to Fuels and Chemicals with Emphasis on the Potential for Biomass-Derived Syngas. Golden, Colorado: National Renewable Energy Laboratory.
- Sun, H. & Schmidt, L. D. 2011. Methanol dehydration to dimethyl ether in a staged autothermal millisecond residence time reactor. *Applied Catalysis A: General*, 404, 81-86.
- Suriapparao, D. V., Pradeep, N. & Vinu, R. 2015. Bio-Oil Production from *Prosopis juliflora* via Microwave Pyrolysis. *Energy & Fuels*, 29, 2571-2581.

- Van Rossum, G., Kersten, S. R. A. & Van Swaaij, W. P. M. 2009. Staged Catalytic Gasification/Steam Reforming of Pyrolysis Oil. *Industrial & Engineering Chemistry Research*, 48, 5857-5866.
- Zhang, L., Xu, C. & Champagne, P. 2010. Overview of recent advances in thermo-chemical conversion of biomass. *Energy Conversion and Management*, 51, 969-982.

Chapter 2

Literature Review

2.1 Reactive Flash Volatilization

During reactive flash volatilization of cellulose Dauenhauer et al. (2007) observed that the solid particles underwent pyrolysis on the surface of the hot catalyst bed forming a film of bio-oil as seen in Figure 2.1.

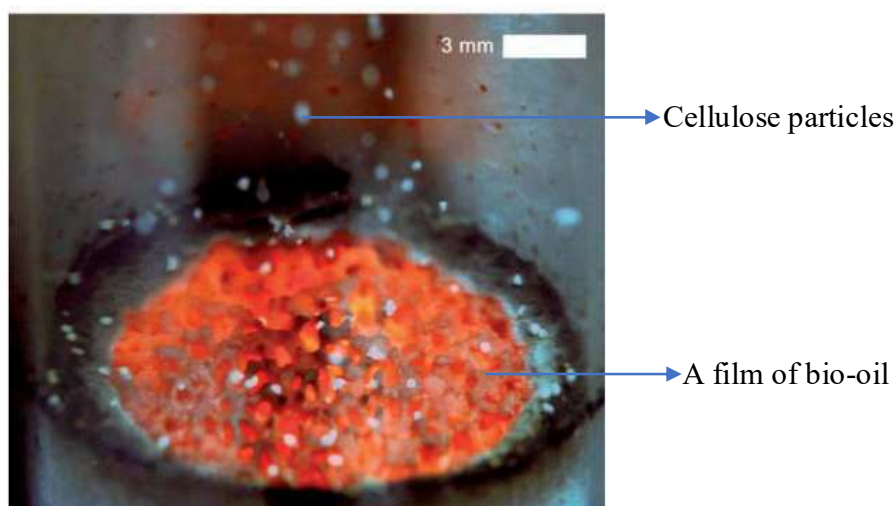


Figure 2.1: Photograph of the front face of a catalyst used in reactive flash volatilization of cellulose particles (230mm) adapted from Dauenhauer et al. (2007) with permission from the publisher

With an aim to develop a low-cost catalyst that combines high activity and selectivity for syngas, Chan and Tanksale (2014) investigated the performance of various nickel-based catalysts supported on gamma alumina with noble metal promoters (Ru, Rh, and Re) for reactive flash volatilization of cellulose. The Re-promoted nickel catalyst showed superiority in activity (the least tar and char formation) followed by the Rh- and Ru-promoted catalysts. The same authors (Chan et al., 2015) also performed thermal gravimetric analysis of reactive flash volatilization of cellulose. From the mass-loss curve that had three distinct weight loss stages (Figure 2.2), the

authors proposed that pyrolytic decomposition of the solid is followed by reforming and char gasification reactions in that order.

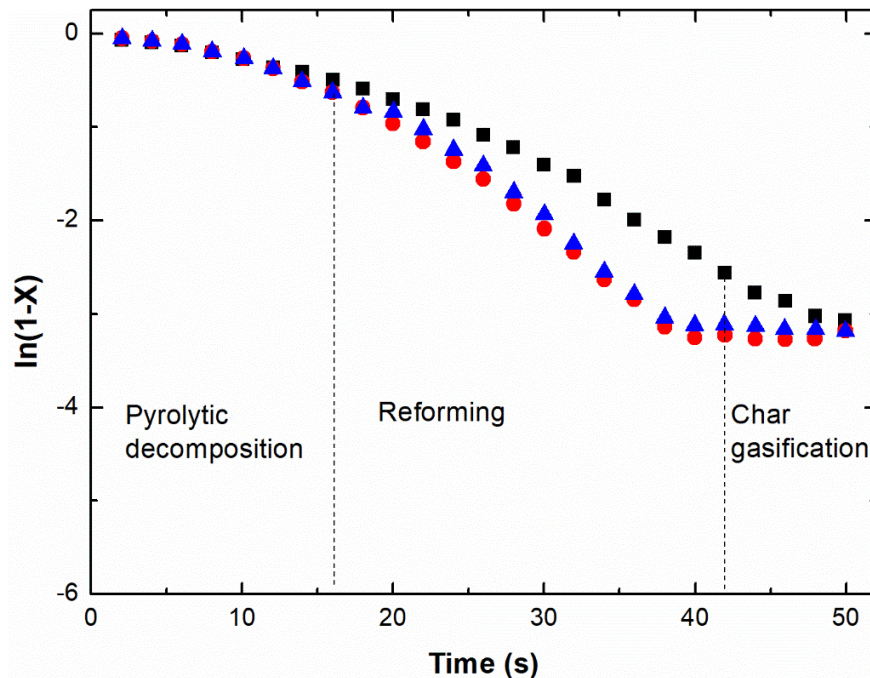


Figure 2.2: Decomposition characteristic of cellulose by reactive flash volatilization using a thermogravimetric analyser at 700°C with catalysts: ■ Re-Ni, ● Rh-Ni, ▲ Ru-Ni adapted from Chan et al. (2015).

To elucidate the reaction chemistry involved in this promising technology, it is important to decouple the pyrolysis chemistry of the solids from the gasification reactions (reforming) involving oxygen and steam. Such an approach can allow to analyse the contribution of the gasifying agents (oxidants) in converting the bio-oil (primary tar compounds) produced on or above the surface of the catalytic bed into a clean syngas free of tar and char. The research hypothesis is that in the presence of oxygen and catalyst, the primary tar compounds undergo partial oxidation and reforming reaction instead of condensation and polymerisation reactions which avoids secondary tar hence coke formation. Hence, the following subsections of this chapter discuss the research efforts to date directed at investigating syngas production from bio-oil with the main focus on air-steam gasification (autothermal reforming) of bio-oil.

2.2 Syngas Production from Bio-oil

Bio-oil is a complex mixture of oxygenates that fall under the following groups: ketones, aldehydes, carboxylic acids, alcohols, and anhydrosugars derived from the thermal breakdown of cellulose and hemicellulose, and phenolic and cyclic oxygenates derived from lignin (Wang et al., 1996). It also has a high-water content of 20-30 wt% (Branca et al., 2003). Table 2.1 shows a typical composition of crude bio-oil derived from pyrolysis of rice husk (Wang et al., 2013).

Table 2.1: A typical composition of crude bio-oil derived from pyrolysis of rice husk (Wang et al., 2013)

Group	Contents (%)	Some of the major oxygenates (%)
Ketones	28.88	Acetol (14.48%), 1-hydroxy-2-butanone (2.18%), and others
Aldehydes	9.32	Furfural (5.61%), 5-Methylfurfural (0.84%), and others
Acids	20.79	Acetic acid (18.18%), propanoic acid (1.27%), and others
Alcohols	0.64	2-Propen-1-ol (0.64%)
Sugars	2.29	d-Mannose (0.94%) and others
Phenols	34.51	Guaiacol (5.5%), 2-methoxy-4-methyl- (3.74%), and others
Others	1.80	Benzofuran, 2,3-dihydro- (1.09)

Although bio-oil has advantages pertaining to its high energy density and easy transportation (compared to raw biomass), improvement of the liquid quality is still a research focus (Bridgwater, 2012). Some of the limitations of bio-oil include issues with its thermal stability (the different oxygenates polymerise) and poor fuel properties such as high oxygen content, viscous, and acidic nature (Renny et al., 2016). Hence, researchers have examined upgrading of bio-oil or bio-oil derived model compounds to syngas through catalytic steam reforming, partial oxidation reforming, and autothermal catalytic reforming (Figure 2.3) (Zheng et al., 2016, Czernik and French, 2014).

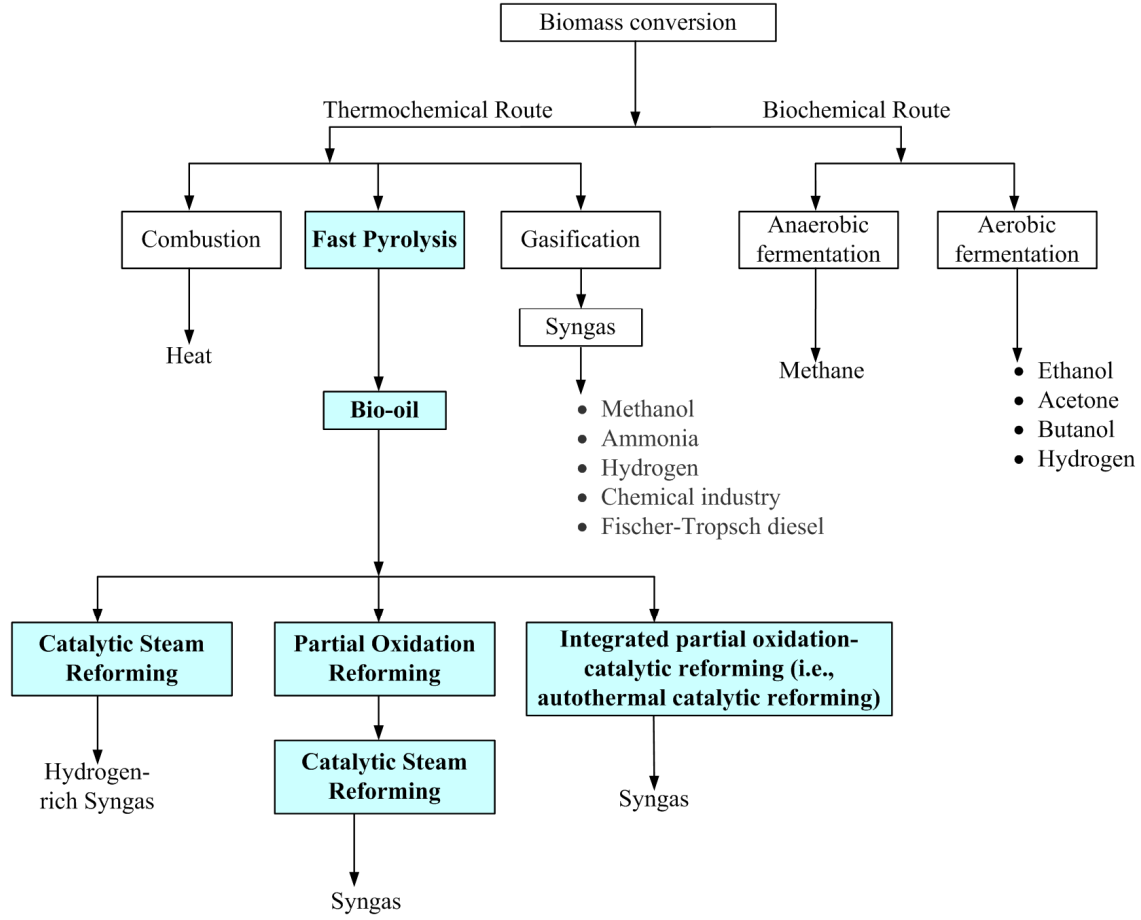
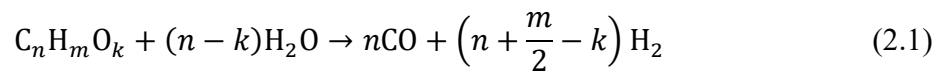


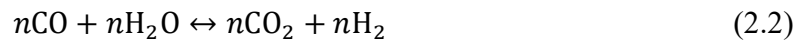
Figure 2.3: Possible routes for bio-oil conversion to syngas

2.2.1 Catalytic Steam Reforming of Bio-oil

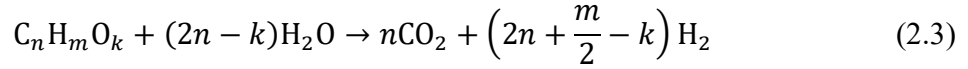
Catalytic steam reforming of bio-oil oxygenates ($C_nH_mO_k$) can be represented by Equation 2.1 (Salehi et al., 2011):



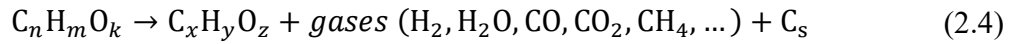
The reforming reaction is accompanied by water-gas shift reaction which governs the final product distribution:



Thus, the complete steam reforming of bio-oil is represented as:



The theoretical maximum hydrogen yield from steam reforming of bio-oil can be estimated based on the stoichiometry of the overall reaction (2.3). However, because oxygenates are thermally unstable at high temperatures (Trane et al., 2012), partial thermal decomposition (Equation (2.4) (Wang et al., 1996)) also occurs simultaneously which can reduce the hydrogen yield from its stoichiometric potential. Other side reactions that can influence hydrogen yield directly or indirectly include methanation reaction (2.5) and Boudouard reaction (2.6).



Chhiti et al. (2011) conducted studies of a non-catalytic steam reforming of pyrolysis oil in an entrained flow reactor at a capacity of 18 g/h. In that work, thermodynamic equilibrium concentration of the gases was only established at temperatures above 1250°C when the steam to bio-oil mass ratio of 4.5 was employed. In a separate study by Trane et al. (2013) in steam reforming of ethanol without a catalyst only 15% carbon conversion was obtained at 700°C.

A number of studies in the literature have demonstrated that adding a catalyst in steam reforming of bio-oil has led to an improved carbon-to-gas conversion and a higher hydrogen yield under relatively lower reaction temperatures often <850°C. At temperatures close to 800°C, Rioche et al. (2005) obtained high hydrogen yield (~60% of the stoichiometric potential) and carbon-to-gas conversion of 90% from steam reforming of beech wood pyrolysis oil over Rh and Pt catalysts with S/C ratio of 10.8. Latif et al. (2014) reported 80% increase in hydrogen yield and an increase in carbon conversion from 79% to 93.1% upon adding a commercial nickel-based catalyst in steam reforming of acetic acid at 700°C, a reaction time of 30s, and S/C of 3. In steam reforming of acetol at 650°C and S/C molar ratio of 5.58, by using a 33% Ni-Al catalyst an increase in carbon

conversion from 24% to 74% and hydrogen yield (0.017 to 0.119 g/g) was obtained by Bimbela et al. (2009). Domine et al. (2008) and Galdámez et al. (2005) also observed that catalyst addition enhanced H₂ productivity and lowered CH₄ formation. In general, adding a catalyst in bio-oil steam reforming not only increases reaction rates (i.e., higher carbon-to-gas conversion), but can also help to adjust the elementary steps to prevent net carbon deposition and water formation (Edwards and Maitra, 1995, Van Rossum et al., 2007).

The National Renewable Energy Laboratory (NREL) has extensively investigated catalytic steam reforming of bio-oil for syngas production (Czernik and French, 2014, Czernik et al., 2007, Czernik et al., 2002). Considerable research effort has also been devoted to catalytic steam reforming of bio-oil model compounds owing to their well-defined structures that can help to gain insights into the catalytic activity (reaction behaviour) and deactivation mechanisms (Baviskar and Vaidya, 2017). In particular, acetic acid from the acids fraction of oxygenates in bio-oil (Hu et al., 2017) and bio-ethanol (Bussi et al., 2017) are the two widely studied model compounds. To allow comparison of steam reforming of different bio-oil oxygenates at similar conditions, Trane et al. (2013) investigated steam reforming of acetol (C₃H₆O₂), ethanol (C₂H₆O), acetic acid (C₂H₄O₂), acetone (C₃H₆O), 1-propanol (C₃H₈O), and propanal (C₃H₆O) over Ni/MgAl₂O₃ catalyst. With a steam to carbon ratio of 6 and temperatures between 400 and 700°C, a higher fraction of by-products (olefines, aldehydes, and hydrocarbons) was produced from the C₃-oxygenates compared to the C₂-oxygenates. In their experiments, catalyst deactivation was observed and was most pronounced for acetol and acetic acid. The reaction temperature had to be kept above 600°C to minimize the fraction of the by-products. The authors also emphasized that stable operation would require high steam to carbon ratios or oxidative reforming.

Catalytic steam reforming of bio-oil is still at an early stage of development mainly due to catalyst deactivation issues from carbon deposition and thermal sintering (Trane et al., 2012, 2013). The selectivity of a catalyst determines the extent of carbon deposition (Wang et al., 1997). Depending on feedstock, temperature, and steam to carbon ratio (S/C) in use, carbon deposits can be formed through, for example, the Boudouard reaction, methane decomposition, and polymerisation of ethene and propene as given in Table 2.2. Carbon monoxide and methane decompose to produce surface atomic carbon. Other higher hydrocarbons may also undergo polymerisation followed by

dehydropolymerisation on the catalyst surface to form an amorphous carbon film which with further aging can lead to graphitic carbon (Gutierrez Ortiz et al., 2017), and precipitation may also take place to form whiskers carbon (graphene tubes) (Cheng et al., 2011a, Trane et al., 2012). Wu and Liu (2010) showed that an increase in steam to carbon ratio suppressed carbon deposition due to steam gasification of the deposited carbon and also because the temperature window between the high and low temperature carbon formation increases with S/C (Trane et al., 2012).

Table 2.2: Cracking reactions that can lead to carbon deposition

Reaction name	Reaction
Boudouard	$2\text{CO} \leftrightarrow \text{C}_s + \text{CO}_2$
Methane decomposition	$\text{CH}_4 \leftrightarrow \text{C}_s + 2\text{H}_2$
Polymerisation	$\text{C}_n\text{H}_m \rightarrow \text{Coke precursors}(\text{olefins} + \text{aromatics}) \rightarrow \frac{m}{2}\text{H}_2 + n\text{C}_s$

In the literature, several methods have been proposed to overcome the issue of carbon deposition on catalyst surfaces. One approach is to add water to bio-oil to separate the aqueous fraction (containing mainly carbohydrate-derived oxygenates such as acetol and acetic acid) from the hydrophobic phase containing lignin-derived oligomers (Galdámez et al., 2005). The aqueous phase is then utilized for catalytic steam reforming experiments (Seyedeyn-Azad et al., 2014). That is primarily because reforming of the water-insoluble fraction can easily form carbon deposits on catalysts (Zheng et al., 2016). A thermal repolymerisation treatment at 500°C has also been applied by Remiro et al. (2013) to separate lignin-derived components from the hydrophilic phase. Nevertheless, in a work by Wang et al. (1997) steam reforming of the aqueous phase separately reduced the hydrogen yield while a prolonged high catalytic activity was achieved.

Development of new catalysts to improve the resistance to carbon deposition and sintering is another option to mitigate the problem with catalyst deactivation. Generally, noble metal catalysts (i.e., Rh, Ru, and Pt) are found to be less prone to carbon deposition (Chhiti et al., 2011, Rennard et al., 2010, Peela and Kunzru, 2011). Nevertheless, these metals are expensive. Instead, in the literature, nickel-based catalysts have widely been studied for steam reforming of oxygenates due

to their relatively low cost, high tar destruction activity (C-C bond breaking), and their ability to promote methane reforming and water-gas shift reactions (Marda et al., 2009). However, these catalysts suffer from a rapid deactivation due to carbon deposition (Guan et al., 2016) and sintering (Mondal et al., 2015). Hence, to maintain their stability over an extended period and enhance their resistance towards carbon deposition, other metals such as Co, Cr, Ca, Ce, Mg, Mn, and Zn have been added to catalyst precursors (Yao et al., 2014). Garcia et al. (2000) showed that cobalt and chromium additives reduced coke formation presumably via slowing down the surface reactions leading to the formation of the coke precursors. Medrano et al. (2011) used Ni-Al catalysts modified with Ca or Mg for catalytic steam reforming of the aqueous fraction of bio-oil. The addition of calcium had rather an undesirable effect that led to the formation of more carbonaceous products while the magnesium enhanced the water-gas shift reaction. In the work by Salehi et al. (2011) adding 12.8 % MgO as a promoter to 18% Ni/Al₂O₃ catalyst led to an increase in hydrogen yield from 54% to 62% in steam reforming of bio-oil (CH_{1.87}O_{0.754}) at 850°C with a low carbon deposition of 8.6%. The same authors also demonstrated that a 0.5% Ru as a promoter is more effective than the 12.8% MgO in terms of both hydrogen yield (77%) and carbon deposition (6%) at the reaction temperature of 850°C. Such observations signify the important role of catalyst additives (promoters) on the quantity and type of carbon deposits (Chen et al., 2017).

To enable protection of the catalyst from deactivation, van Rossum et al. (2007) proposed a two-stage reactor concept consisting of a sand fluidized bed (432-500°C) followed by a fixed catalytic bed (>700°C). The evaporation and cracking of the oil happened in the fluidized bed while the catalytic conditioning of the produced gases occurred in the fixed catalytic bed. From a bench scale unit of the reactor (0.5 kg bio-oil/h), a methane and C₂-C₃ free syngas was produced with H₂/CO molar ratio of 2.6 and a tar content of 0.2 g/Nm³. Besides the tar produced, the carbon yield was also less than 100% which indicates that carbon deposition was still present. Despite much research trying to find a catalyst which is active in reforming bio-oil and also able to maintain activity over a sustained period, to date no such catalyst has been developed. The most significant research involves the use of oxygen and this leads to the next section which presents the work on air-steam gasification.

2.2.2 Air-Steam Gasification (Autothermal Reforming) of Bio-oil

Hydrogen-rich syngas with hydrogen yield (Equation (2.7)) of as high as 95% can be obtained from catalytic steam reforming of bio-oil at relatively high steam to carbon ratios (e.g., S/C=9 (Remiro et al., 2013)). However, the steam reforming reactions are highly endothermic requiring external heat (Marda et al., 2009). The main research goal in bio-oil gasification then focuses on finding ways to operate the process at moderate temperatures (<950°C) without compromising on the amount and quality of syngas being produced and make the process economically viable (Van Rossum et al., 2009). Hence, the addition of oxygen as an oxidizing agent besides the steam is desirable because the oxidative chemistry within the reactor can potentially alleviate the heat loads (Rennard et al., 2010). Van Rossum et al. (2007) observed no additional loss of catalyst activity with time due to the presence of a limited amount of oxygen for nickel-alumina catalysts. Therefore, one way to implement the addition of oxygen to catalytic steam reforming processes can be through a non-catalytic partial oxidation of bio-oil followed by a second step involving catalyst for further reforming and water-gas shift reactions (Marda et al., 2009). The second approach is to have both partial oxidation and catalytic steam reforming reactions occur in a single reactor as illustrated previously in Figure 2.3.

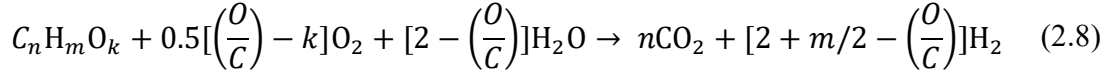
$$\text{Hydrogen Yield } (Y_{H_2}) = \frac{N_{H_2}}{N_{H_2}^{\circ}} \times 100 \quad (2.7)$$

where N_{H_2} is the molar flow rate of H_2 in the product stream and $N_{H_2}^{\circ}$ is the stoichiometric maximum of the bio-oil fed to the reactor according to reaction (2.3).

2.2.2.1 *Non-Catalytic Partial Oxidation of Bio-oil with or without Steam Addition*

In the presence of oxygen, the stoichiometric potential for hydrogen production from air-steam gasification of bio-oil can be calculated based on the overall reaction in Equation (2.8). The reaction is based on the assumption that all the reactions involving oxygen, steam, and the water-gas shift reaction go to completion (García-García et al., 2015). The added oxygen might reduce

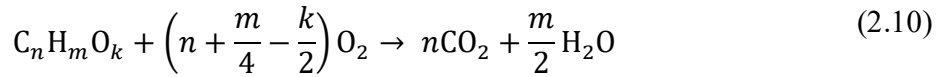
the stoichiometric hydrogen yield that can be obtained from steam reforming as some of the hydrogen could oxidize to form water (Czernik and French, 2014, Rioche et al., 2005).



where the O/C represents the ratio between the moles of oxygen atom in the molecular oxygen and the moles of carbon in organic feed.

Equivalence ratio (λ) (Equation (2.9)) in air and air-steam gasification of bio-oil is defined as the percentage of oxygen added for total combustion of the bio-oil according to the following reaction (2.10) (Van Rossum et al., 2007):

$$\lambda = \frac{\text{Actual oxygen supplied}}{\text{Stoichiometric oxygen required for complete combustion}} \quad (2.9)$$



Bio-oil cannot be completely vaporized due to its tendency to polymerise at temperatures higher than 80°C (Van Rossum et al., 2007). Hence, to prevent charring/deposition of lignin-derived oxygenates on piping and reactor walls, methanol is often added to reduce its viscosity and enhance its stability to help facilitate atomization (Rennard et al., 2010). Marda et al. (2009) obtained a hydrogen yield of 25% of the stoichiometric potential by a non-catalytic partial oxidation of a 50/50 (wt%) poplar bio-oil ($CH_{1.32}O_{0.46} \cdot 0.23H_2O$) and methanol mixture at equivalence ratios between 0.3 and 0.35. Although a high carbon conversion efficiency of up to 95% was achieved, the product gas contained aromatic hydrocarbons such as benzene and other poly-aromatic hydrocarbons (PAHs). A significant amount of H_2O with a yield of 50-60% was also produced from the reaction. The addition of oxygen enhanced the conversion of larger aromatic species to smaller molecules when compared to the pyrolysis of the same feed without oxygen as shown in Figure 2.4.

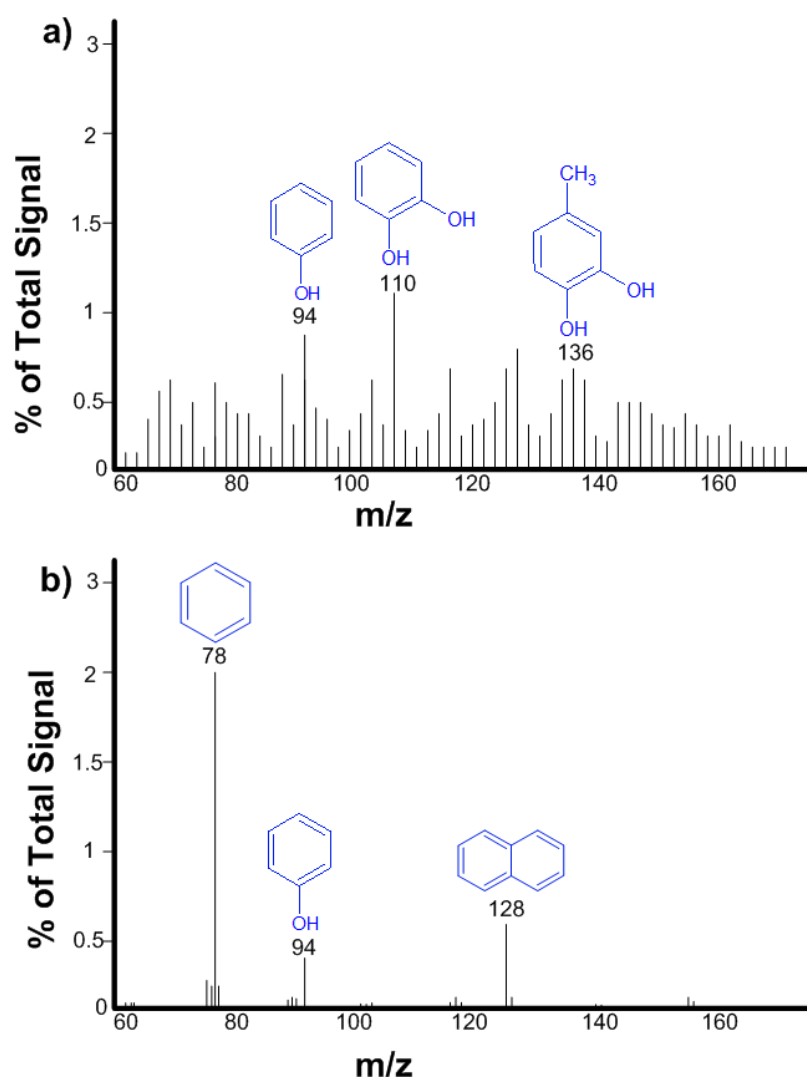


Figure 2.4: The influence of oxygen on the distribution of products a) pyrolysis and b) partial oxidation (Marda et al., 2009)

In a recent work by Zheng et al. (2017) a maximum hydrogen composition of 45 vol% (on dry and N₂ free basis) was produced from air-steam gasification of bio-oil (C_{3.48}H_{4.9}O_{1.74}·1.4H₂O) with a steam to bio-oil ratio of 2.5 and equivalence ratio of 0.4. The reaction happened in an entrained flow gasifier (L=1000mm and 60 mm OD) heated externally to 1000°C. The steam to bio-oil ratio had an optimum point of 2.5 while there was a linear relationship between product gas composition and temperature. The authors highlighted that the steam to bio-oil ratio was a more important parameter for improving the bio-oil gasification performance than the equivalence ratio. One not

so common finding in their work was the decreasing trend of carbon monoxide composition in the product gas with increasing temperature in which the authors proposed that the equilibrium of water-gas shift reaction might not have been reached. The product gas contained comparatively high CO₂ content (>30 vol%).

2.2.2.2 Integrated Partial Oxidation-Catalytic Steam Reforming

A staged partial oxidation-catalytic steam reforming of 90/10 wt% of poplar bio-oil/methanol solution over 1%Rh-1%Ce/Al₂O₃ catalyst was investigated by Rennard et al. (2010). The liquid in a form of fine mist contacted with air and steam in a 32 mm ID and 45 cm long tubular quartz reactor that contained a fixed bed of catalyst in the bottom section. A carbon-to-gas conversion of 91% and hydrogen yield of 7.2 g per 100 g bio-oil was obtained. Nevertheless, the increasing trend of CH₄ concentration in the product gas indicated that catalyst deactivation was underway. The authors highlighted that an upstream freeboard design can help to lessen coke and ash formations which are the main challenges with direct catalytic partial oxidation of bio-oil. Lui et al. (2013) analysed the effect of the distance between an atomizer nozzle and catalyst bed on reactor performance for autothermal reforming of glycerol in dual layer monolith catalyst (BASF Pt and Rh/Pt). The authors identified the optimal operating conditions to produce high yields of H₂ and CO (i.e., H₂/CO molar ratio of 2) with minimal coke formation were the distance between the atomizer and the catalyst bed to be 2 in, O₂/C of 0.15, S/C of 0.8, temperature of 650°C, and atmospheric pressure. The presence of steam in the catalytic processes also helps to prevent formation of hot spots in catalytic beds.

Using a commercial 0.5% Pt/Al₂O₃ catalyst, Czernik et al. (2014) from NREL obtained a hydrogen yield of as high as 83% of the stoichiometric potential (11g H₂/100g bio-oil) from a catalytic reforming of volatilized bio-oil vapours accompanied by further water-gas shift conversion at a low temperature (350°C) over a Fe/Cr catalyst in a second reactor (Figure 2.5). In their experiments, the carbon-to-gas conversion lay in the range of 70-89%. The different operating conditions analysed were S/C ratio (2.8-4.0), the reformer temperature (800°C-850°C), and oxygen to carbon ratio (0.9-1.1). The non-volatile residue (oligomeric lignin and carbohydrates) from the bio-oil

feed (11%-30% of the bio-oil carbon) was retained in the evaporator while the remaining volatile oxygenates were reformed.

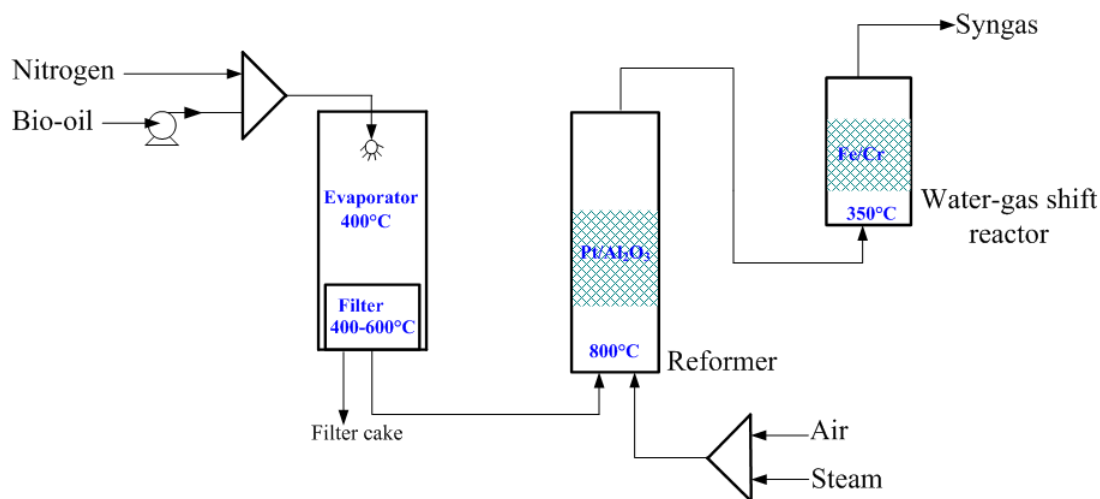


Figure 2.5: The configuration of a bench scale bio-oil reforming reactor system used by Czernik and French (2014)

Mondal et al. (2015) investigated the effects of temperature, ethanol-to-steam molar ratio, ethanol-to-oxygen molar ratio, and space-time on catalytic steam reforming of bio-ethanol over 30%Ni/CeO₂-ZrO₂ and 1%Rh-30%Ni/CeO₂-ZrO₂ catalysts. Rh improved the catalytic activity (conversion from 91 to 100% and hydrogen yield from 3.5 to 4.6 mol/mol) of the 30%Ni/CeO₂-ZrO₂ catalyst by promoting methane steam reforming and water-gas shift reactions. H₂ selectivity increased with increasing contact time while CO and CH₄ selectivity decreased. The complete ethanol conversion was achieved at 600°C with a maximum hydrogen yield of 4.6 mol/mol on the 1%Rh-30%Ni/CeO₂-ZrO₂ catalyst.

2.3 Kinetics of Catalytic Steam Reforming of Bio-oil

2.3.1 Reaction Schemes

Due to the chemical complexity of bio-oil, individual components present in bio-oil have instead been extensively studied to establish a correlation between the structure of bio-oil components and catalyst activity (Takanabe et al., 2006, Kumar et al., 2017). Most of these studies have focused on catalytic steam reforming of acetic acid (Galdámez et al., 2005) and ethanol. Reaction schemes

for steam reforming of oxygenates in the literature vary depending on the reaction conditions under which the studies were conducted: space-time, catalyst composition, and reactor type. Basing on kinetic data of a catalytic steam reforming of acetic acid at 550°C, S/C=6, and on NiO/MgO catalyst Yang et al. (2016) proposed the reaction scheme presented in Table 2.3. Acetone is one of the main intermediate compounds. Lemonidou et al. (2013) also found acetone as an intermediate product along with CH₃* in acetic acid reforming over Rh/La₂O₃/CeO₂-ZrO₂ catalyst. The ketonization and decarboxylation of acetic acid were dominating reactions up to 600°C, and while above 600°C steam reforming and water-gas shift reactions also contributed.

Table 2.3: Possible reactions during steam reforming of acetic acid (Yang et al., 2016)

Reaction	Chemical description
Ketonization	$2\text{CH}_3\text{COOH} \rightarrow \text{CH}_3\text{COCH}_3 + \text{CO}_2 + \text{H}_2\text{O}$
Steam reforming of acetone	$\text{CH}_3\text{COCH}_3 + 3\text{H}_2\text{O} \rightarrow 3\text{CO} + 6\text{H}_2$
Decomposition 1	$\text{CH}_3\text{COOH} \rightarrow \text{CH}_4 + \text{CO}_2$
Decomposition 2	$\text{CH}_3\text{COOH} \rightarrow 2\text{H}_2 + \text{CO}_2 + \text{C}$
Dehydration	$\text{CH}_3\text{COOH} \rightarrow \text{CH}_2\text{CO} + \text{H}_2\text{O}$
Steam reforming of ketene	$\text{CH}_2\text{CO} + \text{H}_2\text{O} \rightarrow 2\text{CO} + 2\text{H}_2$
Water-gas shift reaction	$\text{CO} + \text{H}_2\text{O} \leftrightarrow \text{CO}_2 + \text{H}_2$

The possible reactions in steam reforming of ethanol over a nickel-based catalyst (15%Ni/ γ -Al₂O₃) in a temperature range of 200 to 600°C with a steam-to-ethanol mole ratio of 10 are listed in Table 2.4 (Wu et al., 2014). Acetaldehyde, acetic acid, ethylene, and methane are the main intermediate products. In their work, surface decomposition of methane was identified as the rate-determining step in the process.

Table 2.4: Possible reactions during steam reforming of ethanol (Wu et al., 2014)

Reaction	Chemical description
Dehydration	$\text{CH}_3\text{CH}_2\text{OH} \rightarrow \text{C}_2\text{H}_4 + \text{H}_2\text{O}$
Dehydrogenation	$\text{CH}_3\text{CH}_2\text{OH} \rightarrow \text{CH}_3\text{CHO} + \text{H}_2$
Acetaldehyde decomposition	$\text{CH}_3\text{CHO} \rightarrow \text{CH}_4 + \text{CO}$
Direct ethanol decomposition	$\text{CH}_3\text{CH}_2\text{OH} \rightarrow \text{H}_2 + \text{CH}_4 + \text{CO}$
Steam reforming of acetaldehyde	$\text{CH}_3\text{CHO} + \text{H}_2\text{O} \rightarrow \text{H}_2 + \text{CO}_2 + \text{CH}_4$
Acetic acid formation	$\text{CH}_3\text{CHO} + \text{H}_2\text{O} \rightarrow \text{CH}_3\text{COOH} + \text{H}_2$
Acetic acid decomposition	$\text{CH}_3\text{COOH} \rightarrow \text{CH}_4 + \text{CO}_2$
Steam methane reforming	$\text{CH}_4 + \text{H}_2\text{O} \leftrightarrow \text{CO} + 3\text{H}_2$
Water-gas shift reaction	$\text{CO} + \text{H}_2\text{O} \leftrightarrow \text{CO}_2 + \text{H}_2$

A number of studies (Patel et al., 2013) have also proposed elementary surface reactions in the catalytic steam reforming of ethanol, which can help to obtain mechanistic Langmuir-Hinshelwood-Hougen-Watson (LHHW) and/or Eley-Rideal rate expressions. Based on the proposed reaction schemes, in the presence of steam the main sources of methane are either decomposition reactions or steam reforming of intermediate compounds. A study by Cheng et al. (2011b) found that methanation reaction did not play a major role during glycerol steam reforming.

2.3.2 Kinetic Models

Different models have been used for the design and optimisation of biomass gasification. By applying the integral method of analysis to experimental kinetic data Vaidya and Rodrigues (2006) reported a power law rate expression for steam reforming of ethanol over $\text{Ru}/\gamma\text{-Al}_2\text{O}_3$ catalyst in the temperature range of 873-973 K. The reaction was found to be first order with respect to ethanol and zero order for water with an activation energy value of 96 kJ/mol. For glycerol steam

reforming over Ni/CeO catalyst, Adhikari et al. (2009) found the activation energy and reaction order to be 103.4 kJ/mol and 0.233, respectively.

In a very recent work by Gayubo et al. (2018) a kinetic model for catalytic steam reforming of bio-oil over Ni/La₂O₃-αAl₂O₃ catalyst was reported. The set of reactions included in the model are given in Table 2.5. The rate equations for the bio-oil decomposition considered of the contribution of both the thermal and catalytic routes while the rest are only consequence of the catalyst activity. Arregi et al. (2018) also reported a kinetic model of catalytic steam reforming of bio-oil using *Matlab* as a modelling environment. The model considered four main reactions: the steam reforming of bio-oil, methane and C₂-C₄ hydrocarbons, and the water-gas shift reaction.

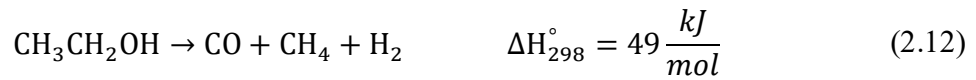
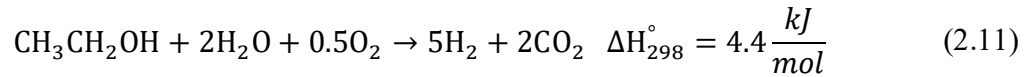
Table 2.5: Proposed reaction steps for bio-oil steam reforming over Ni/La₂O₃-αAl₂O₃ catalyst al. (Gayubo et al., 2018)

No	Reaction	Rate expressions
1	$C_{3.9}H_{6.1}O_{3.0} + 0.9H_2O \rightarrow 3.9CO + 3.95H_2$	$r_1 = \rho_b k_1 p_{bio} p_{H_2O}^{0.9}$
2	$CO + H_2O \leftrightarrow H_2 + CO_2$	$r_2 = \rho_b k_2 p_{bio} \left(p_{CO} p_{H_2O} - \frac{p_{H_2} p_{CO_2}}{K_{eq,2}} \right)$
3	$C_{3.9}H_{6.1}O_{3.0} \rightarrow 0.9CH_4 + 3CO + 1.25H_2$	$r_3 = \rho_b k_3 p_{bio} + k_3^t p_{bio} / p_{H_2O}^{\alpha_{H_2O}}$
4	$C_{3.9}H_{6.1}O_{3.0} \rightarrow 0.96C_2H_5 + 1.5CO_2 + 0.65H_2$	$r_4 = \rho_b k_4 p_{bio} + k_4^t p_{bio} / p_{H_2O}^{\alpha_{H_2O}}$
5	$CH_4 + H_2O \leftrightarrow 3H_2 + CO$	$r_2 = \rho_b k_2 p_{bio} \left(p_{CH_4} p_{H_2O} - \frac{p_{H_2} p_{CO_2}}{K_{eq,2}} \right)$
6	$C_{2.5}H_5 + 2.5H_2O \rightarrow 5H_2 + 2.5CO$	$r_6 = \rho_b k_6 p_{C_{2.5}H_5} p_w^{0.9}$

2.4 Kinetics of Air-Steam Reforming of Bio-Oil

2.4.1 Reaction Schemes

Mondal et al. (2016) used the reactions (2.11-2.12) and the water-gas shift reaction (2.2) to represent the oxidative steam reforming of ethanol over 1%Rh–30%Ni/CeO₂–ZrO₂ catalyst and reported corresponding LHHW rate expressions based on 19 elementary catalytic reaction steps.



A possible reaction scheme for ethanol reforming in presence of oxygen in the feed stream was proposed by Klouz et al. (2002) as given in Table 2.6.

Table 2.6: Possible reaction in steam reforming of ethanol in the presence of oxygen (Klouz et al., 2002)

Reaction	Chemical description
Dehydrogenation	$\text{CH}_3\text{CH}_2\text{OH} \rightarrow \text{CH}_3\text{CHO} + \text{H}_2$
Ethanol decomposition 1	$\text{CH}_3\text{CH}_2\text{OH} \rightarrow \text{H}_2 + \text{CH}_4 + \text{CO}$
Ethanol decomposition 2	$\text{CH}_3\text{CH}_2\text{OH} \rightarrow 2\text{C} + \text{H}_2\text{O} + 2\text{H}_2$
Partial oxidation of ethanol	$\text{CH}_3\text{CH}_2\text{OH} + 1/2\text{O}_2 \rightarrow \text{CH}_3\text{CHO} + \text{H}_2\text{O}$
Complete oxidation of ethanol	$\text{CH}_3\text{CH}_2\text{OH} + 3\text{O}_2 \rightarrow 2\text{CO}_2 + 3\text{H}_2\text{O}$
Carbon combustion	$\text{C} + \text{O}_2 \rightarrow \text{CO}_2$
H ₂ combustion	$\text{H}_2 + 0.5\text{O}_2 \rightarrow \text{H}_2\text{O}$
CO combustion	$\text{CO} + 0.5\text{O}_2 \rightarrow \text{CO}_2$
CH ₄ combustion	$\text{CH}_4 + 2\text{O}_2 \rightarrow \text{CO}_2 + 2\text{H}_2\text{O}$
Steam methane reforming	$\text{CH}_4 + \text{H}_2\text{O} \leftrightarrow \text{CO} + 3\text{H}_2$
Water-gas shift reaction	$\text{CO} + \text{H}_2\text{O} \leftrightarrow \text{CO}_2 + \text{H}_2$

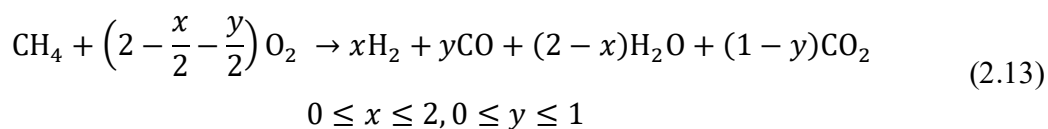
Liu et al. (2013) proposed a key chemical reaction in autothermal reforming of glycerol as shown in Table 2.7.

Table 2.7: Proposed key chemical reactions in autothermal glycerol reforming

Reaction	Chemical description
Steam reforming	$C_3H_8O_3 + 3H_2O \rightarrow 7H_2 + 3CO_2$
Oxidation	$C_3H_8O_3 + 2O_2 \rightarrow 4H_2O + 3CO$
Water-gas shift	$CO + H_2O \leftrightarrow H_2 + CO_2$

2.4.2 Kinetic Models

To get an insight into possible reactions which might occur in autothermal reforming of bio-oil, literature survey was conducted on related kinetic modelling studies i.e., autothermal reforming of methane. Catalytic partial oxidation (CPO) was first applied to convert methane to synthesis gas by Liander (1929). Since then a large number of studies have been devoted on the topic. One important open question is, however, the reaction mechanism of CPO of methane under autothermal conditions (Horn et al., 2007). There are two frequently reported mechanisms: direct and indirect. In the direct mechanism, H_2 and CO are primary reaction products formed by partial oxidation including the competitive formation of H_2O and CO_2 according to Equation 2.13 (Koo et al., 2008, Zhu et al., 2001).



On the other hand, the indirect mechanism proceeds through a two-zone concept with CH_4 complete combustion to H_2O and CO_2 utilizing all the oxygen at the catalyst entrance followed by endothermic steam and/or CO_2 reforming of the unreacted methane downstream (Horn et al., 2007, Souza and Schmal, 2005), Equations (2.14)-(2.16). A variant of the indirect mechanism was reported by Zhu et al. (2001) in which both full combustion and partial oxidation occur simultaneously in the “oxidation zone” while the residual CH_4 is converted to synthesis gas in the “conversion zone”.



De Smet et al. (2001) evaluated the influence of the oxidative kinetics on the performance of an adiabatic fixed bed reactor for methane conversion to synthesis gas applying the indirect reaction mechanism first proposed by Numaguchi and Kikuchi (1988). The water-gas shift reaction (2.2), complete oxidation of methane (reaction 2.14), and steam reforming of methane (2.15) are the reactions considered in the model. Other kinetic modelling studies such as (Hoang et al., 2005, Murmura et al., 2016, Zahedi Nezhad et al., 2009) included complete methane steam reforming to CO_2 and H_2 in addition to the reactions (2.14) and (2.15) and water-gas shift reaction, mostly based on the intrinsic kinetic study by Xu and Froment (1989). However, the complete steam reforming reaction is not an independent reaction in the presence of the water-gas shift reaction in reaction scheme.

2.5 Simulation Models

Thermodynamic models have been widely employed for predicting the product gas composition from steam reforming and autothermal reforming of bio-oil. Thermodynamic models allow to locate regions where a proposed process is likely to occur (Vagia and Lemonidou, 2007). Vagia and Lemonidou (2007) conducted thermodynamic analysis of steam reforming of bio-oil model compounds: acetic acid, acetone, and ethylene glycol. The authors used RGibbs reactor model in Aspen Plus which is based on the minimization of the Gibb's free energy. Peng–Robinson property method was employed for the equilibrium calculations. The effects of temperature (400-1300K), steam-to-fuel ratio (1-9) and pressure (1-20 atm) were evaluated. From the analysis, the increase in temperature and steam-to-fuel ratio favoured hydrogen production while the pressure increase affected its yield negatively. With an assumption that steam reforming reactions of bio-oil at 700°C reach equilibrium and are simultaneous, Zhang et al. (2013) used REquil reactor block in Aspen Plus to model the process. The set of reactions included in the model are given in Table 2.8.

Table 2.8: Simulated steam reforming reactions for steam reforming of bio-oil

Number	Reaction
1	$C_2H_4O_2 \rightarrow 2H_2 + 2CO$
2	$C_3H_6O_2 + 4H_2O \rightarrow 7H_2 + 3CO_2$
3	$C_7H_8O_2 + 12H_2O \rightarrow 16H_2 + 7CO_2$
4	$C_5H_4O_2 + 8H_2O \rightarrow 10H_2 + 5CO_2$
5	$C_6H_8O_2 + 10H_2O \rightarrow 14H_2 + 6CO_2$
6	$C_6H_6O + 11H_2O \rightarrow 14H_2 + 6CO_2$
7	$CH_2O_2 \rightarrow H_2 + CO_2$
8	$CH_4O + H_2O \rightarrow H_2 + CO_2$
9	$CO + H_2O \rightarrow H_2 + CO_2$
10	$CO + 3H_2 \rightarrow CH_3_4 + H_2O$
11	$CH_4 + H_2O \rightarrow CO + 3H_2$
12	$CH_2O_2 \rightarrow H_2O + CO$

Kinetic based simulations are required to closely represent the bio-oil reforming reactions (Vagia and Lemonidou, 2007). In kinetic-based simulation models for biomass gasification processes less attention has been given to modeling the conversion of primary tars i.e., condensable oxygenated hydrocarbons that are produced during the pyrolysis step, which are also the main constituents of bio-oil. Assumptions such as a tar free gas are often considered (Nikoo and Mahinpey, 2008, Ahmed et al., 2015). Kaushal and Tyagi (2017) used a power-law rate expression to represent the kinetics of primary tar conversion (Equation (2.17)) when modelling biomass gasification in a bubbling fluidized bed reactor using Aspen Plus simulator. The rate equation used for the tar cracking is given in Equation (2.18). The values for the relative yield of the cracking products (γ_j) are listed in Table 2.9, however no explanation was given as to how these values were obtained. The model assumed 22% of the primary tar remained unchanged in the gasification step.

$$tar \rightarrow \gamma_{CO}CO + \gamma_{CO_2}CO_2 + \gamma_{CH_4}CH_4 + \gamma_{H_2}H_2 + \gamma_{tar_inert}tar_{inert} \quad (2.17)$$

$$r_{j_{crack}} = \gamma_j 10^{4.98} \exp\left(-\frac{93.37}{RT}\right)(w_{tar}\rho_g) \quad (2.18)$$

where ($w_{tar}\rho_g$) is the amount of tar in gas phase.

Table 2.9: Relative yield of tar cracking product (Kaushal and Tyagi, 2017)

Species	γ_j	Species	γ_j
CO	0.78×0.722	CH ₄	0.78×0.113
CO ₂	0.78×0.142	Tar ₁	-1
H ₂	0.78×0.022	Tar ₂	0.22

2.6 Summary and Research Gaps

From the literature survey, the main points are summarized as below:

- Reactive flash volatilization is a promising method for a clean syngas production from lignocellulosic biomass. However, further study is required to analyse how the gasifying agents (steam and oxygen) influence of the overall conversion process through analysing the pyrolysis and reforming reactions separately.
- By adding oxygen in catalytic steam reforming of bio-oil the exothermic combustion reaction can help to satisfy the energy demand of the endothermic steam reforming reactions and suppresses carbon formation. The presence of steam in the process also help to prevent hot spots in catalytic beds which might otherwise occur in direct catalytic partial oxidation of bio-oil.
- Rhodium and ruthenium as catalyst additives have been reported to promote methane reforming and water-gas shift reactions.
- The chemistry in bio-oil gasification is dependent on reaction conditions: feedstock, type of gasifying agent in use, catalyst composition, temperature, and reactor configuration. For instance, contradicting trends for carbon monoxide concentration with temperature has been reported in the literature.
- An upstream freeboard design can help to lessen coke formation in bio-oil reforming

Research Gaps:

- In the literature, a freeboard design of the gasifier along with oxygen as an additional oxidant has been reported to lessen coke formation in bio-oil (primary tar) reforming. Nevertheless, although there are a few experimental studies on air-steam reforming of bio-oil, the extent and nature of bio-oil conversion in the reactor freeboard have not been studied.
- Acetol is the second most abundant constituent of aqueous phase bio-oil next to acetic acid (26.48 wt%) with a 22.92 wt% concentration (Wang et al., 2013). However, unlike acetic acid, there are only a few reported studies of catalytic steam reforming of acetol. Most importantly, the reaction behaviour of acetol reforming in the presence of oxygen (i.e., under the conditions of reactive flash volatilization) has not been reported in the literature. During reaction lignin and lignin-derived compounds tend to easily polymerise, which can cause catalyst deactivation. Thus, to obtain knowledge about the reaction behavior of the phenolic fraction of bio-oil under the conditions of reactive flash volatilization, a study utilizing primary tar compounds such as guaiacol would be of interest. Since the C:O ratio in acetol and guaiacol lie in close proximity to the crude and aqueous bio-oil (Figure 2.6), the information which can be obtained from the reforming of these primary tar compounds will be useful to understand the nature of reactive flash volatilization of biomass.
- No kinetic-based simulation model has yet been reported for air-steam reforming of bio-oil. Moreover, in the literature kinetic models or correlation used to represent the thermal decomposition of primary tar compounds in Aspen Plus models are not validated against experimental data.

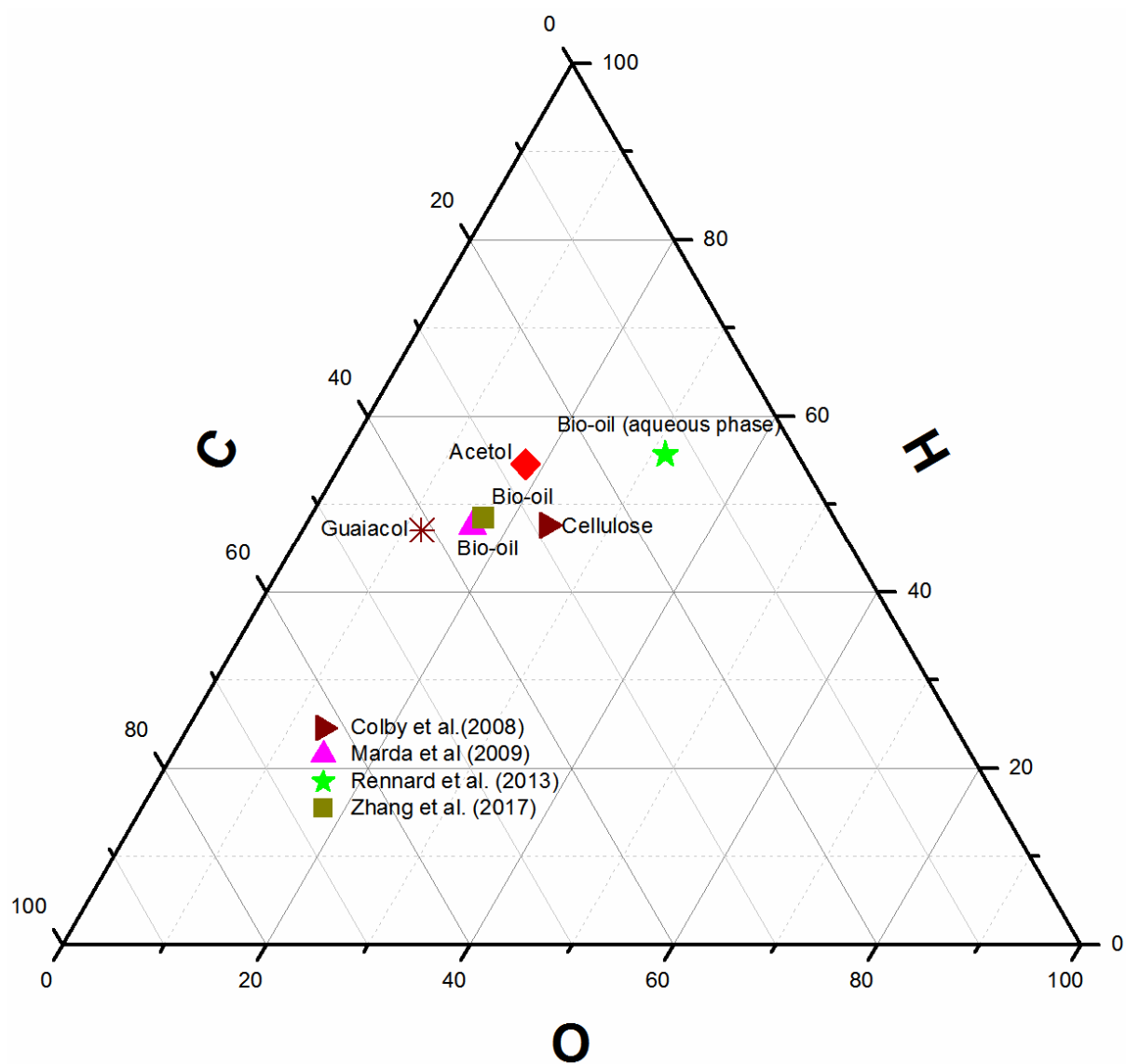


Figure 2.6: C:O ratio for different bio-oil and bio-oil model compounds

References

- Adhikari, S., Fernando, S. D. & Haryanto, A. 2009. Kinetics and reactor modeling of hydrogen production from glycerol via steam reforming process over Ni/CeO₂ catalysts. *Chemical Engineering & Technology*, 32, 541-547.
- Ahmed, A. M. A., Salmiaton, A., Choong, T. S. Y. & Wan Azlina, W. a. K. G. 2015. Review of kinetic and equilibrium concepts for biomass tar modeling by using Aspen Plus. *Renewable and Sustainable Energy Reviews*, 52, 1623-1644.
- Arregi, A., Lopez, G., Amutio, M., Barbarias, I., Santamaria, L., Bilbao, J. & Olazar, M. 2018. Kinetic study of the catalytic reforming of biomass pyrolysis volatiles over a commercial Ni/Al₂O₃ catalyst. *International Journal of Hydrogen Energy*.
- Baviskar, C. V. & Vaidya, P. D. 2017. Steam reforming of model bio-oil compounds 2-butanone, 1-methoxy-2-propanol, ethyl acetate and butyraldehyde over Ni/Al₂O₃. *International Journal of Hydrogen Energy*, 42, 21667-21676.
- Bimbela, F., Oliva, M., Ruiz, J., García, L. & Arauzo, J. 2009. Catalytic steam reforming of model compounds of biomass pyrolysis liquids in fixed bed: Acetol and n-butanol. *Journal of Analytical and Applied Pyrolysis*, 85, 204-213.
- Branca, C., Giudicianni, P. & Di Blasi, C. 2003. GC/MS Characterization of liquids generated from low-temperature pyrolysis of wood. *Industrial & Engineering Chemistry Research*, 42, 3190-3202.
- Bridgwater, A. V. 2012. Review of fast pyrolysis of biomass and product upgrading. *Biomass and Bioenergy*, 38, 68-94.
- Bussi, J., Musso, M., Quevedo, A., Faccio, R. & Romero, M. 2017. Structural and catalytic stability assessment of Ni-La-Sn ternary mixed oxides for hydrogen production by steam reforming of ethanol. *Catalysis Today*, 296, 154-162.
- Chan, F. L. & Tanksale, A. 2014. Catalytic steam gasification of cellulose using reactive flash volatilization. *ChemCatChem*, 6, 2727-2739.
- Chan, F. L., Umeki, K. & Tanksale, A. 2015. Kinetic study of catalytic steam gasification of biomass by using reactive flash volatilisation. *ChemCatChem*, 7, 1329-1337.
- Chen, J., Sun, J. & Wang, Y. 2017. Catalysts for Steam Reforming of Bio-oil: A Review. *Industrial & Engineering Chemistry Research*, 56, 4627-4637.
- Cheng, C. K., Foo, S. Y. & Adesina, A. A. 2011a. Carbon deposition on bimetallic Co-Ni/Al₂O₃ catalyst during steam reforming of glycerol. *Catalysis Today*, 164, 268-274.

- Cheng, C. K., Foo, S. Y. & Adesina, A. A. 2011b. Steam reforming of glycerol over Ni/Al₂O₃ catalyst. *Catalysis Today*, 178, 25-33.
- Chhiti, Y., Salvador, S., Commandré, J.-M., Broust, F. & Couhert, C. 2011. Wood bio-oil noncatalytic gasification: influence of temperature, dilution by an alcohol and ash content. *Energy & Fuels*, 25, 345-351.
- Colby, J. L., Dauenhauer, P. J. & Schmidt, L. D. 2008. Millisecond autothermal steam reforming of cellulose for synthetic biofuels by reactive flash volatilization. *Green Chemistry*, 10, 773-783.
- Czernik, S., Evans, R. & French, R. 2007. Hydrogen from biomass-production by steam reforming of biomass pyrolysis oil. *Catalysis Today*, 129, 265-268.
- Czernik, S. & French, R. 2014. Distributed production of hydrogen by auto-thermal reforming of fast pyrolysis bio-oil. *International Journal of Hydrogen Energy*, 39, 744-750.
- Czernik, S., French, R., Feik, C. & Chornet, E. 2002. Hydrogen by catalytic steam reforming of liquid byproducts from biomass thermoconversion processes. *Industrial & Engineering Chemistry Research*, 41, 4209-4215.
- De Smet, C. R. H., De Croon, M. H. J. M., Berger, R. J., Marin, G. B. & Schouten, J. C. 2001. Design of adiabatic fixed-bed reactors for the partial oxidation of methane to synthesis gas. Application to production of methanol and hydrogen-for-fuel-cells. *Chemical Engineering Science*, 56, 4849-4861.
- Domine, M. E., Iojoiu, E. E., Davidian, T., Guilhaume, N. & Mirodatos, C. 2008. Hydrogen production from biomass-derived oil over monolithic Pt- and Rh-based catalysts using steam reforming and sequential cracking processes. *Catalysis Today*, 133-135, 565-573.
- Edwards, J. H. & Maitra, A. M. 1995. The chemistry of methane reforming with carbon dioxide and its current and potential applications. *Fuel Processing Technology*, 42, 269-289.
- Fan, L., Zhang, Y., Liu, S., Zhou, N., Chen, P., Cheng, Y., Addy, M., Lu, Q., Omar, M. M., Liu, Y., Wang, Y., Dai, L., Anderson, E., Peng, P., Lei, H. & Ruan, R. 2017. Bio-oil from fast pyrolysis of lignin: Effects of process and upgrading parameters. *Bioresource Technology*, 241, 1118-1126.
- Galdámez, J. R., García, L. & Bilbao, R. 2005. Hydrogen production by steam reforming of bio-oil using coprecipitated Ni–Al catalysts. Acetic Acid as a Model Compound. *Energy & Fuels*, 19, 1133-1142.
- García-García, I., Acha, E., Bizkarra, K., Martínez De Ilarduya, J., Requies, J. & Cambra, J. F. 2015. Hydrogen production by steam reforming of m-cresol, a bio-oil model compound, using catalysts supported on conventional and unconventional supports. *International Journal of Hydrogen Energy*, 40, 14445-14455.

- Garcia, L. A., French, R., Czernik, S. & Chornet, E. 2000. Catalytic steam reforming of bio-oils for the production of hydrogen: effects of catalyst composition. *Applied Catalysis A: General*, 201, 225-239.
- Gayubo, A. G., Valle, B., Aramburu, B., Montero, C. & Bilbao, J. 2018. Kinetic model considering catalyst deactivation for the steam reforming of bio-oil over Ni/La₂O₃- α -Al₂O₃. *Chemical Engineering Journal*, 332, 192-204.
- Guan, G., Kaewpanha, M., Hao, X. & Abudula, A. 2016. Catalytic steam reforming of biomass tar: Prospects and challenges. *Renewable and Sustainable Energy Reviews*, 58, 450-461.
- Gutierrez Ortiz, F. J., Campanario, F. J. & Ollero, P. 2017. Effect of mixing bio-oil aqueous phase model compounds on hydrogen production in non-catalytic supercritical reforming. *Reaction Chemistry & Engineering*, 2, 679-687.
- Hoang, D. L., Chan, S. H. & Ding, O. L. 2005. Kinetic modelling of partial oxidation of methane in an oxygen permeable membrane reactor. *Chemical Engineering Research and Design*, 83, 177-186.
- Horn, R., Williams, K. A., Degenstein, N. J., Bitsch-Larsen, A., Dalle Nogare, D., Tupy, S. A. & Schmidt, L. D. 2007. Methane catalytic partial oxidation on autothermal Rh and Pt foam catalysts: oxidation and reforming zones, transport effects, and approach to thermodynamic equilibrium. *Journal of Catalysis*, 249, 380-393.
- Hu, X., Dong, D., Shao, X., Zhang, L. & Lu, G. 2017. Steam reforming of acetic acid over cobalt catalysts: Effects of Zr, Mg and K addition. *International Journal of Hydrogen Energy*, 42, 4793-4803.
- Kaushal, P. & Tyagi, R. 2017. Advanced simulation of biomass gasification in a fluidized bed reactor using ASPEN PLUS. *Renewable Energy*, 101, 629-636.
- Klouz, V., Fierro, V., Denton, P., Katz, H., Lisse, J. P., Bouvot-Mauduit, S. & Mirodatos, C. 2002. Ethanol reforming for hydrogen production in a hybrid electric vehicle: process optimisation. *Journal of Power Sources*, 105, 26-34.
- Koo, K., Yoon, J., Lee, C. & Joo, H. 2008. Autothermal reforming of methane to syngas with palladium catalysts and an electric metal monolith heater. *Korean Journal of Chemical Engineering*, 25, 1054-1059.
- Kumar, A., Chakraborty, J. P. & Singh, R. 2017. Bio-oil: the future of hydrogen generation. *Biofuels*, 8, 663-674.
- Latifi, M., Berruti, F. & Briens, C. 2014. Non-catalytic and catalytic steam reforming of a bio-oil model compound in a novel "Jiggle Bed" Reactor. *Fuel*, 129, 278-291.

- Lemonidou, A. A., Vagia, E. C. & Lercher, J. A. 2013. Acetic Acid Reforming over Rh Supported on $\text{La}_2\text{O}_3/\text{CeO}_2\text{-ZrO}_2$: Catalytic Performance and Reaction Pathway Analysis. *Acs Catalysis*, 3, 1919-1928.
- Liander, H. 1929. The utilisation of natural gases for the ammonia process. *Transactions of the Faraday Society*, 25, 462-472.
- Liu, Y., Farrauto, R. & Lawal, A. 2013. Autothermal reforming of glycerol in a dual layer monolith catalyst. *Chemical Engineering Science*, 89, 31-39.
- Marda, J. R., Dibenedetto, J., Mckibben, S., Evans, R. J., Czernik, S., French, R. J. & Dean, A. M. 2009. Non-catalytic partial oxidation of bio-oil to synthesis gas for distributed hydrogen production. *International Journal of Hydrogen Energy*, 34, 8519-8534.
- Medrano, J. A., Oliva, M., Ruiz, J., García, L. & Arauzo, J. 2011. Hydrogen from aqueous fraction of biomass pyrolysis liquids by catalytic steam reforming in fluidized bed. *Energy*, 36, 2215-2224.
- Mondal, T., Pant, K. K. & Dalai, A. K. 2015. Catalytic oxidative steam reforming of bio-ethanol for hydrogen production over Rh promoted $\text{Ni/CeO}_2\text{-ZrO}_2$ catalyst. *International Journal of Hydrogen Energy*, 40, 2529-2544.
- Mondal, T., Pant, K. K. & Dalai, A. K. 2016. Mechanistic kinetic modeling of oxidative steam reforming of bioethanol for hydrogen production over $\text{Rh-Ni/CeO}_2\text{-ZrO}_2$ catalyst. *Industrial & Engineering Chemistry Research*, 55, 86-98.
- Murmura, M. A., Diana, M., Spera, R. & Annesini, M. C. 2016. Modeling of autothermal methane steam reforming: comparison of reactor configurations. *Chemical Engineering and Processing: Process Intensification*, 109, 125-135.
- Nikoo, M. B. & Mahinpey, N. 2008. Simulation of biomass gasification in fluidized bed reactor using ASPEN PLUS. *Biomass and Bioenergy*, 32, 1245-1254.
- Numaguchi, T. & Kikuchi, K. 1988. Intrinsic kinetics and design simulation in a complex reaction network; steam-methane reforming. *Chemical Engineering Science*, 43, 2295-2301.
- Patel, M., Jindal, T. K. & Pant, K. K. 2013. Kinetic study of steam reforming of ethanol on ni-based ceria-zirconia catalyst. *Industrial & Engineering Chemistry Research*, 52, 15763-15771.
- Peela, N. R. & Kunzru, D. 2011. Oxidative steam reforming of ethanol over Rh based catalysts in a micro-channel reactor. *International Journal of Hydrogen Energy*, 36, 3384-3396.
- Remiro, A., Valle, B., Aguayo, A. T., Bilbao, J. & Gayubo, A. G. 2013. Steam reforming of raw bio-oil in a fluidized bed reactor with prior separation of pyrolytic lignin. *Energy & Fuels*, 27, 7549-7559.

- Rennard, D., French, R., Czernik, S., Josephson, T. & Schmidt, L. 2010. Production of synthesis gas by partial oxidation and steam reforming of biomass pyrolysis oils. *International Journal of Hydrogen Energy*, 35, 4048-4059.
- Renny, A., Santhosh, V., Somkuwar, N., Gokak, D. T., Sharma, P. & Bhargava, S. 2016. Pyrolysis of de-oiled seed cake of *Jatropha Curcas* and catalytic steam reforming of pyrolytic bio-oil to hydrogen. *Bioresource Technology*, 220, 151-160.
- Rioche, C., Kulkarni, S., Meunier, F. C., Breen, J. P. & Burch, R. 2005. Steam reforming of model compounds and fast pyrolysis bio-oil on supported noble metal catalysts. *Applied Catalysis B: Environmental*, 61, 130-139.
- Salehi, E., Azad, F. S., Harding, T. & Abedi, J. 2011. Production of hydrogen by steam reforming of bio-oil over Ni/Al₂O₃ catalysts: Effect of addition of promoter and preparation procedure. *Fuel Processing Technology*, 92, 2203-2210.
- Seyedeyn-Azad, F., Abedi, J. & Sampouri, S. 2014. Catalytic steam reforming of aqueous phase of bio-oil over ni-based alumina-supported catalysts. *Industrial & Engineering Chemistry Research*, 53, 17937-17944.
- Souza, M. M. V. M. & Schmal, M. 2005. Autothermal reforming of methane over Pt/ZrO₂/Al₂O₃ catalysts. *Applied Catalysis A: General*, 281, 19-24.
- Takanabe, K., Aika, K.-I., Inazu, K., Baba, T., Seshan, K. & Lefferts, L. 2006. Steam reforming of acetic acid as a biomass derived oxygenate: Bifunctional pathway for hydrogen formation over Pt/ZrO₂ catalysts. *Journal of Catalysis*, 243, 263-269.
- Trane, R., Dahl, S., Skjøth-Rasmussen, M. S. & Jensen, A. D. 2012. Catalytic steam reforming of bio-oil. *International Journal of Hydrogen Energy*, 37, 6447-6472.
- Trane, R., Resasco, D. E. & Jensen, A. D. 2013. Steam reforming of light oxygenates. *Catalysis Science & Technology*, 3, 3292-3302.
- Vagia, E. C. & Lemonidou, A. A. 2007. Thermodynamic analysis of hydrogen production via steam reforming of selected components of aqueous bio-oil fraction. *International Journal of Hydrogen Energy*, 32, 212-223.
- Vaidya, P. D. & Rodrigues, A. E. 2006. Kinetics of steam reforming of ethanol over a ru/al₂o₃ catalyst. *Industrial & Engineering Chemistry Research*, 45, 6614-6618.
- Van Rossum, G., Kersten, S. R. A. & Van Swaaij, W. P. M. 2007. Catalytic and noncatalytic gasification of pyrolysis oil. *Industrial & Engineering Chemistry Research*, 46, 3959-3967.
- Van Rossum, G., Kersten, S. R. A. & Van Swaaij, W. P. M. 2009. Staged catalytic gasification/steam reforming of pyrolysis oil. *Industrial & Engineering Chemistry Research*, 48, 5857-5866.

- Wang, D., Czernik, S., Montané, D., Mann, M. & Chornet, E. 1997. Biomass to hydrogen via fast pyrolysis and catalytic steam reforming of the pyrolysis oil or its fractions. *Industrial & Engineering Chemistry Research*, 36, 1507-1518.
- Wang, D., Montané, D. & Chornet, E. 1996. Catalytic steam reforming of biomass-derived oxygenates: acetic acid and hydroxyacetaldehyde. *Applied Catalysis A: General*, 143, 245-270.
- Wang, S., Li, X., Zhang, F., Cai, Q., Wang, Y. & Luo, Z. 2013. Bio-oil catalytic reforming without steam addition: Application to hydrogen production and studies on its mechanism. *International Journal of Hydrogen Energy*, 38, 16038-16047.
- Wu, C. & Liu, R. 2010. Carbon deposition behavior in steam reforming of bio-oil model compound for hydrogen production. *International Journal of Hydrogen Energy*, 35, 7386-7398.
- Wu, Y. J., Santos, J. C., Li, P., Yu, J. G., Cunha, A. F. & Rodrigues, A. E. 2014. Simplified kinetic model for steam reforming of ethanol on a Ni/Al₂O₃ catalyst. *The Canadian Journal of Chemical Engineering*, 92, 116-130.
- Xu, J. & Froment, G. F. 1989. Methane steam reforming, methanation and water-gas shift: I. Intrinsic kinetics. *AIChE Journal*, 35, 88-96.
- Yang, X., Wang, Y., Li, M., Sun, B., Li, Y. & Wang, Y. 2016. Enhanced Hydrogen Production by Steam Reforming of Acetic Acid over a Ni Catalyst Supported on Mesoporous MgO. *Energy & Fuels*, 30, 2198-2203.
- Yao, D., Wu, C., Yang, H., Hu, Q., Nahil, M. A., Chen, H. & Williams, P. T. 2014. Hydrogen production from catalytic reforming of the aqueous fraction of pyrolysis bio-oil with modified Ni–Al catalysts. *International Journal of Hydrogen Energy*, 39, 14642-14652.
- Zahedi Nezhad, M., Rowshanzamir, S. & Eikani, M. H. 2009. Autothermal reforming of methane to synthesis gas: Modeling and simulation. *International Journal of Hydrogen Energy*, 34, 1292-1300.
- Zhang, Y., Brown, T. R., Hu, G. & Brown, R. C. 2013. Comparative techno-economic analysis of biohydrogen production via bio-oil gasification and bio-oil reforming. *Biomass and Bioenergy*, 51, 99-108.
- Zheng, J.-L., Zhu, M.-Q., Wen, J.-L. & Sun, R.-C. 2016. Gasification of bio-oil: Effects of equivalence ratio and gasifying agents on product distribution and gasification efficiency. *Bioresource Technology*, 211, 164-172.
- Zheng, J.-L., Zhu, Y.-H., Zhu, M.-Q., Wu, H.-T. & Sun, R.-C. 2017. Bio-oil gasification using air-steam as gasifying agents in an entrained flow gasifier. *Energy*.
- Zhu, J., Zhang, D. & King, K. D. 2001. Reforming of CH₄ by partial oxidation: thermodynamic and kinetic analyses. *Fuel*, 80, 899-905.

Chapter 3

Thermodynamic Equilibrium Model for Reactive Flash Volatilization of Cellulose using Aspen Plus

3.1 Introduction

Based on a one-dimensional model of a particle which is described in Appendix 3A, the heating rate for a single particle before it hits the catalytic bed was found as being high (>800 K/s) as depicted in Figure 3.1. Hence, with this high heating rate in the freeboard and the knowledge that the bed is preheated to high temperature, pyrolysis of the cellulose particles on or above the catalytic bed will be fast (~ 75 ms), Figure 3.2. The kinetics of reactive flash volatilization of cellulose thus reduces to reforming of the primary tar compounds.

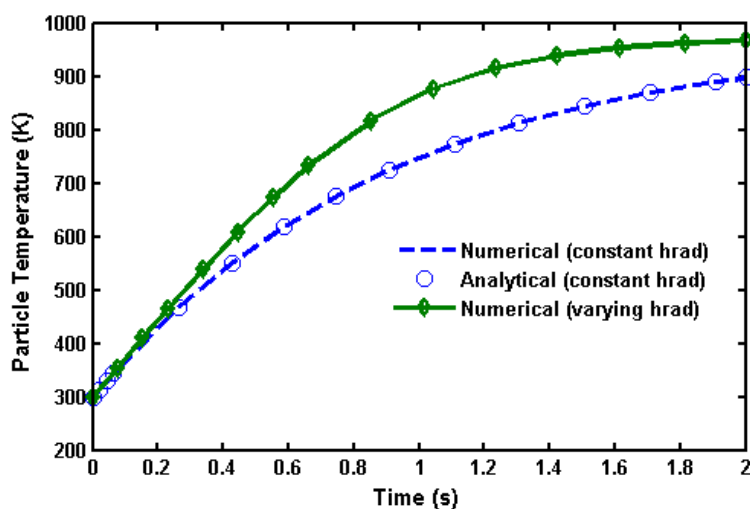


Figure 3.1: Numerical and analytical solutions for particle temperature with constant and variable h_{rad}

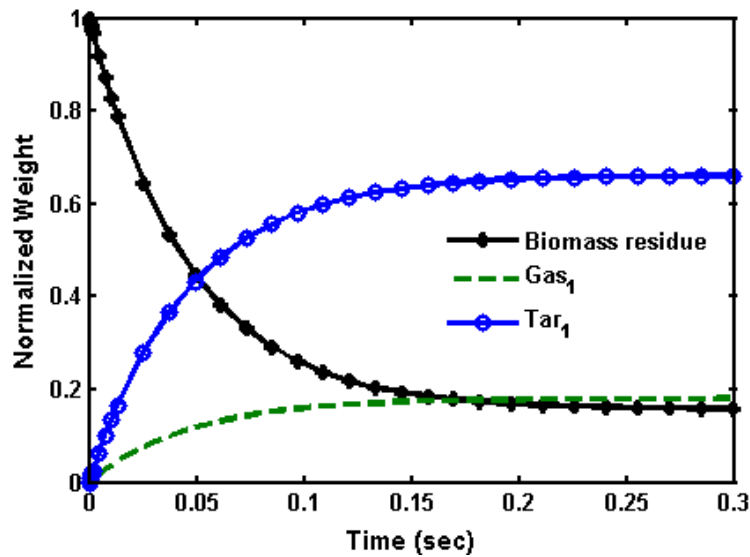


Figure 3.2: Pyrolysis product distribution at a reaction temperature of 700°C

To get a preliminary insight into the nature of a new process, equilibrium models have the advantage that they are independent of the gasifier design and unlike kinetic models they are not limited to a specified range of operating conditions (Silva and Rouboa, 2014). Aspen Plus simulator has been successfully used in modelling various biomass (Nikoo and Mahinpey, 2008) and coal (Biagini et al., 2009) gasification processes. Modelling for the pyrolysis step in biomass gasification using Aspen Plus has often been done by considering that the biomass decomposes into its constituent elements: C, H, O, N, S, and Cl (Nikoo and Mahinpey, 2008). This assumption, however, does not account for the true phenomenological mechanisms. To account for these mechanisms Abdelouahed et al. (2012) used empirical correlations from the literature for predicting product yield of spruce pyrolysis as a function of reactor temperature. In their model benzene, toluene, naphthalene, and phenol were the secondary/tertiary tar model compounds used. The challenge with the applied pyrolysis correlations is, however, depending on the type of the feedstock and operating conditions of the gasifier, the chosen secondary/tertiary tar model compounds might not be good representatives. Pyrolysis tar has also been modelled taking single model compounds such as anthracene (a tertiary tar compound) (Biagini et al., 2009). Sharma et al. (2014) reported an Aspen Plus model which incorporated a novel biomass decomposition approach of converting the biomass into products: C, H₂O, CO, CO₂, CH₄, H₂, and tar. Nevertheless, there was no information provided regarding compounds that make up the tar other

than its yield. Hence, depending on the nature of a thermochemical process under study, it is of paramount importance to incorporate a suitable procedure for modelling the pyrolysis step as it has a significant influence on the final product gas composition.

In the current study, an Aspen Plus simulation model is developed for reactive flash volatilization of cellulose for syngas production. Apart from thermodynamic calculations done by Colby et al. (2008) using HSC chemistry, no other model has been reported for this process. A novel decomposition submodel has been included for predicting the yield distribution of tar constituting compounds. The objective of this equilibrium modelling is to better understand the nature of the process and assist with the choice of primary tar model compounds for the experimental study.

The simulation model was validated against experimental data from Colby et al. (2008) for reactive flash volatilization of cellulose. The experiment was conducted by direct impingement of cellulose particles onto a preheated catalyst bed (700°C) in the presence of steam and oxygen as described in Chapter 2 (Figure 2.1). The selectivity to product species was calculated as the ratio of moles of atoms (C or H) in the product species to atoms in the feed cellulose.

3.2 Model Data

3.2.1 Feedstock Conditions

Cellulose accounts as high as 50 wt% of lignocellulosic biomass (Asghari and Yoshida, 2010). Hence, its conversion behaviour into syngas is considered vital for understanding lignocellulosic biomass conversion processes (Shen et al., 2011). Based on the ultimate analysis taken from Wang et al. (2012) (Table 3.1), the higher heating value of cellulose was calculated as 17.7 MJ/kg using the empirical formula in Equation (3.1) (Sheng and Azevedo, 2005).

$$\text{HHV (MJ/kg)} = 0.3137C + 0.7009H + 0.0318O - 1.3675 \quad (3.1)$$

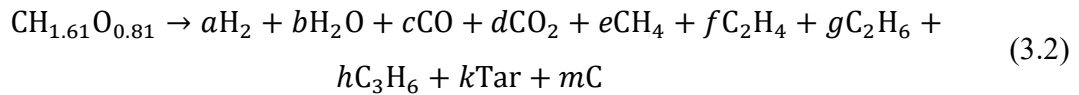
where C, H, and O are the compositions (wt%) of carbon, hydrogen, and oxygen elements, respectively.

Table 3.1: Proximate and ultimate analysis of cellulose on a dry basis (Wang et al., 2012)

Proximate analysis (wt%)		Ultimate analysis (wt%)	
Moisture content	3.89	C	43.26
Fixed carbon	4.76	H	5.78
Volatile matter	91.35	O	46.57

3.2.2 Cellulose Decomposition

Initially, cellulose thermally decomposes to gas, tar, and char (Equation (3.2)) before undergoing subsequent secondary reactions. The chemical formula of cellulose, $\text{CH}_{1.61}\text{O}_{0.81}$, is based on the ultimate analysis. In most cases, the constituents of the gas are well-known: H_2 , CO , CO_2 , H_2O , CH_4 , C_2H_4 , C_2H_6 , and C_3H_6 (Piskorz et al., 1986). In the current study solid carbon represents char.



Yield distribution of the decomposition products needs to be known first for modelling the pyrolysis step of the reactive flash volatilization of cellulose in Aspen Plus. Experimental data by Piskorz et al. (1986) for fast pyrolysis of cellulose from a bench scale fluidized bed reactor was used to get the yield for the gas, tar, and char (Table 3.2). The experimental data were chosen because it has the closest operating conditions to the present model. The data were for pyrolysis temperature of 550°C and a vapour residence time of 0.54 s.

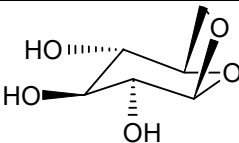
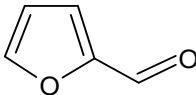
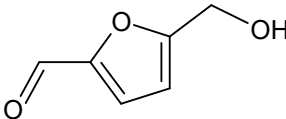
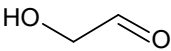
Table 3.2: The product yield from fast pyrolysis of cellulose at 550°C (Piskorz et al., 1986)

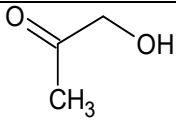
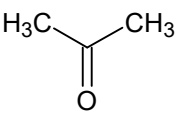
Compound	Yield (% of feed)
Tar	58.58
H_2O	10.17
Char	6.70
H_2	0.06
CO	9.23

Compound	Yield (% of feed)
CO ₂	7.47
CH ₄	0.41
C ₂ H ₄	0.27
C ₂ H ₆	0.11
C ₃ H ₆	0.31

However, generally in the literature the type and composition of tar-constituting compounds have not been well-defined and standardized. Hence, it was necessary to first identify the possible tar compounds from fast pyrolysis of cellulose from the literature and develop a mathematical model for calculating their corresponding yield within the 58.58% tar. Based on our literature survey, the most probable compounds in bio-oil from cellulose pyrolysis (under temperature of 700°C) are levoglucosan, furfural, 5-hydroxymethyl-furfural, hydroxyacetaldehyde, acetol, and acetone (Wang et al., 2013, Shen and Gu, 2009, Berkowitz-Mattuck and Noguchi, 1963). Table 3.3 includes the chemical structures of these model compounds, taken from the NIST chemistry webbook. More details of the modelling approach for the decomposition submodel are provided in subsequent section.

Table 3.3: Chemical structure of the primary tar model compounds used to represent pyrolysis oil from cellulose

Compound	Chemical structure
Levoglucosan	
Furfural	
5-hydroxymethyl-furfural,	
Hydroxyacetaldehyde	

Compound	Chemical structure
Acetol	
Acetone	

3.3 Modelling Approach

3.3.1 Cellulose Decomposition Submodel

The elemental mass balance of C, H, and O in the overall decomposition reaction (Equation (3.2)) resulted in three degrees of freedom. An error objective function was minimized to solve for the unknown parameters which correspond to the yield of the individual tar compounds. The non-linear programming was solved using genetic algorithm (GA) solver in MATLAB and Figure 3.3 illustrates the optimization framework.

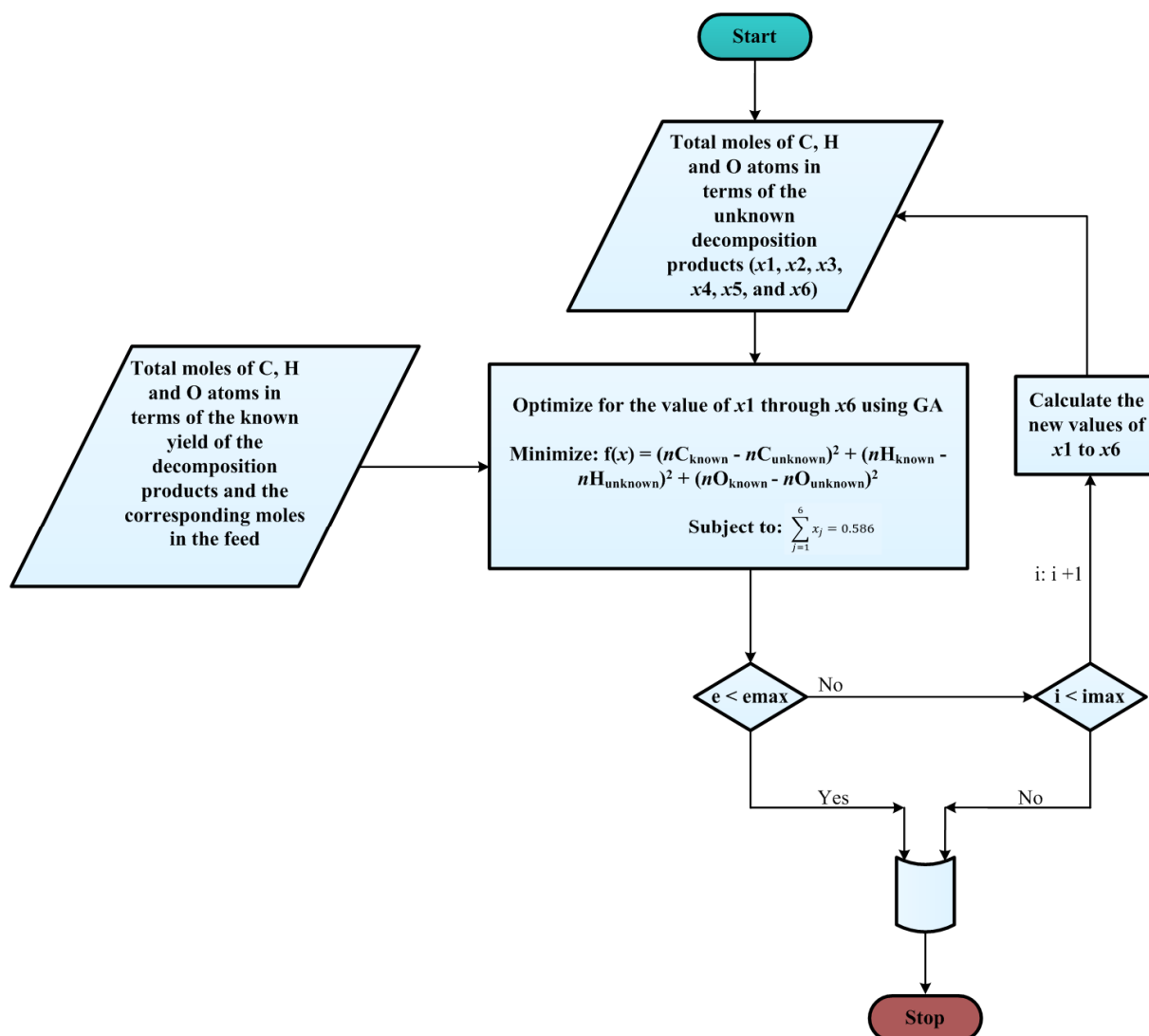


Figure 3.3: Optimization framework for calculating the yields of tar compounds

3.3.2 Aspen Plus Simulation Model

Thermodynamic equilibrium model for the reactive flash volatilization of cellulose was developed using the RYield and RGibbs reactor blocks in Aspen Plus (Figure 3.4). The feed cellulose was specified as nonconventional component and its enthalpy and densities were calculated using HCOALGEN and DCOALIGT models, respectively. The Redlich-Kwong-Aspen (RK-Aspen) equation of state was used to estimate physical properties of the conventional components. RKS-Aspen is a recommended method for hydrocarbon systems (Abdelouahed et al., 2012). Table 3.4

includes an example for the composition of the streams from the partial oxidation and steam reforming steps of the process.

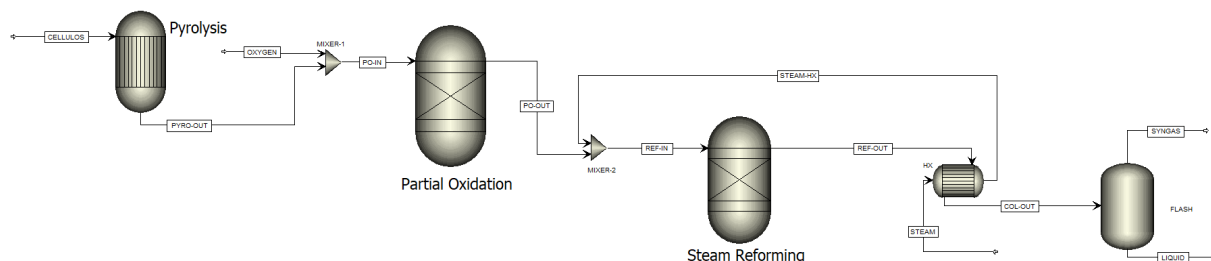


Figure 3.4: Aspen Plus simulation model for reactive flash volatilization of cellulose

Table 3.4: Example of composition of the streams from the partial oxidation and stream reforming steps of the process at 700°C, S/C=1.2, and C/O=0.9

Compound	PO-OUT		REF-OUT	
	Molar flow (mol/sec)	mol% (dry basis)	Molar flow (mol/sec)	mol% (dry basis)
H ₂ O	1.01	--	3.71	--
H ₂	1.22	29.7	1.81	38.6
CO	1.23	29.9	0.66	14.1
CO ₂	1.65	40.2	2.22	47.2
CH ₄	0.0069	0.17	0.0012	0.025
C ₂ H ₄	5.3×10 ⁻⁹	0	1.2×10 ⁻¹⁰	0
C ₂ H ₆	5.6×10 ⁻⁹	0	1.2×10 ⁻¹⁰	0
C ₃ H ₆	1.4×10 ⁻¹³	0	3.9×10 ⁻¹⁶	0

The RYield reactor block was used to model the pyrolysis step of the process. The yield distribution of the decomposition products required by the reactor block was specified based on experimental measurements from the literature (Table 3.2) combined with the calculated yields of the primary tar compounds obtained from the decomposition submodel. This reactor block is useful for modelling reacting systems when reaction stoichiometry and kinetics are unknown. Additional settings for the reactor model are pressure of 1 atm and temperature of 550°C. On the other hand, the partial oxidation and steam reforming steps of the process were represented using

the two RGibbs reactor blocks, which are based on minimization of the total Gibbs free energy of the reacting system (Equation 3.3) to calculate the yield and composition of individual components of the outlet gas. The initial setting for the operating temperatures for these two reactor models was 700°C with the assumption of isothermal condition that the reactor temperature to be independent of the other operating conditions (Vagia and Lemonidou, 2007).

$$G_{\text{total}} = \sum_{i=1}^N n_i \mu_i \quad (3.3)$$

where n_i and μ_i are the number of moles and chemical potential of species i , respectively.

Assuming ideal gas behaviour of the gases (at high temperature and low pressure), the chemical potential of the individual gas components can be calculated using Equation (3.4). Hence, substituting Equation (3.4) into (3.3) gives the final form of the equation for the total Gibbs free energy, Equation (3.5). Accordingly, the objective function for the simulation is then to find the moles of the individual reaction components (n_i) by minimizing Equation (3.5) subject to the constraint of the elemental mass in Equation (3.6).

$$\mu_i = \Delta G_{f,i}^0 + RT \ln \left(\frac{n_i}{n_{\text{total}}} \right) \quad (3.4)$$

$$G_{\text{total}} = \sum_{i=1}^N n_i \Delta G_{f,i}^0 + \sum_{i=1}^N n_i RT \ln \left(\frac{n_i}{n_{\text{total}}} \right) \quad (3.5)$$

$$\sum_{i=1}^N a_{ij} n_i = A_j \quad (3.6)$$

where a_{ij} is the number of atoms of the j^{th} element in a mole of i^{th} species and A_j is the total number of atoms of the j^{th} element in the reaction mixture.

3.4 Result and Discussion

3.4.1 Calculated Yield of the Tar Compounds

The calculated yield of the tar compounds is given in Table 3.5.

Table 3.5: Calculated yield for selected tar compounds from flash pyrolysis of cellulose

Tar compound	Formula	Calculated yield
Hydroxyacetaldehyde	C ₂ H ₄ O ₂	0.209
Levogluconan	C ₆ H ₁₀ O ₅	0.11
Acetol	C ₃ H ₆ O ₂	0.103
Acetone	C ₃ H ₆ O	0.085
5-Hydroxymethylfurfural	C ₆ H ₆ O ₃	0.075
Furfural	C ₅ H ₄ O ₂	0.045
Total		0.582

3.4.2 Mass Balance

In the simulation, in addition to converging the overall mass balance, the check for the atom balance closure is also crucial. This is because, any assumption taken for modelling the pyrolysis step of the process can have a significant influence on the overall mass balance of the process. Table 3.6 shows an example of the atom balance calculations at reaction temperature of 900°C, S/C=1.2 and C/O=0.6. The deviation for atom balance on the basis of C, H, and O atoms was calculated based on Equation (3.7) and is within an acceptable range (<1.5%).

$$\% \text{ Error} = \frac{\text{Moles in the feed} - \text{Moles in the product}}{\text{Moles in the feed}} \times 100 \quad (3.7)$$

Table 3.6: An example mass balance table

Moles in the feed			Moles in the product gas					% Error		
C	H	O	CH ₄	CO ₂	CO	H ₂	H ₂ O	C	H	O
2.88	11.54	10.59	1×10 ⁻⁷	2.54	0.34	0.54	5.16	0.01	1.3	0.02

3.4.3 Effect of Reaction Conditions

The effect of S/C and C/O ratios was studied by varying temperature. Table 3.7 shows a set of independent reactions that can possibly occur in the partial oxidation and steam reforming steps of the process.

Table 3.7: Possible reactions in the partial oxidation and steam reforming steps of the process

Reaction steps	Reactions	ΔH_r° (kJ/mol)
Partial oxidation	$C_xH_yO_z + aO_2 \rightarrow bH_2 + cCO + dCO_2 + eCH_4 + fH_2O + \text{Heat}$	
	$C + 0.5O_2 \rightarrow CO$	-112
	$CO + 0.5O_2 \rightarrow CO_2$	-283
	$H_2 + 0.5O_2 \rightarrow H_2O$	-242
Steam	$CO + H_2O \rightarrow CO_2 + H_2$	-41
reforming	$CH_4 + H_2O \rightarrow CO + 3H_2$	+206

Figure 3.5 shows the selectivity to H₂ and CO from the partial oxidation in the absence of steam. The increase in C/O ratios has a positive influence on the selectivity of hydrogen and CO due to partial oxidation.

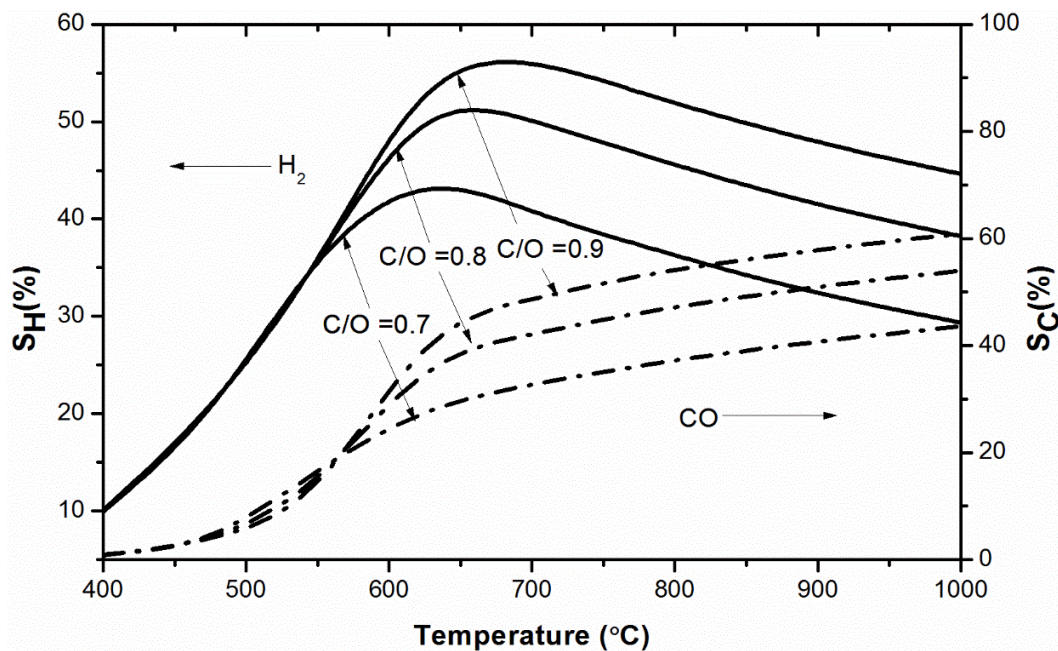


Figure 3.5: The conversion of cellulose by partial oxidation at C/O = 0.7, 0.8, and 0.9 with no steam

It can be seen from Figure 3.6 that the addition of more steam enhanced the selectivity to H_2 and the highest value increases to close to 85% at S/C ratio of 2.4, C/O ratio of 0.8, and a temperature of around 550°C. That is attributable to the contribution of the steam reforming reactions in Table 3.7 that lead to production of more H_2 . The same trend and similar values were reported by Colby et al. (2008) for the effects of S/C and C/O ratios using HSC chemistry software. However, the drawback in using the HSC chemistry software for equilibrium calculation is that no information can be deduced on the nature of reactions inside the reactor.

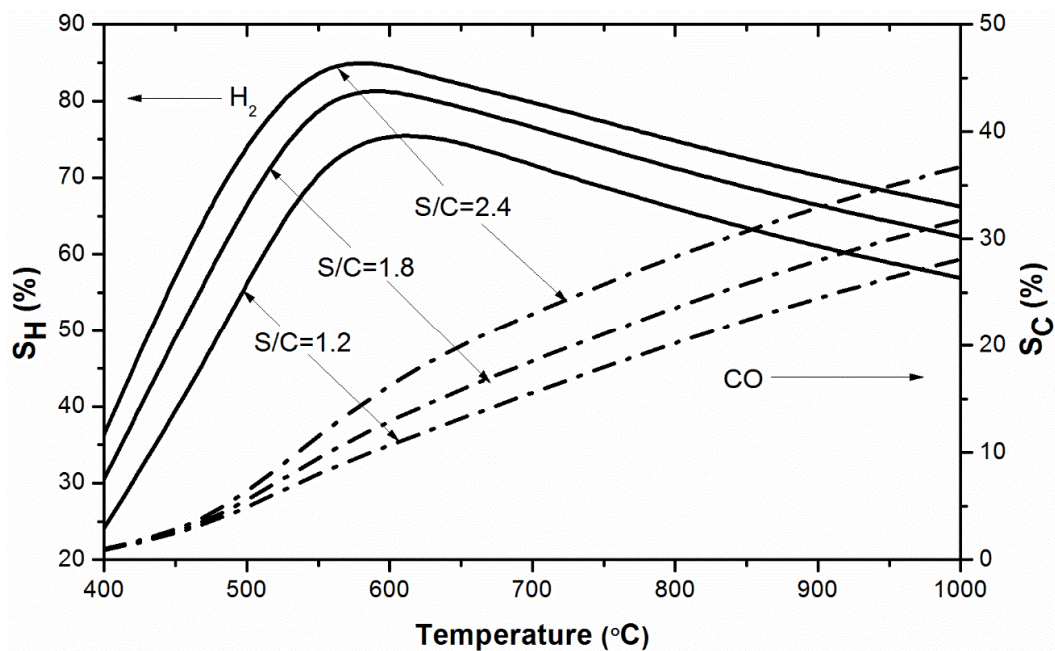


Figure 3.6: The conversion of cellulose to equilibrium products with steam at $C/O = 0.8$ for three different S/C ratios

The combined effect of steam (with 0%, 19%, 39%, and 59%) and C/O ratios were analysed and compared with the experimental data from Colby et al. (2008) shown in Figure 3.7. The simulation results are for 1 atm and the temperature of the catalyst bed at 10 mm downstream of the front face reported by Colby et al. (2008) (Appendix 3B). The CO yield in the product gas is seen to be highly dependent on the amount of steam and oxygen used. Under the zero-steam condition, the equilibrium model over predicts water content whereas the hydrogen content is under predicted. A quantitative comparison between simulation and experimental data is shown in Figure 3.8.

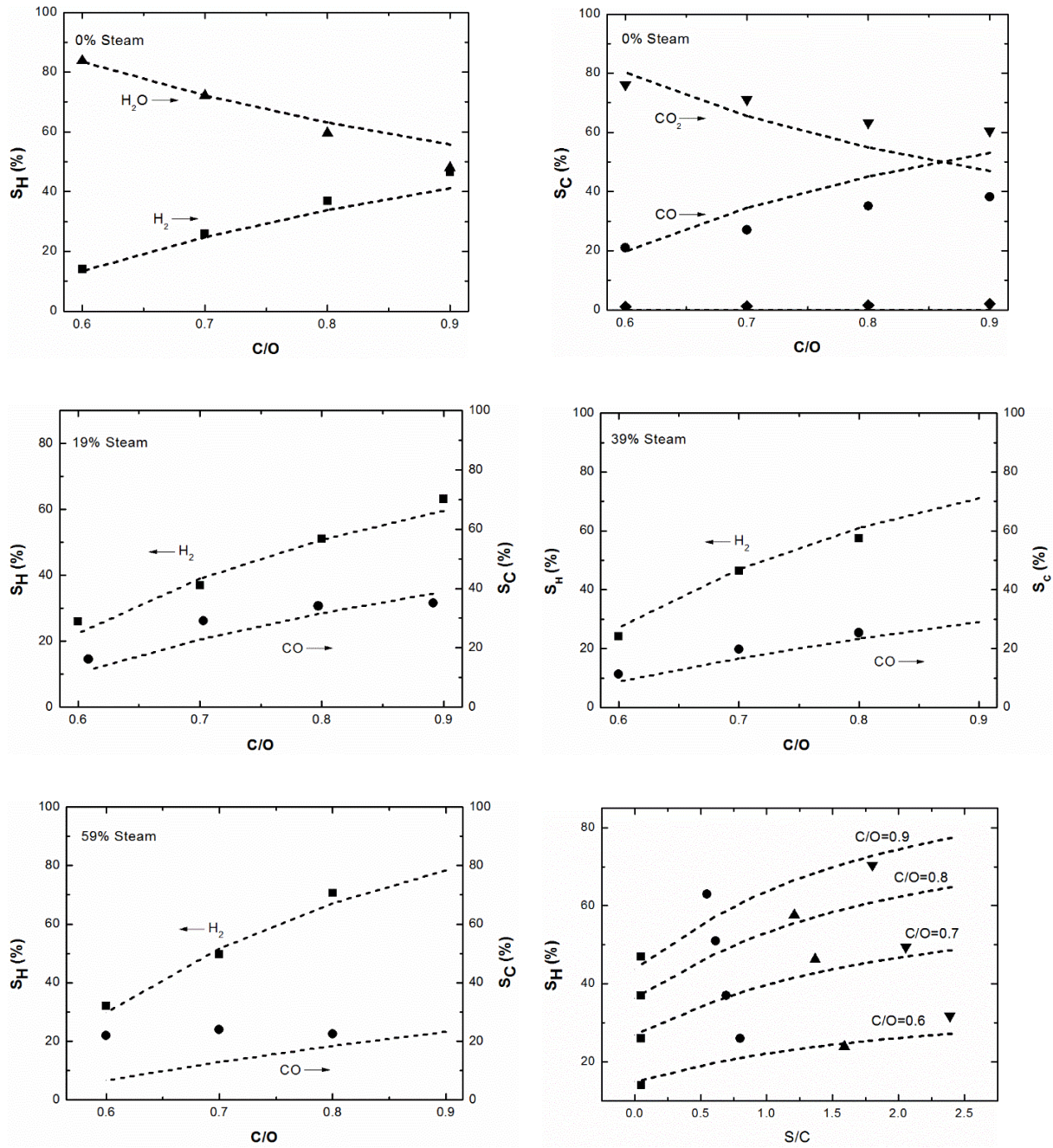


Figure 3.7: The selectivity of H_2 (■), H_2O (▲), CO (●), CO_2 (▼), and CH_4 (◆): the dash lines represent simulation results while the bullet points are experimental data from Colby et al. (2008)

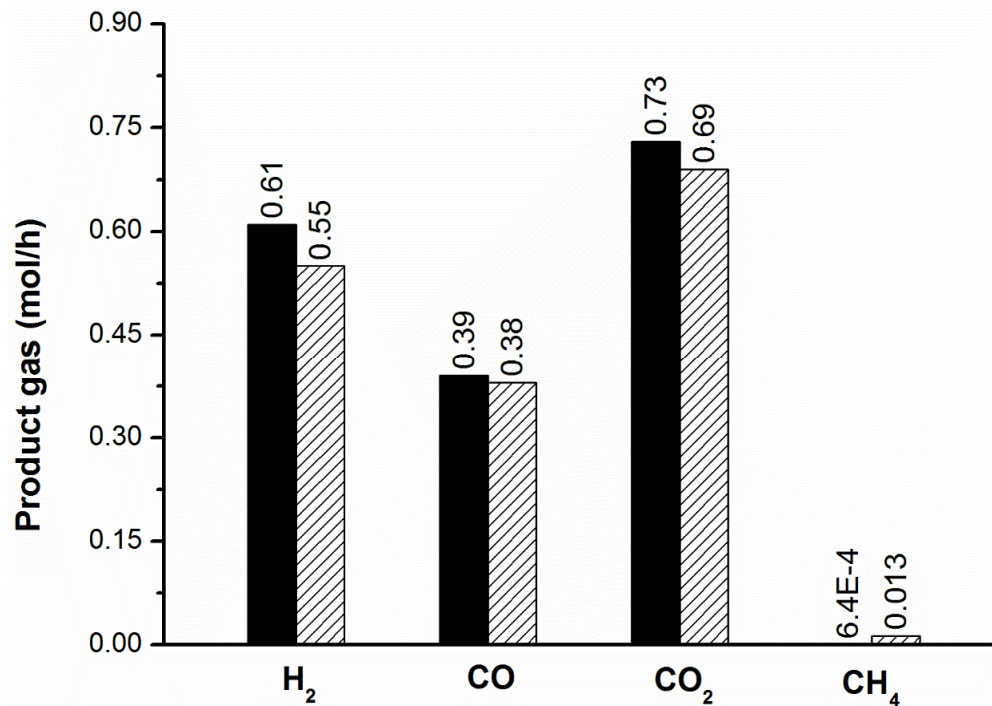


Figure 3.8: Comparison between simulated results and experimental data from Colby et al. (2008) at $T = 730^{\circ}\text{C}$, $\text{C/O} = 0.9$, and $\text{S/C} = 0.55$: ■ simulated data and ▨ experimental data

3.4.4 Energy Balance

Comparison was also made between energy balance calculations done using the simulation results and the experimental data from Colby et al. (2008) (Table 3.8) to check the heat nature (endothermic/exothermic) of the process.

Table 3.8: Experimental data from reactive flash volatilization of cellulose (Colby et al., 2008)

Gasifier conditions	Mass flow/g h ⁻¹	30
	Temperature/°C	730
	C/O ratio	0.9
	S/C ratio	0.55
Product gas (mol/sec)	H ₂	0.55
	H ₂ O	0.29
	CO	0.38
	CO ₂	0.69
	CH ₄	0.013

Steam temperature was considered to be 150°C and no heat loss in the process. The heat duty for product gas from the experiment was calculated using Equation (3.8).

$$Q = \sum_{S_{out}} \sum_i n_i H_i - \sum_{S_{in}} \sum_i n_i H_i \quad (3.8)$$

where S_{out} and S_{in} are the gas streams entering and leaving the reactor, respectively. H_i (kJ/mol) is the total enthalpy of component i at a given temperature and Equation (3.9) was used to calculate its value.

$$H_i = H_{f,i}^\circ + \Delta H_i \quad (3.9)$$

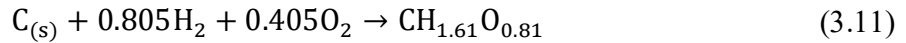
where $H_{f,i}^\circ$ is the standard heat of formation of individual components, and ΔH_i is defined as follows:

$$\Delta H_i = \int_{T_1}^{T_2} C_{p,i} dT \quad (3.10)$$

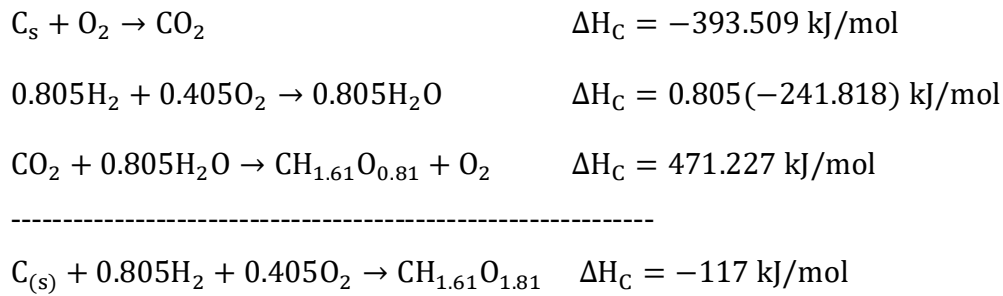
where $C_{p,i}$ is the heat capacity for individual components in kJ/mol.°C. The heat capacity of the product gas components (CO, CO₂, CH₄, H₂O, and H₂) as a function of temperature was taken

from Felder and Rousseau (2005) and a built-in solver in Matlab called “*quad*” was used to numerically evaluate the integral in Equation (3.10).

The heat of formation of 1 mole of cellulose from solid carbon, hydrogen and oxygen can be represented as follows:



However, in reality the above reaction (Equation (3.11)) cannot occur thermodynamically. Hence, $CH_{1.61}O_{0.81}$ is considered to be formed according to the following three reactions (Zainal et al., 2001):



Hence, the heat of formation of cellulose is calculated as -117 kJ/mol. Based on these calculations, the process was found to be endothermic according to the model results, whereas it is exothermic based on the experimental data, Table 3.9. One probable reason for the discrepancy is that in the simulation the temperature was considered to be independent of the other operating conditions (such as the level of oxygen content in the feed), which is the common assumption for equilibrium modelling (Vagia and Lemonidou, 2007). However, this practice is suitable for equilibrium composition calculations, but not for practical applications because the increase in the oxygen feed can lead to a higher temperature in the reactor (Biagini et al., 2009).

Table 3.9: Energy balance comparison between experimental and model results with cellulose 30 g/hr, C/O=0.9, S/C=0.55, and temperature 730°C

Reactor Model	Energy (kW)	Experimental (kW)
Pyrolysis (RYield)	0.15	-
Partial oxidation (RGibbs)	-0.06	-
Steam reforming (RGibbs)	0.0025	-
Balance	0.093 kW	-0.075 kW

3.5 Conclusions

The model provided insight into the nature of reactive flash volatilization of cellulose for syngas production. The pyrolysis, partial oxidation, and steam reforming steps of the process represented the process closely. The effects of the operating conditions on the selectivity of hydrogen and carbon were investigated over a wider range. Results obtained from this work was used for choosing a model compound of bio-oil from cellulose pyrolysis for an experimental study aiming to investigate potential causes for the deviations in the prediction.

References

- Abdelouahed, L., Authier, O., Mauviel, G., Corriou, J. P., Verdier, G. & Dufour, A. 2012. Detailed modeling of biomass gasification in dual fluidized bed reactors under aspen plus. *Energy & Fuels*, 26, 3840-3855.
- Asghari, F. S. & Yoshida, H. 2010. Conversion of Japanese red pine wood (*Pinus densiflora*) into valuable chemicals under subcritical water conditions. *Carbohydrate Research*, 345, 124-131.
- Balat, M., Balat, M., Kırtay, E. & Balat, H. 2009. Main routes for the thermo-conversion of biomass into fuels and chemicals. Part 1: Pyrolysis systems. *Energy Conversion and Management*, 50, 3147-3157.
- Berkowitz-Mattuck, J. B. & Noguchi, T. 1963. Pyrolysis of untreated and APO-THPC treated cotton cellulose during one-second exposure to radiant flux levels of 5–25 cal./cm.²-sec. *Journal of Applied Polymer Science*, 7, 709-725.
- Biagini, E., Bardi, A., Pannocchia, G. & Tognotti, L. 2009. Development of an Entrained Flow Gasifier Model for Process Optimization Study. *Industrial & Engineering Chemistry Research*, 48, 9028-9033.
- Chan, W. R., Kelbon, M. & Krieger, B. B. 1985. Modelling and experimental verification of physical and chemical processes during pyrolysis of a large biomass particle. *Fuel*, 64, 1505-1513.
- Colby, J. L., Dauenhauer, P. J. & Schmidt, L. D. 2008. Millisecond autothermal steam reforming of cellulose for synthetic biofuels by reactive flash volatilization. *Green Chemistry*, 10, 773-783.
- Dauenhauer, P. J., Colby, J. L., Balonek, C. M., Suszynski, W. J. & Schmidt, L. D. 2009. Reactive boiling of cellulose for integrated catalysis through an intermediate liquid. *Green Chemistry*, 11, 1555-1561.
- Di Blasi, C. 2004. Modeling wood gasification in a countercurrent fixed-bed reactor. *AIChE Journal*, 50, 2306-2319.
- Di Blasi, C. & Russo, G. 1993. Modeling of transport phenomena and kinetics of biomass pyrolysis. In: A.V., B. (ed.) *Advances in Thermochemical Biomass Conversion*. Dordrecht: Springer.
- Felder, R. M. & Rousseau, R. W. 2005. *Elementary Principles of Chemical Processes*, USA, John Wiley & Sons, Inc.
- Koufopoulos, C. A., Papayannakos, N., Maschio, G. & Lucchesi, A. 1991. Modelling of the pyrolysis of biomass particles. Studies on kinetics, thermal and heat transfer effects. *The Canadian Journal of Chemical Engineering*, 69, 907-915.

- Ku, X., Li, T. & Løvås, T. 2013. Influence of drag force correlations on periodic fluidization behavior in Eulerian–Lagrangian simulation of a bubbling fluidized bed. *Chemical Engineering Science*, 95, 94-106.
- Morsi, S. A. & Alexander, A. J. 1972. An investigation of particle trajectories in two-phase flow systems *J. Fluid Mech.*, 55, 193-208.
- Nikoo, M. B. & Mahinpey, N. 2008. Simulation of biomass gasification in fluidized bed reactor using ASPEN PLUS. *Biomass and Bioenergy*, 32, 1245-1254.
- Papadakis, K., Bridgwater, A. V. & Gu, S. 2008. CFD modelling of the fast pyrolysis of biomass in fluidised bed reactors, Part A: Eulerian computation of momentum transport in bubbling fluidised beds. *Chemical Engineering Science*, 63, 4218-4227.
- Piskorz, J., Desmond, R. & Scott, D. S. 1986. On the mechanism of the rapid pyrolysis of cellulose. *Journal of Analytical and Applied Pyrolysis*, 9, 121-137.
- Sharma, A. M., Kumar, A., Madihally, S., Whiteley, J. R. & Huhnke, R. L. 2014. Prediction of biomass-generated syngas using extents of major reactions in a continuous stirred-tank reactor. *Energy*, 72, 222-232.
- Shen, D., Xiao, R., Gu, S. & Luo, K. 2011. The pyrolytic behavior of cellulose in lignocellulosic biomass: a review. *RSC Advances*, 1, 1641-1660.
- Shen, D. K. & Gu, S. 2009. The mechanism for thermal decomposition of cellulose and its main products. *Bioresource Technology*, 100, 6496-6504.
- Sheng, C. & Azevedo, J. L. T. 2005. Estimating the higher heating value of biomass fuels from basic analysis data. *Biomass and Bioenergy*, 28, 499-507.
- Silva, V. & Rouboa, A. 2014. Optimizing the gasification operating conditions of forest residues by coupling a two-stage equilibrium model with a response surface methodology. *Fuel Processing Technology*, 122, 163-169.
- Sommerfeld, M. 2000. Theoretical and experimental modelling of particulate flows. Institut für Verfahrenstechnik
- Vagia, E. C. & Lemonidou, A. A. 2007. Thermodynamic analysis of hydrogen production via steam reforming of selected components of aqueous bio-oil fraction. *International Journal of Hydrogen Energy*, 32, 212-223.
- Wang, S., Guo, X., Liang, T., Zhou, Y. & Luo, Z. 2012. Mechanism research on cellulose pyrolysis by Py-GC/MS and subsequent density functional theory studies. *Bioresource Technology*, 104, 722-728.

- Wang, Y., Hu, X., Song, Y., Min, Z., Maurant, D., Li, T., Gunawan, R. & Li, C.-Z. 2013. Catalytic steam reforming of cellulose-derived compounds using a char-supported iron catalyst. *Fuel Processing Technology*, 116, 234-240.
- Zainal, Z. A., Ali, R., Lean, C. H. & Seetharamu, K. N. 2001. Prediction of performance of a downdraft gasifier using equilibrium modeling for different biomass materials. *Energy Conversion and Management* 42, 1499-1515.

Chapter 4

Experiment Methods

4.1 Introduction

In Chapter 2, it was concluded that the kinetic and reaction mechanism of autothermal reforming of bio-oil or its model compounds is not well established in the published literature. Chan and Tanksale (2015) proposed the process steps for reactive flash volatilization of cellulose: pyrolysis, reforming, and char gasification as discussed in Chapter 2 (Section 2.1 and Figure 2.3). The present work has investigated the nature of the reactions in the reforming step of the process. A steady state experimental kinetic analysis was conducted for selected primary tar compounds derived from pyrolysis of the cellulose (acetol) and lignin (guaiacol) under reactive flash volatilization conditions. Acetol has the highest content in the ketonic fraction of bio-oil and has been reported to be stable in temperatures range of 500 to 830°C (Bimbela et al., 2009, Medrano et al., 2009). It is formed through a successive dehydration and carbonyl transfer of a four-carbon fragment from the cellulose monomer, D-glucopyranose (an open-chain form of glucose shown in Chapter 1, Figure 1.3), as in Figure 4.1 (Wang and Luo, 2017). The methoxy (CH₃O) groups (Figure 4.2) in lignin and lignin-derived compounds can easily polymerise to carbonaceous deposit on reactor walls which poses impediment in bio-oil conversion (Fan et al., 2017, Morf et al., 2002). Guaiacol comes from the coniferyl alcohol, one of the building blocks of lignin (Chapter 1, Figure 1.3) and Figure 4.2 shows its chemical structure.

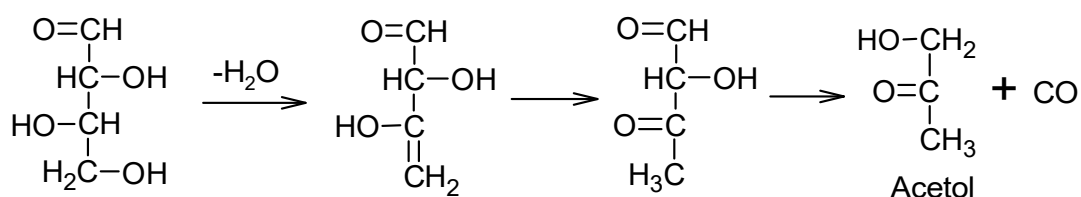


Figure 4.1: the formation path of acetol (Wang and Luo, 2017)

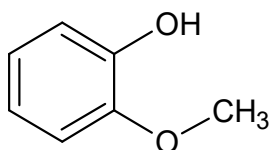


Figure 4.2: Chemical structure of guaiacol

The kinetic study aimed to develop an understanding of conversion behaviour of these model primary tar species (which are also major compounds present in bio-oil) by using a low-cost nickel-based catalyst (1%Rh-10%Ni/ γ -Al₂O₃) in which the 1 wt% rhodium was used as a promoter. The nature and extent of conversion, the performance of the catalyst, and potential carbon forming conditions will be investigated.

4.2 Experimental Setup

Figure 4.3 illustrates the schematic diagram of the experimental rig used for the kinetic analysis of acetol and guaiacol conversion under the conditions of reactive flash volatilization. The flow rates of oxygen and nitrogen gases were regulated using Teledyne 400 series mass flow controller (0-1000 cm³/min). Water, was delivered to an evaporator (DLI series, Brook Instrument) by a high-performance liquid chromatograph metering pump (Alltech, model 426) at rates between 0.08 to 0.17 ml/min. The evaporator was set at a temperature of 180°C to ensure that water was in superheated vapour form before entering the reactor. Furthermore, the transport of the water vapour and liquid organic feed was assisted by the nitrogen gas that flowed through the same tube. A computer-controlled syringe pump was used for the organic feed injection. Because of the high temperatures encountered at the inlet of the reactor, the liquid organic feed was converted to gas in the reactor freeboard prior to reaching the catalyst bed. A pressure gauge mounted at the mixing point of the reactant gases monitored the pressure within the reactor.

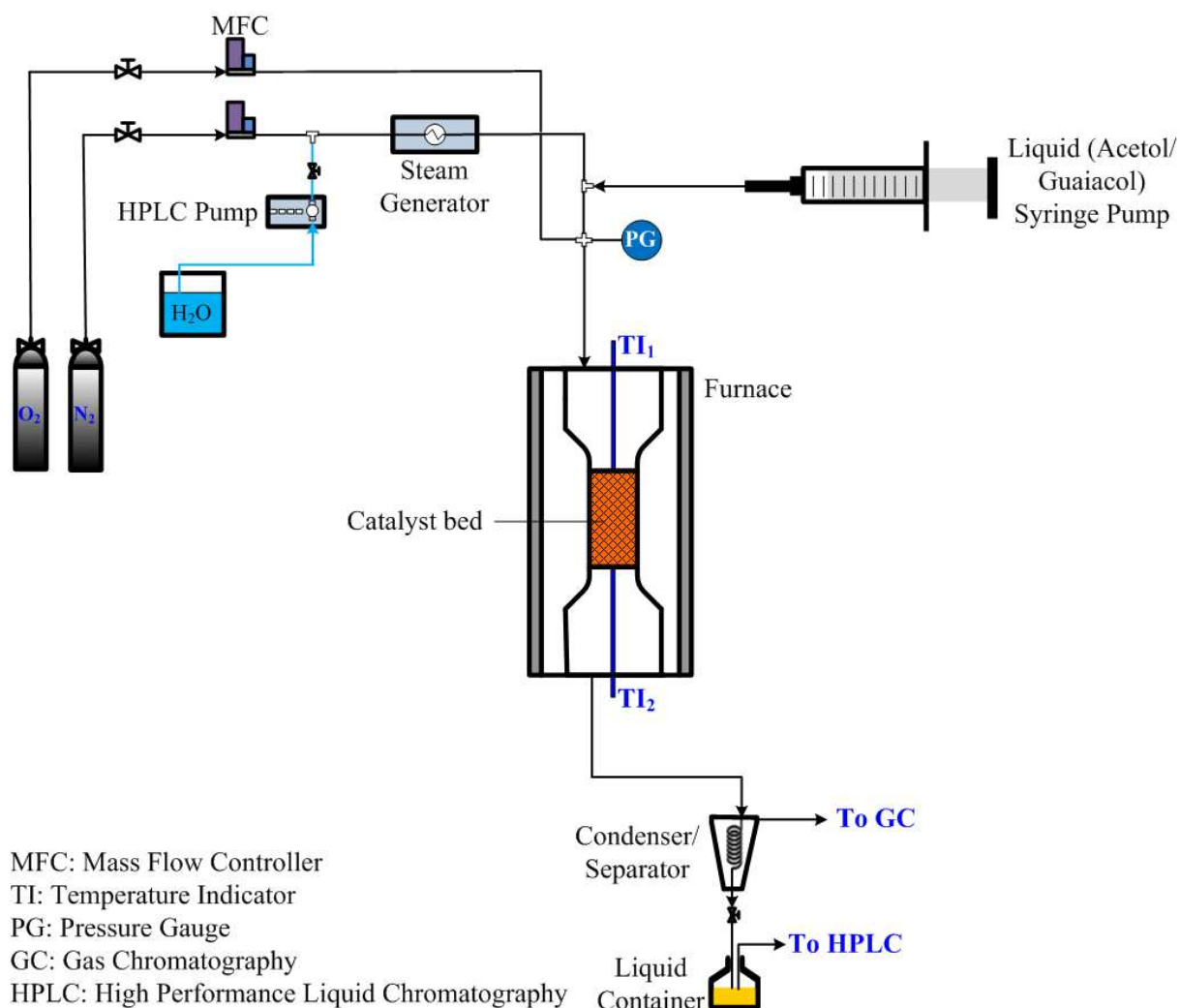


Figure 4.3: Schematic of the experimental system used for kinetic analysis of primary tar model compounds

A fixed-bed flow reactor made of a quartz tube with dimensions depicted in Figure 4.4 was used for the experiments. The reactor was designed to get better temperature control in the catalytic zone. Moreover, the use of the quartz tube eliminated a probable catalytic contribution of reactor walls that are made rather from stainless steel (Horn et al., 2007, Bimbela et al., 2009). A 0.5 to 0.8 g powder of Rh-Ni/ γ - Al_2O_3 catalyst ($\sim 100 \mu m$) held in place by quartz frit constituted the catalytic bed. The powder form of the catalyst limits the diffusion resistance within the pores that can prevail during reaction (Pawar et al., 2015). In all the experiments, the catalyst was mixed with 10 wt% quartz wool to reduce pressure drop across the bed and also help to prevent hot spots. All

the experiments were conducted at atmospheric pressure and under approximately isothermal conditions at temperatures between 700 and 800°C. The choice of the temperature range aimed to imitate the actual process conditions and to also avoid measuring only the equilibrium conversions beyond 800°C (Xu and Froment, 1989). The reactor was externally heated to maintain an approximately uniform temperature. Measurements of the catalyst bed temperature at the front and back faces were carried out using K-type thermocouples placed axially at the centre. All the feeding lines outside of the furnace were also covered by thermal insulation to lessen heat losses. Furthermore, to minimize the problem with temperature gradients in the kinetic study, efforts have been made to obtain isothermal gas temperatures using a diluted feed with <7% vol%.

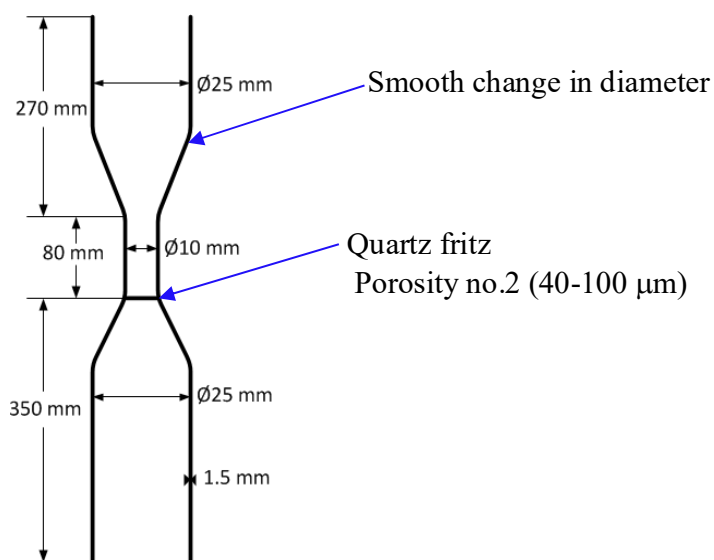


Figure 4.4: Dimensions of the reactor used for the kinetic analysis

The section of the reactor above the catalyst bed is referred to as the freeboard. It is designed to be a well-mixed zone. The gaseous reactor effluent leaving the coiled condenser was analysed using a gas chromatograph (GC), whereas the liquid samples were analysed using a high-performance liquid chromatograph (HPLC). For the initial few experiments, the gaseous stream leaving the condenser was directed to bubble through an impinger bottle filled with distilled water and immersed in ice-water to examine the presence of any more condensable gases. The analysis procedures for the gas and liquid samples are discussed in detail in Section 4.7.

4.3 Materials

Acetol and guaiacol used in the experiments were purchased from Sigma-Aldrich with the technical grades of 90 and ≥ 99 %, respectively. Oxygen, nitrogen, argon, and hydrogen cylinders with purity of 99.995% were purchased from Air Liquide, Australia. The physical properties of acetol and guaiacol are listed in Table 4.1.

Table 4.1: Physical properties of acetol and guaiacol

Properties	Acetol	Guaiacol
Molecular weight (g/mol)	74.08	124.14
Density at 25°C (g/cm ³)	1.082	1.129
Boiling point (°C)	145	205

4.4 Calibrations

The mass flow controllers were calibrated every time before experiments in the range of flows required for the reactions. Actual flow rates were measured with a bubble-O-meter. Sample calibration plots for the mass flow controllers are included in Appendix 4A. A NEWERA syringe pump was calibrated using flows measured within a given time intervals (Appendix 4B).

The HPLC metering pump was calibrated in the range of liquid water required for the reaction conditions (Appendix 4C). The GC calibrations were performed for individual gases with different concentrations and the calibration plots are presented in Appendix 4D. The calibration for the HPLC that was used for unconverted acetol feed analysis was done by diluting a knowing volume of the sample with water and the calibration plot is included in Appendix 4E.

4.5 Catalyst Preparation

Some preliminary experiments on 1%Ru-10%Ni/Al₂O₃ catalyst (1 wt% Ru, 10 wt% Ni, and the remainder being γ -Al₂O₃ as the support) did not yield satisfactory product gas distribution from the acetol conversion (see Appendix 4F). For this reason, 1%Rh-10%Ni/Al₂O₃ was the second

potential catalyst material tested. The mass composition of the catalysts was based on an earlier work from our research group by Chan and Tanksale (2014).

The wet impregnation method was applied for loading the Rh and Ni active metals onto the alumina support. This procedure comprised four successive major steps: preparing the aqueous solution, drying, calcination, and activation. At first, a measured quantity of rhodium (III) chloride hydrate and nickel (II) nitrate hexahydrate metal precursors were dissolved in deionized water (i.e., ~150 ml of water to prepare 15 grams of catalyst) in the presence of the alumina support. Subsequently, the slurry was stirred for 6 hours at 65°C. It was then dried in a muffle furnace at 105°C for 12 hours and further calcined in air at 600°C for 6 hours to remove any volatile matters. For activation, the catalyst was loaded into the quartz tube reactor and reduced in-situ in a mixture of H₂ (50%)/ N₂ at 400°C for 3 hours.

4.6 Catalyst Characterization

The catalyst morphology and structure characterizations before and after the experiments were performed with the following techniques: BET surface area was measured by N₂ adsorption using 3Flex™ Micrometrics adsorption instrument, high-resolution transmission microscope (TEM) (FEI Tecnai G2 T20 TWIN) at 200 kV, and temperature-programmed reduction (TPR). Details of the apparatus used for the TPR measurement are described elsewhere (Chan and Tanksale, 2014). The catalyst showed a type IV adsorption isotherm (Figure 4.5) with the hysteresis loop indicating mesoporous characteristics of the catalyst surfaces. The surface area analysis was done through adsorption of liquid nitrogen at 77.344 K and the results from the analysis are included in Table 4.2.

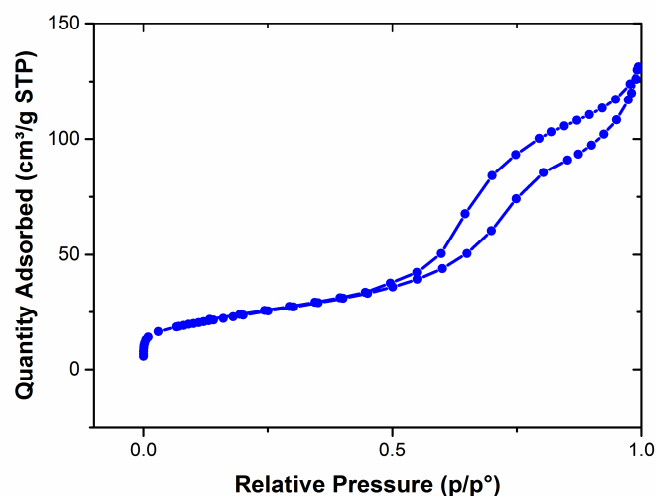


Figure 4.5: Adsorption isotherm for the Rh-Ni/Al₂O₃ catalyst

Table 4.2: Surface area and pore size analysis of fresh Rh-Ni/Al₂O₃ catalyst

BET Surface area	Average pore size ^a (Å)	Total pore volume ^b (cm ³ g ⁻¹)
85.5	78.6	0.17

^a Adsorption average pore diameter (4 V/Å by BET)

^b Single point adsorption total pore volume of pores less than 403.122 Å diameter at p/p° = 0.95

The catalyst resistance to coke deposition and its thermal stability are important factors that govern its durability. Thus, the spent catalyst samples from the acetol experiments were analysed for carbon, hydrogen, and nitrogen (CHN). TEM images for catalysts used for acetol and guaiacol experiments also gave evidence on whether coke was deposited on the catalyst surface. The results from the CHN and TEM analysis are presented Sections 5.2 and 5.3 of Chapter 5.

The H₂-TPR analysis for a fresh 200 mg Rh-Ni/Al₂O₃ catalyst was conducted in 5% H₂/Ar (60ml/min) and the temperature was raised from 23°C to 800°C at the rate of 10°C/min. The reduction profile from the TPR measurement is shown in Figure 4.6. The temperature (approximately 400-410°C) at which the most prominent peak, i.e., the highest hydrogen uptake, occurred denotes the optimal reduction temperature. Kim (2004) stated that the lower reduction temperature is due to the ability of the metal (Rh-Ni) to spill over the hydrogen to the support. The

lower reduction temperature results in the higher availability of the catalyst active sites (Phanikrishna Sharma et al., 2015).

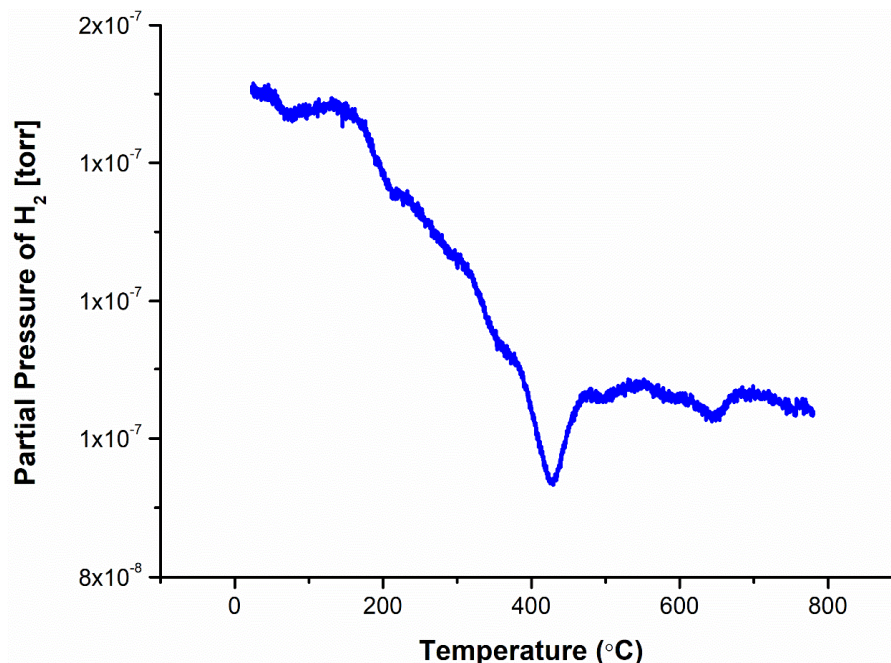


Figure 4.6: Reduction temperature profile for the Rh-Ni/Al₂O₃ catalyst

4.7 Experimental Procedures

4.7.1 Experimental Design

Data collection from kinetic experiments is time-consuming because only a limited amount of data can be obtained from each experiment. Therefore, it was necessary to design the experiment in such a way that as much reliable information (i.e., with no variability) can be obtained from a relatively small number of runs. Consequently, a two-level fractional factorial design was employed to analyse the influence of steam-to-carbon (S/C) ratio (1.2-2.4), carbon-to-oxygen (C/O) ratio (1.3-1.7), catalyst bed temperature (700-800 °C), catalyst weight (0.5-0.8 g), and gas hourly space velocity (GHSV) (1.4×10^4 - 1.7×10^4 h⁻¹) on the product gas composition (i.e. the responses). Designing the experiment in this manner enables to determine the individual and interactive effects (if any) of several factors through manipulating them at the same time. The partial pressures of the reactant gases were varied as S/C and C/O ratios were changed. However, the feed rates of acetol

and guaiacol were kept constant at 0.085 ml/min and 0.0575 ml/min, respectively. The higher total flow rate (GHSV= $1.7 \times 10^4 \text{ h}^{-1}$) was limited by the reactor capacity. C/O was defined as the molar ratio of carbon in the organic feed to the atomic oxygen in the feed oxygen gas. The gas hour space velocity was defined as the ratio between the total gas volumetric flow rate calculated at 300°C and the catalyst bed volume. The nitrogen gas flow rates were adjusted such that the required gas hourly space velocity for every experiment was maintained. The design matrix for acetol and guaiacol experiments are given in Tables 4.3 and 4.4, respectively. Based on analysis of experimental results from the acetol conversion, catalyst mass for the guaiacol runs was kept constant at 0.5 g.

Table 4.3: Experimental design matrix for acetol experiments

Std	RunNo.	T (°C)	S/C	C/O	GHSV(h^{-1})	Catalyst (g)
4	1	800	2.4	1.3	17000	0.5
7	2	700	2.4	1.7	14000	0.5
1	3	700	1.2	1.3	17000	0.8
2	4	800	1.2	1.3	14000	0.5
6	5	800	1.2	1.7	14000	0.8
8	6	800	2.4	1.7	17000	0.8
5	7	700	1.2	1.7	17000	0.5
3	8	700	2.4	1.3	14000	0.8

*Std (standard order) is the non-randomized order of the runs.

Table 4.4: Experimental design matrix for guaiacol experiments

Std	Run No.	T (°C)	S/C	C/O	GHSV(h ⁻¹)
3	1	700	1.2	1.15	17000
2	2	700	2.4	0.85	17000
7	3	800	1.2	1.15	14000
6	4	800	2.4	0.85	14000
4	5	700	2.4	1.15	14000
8	6	800	2.4	1.15	17000
1	7	700	1.2	0.85	14000
5	8	800	1.2	0.85	17000

4.7.2 Reactor Operating Procedures

Once the catalyst activation was complete, the reactor was heated to a desired reaction temperature at 10 °C/min in the presence of N₂ (300 ml/min) that helps to outgas the reactor (flash out any residual H₂) and keep the catalyst in the reduced state. After the reaction temperature was reached the nitrogen flow was adjusted to the required amount for a specific experiment. Oxygen flow was introduced into the reactant stream after the water and acetol (or guaiacol) feed to avoid potential re-oxidation of the catalyst.

4.7.3 Gas Sampling and Analysis

Gas samples were intermittently collected, 30 minutes after each experiment was begun, with Tedlar gas sampling bag over a period of four hours gasification time. To ensure that pressure in the system was not affected by the sampling practice, a t-connection was inserted between the bubble flow meter (bubble-O-meter) and the reactor outlet as shown in Figure 4.7. This configuration allowed the gas coming from the reactor to go directly to the bubble flow meter if the pressure in the gas bag reached one atmosphere. In so doing, the reaction upstream of the sampling port was not affected by any pressure fluctuation that may be induced during sampling.

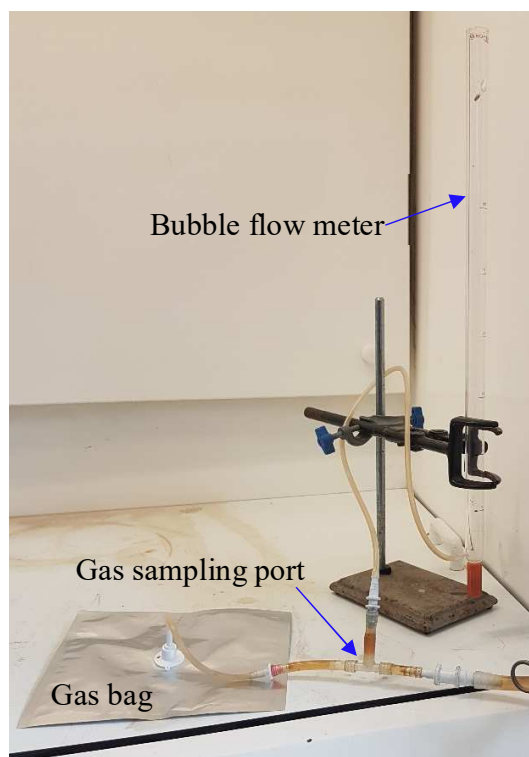


Figure 4.7: Gas sampling arrangement

The gas chromatograph (GC-2014, Shimadzu) used for the analysis has a molecular sieve 5A (6 ft \times $\frac{1}{8}$ in. and mesh 80/100) and porous polymer (6 ft \times $\frac{1}{8}$ in. and mesh 80/100) columns. It is equipped with a flame ionization detector for quantifying the content of carbon-containing components (CO, CO₂, CH₄, and C₂ compounds) and a thermal conductivity detector for H₂, N₂ and O₂ gases. The GC uses a valve injection system and argon was the carrier gas used for the analysis. The composition quantified for any given gas sample represented an average value over the time period used to collect the sample with a gas bag.

The yield of each product is calculated based on the feed gas flow rate and the dry gas composition obtained from the GC. The total molar flow rate of the reactor effluent on dry basis was calculated based on nitrogen balance as given in Equation 4.1. The C, H, and O atoms balances were closed within the accuracy of $\pm 5\%$ and a sample calculation is shown in Appendix 4G.

$$n_{out} = \frac{n_{N_2(feed)}}{y_{N_2}} \quad (4.1)$$

where y_{N_2} represents the mole fraction of argon in the outlet gas.

4.7.4 Liquid Condensate Sampling and Analysis

High performance liquid chromatograph with column having stationary phase for carbohydrates separation (Rezex RHM-Monosaccharide, 300×7.8 mm) and with diode array detector was used to determine concentrations of unconverted acetol in liquid samples from the condenser. Deionized water at room temperature was the mobile phase used for the separation. Samples for the analysis were collected once every experimental run was completed. Total carbon in the liquid samples both for the acetol and guaiacol experiments was also analysed using a Shimadzu TOC-L Analyser.

4.7.5 Gas Composition Analysis from the Reactor Freeboard

To examine the nature of any reaction that may be occurring prior to the catalyst bed, i.e., within the freeboard, samples were drawn from this section after steady state was attained. This was done by inserting a capillary tube from the reactor top head. Identities of species in the gas samples was determined using a residual gas analyser (RGA 300, SRS) in a high vacuum chamber ($<10^{-4}$ mbar). Figure 4.8 illustrates the working principle behind the RGA. Different gas species are ionized and the ions with specific mass-to-charge (m/z) ratios are detected separately. The number of ionized molecules is proportional to partial pressures of the corresponding gas in the sample.

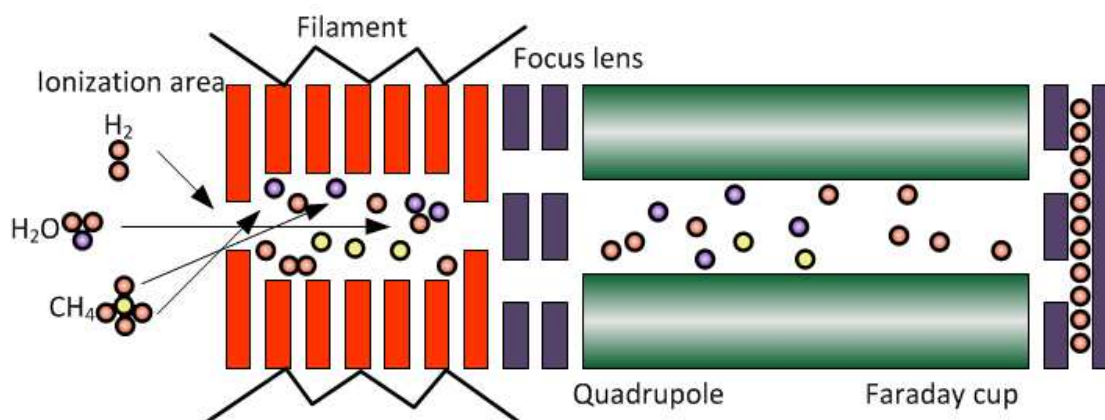


Figure 4.8: The working principle of RGA. Redrawn and slightly modified from (Brillson, 2016) and reproduced with permission from the publisher.

To determine the extent of conversion and composition of the gas produced from the acetol feed in the reactor freeboard, gas samples of 20 ml each were periodically taken. Helium was the carrier gas used for the analysis. The assignment of m/z ratios for individual products were based on mass spectra found in the National Institute for Standards (NIST). The ionization energy of 45 eV was used for this study. The RGA was calibrated for H_2 ($m/z=2$), CO ($m/z=28$), CO_2 ($m/z=44$), CH_4 ($m/z=16$), O_2 ($m/z=32$), H_2O ($m/z=18$), and Ar ($m/z=40$). The calibration curves constructed for known concentrations of the compounds against the corresponding areas under the peaks are included in Appendix 4H. The baseline was subtracted and the area under the peaks was calculated using the trapezoidal rule for integration. The instrument used for this analysis is shown in Figure 4.9.

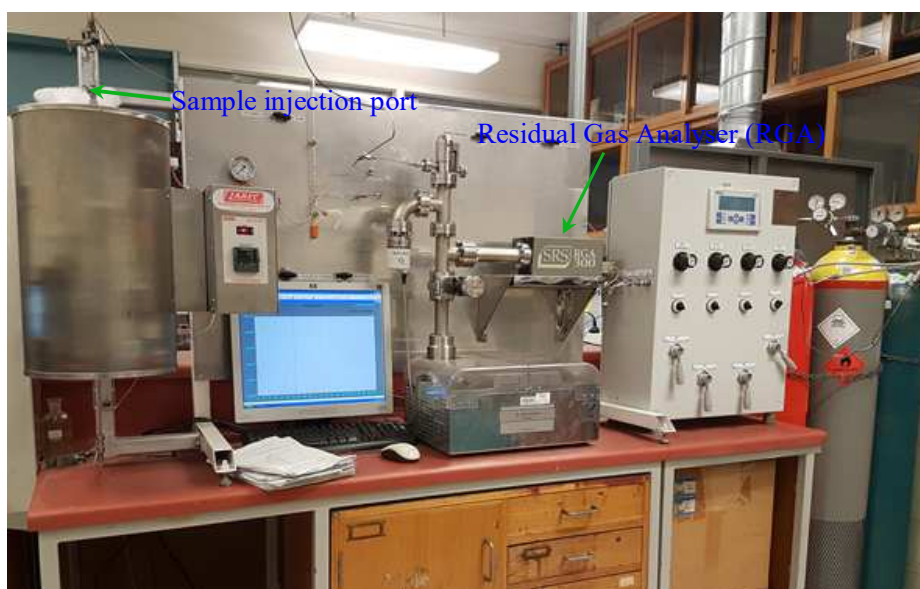


Figure 4.9: The instrument used for the gas analysis from the reactor freeboard

Since acetol has the tendency to stick to the walls inside the instrument, it exhibited considerable variation in its signal when an attempt was made to do calibration measurements in its vapour form. Clair et al. (2014) were able to quantify acetol in situ using a tandem (triple quadrupole) chemical ionization mass spectrometry (CIMS) instrument in which the sample took less than 1s to get detected. In the current instrument configuration (Figure 4.9), however, the sample spent relatively longer time inside the instrument before being detected. Therefore, argon in the reactant feed stream was instead used as a tie component for mass balance calculations.

Mass-to-charge ratios for an unconverted acetol were chosen based on analysis performed by taking sample of a vapour present in the headspace of a vial with a septum cap. The vial was immersed in a water bath at 61°C. The ratio of the signal intensities of ion fragments with $m/z=29$ and $m/z=27$ (Figure 4.10) was used to verify the presence of any unconverted acetol after the reactions in the reactor freeboard. Figure 4.10 depicts the fragment ions detected from acetol calibration.

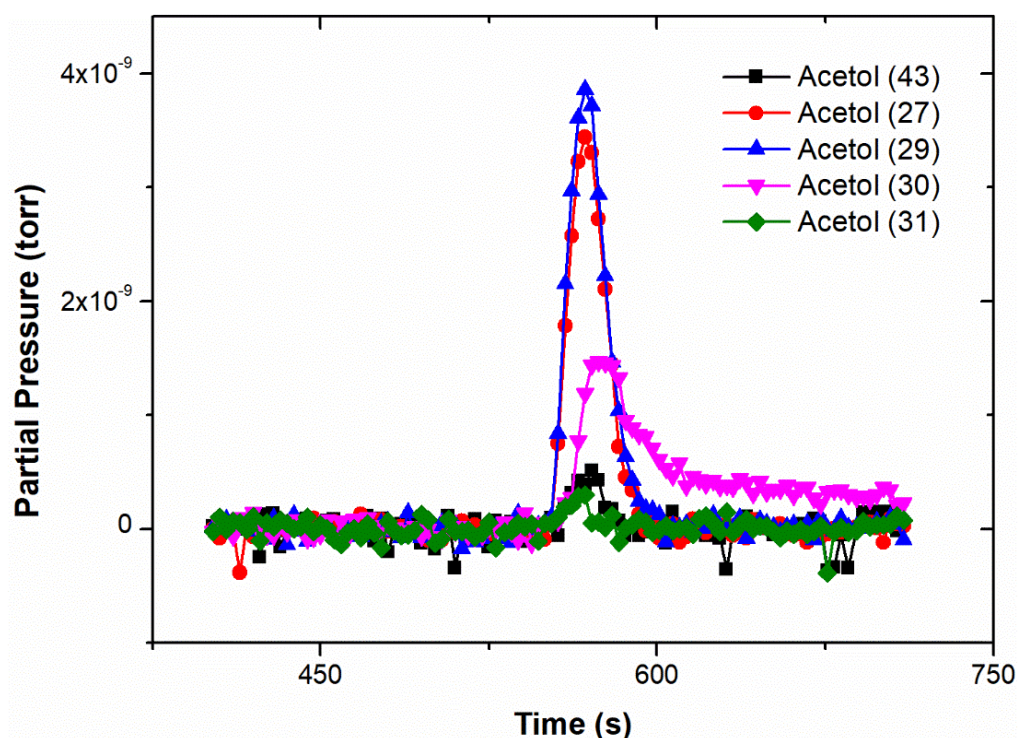


Figure 4.10: Fragment ions from acetol sample analysis using the RGA at 61°C

References

- Bimbela, F., Oliva, M., Ruiz, J., García, L. & Arauzo, J. 2009. Catalytic steam reforming of model compounds of biomass pyrolysis liquids in fixed bed: Acetol and n-butanol. *Journal of Analytical and Applied Pyrolysis*, 85, 204-213.
- Brillson, L. J. 2016. *An Essential Guide to Electronic Material Surfaces and Interfaces*, John Wiley & Sons.
- Chan, F. L. & Tanksale, A. 2014. Catalytic steam gasification of cellulose using reactive flash volatilization. *ChemCatChem*, 6, 2727-2739.
- Chan, F. L., Umeki, K. & Tanksale, A. 2015. Kinetic Study of Catalytic Steam Gasification of Biomass by Using Reactive Flash Volatilisation. *ChemCatChem*, 7, 1329-1337.
- Clair, J. M. S., Spencer, K. M., Beaver, M. R., Crounse, J. D., Paulot, F. & Wennberg, P. O. 2014. Quantification of hydroxyacetone and glycolaldehyde using chemical ionization mass spectrometry. *Atmos. Chem. Phys.*, 14, 4251-4262.
- Fan, L., Zhang, Y., Liu, S., Zhou, N., Chen, P., Cheng, Y., Addy, M., Lu, Q., Omar, M. M., Liu, Y., Wang, Y., Dai, L., Anderson, E., Peng, P., Lei, H. & Ruan, R. 2017. Bio-oil from fast pyrolysis of lignin: Effects of process and upgrading parameters. *Bioresource Technology*, 241, 1118-1126.
- Horn, R., Williams, K. A., Degenstein, N. J., Bitsch-Larsen, A., Dalle Nogare, D., Tupy, S. A. & Schmidt, L. D. 2007. Methane catalytic partial oxidation on autothermal Rh and Pt foam catalysts: Oxidation and reforming zones, transport effects, and approach to thermodynamic equilibrium. *Journal of Catalysis*, 249, 380-393.
- Kim, J. P. 2004. Effect of palladium and nickel on the temperature programmed reduction of metal oxides and metal oxide layers. *Korean J. Chem*, 21, 385-388.
- Medrano, J. A., Oliva, M., Ruiz, J., García, L. & Arauzo, J. 2009. Catalytic steam reforming of model compounds of biomass pyrolysis liquids in fluidized bed reactor with modified Ni/Al catalysts. *Journal of Analytical and Applied Pyrolysis*, 85, 214-225.
- Morf, P., Hasler, P. & Nussbaumer, T. 2002. Mechanisms and kinetics of homogeneous secondary reactions of tar from continuous pyrolysis of wood chips. *Fuel*, 81, 843-853.
- Pawar, V., Ray, D., Subrahmanyam, C. & Janardhanan, V. M. 2015. Study of short-term catalyst deactivation due to carbon deposition during biogas dry reforming on supported Ni catalyst. *Energy & Fuels*, 29, 8047-8052.
- Phanikrishna Sharma, M. V., Akyurtlu, J. F. & Akyurtlu, A. 2015. Autothermal reforming of isobutanol over promoted nickel xerogel catalysts for hydrogen production. *International Journal of Hydrogen Energy*, 40, 13368-13378.

Wang, S. & Luo, Z. 2017. *Pyrolysis of Biomass*, Berlin, De Gruyter.

Xu, J. & Froment, G. F. 1989. Methane steam reforming, methanation and water-gas shift: I. Intrinsic kinetics. *AIChE Journal*, 35, 88-96.

Chapter 5

Air-Steam Reforming of Acetol and Guaiacol under Reactive Flash Volatilization Conditions

5.1 Introduction

This chapter discusses the results from the air-steam reforming of acetol and guaiacol under reactive flash volatilization conditions. Acetol is presented first and then guaiacol. Results are given for the composition analysis of gas samples from the freeboard region, followed by the discussion on the kinetic behaviour of the overall conversion process.

5.2 Acetol Conversion

5.2.1 Reactor Freeboard Gas Composition Analysis

Figure 5.1 shows the product distribution from acetol decomposition in the reactor freeboard at four different reaction temperatures. Each of the experimental data points was taken after the reactor had run for at least one hour to make sure that stable operation was achieved earlier on and they represent average value of at least duplicate samples. Although oxygen is fed into the reactor, no significant oxygen is detected and therefore it is not shown in Figure 5.1. It is therefore concluded that the oxygen gas in the feed stream was fully consumed in the freeboard reaction and its signal intensity is shown in Appendix 5A.

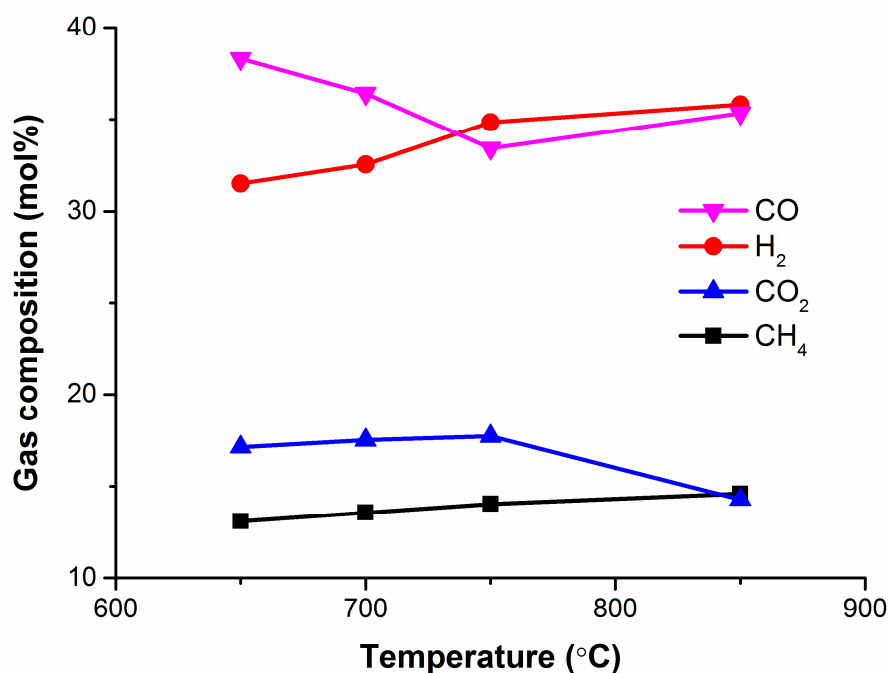


Figure 5.1: The gas composition from the reactor freeboard (dry and argon free basis):
acetol=0.089 ml/min, GHSV=15500h⁻¹, C/O=1.7, and S/C=1.2

The results in Figure 5.1 suggests a two-stage process. The extent of the reactions (notably cracking and oxidation) varied linearly with temperature up to 750°C. From a partial oxidation of bio-oil Zheng et al. (2017) also reported a decreasing trend of CO concentration with temperature rise. Above 750°C, however, different reactions involving steam can occur that promote CO production. From these results, it can be inferred that below the reaction temperature of 750°C steam had no significant influence on acetol conversion in the freeboard.

At the lowest temperature tested (650°C), 63% of the carbon in the acetol feed was converted to C₁ products that include CO, CO₂, and CH₄, Figure 5.2. The rest of the carbon is potentially present as unconverted acetol, formaldehyde, or other intermediate products. This will be discussed later in this section. The ratio of experimental signals at m/z=29 and m/z=27 (summarized in Table 5.1) differed from the value obtained from a one-point calibration of acetol. Bimbela et al. (2009) observed 24% carbon conversion from acetol reforming (with no added oxygen) at 650°C

comparable with the present work. The elemental (C, H, and O) mass balance calculations for the individual reaction temperatures are included in Appendix 5B.

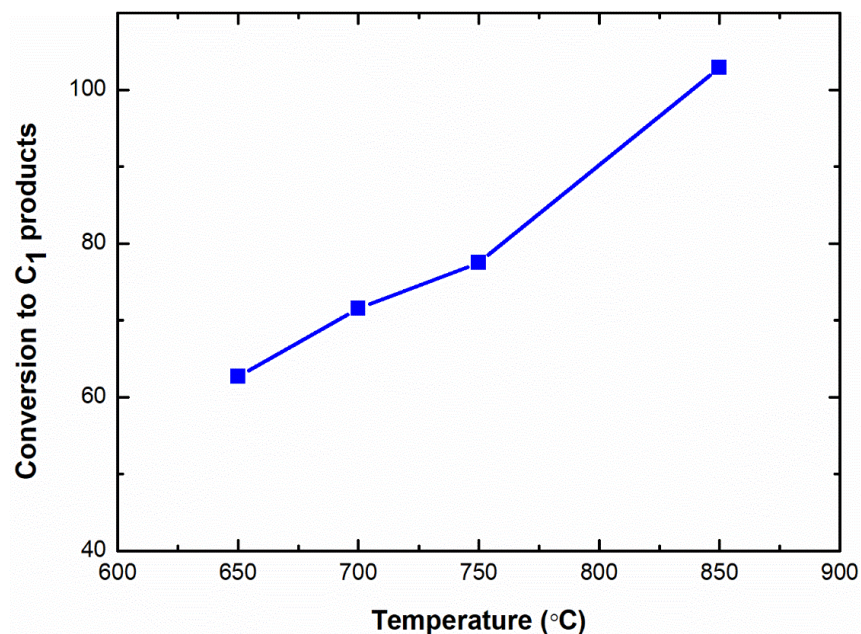


Figure 5.2: The conversion of acetol to C₁ products: 0.089 ml/min acetol, GHSV=15500h⁻¹, C/O=1.7, and S/C=1.2

Table 5.1: Signal ratios of m/z=29 to m/z=27

T (°C)	Calibration for Acetol (m/z=29)/(m/z=27))	Experimental (m/z=29)/(m/z=27)
650	1.18	1.62
700	1.18	1.15
750	1.18	1.07

Figure 5.3 shows the reactor effluent gas composition as a function of temperature. The decreasing trend of methane with the temperature rise suggests the occurrence of catalytic steam reforming of methane (reaction (5.8)). Similarly, steam reforming of the unconverted acetol or intermediate products can also contribute to H₂ and CO yield (reaction (5.9)). Similar trends were observed in steam reforming of acetic acid by Vagia et al. (2007).

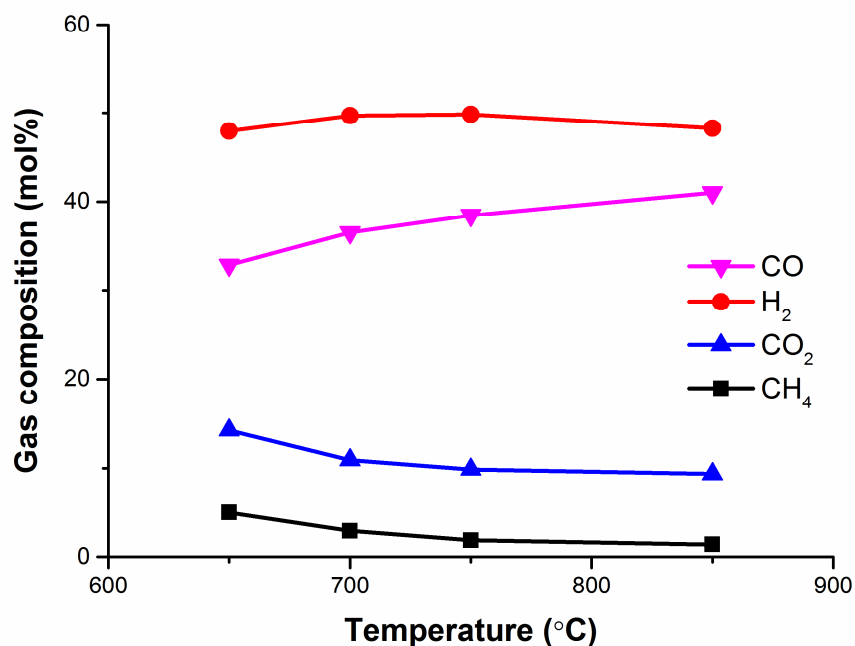


Figure 5.3: Product gas composition from the reactor outlet: acetol=0.089 ml/min, 0.345 g of Rh-Ni/ γ -Al₂O₃ catalyst and 0.05 g quartz wool, GHSV=15500h⁻¹, C/O=1.7, and S/C=1.2

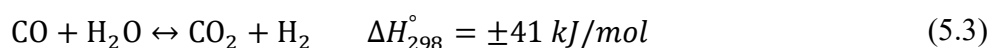
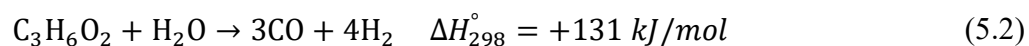
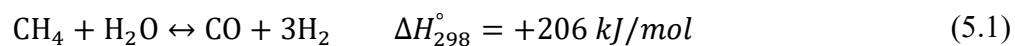


Figure 5.4 shows a comparison of the effluent gas composition from the present study with the work of Ramos et al. (2007) on catalytic steam reforming of acetol. As can also be seen from the figure, contrary to steam reforming of bio-oil that targets high hydrogen yield, in air-steam reforming of bio-oil it is aimed instead at maximizing the selectivity to syngas (H₂ + CO). The other important difference is a complete conversion of the carbon feed was not achieved in Ramos et al. (2007).

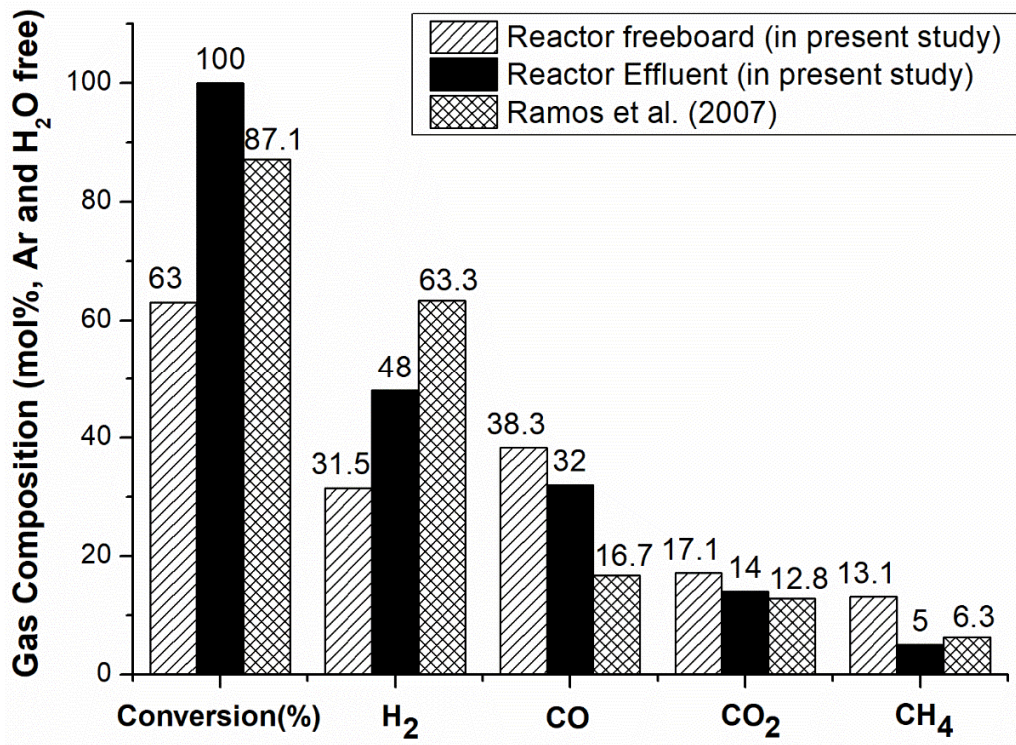


Figure 5.4: Comparison of the gas composition between the present study at 650°C (0.345 g Rh-Ni/ γ -Al₂O₃ catalyst, GHSV=15500h⁻¹, C/O=1.7, and S/C=1.2) with the work of Ramos et al. (2007) at 650°C (0.8 g Ni-Al catalyst, G_{C1}H₂SV=22323h⁻¹, C/O=0, and S/C=4.6)

5.2.1.1 Arrhenius Plot

The first stage, 650-750°C in Figure 5.1, involving cracking and oxidation reactions could be explained by Arrhenius temperature dependence. The freeboard section of the reactor is considered a well-mixed zone of constant volume. Hence, at steady state the mole balance equation for species i under isothermal condition can be written as:

$$0 = QC_i^{in} - QC_i + r_i V \quad (5.4)$$

$$C_i - C_{in}^i = r_i \frac{V}{Q} \quad (5.5)$$

Introducing the space time $\tau = V/Q$ and conversion $X = (C_{in}^i - C^i)/C_{in}^i$, Equation (5.12) can be rewritten as:

$$\frac{X}{\tau} = -\frac{r_i}{C_{in}^i} \quad (5.6)$$

Thus, with an assumption of a first-order reaction in terms of acetol concentration and applying Equation (5.13) for the different values of temperature, activation energy of acetol decomposition was calculated as 56.4 kJ/mol and a frequency factor of 239.4 s⁻¹, Figure 5.5. This activation energy value is comparable to the work of Vaidya and Rodrigues (2006) for steam reforming of ethanol over Ru/ γ -Al₂O₃ catalyst: 96 kJ/mol. The oxygen present in the reaction mixture for the present study lowers the activation energy.

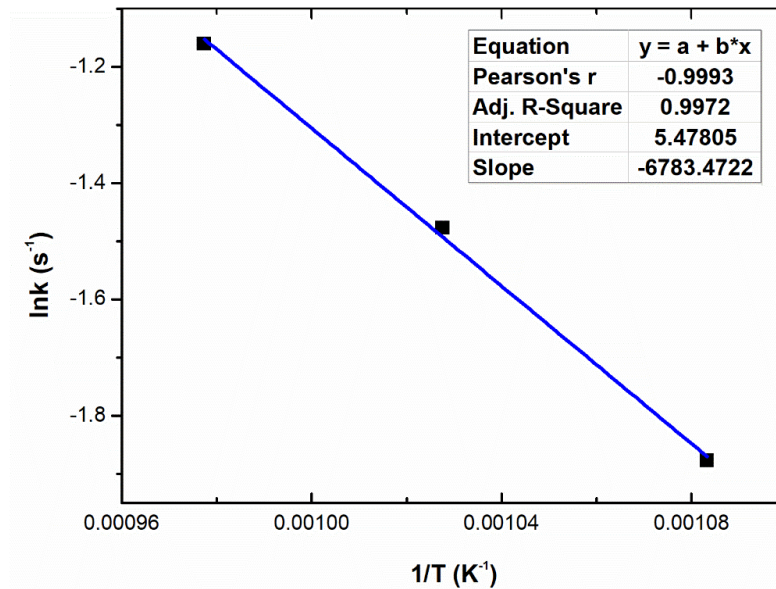


Figure 5.5: Arrhenius plot for rate of acetol decomposition

5.2.2 Catalyst Bed Temperature Measurements

Based on the temperature profiles of the catalyst bed (Figure 5.6), measured by inserting thermocouples from the front and back faces of the bed, the partial oxidation and thermal cracking of the acetol (the volatile) and gases preceded steam reforming. This observation agrees with our proposition in the reaction mechanism analysis for the freeboard. The back-face temperature decreased by 35°C attributable to the highly endothermic nature of the reforming reactions.

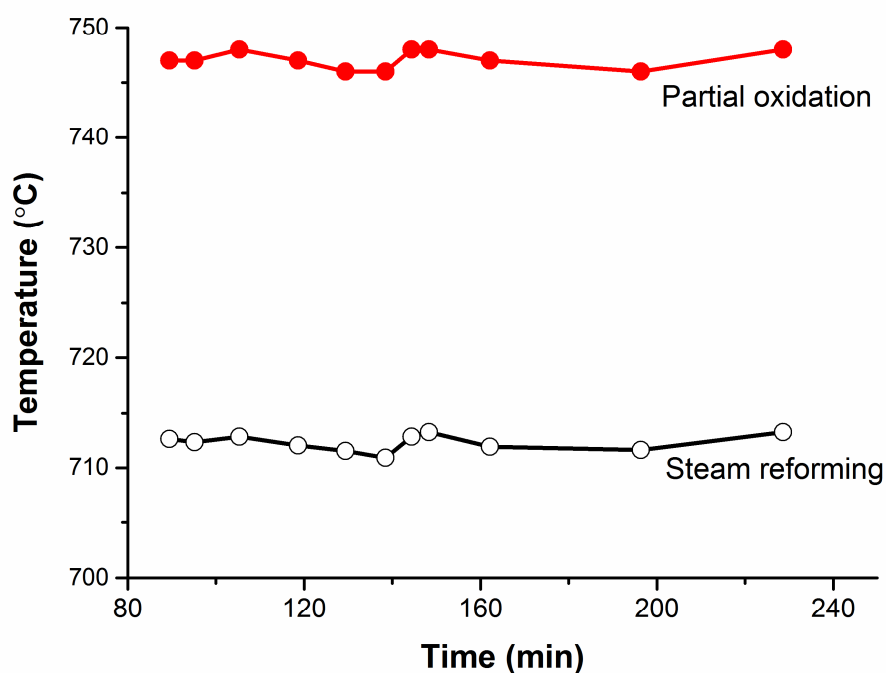


Figure 5.6: Catalyst bed temperature for acetol conversion: acetol=0.115 ml/min, 0.5 g catalyst, GHSV=17000h⁻¹, S/C=1.2, and C/O=1.3

5.2.3 Experimental Matrix Results for Acetol Conversion

The experimental matrix results from the acetol conversion are set out in Table 5.2. The H₂ to CO molar ratio close to 2 is suitable for methanol synthesis (Chapter 1, Table 1.1). The effects of the individual factors on the product gas composition are discussed in the upcoming subsections.

Table 5.2: Composition of the product gas (dry and N₂ free basis) from acetol conversion

Std Run		Factor					Response (mol%)				
		S/C	C/O	T (°C)	GHSV (h ⁻¹)	Catalyst (g)	H ₂	CO	CO ₂	CH ₄	H ₂ /CO
4	1	2.4	1.3	800	17000	0.5	64	19	15.9	0.4	3.3
7	2	2.4	1.7	700	14000	0.5	64	16	18.9	1.0	4.0
1	3	1.2	1.3	700	17000	0.8	51	25	20.5	1.8	2.0
2	4	1.2	1.3	800	14000	0.5	59	28	11.1	0.7	2.1
6	5	1.2	1.7	800	14000	0.8	60	26	12.2	0.7	2.3
8	6	2.4	1.7	800	17000	0.8	60	20	18.7	0.6	3.1
5	7	1.2	1.7	700	17000	0.5	56	21	20.3	1.7	2.7
3	8	2.4	1.3	700	14000	0.8	62	18	18.3	1.1	3.5

Figure 5.7 illustrates a sample result from the experimental matrix (Run 4). A stable steady state operation was achieved approximately an hour after the start of the reaction. The process exhibited high selectivity to H₂ and CO and the time evolution of the gas yields did not exhibit catalyst deactivation. Sample gas chromatograms from the analysis are presented in Appendix 5C.

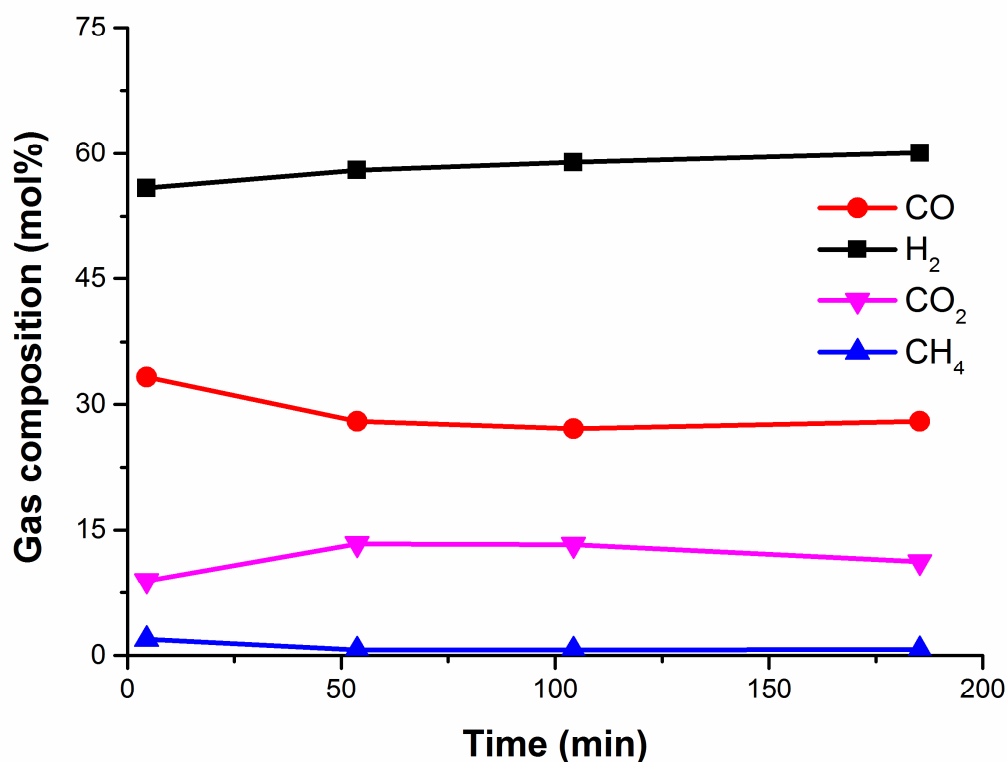


Figure 5.7: Product gas distribution on dry and N₂ free basis: acetol=0.085 ml/min, 0.5 g Rh-Ni/ γ -Al₂O₃ catalyst, T=800°C, GHSV=14000h⁻¹, C/O=1.3, and S/C=1.2

5.2.3.1 Liquid Condensate Analysis

The total carbon in the liquid condensates was determined using a TOC analyser. In all the experimental runs, the carbon-to-gas conversion was complete and the experiments proceeded smoothly, and Table 5.3 shows an example result.

Table 5.3: An example TOC analysis result for a liquid sample

Liquid Sample (g)	TOC (mg/L)	Moles of carbon (C) in the condensate	Total moles of C in the feed	Conversion
6.86	2.84	1.6×10^{-3}	0.794	99.998

Liquid samples were also analysed using HPLC to check for the presence of any unconverted acetol. The condensate had a light yellowish colour and the acetol concentration from all the runs

was less than 0.6 vol%. Figure 5.8 shows a sample result from the analysis with the acetol peak area of 9777.43 (mAU*s).

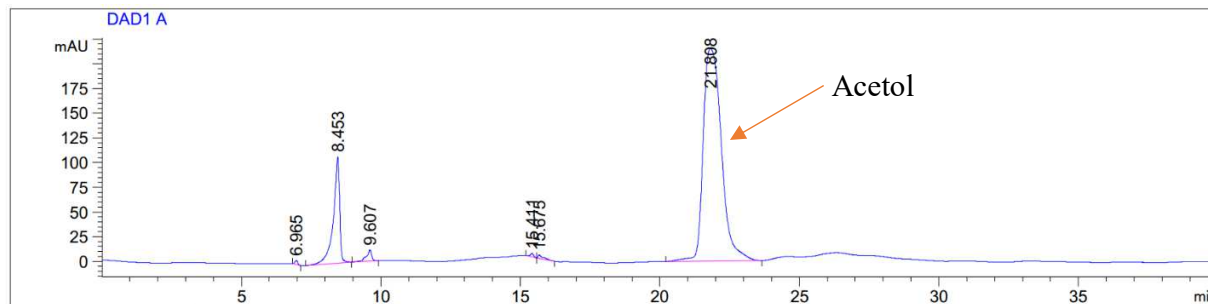


Figure 5.8: Acetol concentration in the liquid sample using HPLC

5.2.3.2 Effect of Temperature

Over the studied temperature range of 700-800°C, an increase in temperature enhanced the endothermic catalytic steam reforming of methane to H₂ and CO according to reaction (5.8), Figure 5.9. The gas composition trends are in line with the results presented earlier in Figure 5.3. As discussed, with an increase in temperature the water-gas shift reaction equilibrium will be shifted toward the reactant side (CO and H₂O) leading to the decrease in CO₂ composition in the product gas. Although hydrogen is as well consumed in the reverse water-gas shift reaction, its net concentration increased because the steam reforming reactions of methane and unconverted acetol (reactions (5.1) and (5.2)) produce more H₂.

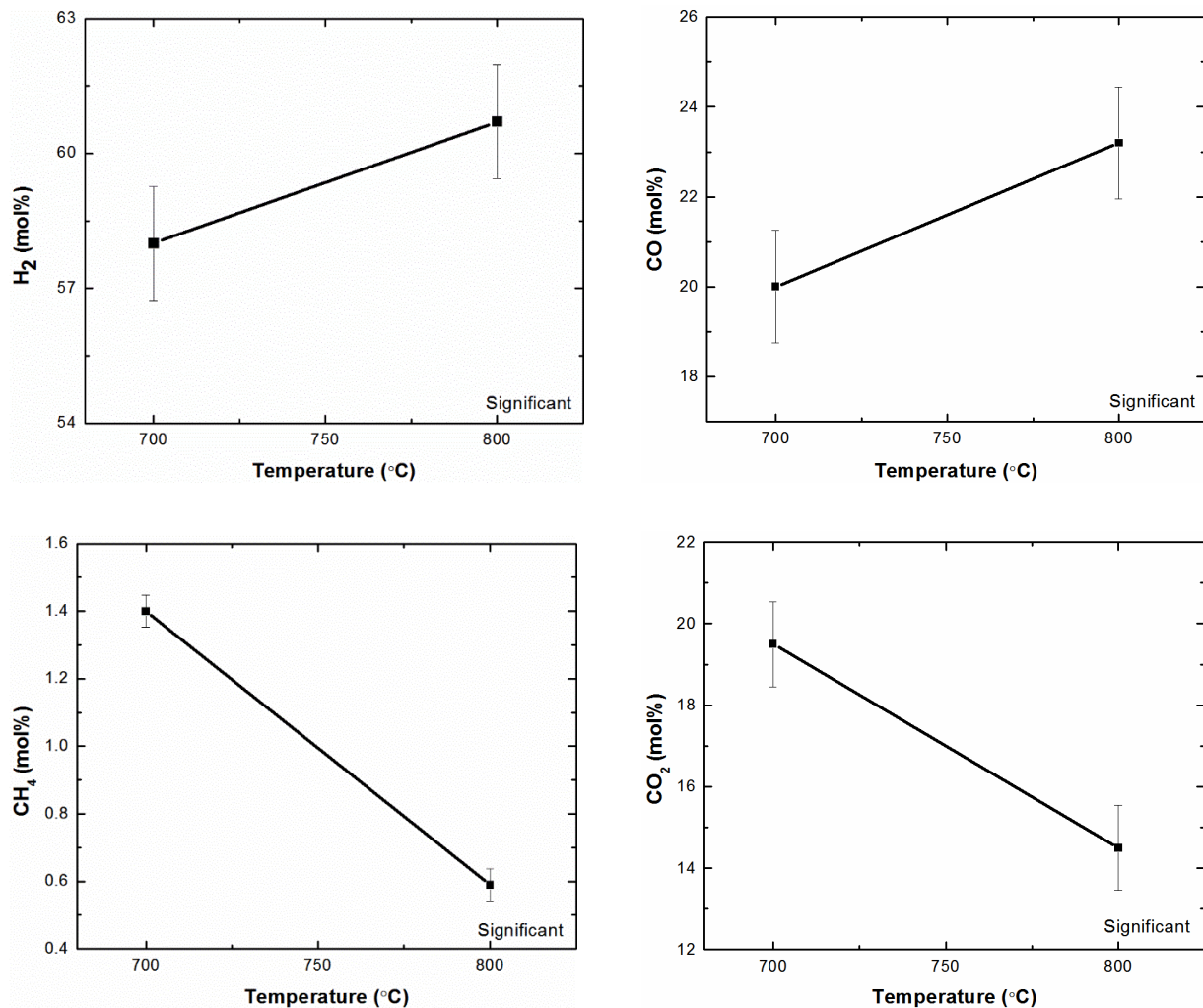


Figure 5.9: Effect of temperature on product gas composition: acetol=0.085 ml/min, 0.5 g catalyst, GHSV=15500 h⁻¹, C/O=1.5, and S/C=1.8

5.2.3.3 Effect of Molar S/C ratio

Since CO is primarily generated via the partial oxidation and cracking reactions in the freeboard (Figure 5.1), adding more steam in the reactor enhances its conversion to H₂ and CO₂ through the water-gas shift reaction within the catalyst bed, Figure 5.10. In the literature, Ni-based catalysts are known to promote water-gas shift reaction (Guan et al., 2016, Baviskar and Vaidya, 2017). In addition, steam gasification of char also favours H₂ production based on reaction (5.7). Nevertheless, the rise in the steam partial pressure appear to have little effect on the net CO₂ concentration though it showed an increasing tendency.

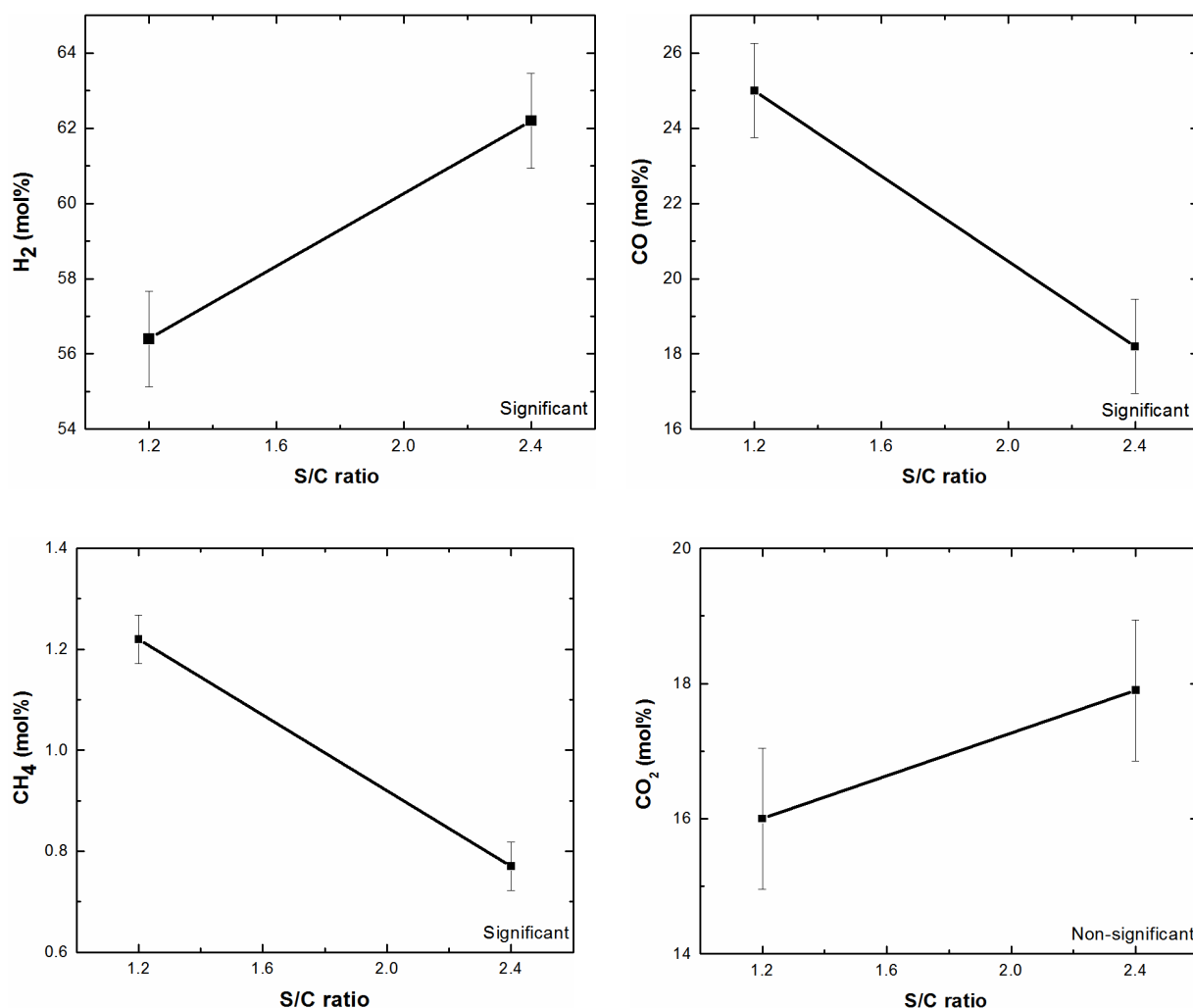


Figure 5.10: Effect of S/C ratio on product gas composition: acetol=0.085 ml/min, 0.65 g catalyst, T=750°C, GHSV=15500h⁻¹, and C/O=1.5



5.2.3.4 Effect of Gas Hourly Space Velocity

As shown in Figure 5.11, the increase in space velocity from 14000h⁻¹ to 17000h⁻¹ led to the increase in methane content because a lesser amount of the methane produced in the freeboard takes part in the subsequent combustion reaction in the freeboard itself. Similar trends for the effect of space velocity have been observed by Sakaguchi et al. (2010).

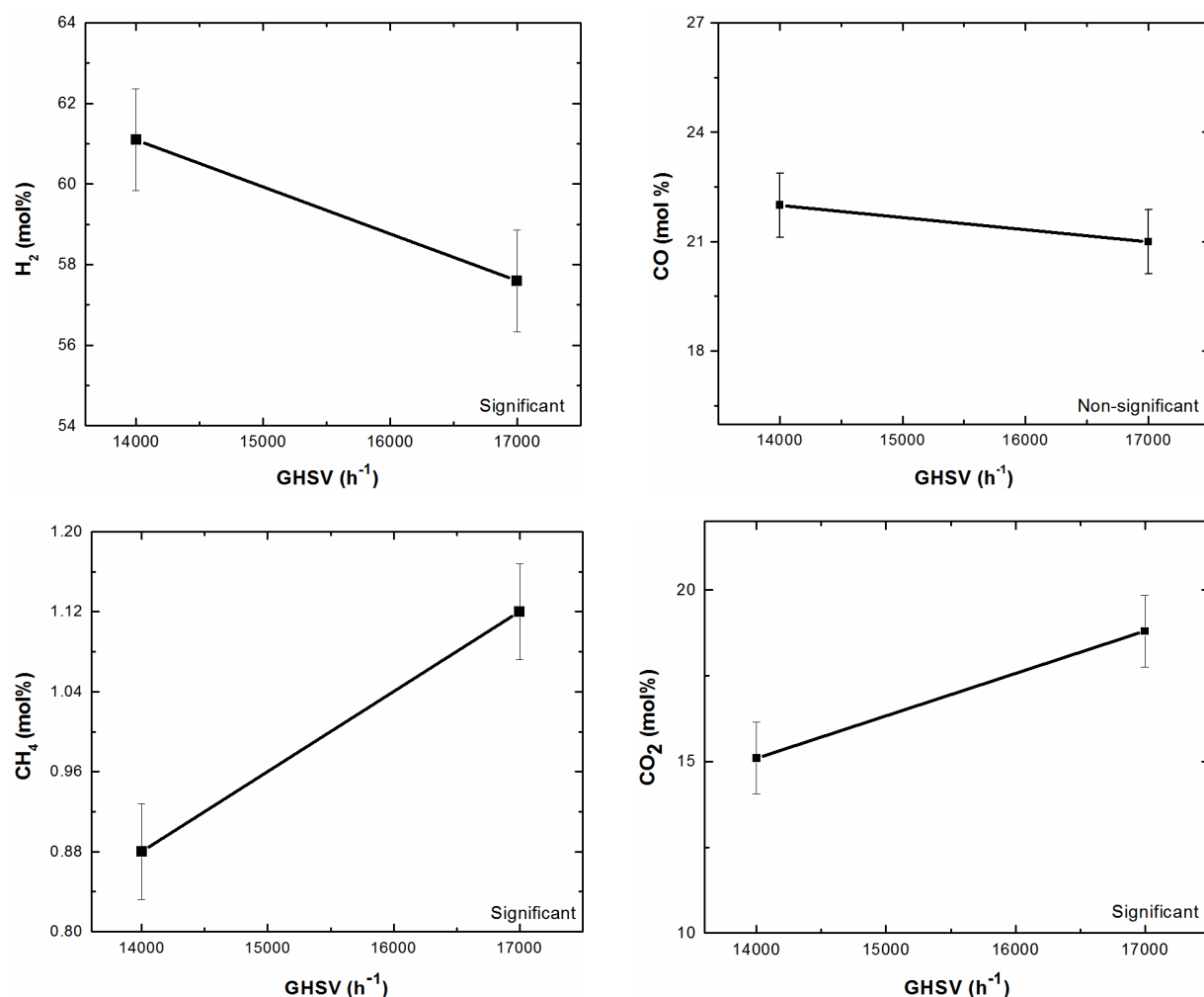


Figure 5.11: Effect of GHSV on product gas composition: acetol=0.085ml/min, 0.65 g catalyst, T=750°C, C/O=1.5, and S/C=1.8

5.2.3.5 Effect of Molar C/O ratio

The change in molar C/O ratio had a limited influence on the CO₂ yield under the conditions tested (1.3-1.7), Figure 5.12. These results match the trends observed from a one-factor-at-a-time experiment shown in Figure 5.13. From Figure 5.13, at higher oxygen content in the feed (lower C/O) the combustion of CO is seen to be a dominant source of CO₂ that happens in the freeboard region itself. However, as the oxygen content reduces the decarboxylation of intermediates (for example, acetic acid as discussed in the Chapter 6) would be the only source of CO₂. For this

reason, reducing the oxygen content further (higher C/O) would not bring significant change in the CO₂ yield in the product gas.

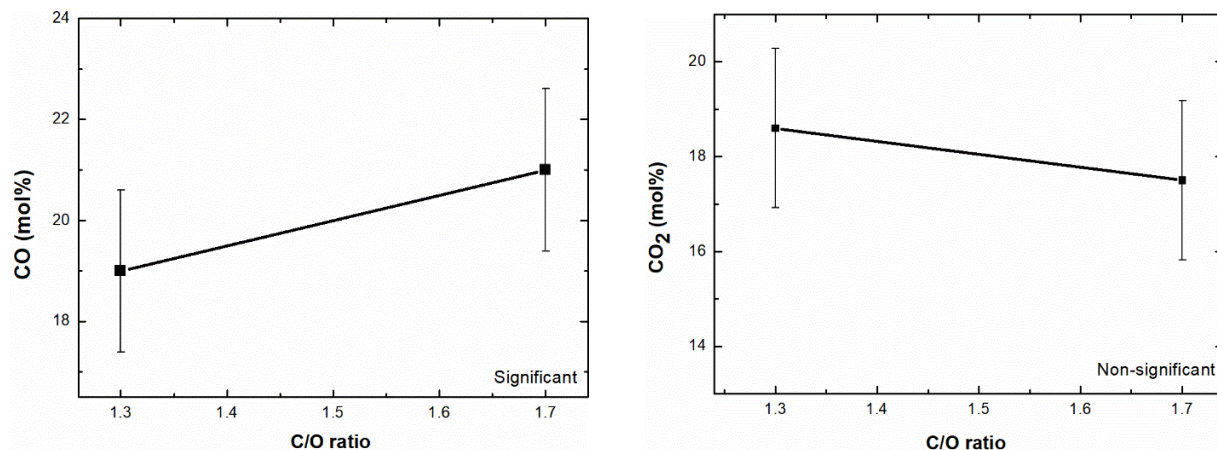


Figure 5.12: Effect of C/O ratio on product gas composition: acetol=0.085ml/min, 0.65g catalyst, T=750°C, GHSV=15500 h⁻¹, and S/C=1.8

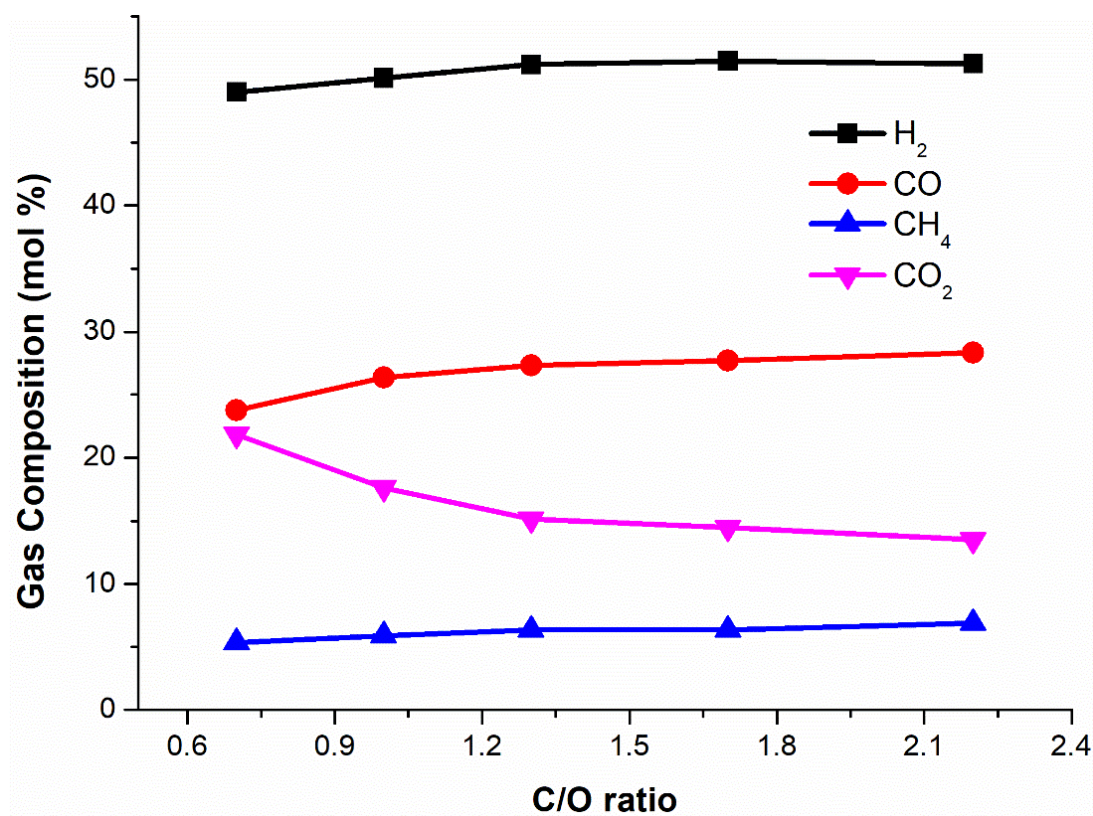


Figure 5.13: Effect of C/O ratio on product gas composition at acetol=0.085 ml/min, 0.5 g catalyst, T=650°C, GHSV=17000h⁻¹, and S/C=1.2

5.2.3.6 Effect of Catalyst Loading

The catalyst loading of 0.5 and 0.8 had similar results suggesting that the 0.5 g was efficient for the reforming of acetol. Nevertheless, reducing the catalyst weight below the 0.5 g is expected to bring significant change in product distribution. To check this, a comparison was made between the product distribution at 700°C from Figure 5.3 and the gas yield from the design of experiments method under the same operating conditions except the catalyst loading as given in Table 5.4. The higher catalyst loading improved H₂ production via the catalytic water-gas shift reaction.

Table 5.4: Comparison between gas yield at 700°C from Figure 5.3 and the gas yield from the design of experiments method: T=700°C, GHSV=15500h⁻¹, C/O=1.7, and S/C=1.2

Parameter	Value	
	Result from Figure 5.3 at 700°C	Design of experiments method
Catalyst loading (g)	0.345	0.503
Gas yields (mol%)		
H ₂	50	55
CO	36	23
CO ₂	10	18.6
CH ₄	3	1.7

5.2.3.7 Effect of Operating Conditions on H₂/CO and CO/CO₂ ratios

The ratio between steam and carbon (S/C) is the most important factor that significantly alters the molar H₂/CO ratio (Figure 5.14). On the other hand, temperature, S/C ratio, GHSV, and C/O ratio all have influence on the CO/CO₂ molar ratio, Figure 5.15.

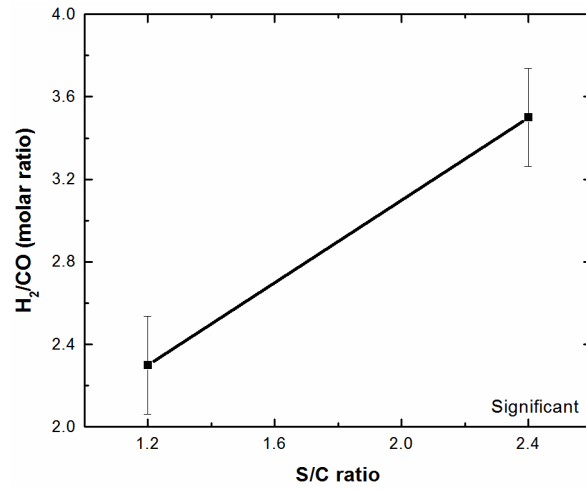


Figure 5.14: Effect of S/C ratio on the molar ratio of H₂/CO: 0.65 g catalyst, T=750°C, GHSV=15500 h⁻¹, and C/O=0.75

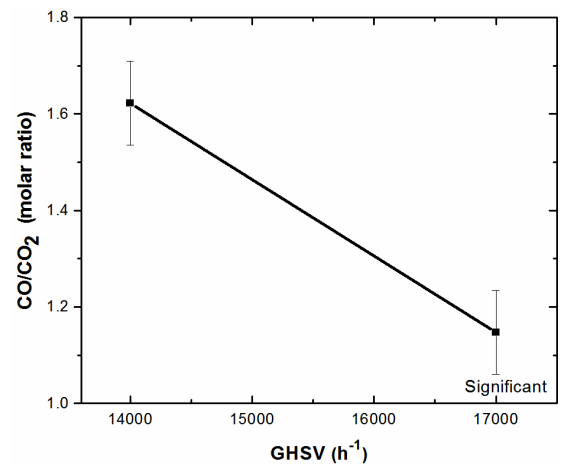
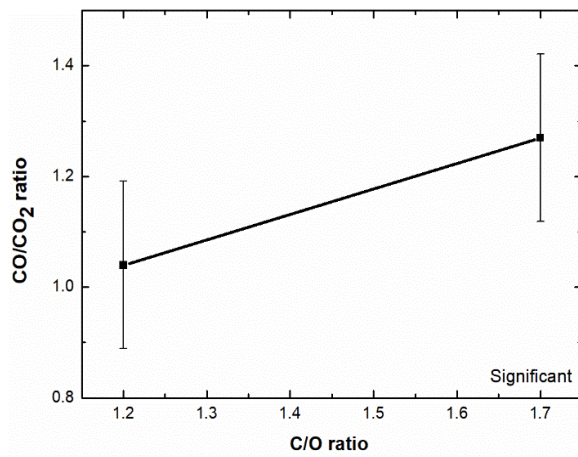
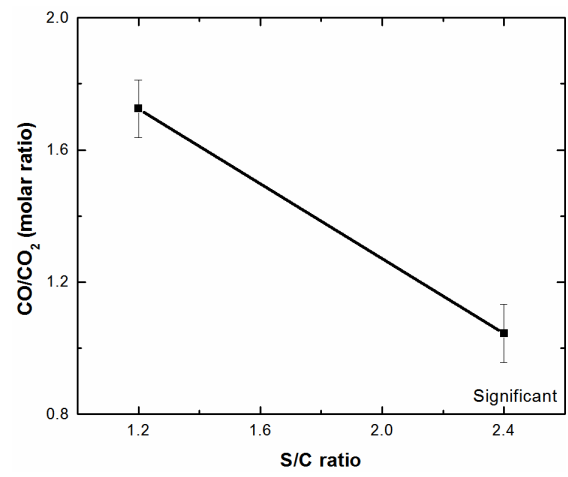
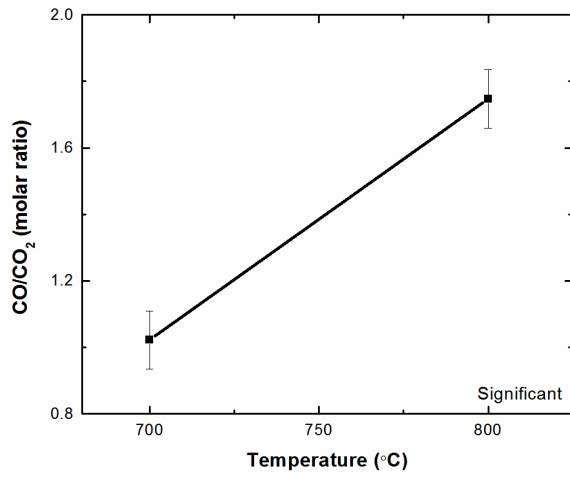


Figure 5.15: Effect of temperature, S/C ratio, C/O ratio and GHSV on CO/CO₂ molar ratio

5.2.3.8 Characterization of Spent Catalyst

Figure 5.16 shows the TEM images of the fresh and spent catalyst samples. The active sites (dark spots) in the fresh catalyst are well-dispersed (no particle aggregation) over the porous alumina support. The uniform distribution of the active sites can contribute to lessen carbon deposition. After the reaction, no obvious carbon nanofibers or nanotubes was observed on the spent catalyst sample.

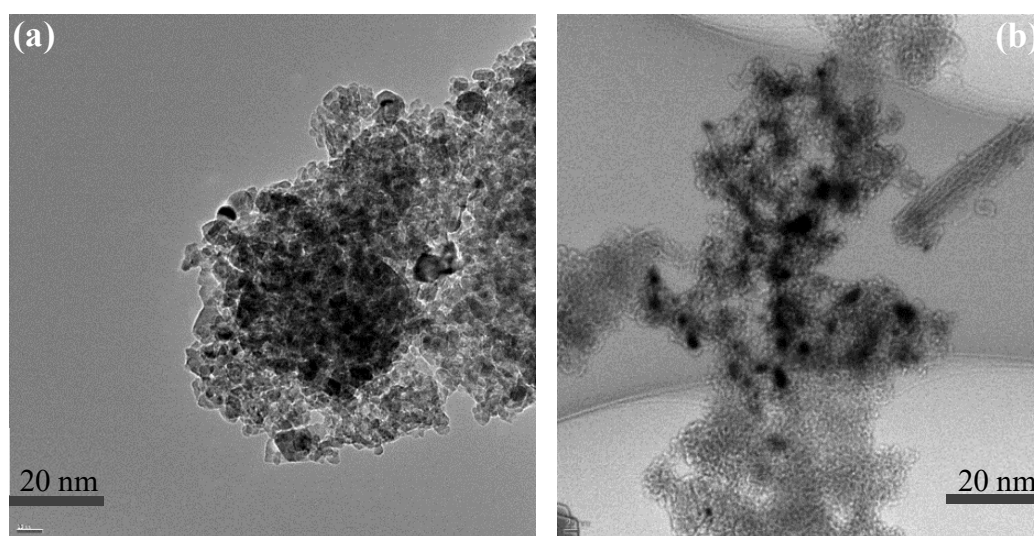


Figure 5.16: TEM images of Rh-Ni/Al₂O₃ catalyst surface (a) fresh (b) spent catalyst after 4 hours reaction from acetol conversion: T=700°C, C/O=1.3, and S/C= 2.4

CHN analysis results for spent catalyst samples from all the experimental runs are summarized in Table 5.5. The carbon content on the catalyst samples were less than 6 wt% that corresponds to ~0.3% of the total moles of carbon fed to the reactor. Run 6 (T=800°C, GHSV=17000h⁻¹, C/O=1.7, and S/C=2.4) resulted in the least char formation (0.99 wt%) denotes the role of the higher steam partial pressure, space velocity, and temperature in preventing and/or reforming char. Increasing the oxygen content in the feed affects the product composition in two ways. One is, the CO combustion will lead to more CO₂ production and the second is the higher oxygen content might lead to other decomposition products which might produce char.

Table 5.5: CHN analysis results of Rh-Ni/ γ -Al₂O₃ spent catalyst from the acetol experiments

Run	S/C	C/O	T (°C)	GHSV (h ⁻¹)	Catalyst (g)	C (%)	H (%)
1	2.4	1.3	800	17000	0.5	5.88	0.51
2	2.4	1.7	700	14000	0.5	5.88	0.44
3	1.2	1.3	700	17000	0.8	2.96	0.46
4	1.2	1.3	800	14000	0.5	5.26	0.42
5	1.2	1.7	800	14000	0.8	2.31	0.37
6	2.4	1.7	800	17000	0.8	0.99	0.38
7	1.2	1.7	700	17000	0.5	1.98	0.42
8	2.4	1.3	700	14000	0.8	2.95	0.42

5.2.3.9 Carbon Forming Region

Under deactivating conditions (T=500°C, S/C=0, and C/O=1.3), from visual inspection the acetol feed produced carbonaceous residue on the reactor wall close to the catalyst bed as well on the surface of the catalyst bed itself, Figure 5.17. A smooth operation of the process was not possible as a measurable carbon (Table 5.6) deposited on the catalyst bed clogged the reactor. The catalyst deactivation occurred due to the low catalyst bed temperature not conducive to support reforming of volatiles and char.



Figure 5.17: Picture of the reactor after reaction: T=500°C, 0.5 g of Rh-Ni/ γ -Al₂O₃, C/O=1.3, and S/C=0

Table 5.6: Catalyst weight before and after the reaction

Quartz wool (g)	Fresh Catalyst + wool (g)	Spent catalyst + wool (g)	Amount of carbon (g)
0.051	0.55	0.657	0.11

Figure 5.18b shows the TEM image for a spent catalyst under the carbon forming conditions (temperature of 500°C, C/O ratio of 1.3, and with no added steam), and a graphitic carbon is observed.

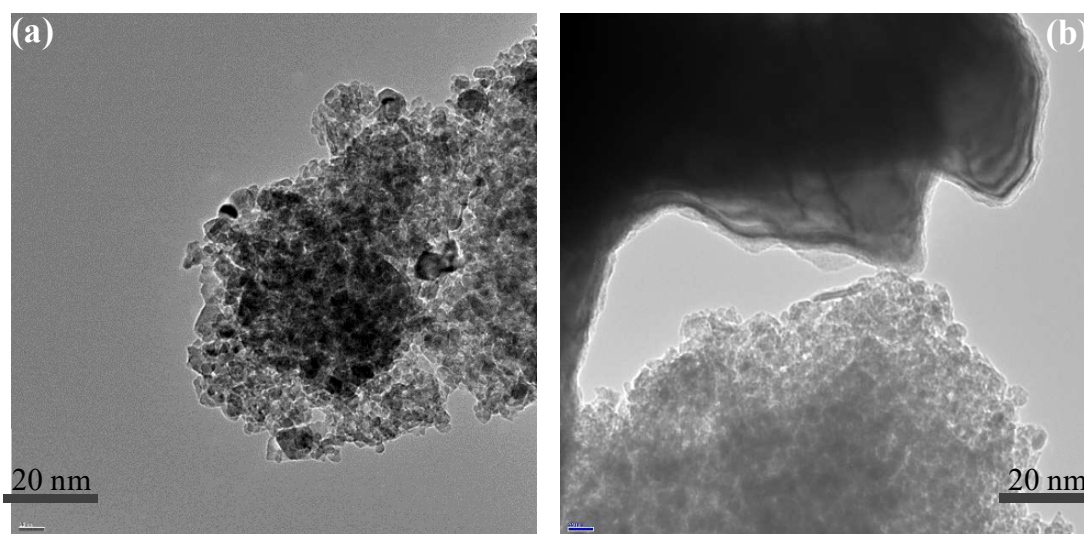


Figure 5.18: TEM images of (a) fresh sample of Rh-Ni/Al₂O₃ catalyst (b) spent catalyst after 4 hours reaction at temperature of 500°C, S/C=0, and C/O=1.3

The graph presented previously in Figure 5.13 is from a one-factor-at-a-time experiment that aimed at identifying the boundary for a carbon forming region for the reaction temperature of 650°C. This experiment was conducted by varying the oxygen content of the feed stream while keeping the other operating parameters constant. The total time for the experimental run was more than 9 hours (560 min) with no operational issues encountered. The boundary of the carbon forming region lies between C/O ratio of 1.7 and 2. At C/O=2 an observable carbonaceous deposit was seen on the reactor wall in the freeboard. Table 5.7 shows the composition of the reactor effluent gas at the C/O ratio of 2. Equilibrium model results under these reaction conditions (T=650°C, C/O=2, and S/C=1.2) showed no carbon formation as marked (*) on Figure 5.19 but in

reality, a carbonaceous deposit was formed. Any point that lies to the right of the curves (operating temperature lines) is inside the no carbon forming region. Therefore, equilibrium models have a limitation on identifying carbon forming conditions.

Table 5.7: Product gas composition on nitrogen free basis: acetol=0.085 ml/min, 0.5 g of catalyst, T=650°C, GHSV=17000h⁻¹, C/O=2, and S/C=1.2

Time (hr)	Gas yield (mol%)			
	H ₂	CO	CH ₄	CO ₂
0.5	58.6	22.4	7.6	11.4
1.6	49.6	29.8	7.5	13.1
2.25	49.5	29.9	7.4	13.1
2.9	49.7	29.9	7.4	12.9

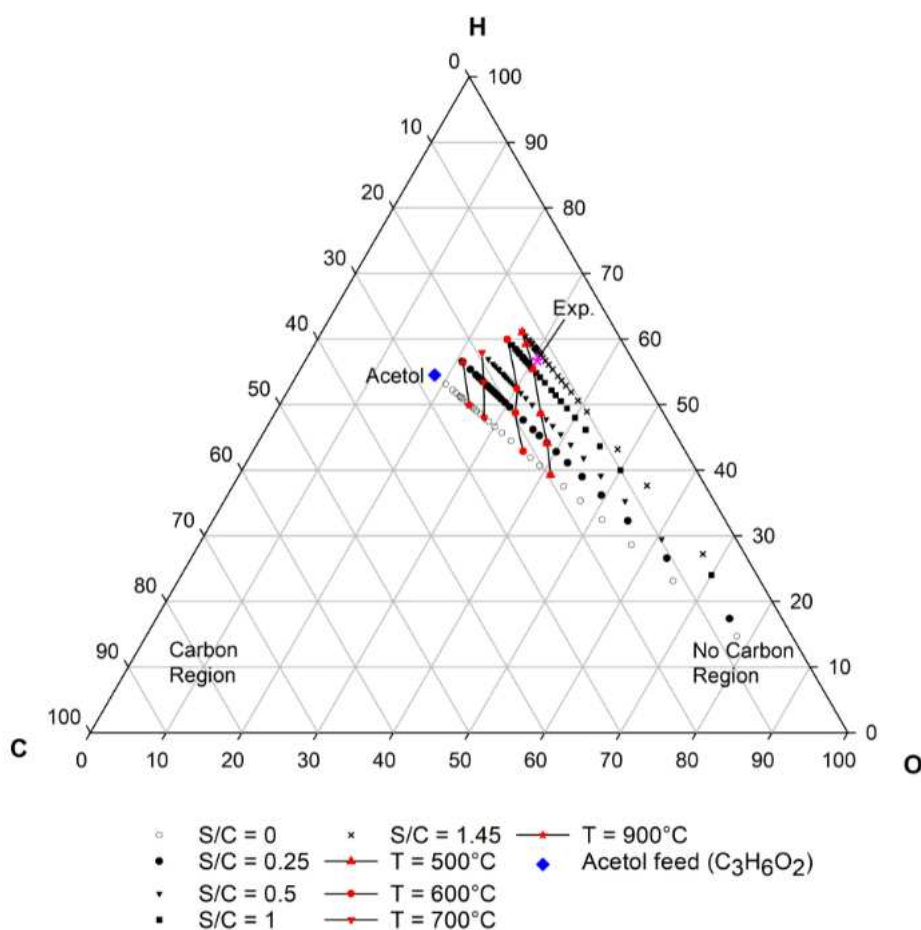


Figure 5.19: Carbon forming region for acetol conversion from an equilibrium model

5.3 Guaiacol Conversion

As discussed before, the methoxy (CH_3O) groups in lignin-derived compounds can easily polymerise to carbonaceous deposits on reactor walls. Thus, to initially check the nature of the conversion process, two separate runs under similar conditions were performed. The results from these two experiments (Figures 5.20 and 5.21) were in good agreement with each other and as well confirmed the reproducibility of the results. The H_2 yield was slightly higher for a C/O ratio of 1.15 because the amount of H_2 that takes part in the combustion reaction has reduced.

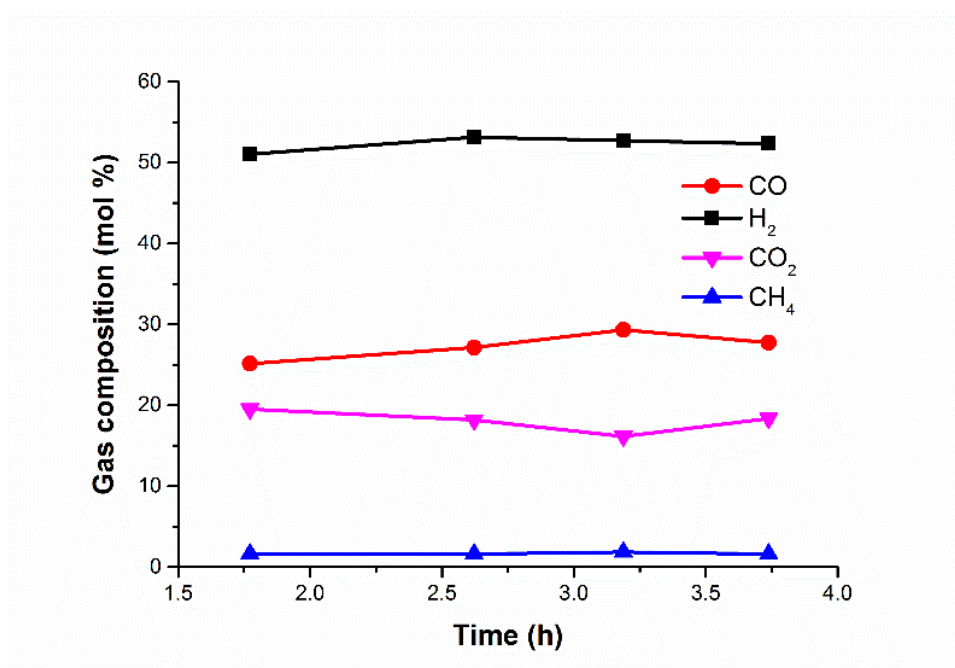


Figure 5.20: Guaiacol conversion: guaiacol=0.06 ml/min, 0.5 g of Rh-Ni/ $\gamma\text{Al}_2\text{O}_3$ catalyst, $T=700^\circ\text{C}$, GHSV=17000 h^{-1} , C/O=0.85, and S/C=1.2

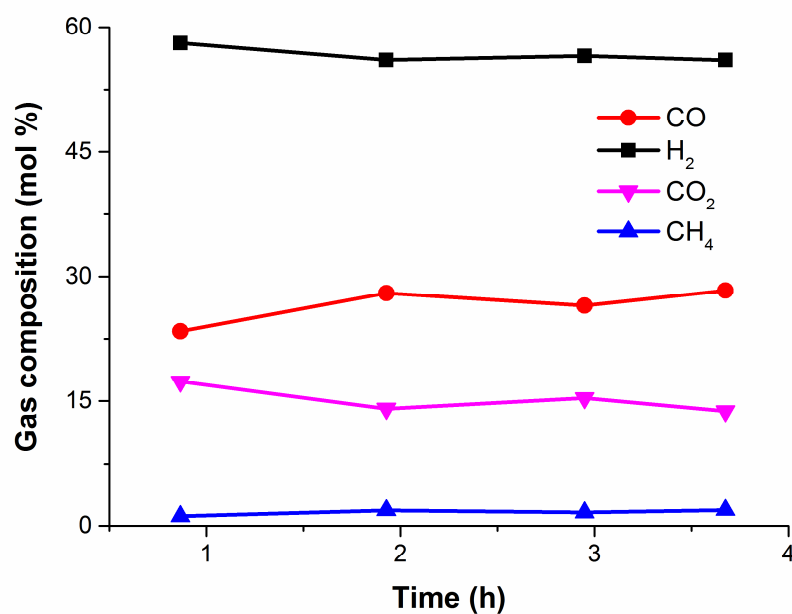


Figure 5.21: Guaiacol conversion: guaiacol=0.0575 ml/min, 0.5 g catalyst, $T=700^{\circ}\text{C}$, $\text{GHSV}=17000\text{h}^{-1}$, $\text{C/O}=1.15$, and $\text{S/C}=1.2$

With no catalyst added in the reactor (a quartz wool being the only constituent of the bed) the guaiacol conversion led to a formation of high amount carbonaceous residue as shown in Figure 5.22a. This problem was solved when a catalyst was used, Figure 5.22b. During experiments, the reactor temperature had to be kept above 600°C to avoid formation of carbonaceous deposit.



Figure 5.22: Guaiacol conversion a) without a catalyst and b) in the presence of catalyst

5.3.1 Catalyst Bed Temperature Measurements

The guaiacol conversion showed similar behaviour as that of the acetol feed conversion and the catalyst bed temperature dropped by 30°C, Figure 5.23.

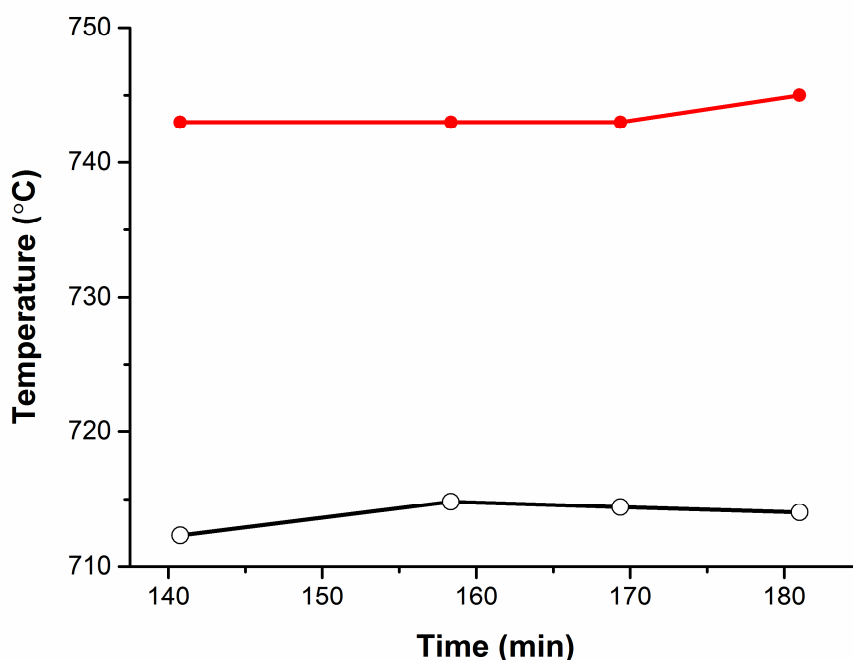


Figure 5.23: Catalyst bed temperature of guaiacol conversion: 0.1 ml/min guaiacol, GHSV=17000h⁻¹, C/O=1.15, and S/C=1.2

5.3.2 Experimental Matrix Results for Guaiacol Conversion

Unlike experimenting with one factor at a time, design of experiments enables to determine the individual and interactive effects of many factors simultaneously. Table 5.8 shows results for the experimental design matrix from the guaiacol conversion. Smooth operation of the reaction was achieved throughout the 5 hours reaction times. In run 5 and 6 (at high steam-to-carbon ratio (S/C=2.4) and low oxygen feed (C/O=1.15)), however, some carbonaceous deposit was formed at the entrance of the reactor. Generally, guaiacol conversion requires higher amount of oxygen when compared to acetol specially when a higher amount of steam is being used (S/C=2.4). That consequently led to a higher CO₂ yield compared to the acetol conversion.

Table 5.8: Results from guaiacol conversion experiments

Std	Run	Factor				Response (mol%)				
		S/C	C/O	T (°C)	GHSV (h ⁻¹)	H ₂	CO	CO ₂	CH ₄	H ₂ /CO
3	1	1.2	1.15	700	17000	56.52	26.5	15.35	1.62	2.13
2	2	2.4	0.85	700	17000	64.36	8.61	26.58	0.45	7.47
7	3	1.2	1.15	800	14000	54.32	24.54	20.45	0.68	2.21
6	4	2.4	0.85	800	14000	61.01	11.64	26.52	0.83	5.24
4	5	2.4	1.15	700	14000	60.16	9.13	30.23	0.47	6.59
8	6	2.4	1.15	800	17000	62.07	15.27	22.2	0.46	4.06
1	7	1.2	0.85	700	14000	50.64	22.08	25.75	1.53	2.29
5	8	1.2	0.85	800	17000	52.64	27.22	19.35	0.78	1.93

5.3.2.1 Liquid Condensate Analysis

TOC analysis result for Run 2 in the experimental matrix is included in Table 5.9. The carbon conversion for the guaiacol feed is almost 100%.

Table 5.9: An example TOC analysis result for a liquid sample

Liquid Sample (g)	TOC result (mg/L)	Moles of Carbon in the condensate	Total moles of carbon fed	Conversion
9.505	0.9302	7.4×10^{-4}	1.18	99.937

5.3.2.2 Effect of Temperature

Temperature had a similar influence on the product gas composition from guaiacol conversion as acetol. The methane yield decreases with the increase in temperature due to the endothermic steam reforming of methane, Figure 5.24. The temperature increase, however, did not bring significant change to the net yield for CO₂ and H₂.

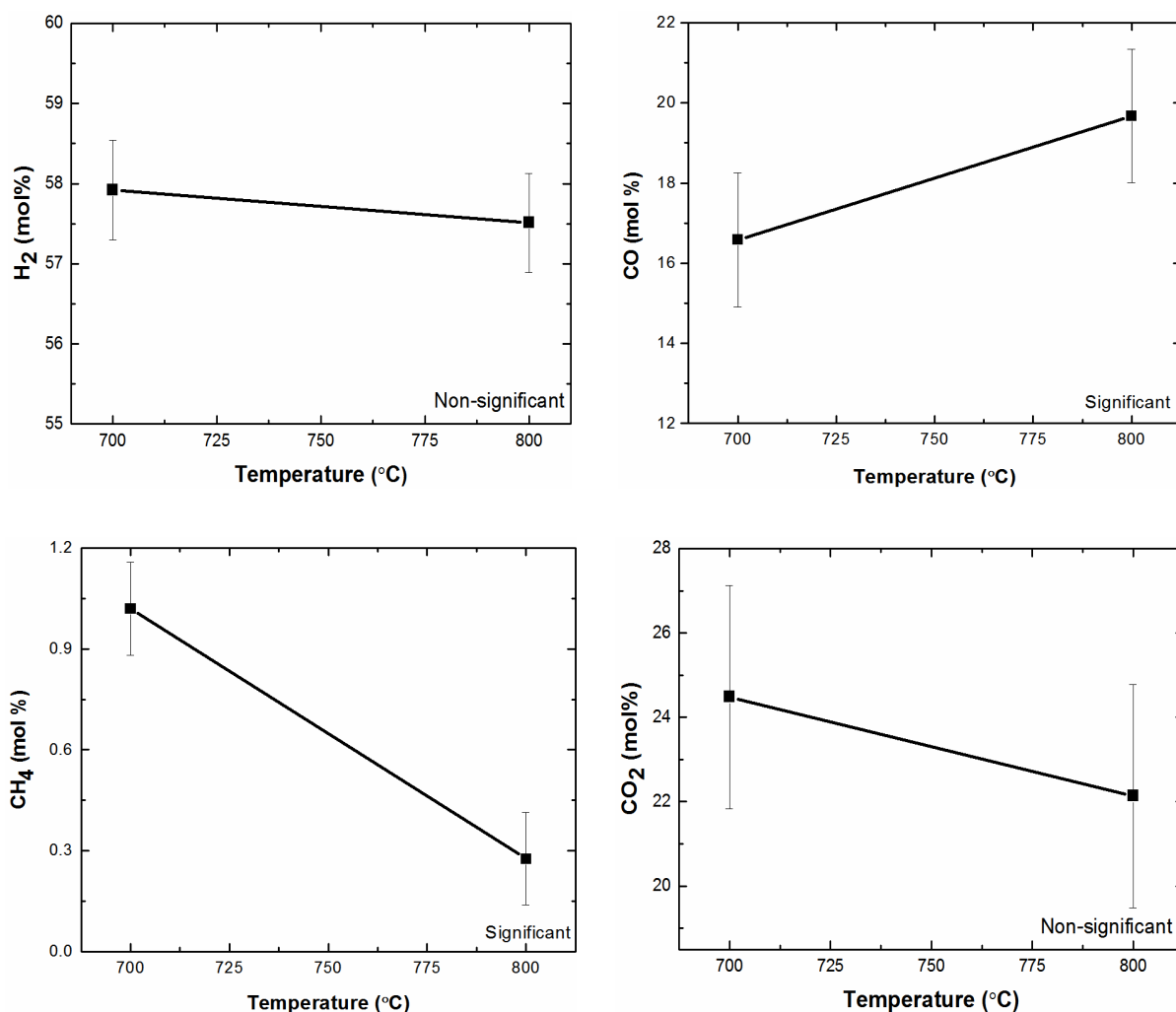


Figure 5.24: Effect of temperature on product gas composition: 0.0575 ml/min guaiacol, 0.5 g catalyst, GHSV=15500 h⁻¹, C/O=1, and S/C=1.8

5.3.2.3 Effect of Molar S/C ratio

From Figure 5.25, the increase in steam partial pressure enhances steam reforming reactions, for instance methane reforming reaction (5.1), which are sources of hydrogen. The water-gas shift reaction (5.3) is also promoted under this condition that can lead to a production of more H₂ and CO₂.

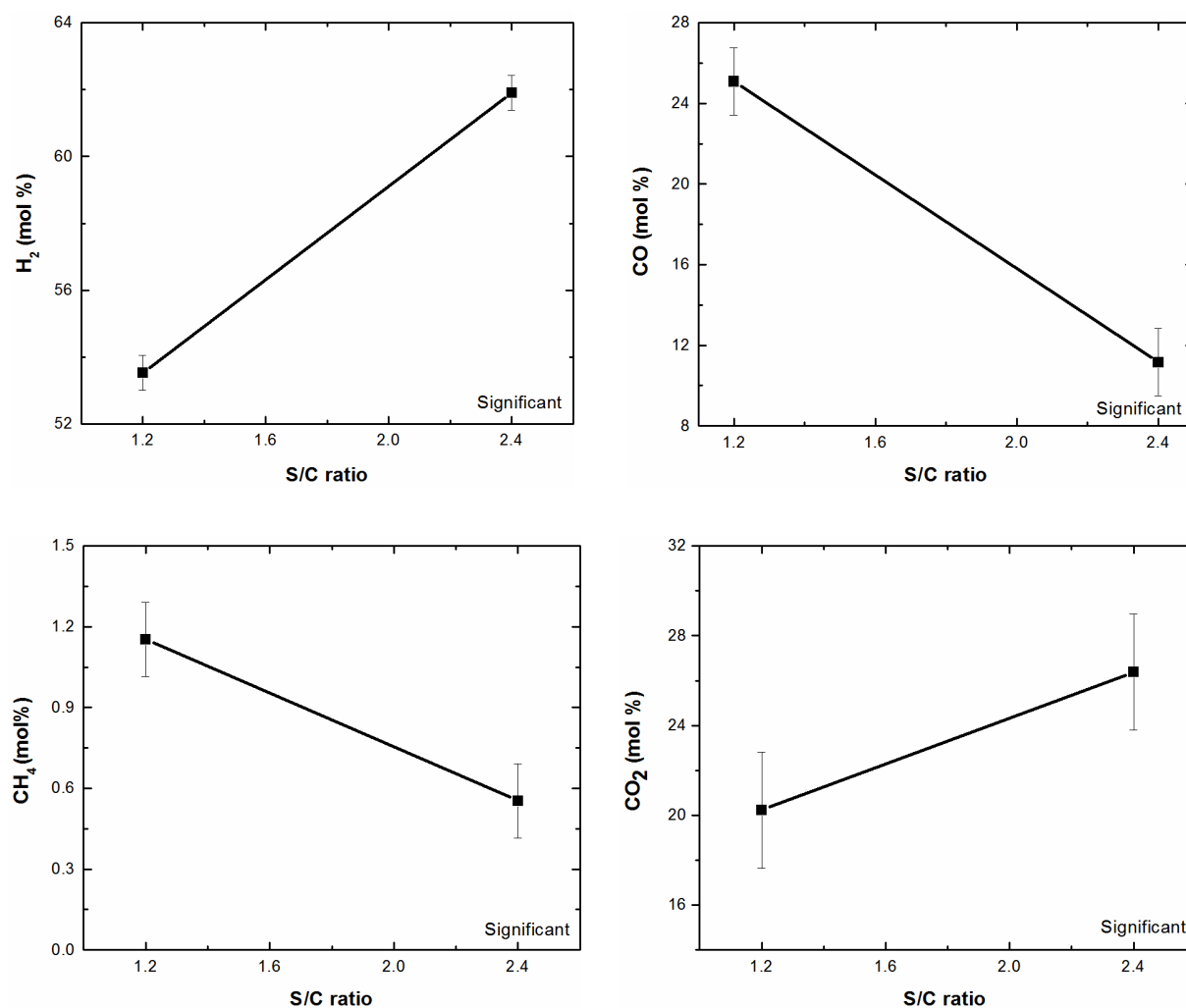


Figure 5.25: Effect of S/C ratio on product gas composition: guaiacol=0.0575 ml/min, 0.5 g catalyst, T=750°C, GHSV=15500 h⁻¹, and C/O=1

For the methane and hydrogen yield in the product gas, there is an interaction effect between S/C ratio and temperature and S/C ratio and C/O ratio, respectively, as shown in Figure 5.26. For example, at the lower temperature setting (700°C), the increase in S/C ratio had a significant effect on methane yield but not at the higher reaction temperature (800°C).

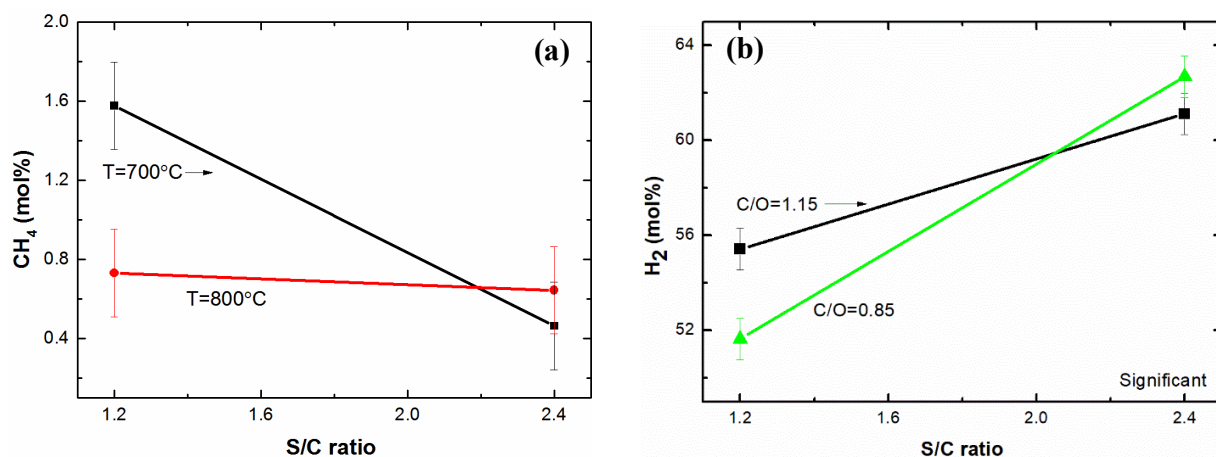


Figure 5.26: Interactive effect of (a) S/C ratio and temperature on methane yield: GHSV=15500 h^{-1} and C/O=1 (b) S/C ratio and C/O ratio on H_2 yield: $T=750^\circ\text{C}$ and GHSV=15500 h^{-1}

5.3.2.4 Effect of Gas Hourly Space Velocity

As shown in Figure 5.27, the change in the gas space velocity had a positive influence on H_2 yield while the CO_2 yield was affected negatively.

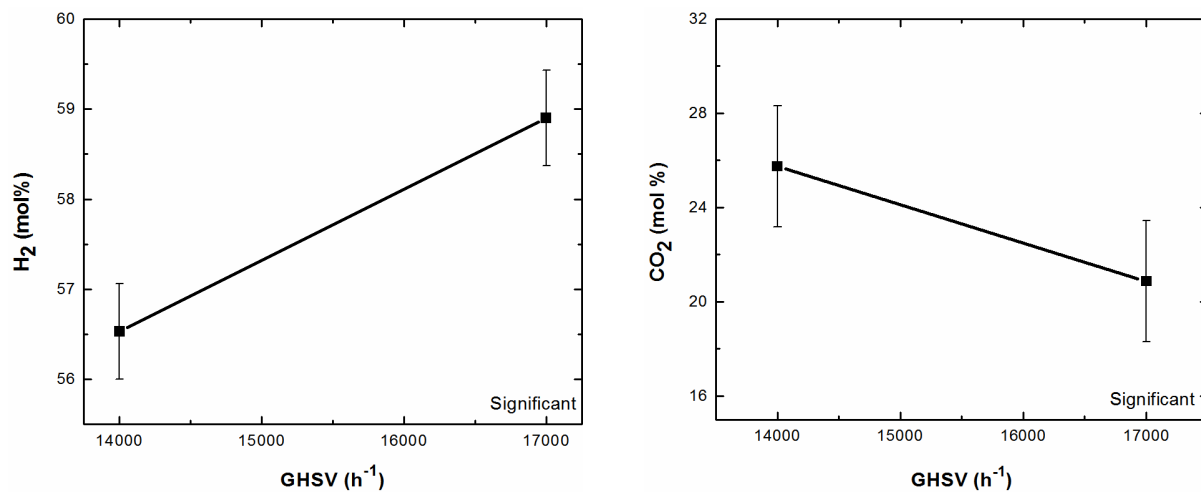


Figure 5.27: Effect of temperature on gas product composition: guaiacol=0.0575 ml/min, 0.5 g catalyst, C/O=1, and S/C=1.8

5.3.2.5 Effect of Molar C/O ratio

For guaiacol conversion the decrease in C/O ratio brought a favourable influence on hydrogen composition as a lesser amount of hydrogen undergoes combustion to H_2O , Figure 5.28.

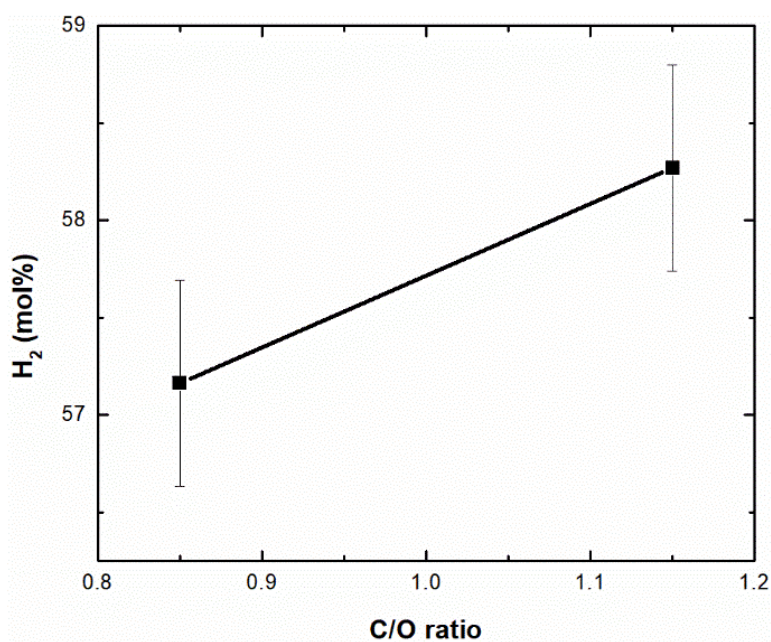


Figure 5.28: Effect of temperature on gas product composition: guaiacol=0.0575 ml/min, 0.5 g catalyst, GHSV=15500 h⁻¹, C/O=1, and S/C=1.8

5.3.2.6 Effect of Operating Conditions on H_2/CO and CO/CO_2 ratios

As shown in Figure 5.29, S/C ratio has a significant influence on H_2/CO and C/O ratios.

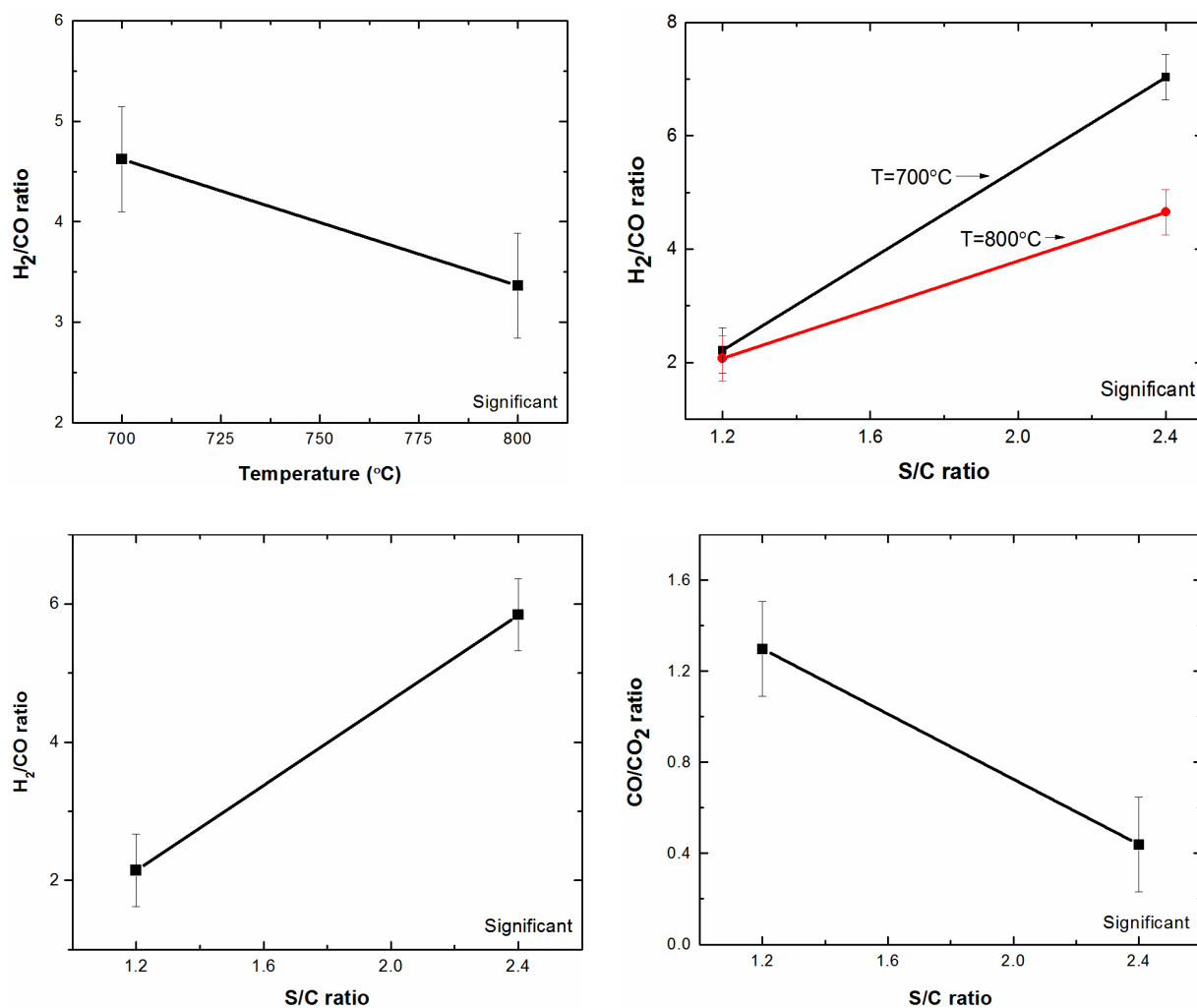


Figure 5.29: Effect temperature and S/C ratio on molar ratio of H_2/CO and CO/CO_2

5.3.2.7 Characterization of Spent Catalyst

Figure 5.30 shows the morphology of the spent catalyst from the guaiacol conversion. There is no carbon deposition observed on the catalyst surface.

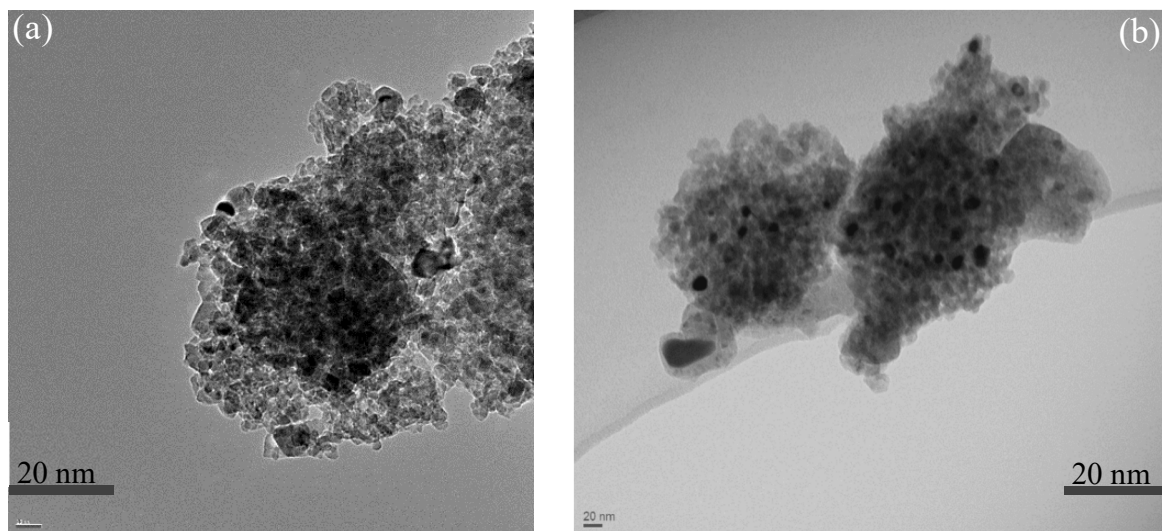


Figure 5.30: TEM images of Rh-Ni/Al₂O₃ catalyst surface (a) fresh catalyst (b) spent catalyst after 4 hours reaction time for guaiacol conversion: T=700°C, C/O=0.85, and S/C=1.2

5.4 Conclusions

Both the reactions in the freeboard and the catalytic reactions are important for the gas conversion and carbon formation. Moreover, both acetol and guaiacol can be converted without carbon formation, and in the case of guaiacol it is a major achievement.

References

- Baviskar, C. V. & Vaidya, P. D. 2017. Steam reforming of model bio-oil compounds 2-butanone, 1-methoxy-2-propanol, ethyl acetate and butyraldehyde over Ni/Al₂O₃. *International Journal of Hydrogen Energy*, 42, 21667-21676.
- Bimbela, F., Oliva, M., Ruiz, J., García, L. & Arauzo, J. 2009. Catalytic steam reforming of model compounds of biomass pyrolysis liquids in fixed bed: Acetol and n-butanol. *Journal of Analytical and Applied Pyrolysis*, 85, 204-213.
- Guan, G., Kaewpanha, M., Hao, X. & Abudula, A. 2016. Catalytic steam reforming of biomass tar: Prospects and challenges. *Renewable and Sustainable Energy Reviews*, 58, 450-461.
- Ramos, M. C., Navascués, A. I., García, L. & Bilbao, R. 2007. Hydrogen production by catalytic steam reforming of acetol, a model compound of bio-oil. *Industrial & Engineering Chemistry Research*, 46, 2399-2406.
- Sakaguchi, M., Watkinson, A. P. & Ellis, N. 2010. Steam gasification of bio-oil and bio-oil/char slurry in a fluidized bed reactor. *Energy & Fuels*, 24, 5181-5189.
- Vagia, E. C. & Lemonidou, A. A. 2007. Thermodynamic analysis of hydrogen production via steam reforming of selected components of aqueous bio-oil fraction. *International Journal of Hydrogen Energy*, 32, 212-223.
- Vaidya, P. D. & Rodrigues, A. E. 2006. Kinetics of steam reforming of ethanol over a Ru/Al₂O₃ catalyst. *Industrial & Engineering Chemistry Research*, 45, 6614-6618.
- Zheng, J.-L., Zhu, Y.-H., Zhu, M.-Q., Wu, H.-T. & Sun, R.-C. 2017. Bio-oil gasification using air-steam as gasifying agents in an entrained flow gasifier. *Energy*.

Chapter 6

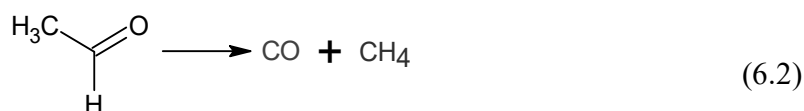
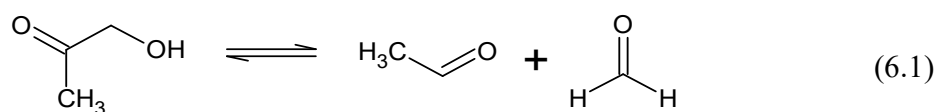
Kinetic Model of Air-Steam Reforming of Acetol

6.1 Introduction

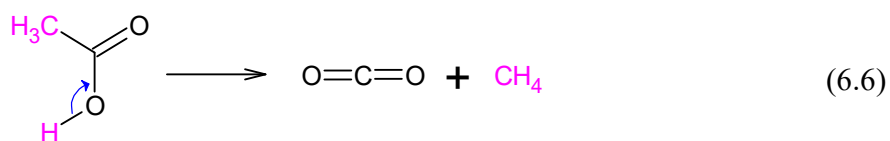
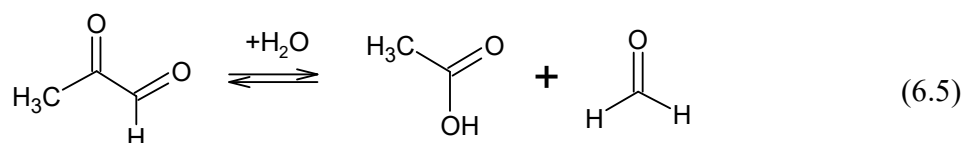
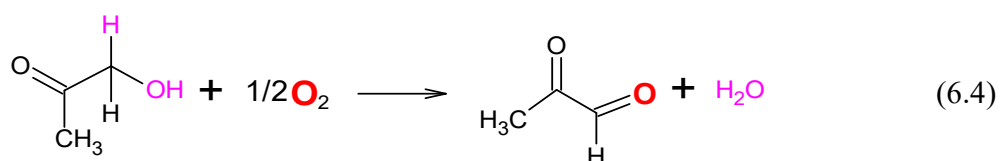
A kinetic-based simulation model for air-steam reforming of acetol was developed using the Aspen Plus simulation package. The contributions of the reactions, both in the reactor freeboard and the catalytic bed, to the final product distribution have been assessed using experimental data and kinetic information from the literature. Several different rate expressions with corresponding kinetic parameters were tested. In particular the kinetics for the water-gas shift and methane reforming reactions were assessed and the ones that best fitted the experimental data are reported.

6.2 Model Development

Based on the experimental measurements of the gas compositions from the reactor freeboard (Chapter 5) and literature sources, possible global cracking and combustion reactions are proposed to describe the acetol conversion in the freeboard. According to literature, thermal decomposition of acetol leads to formation of acetaldehyde and formaldehyde as the two primary products based on reaction (6.1) (Shafizadeh and Lai, 1972). Acetaldehyde is a precursor for methane and carbon monoxide formation (reaction (6.2) (Winkler et al., 1935) while thermal decomposition of formaldehyde produces hydrogen and carbon monoxide, reaction (6.3) (Saito et al., 1985).



Acetol can also undergo oxidative dehydrogenation to form pyruvaldehyde (methylglyoxal) as reaction (6.4) (Ai and Ohdan, 1999). The methylglyoxal thus formed can further react with water (hydration) to form acetic acid and formaldehyde as reaction (6.5) (Liang et al., 2015). From our analysis of gas samples taken from the reactor freeboard using the RGA, there were signals at $m/z=27$, 29, and 30, which are common signature peaks for acetol, acetic acid, and formaldehyde (Appendix 6A). Thermal decarboxylation of acetic acid can lead to production of CH_4 and CO_2 according to reaction (6.6) (Nguyen et al., 1995).



In addition, the pyrolysis and oxidation products (CO , H_2 , and CH_4) can undergo oxidation/partial oxidation to CO_2 and H_2O . Therefore, based on the experimental sensitivity analysis results and literature sources the possible global cracking and combustion reactions describing the acetol conversion in the freeboard region are included in Table 6.1.

Table 6.1: Possible major reactions in the reactor freeboard

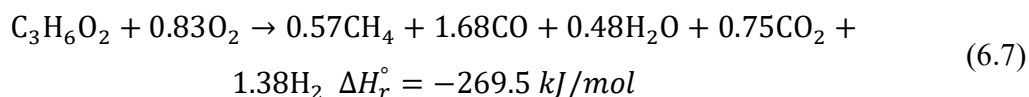
No.	Reaction	Chemical description	ΔH_r° (kJ/mol)	$\Delta G_r(650^\circ\text{C})$ (kJ/mol)
1	Acetol decomposition	$\text{C}_3\text{H}_6\text{O}_2 \rightarrow \text{CH}_3\text{CHO} + \text{CH}_2\text{O}$	83.5	-106.1
2	Acetaldehyde decomposition	$\text{CH}_3\text{CHO} \rightarrow \text{CH}_4 + \text{CO}$	-14.7	-138.3
3	Formaldehyde decomposition	$\text{CH}_2\text{O} \rightarrow \text{CO} + \text{H}_2$	60.2	-12.0
4	Partial oxidation of acetol	$\text{C}_3\text{H}_6\text{O}_2 + 1/2\text{O}_2 \rightarrow \text{CH}_3\text{COOH} + \text{CH}_2\text{O}$	-180.7	-305.4
5	Decarboxylation of acetic acid	$\text{CH}_3\text{COOH} \rightarrow \text{CH}_4 + \text{CO}_2$	-33.5	-141.9
6	Methane combustion	$\text{CH}_4 + 1/2\text{O}_2 \rightarrow 2\text{H}_2 + \text{CO}$	-35.7	-192.9
7	H ₂ combustion	$\text{H}_2 + 1/2\text{O}_2 \rightarrow \text{H}_2\text{O}$	-241.8	-200.8
8	CO combustion	$\text{CO} + 1/2\text{O}_2 \rightarrow \text{CO}_2$	-282.9	-202.9

From the reactions in Table 6.1, acetol decomposition can be represented by the sum of reactions 1 to 3 while reactions 3 to 6 represent the partial oxidation of acetol. The combustion reactions of H₂ and CO were considered individually. Subsequently, the sum of the deviations between calculated and observed product distributions was minimized and the contributions of the individual reactions in Table 6.2 were determined.

Table 6.2: Proposed major reactions for acetol conversion in the reactor freeboard

No.	Reaction	Chemical description	Relative extent of reaction
1	Acetol decomposition	$C_3H_6O_2 \rightarrow CH_4 + 2CO + H_2$	1.8
2	Partial oxidation of acetol	$C_3H_6O_2 + O_2 \rightarrow 3H_2 + CO_2 + 2CO$	1.4
3	H ₂ combustion	$H_2 + 0.5O_2 \rightarrow H_2O$	1.5
4	CO combustion	$CO + 0.5O_2 \rightarrow CO_2$	1

Therefore, the overall reaction stoichiometry for acetol decomposition in the freeboard can be written as:



The major advantage of Aspen Plus for process simulation is, it profoundly reduces the time required for compilation and critical evaluation of physical and chemical properties of reaction components, which underlie difficulties in process model development. Figure 6.1 shows the reaction setup used to simulate the reforming of acetol in Aspen Plus. The Redlich-Kwong-Aspen (RK-Aspen) property method was used for the simulation, which is a recommended method for hydrocarbon systems (Abdelouahed et al., 2012). The overall energy balance, the difference in sensible heat of the inlet and outlet streams, for autothermal reforming of acetol (Figure 6.1) is 7.4×10^{-6} J caused by the calculation tolerance of the solver for the simulation.

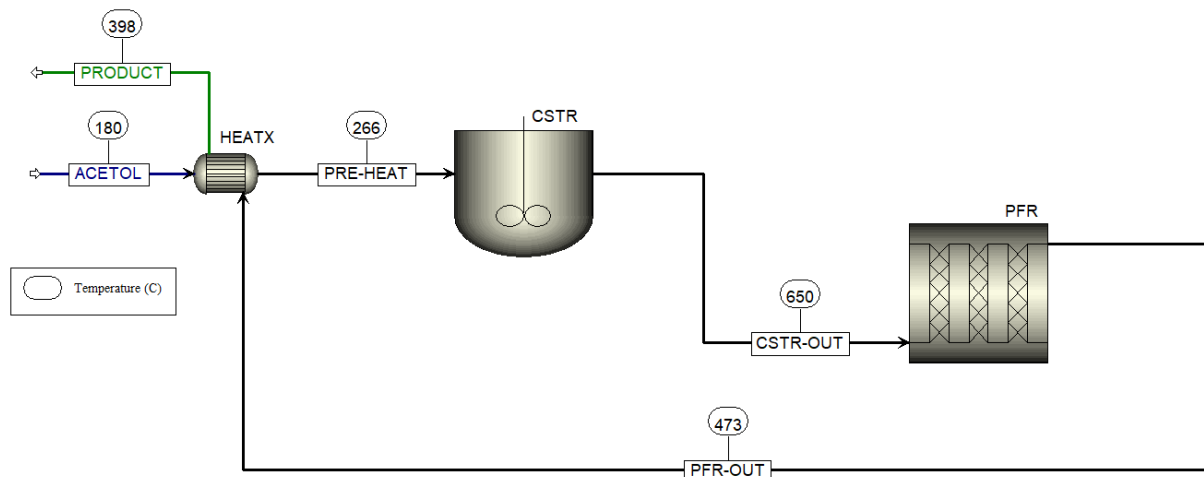


Figure 6.1: Aspen Plus simulation setup for autothermal reforming of acetol

The feed mixture at 180°C is fed to an isothermal continuously stirred tank reactor (CSTR) after passing through a heat exchanger. The CSTR was used to simulate the kinetics of the partial oxidation and decomposition of acetol (reaction 6.7) in the freeboard and the values of the kinetic parameters (239.4 s^{-1} and 56.4 kJ/mol) presented in Chapter 5 were used here. The influence of water-gas shift reaction on gas composition in the freeboard was also evaluated by incorporating kinetics for uncatalyzed water-gas shift reaction from the literature (Bustamante et al., 2005, Hadman et al., 1932), Equation (6.8). Table 6.3 includes values of the activation energy and pre-exponential factor for the forward water-gas shift reaction.

$$r = k[\text{CO}]^{0.5}[\text{H}_2\text{O}] \quad (6.8)$$

Table 6.3: Values of the kinetic parameters for uncatalyzed water-gas shift reaction

Reaction	Preexponential Factor	Activation Energy (kJ/mol)
	$\left(\left(\frac{\text{cm}^3}{\text{mol}}\right)^{0.5} \text{s}^{-1}\right)$	
$\text{CO} + \text{H}_2\text{O} \leftrightarrow \text{CO}_2 + \text{H}_2$	2.22×10^{14}	316.2

The plug flow reactor model (PFR) was used to represent the catalytic steam reforming of unconverted acetol (or intermediates) and methane, thermal and catalytic decomposition of unconverted acetol (or intermediates), and catalytic water-gas shift reaction. Tables 6.4 and 6.5 present the kinetic information for the reactions included in the PFR reactor model. The rate

expression for the catalytic water-gas shift reaction was taken from the work by Lei et al. (2005) which aimed at quantifying the advantage of the rhodium metal promoter. Due to the low content of carbon observed in the experiments, reactions involving carbon formation were not considered. However, an equilibrium reactor after the CSTR was used to evaluate the thermodynamic probability of carbon formation reaction.

Table 6.4: Rate equations for the reactions used to simulate the PFR

No.	Reaction	Rate expression	Reference
1	$C_3H_6O_2 + H_2O \rightarrow 3CO + 4H_2$	$r_1 = k_1 y_{BO} y_{H_2O}$	(Arregi et al., 2018)
2	$C_3H_6O_2 \rightarrow CO + CH_4 + H_2$	$r_2 = k_2 p_{BO} + \frac{k_2^* p_{BO}}{p_{H_2O}^\alpha}$	(Gayubo et al., 2018)
3	$CH_4 + H_2O \rightarrow 3H_2 + CO$	$r_3 = k_3 y_{CH_4} y_{H_2O}$	(Arregi et al., 2018)
4	$CO + CO_2 \leftrightarrow H_2 + CO$	$r_4 = k_4 p_{CO}^{0.64} p_{H_2O}^{0.5} - k_4' p_{CO_2}^{0.46} p_{H_2}^{0.73}$	(Lei et al., 2005)

BO represents bio-oil (i.e., acetol) and k_2^* is the rate constant for the non-catalytic thermal decomposition route of acetol.

Table 6.5: Values of the Arrhenius parameters for reactions in the PFR

No.	Pre-exponential Factor	Unit	Activation energy (kJ/mol)	Catalyst
1	6.0×10^{-3}	$mol\ g_{cat}^{-1} \cdot s^{-1}$	14.5	Ni/Al ₂ O ₃
2	0.96	$k_2\ (mol/(g_{cat} \cdot h \cdot atm))$	71.64	Ni/La ₂ O ₃ - α -Al ₂ O ₃
	2.4×10^{-3}	$k_2^*\ (mol/(cm^3 \cdot h \cdot atm))$	93.66	-
3	1.3×10^{-2}	$mol\ g_{cat}^{-1} \cdot s^{-1}$	20.7	Ni/Al ₂ O ₃
4	0.0041	$k_4\ (mol/(g_{cat} \cdot s \cdot kpa^{1.14}))$	33.6	Rh-Fe ₃ O ₄ -Cr ₂ O ₃
	0.024	$k_4'\ (mol/(g_{cat} \cdot s \cdot kpa^{1.19}))$	50.1	

The simulation conditions for PFR including reactor dimensions, bed void fraction, and catalyst density are listed in Table 6.6.

Table 6.6: Simulation conditions for the PFR

Parameter	Value
Reactor length (cm)	2.5
Reactor diameter (mm)	10
Void fraction	0.43
Catalyst density (kg/m ³)	1970

The performance of the PFR was tested for two modes of operations. In Case 1, it operates with a known outlet bed temperature drop of 35°C that was measured during the experiments, and the second one examines the adiabatic case. The results of these two scenarios will be discussed in the same order.

6.3 Results and Discussion

Figure 6.2 shows the acetol conversion with reaction temperature (furnace temperature) in the CSTR. The model predictions are in good agreement with the experimental data. The conversion was found to be highly sensitive to the volume of the freeboard region (residence time), which has also been highlighted by Lui et al. (2013) in autothermal reforming of glycerol. In their work, the position of an atomizer nozzle (for glycerol-water mixture) relative to the catalytic bed was varied to analyse its influence on the distribution of products exiting the catalytic bed. The authors theorised that the variation in product distribution with the change in the distance between the atomizer and catalytic bed could be because the non-catalytic zone (freeboard) upstream of the catalytic bed possibly expands. In the current study, the extent of conversion in this section of the reactor have been investigated and the possible reaction schemes has been proposed, as discussed earlier.

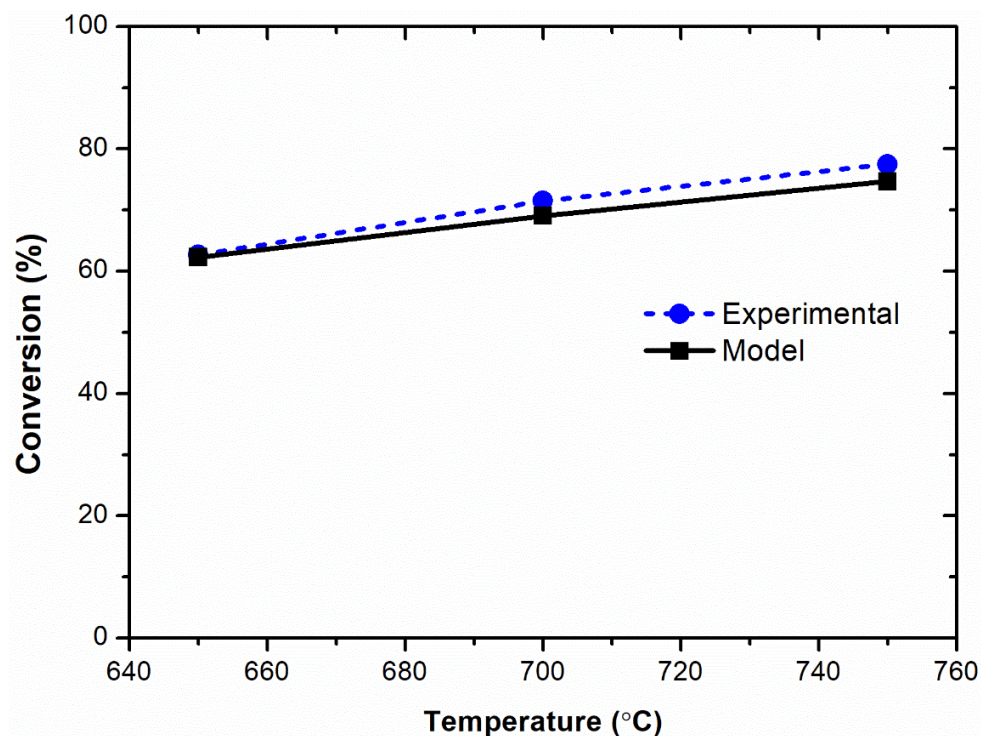


Figure 6.2: Effect of reaction temperature on acetol conversion in the freeboard: the dotted line represents experimental data and the solid lines for the model predictions

A comparison of model prediction against the experimental data for product distribution at the exit of the CSTR is presented in Table 6.7. The deviation between the two results is computed according to Equation (6.9) and is within an acceptable range.

Table 6.7: Comparison of the composition of the gaseous product exiting the CSTR: model (Mod.) and experimental (Exp.) values

Mole flow (mol/h)	650°C			700°C			750°C		
	Mod.	Exp.	Error (%)	Mod.	Exp.	Error (%)	Mod.	Exp.	Error (%)
C ₃ H ₆ O ₂	0.029	0.029	0.977	0.024	0.022	8.323	0.020	0.018	12.497
CH ₄	0.028	0.028	1.080	0.031	0.034	8.595	0.033	0.039	14.989
H ₂	0.067	0.068	0.548	0.074	0.081	7.691	0.081	0.097	17.031
CO	0.082	0.082	0.437	0.091	0.090	0.324	0.098	0.093	5.259
CO ₂	0.037	0.037	0.522	0.040	0.043	6.816	0.044	0.049	11.362

$$Error (\%) = \left| \frac{Experimental - Model}{Experimental} \right| \times 100\% \quad (6.9)$$

As previously shown in Figure 5.1 (Chapter 5), a decreasing trend of CO composition with temperature rise was observed and a similar trend was also reported by Zheng et al. (2018) in a non-catalytic air-steam reforming of bio-oil. This trend is not common in biomass gasification and Zheng et al. (2018) postulated that the equilibrium of water-gas shift reaction might not have been reached. To test this hypothesis, in the current study the kinetics of non-catalysed water-gas shift reaction (6.8) was included in the CSTR model and was found to have no significant contribution to the product distribution.

Figure 6.3 shows the composition of the product gas from the plug flow reactor as a function of the operating temperature (furnace temperature) for Case 1. The extent of methane reforming is much lower compared to steam reforming of acetol (or intermediate compounds) as it has also been stated by Gayubo et al. (2018). At the lowest temperature tested (650°C) the H₂/CO ratio is 1.5 which can be used in formaldehyde (Bahmanpour et al., 2015) or oxo-alcohols synthesis.

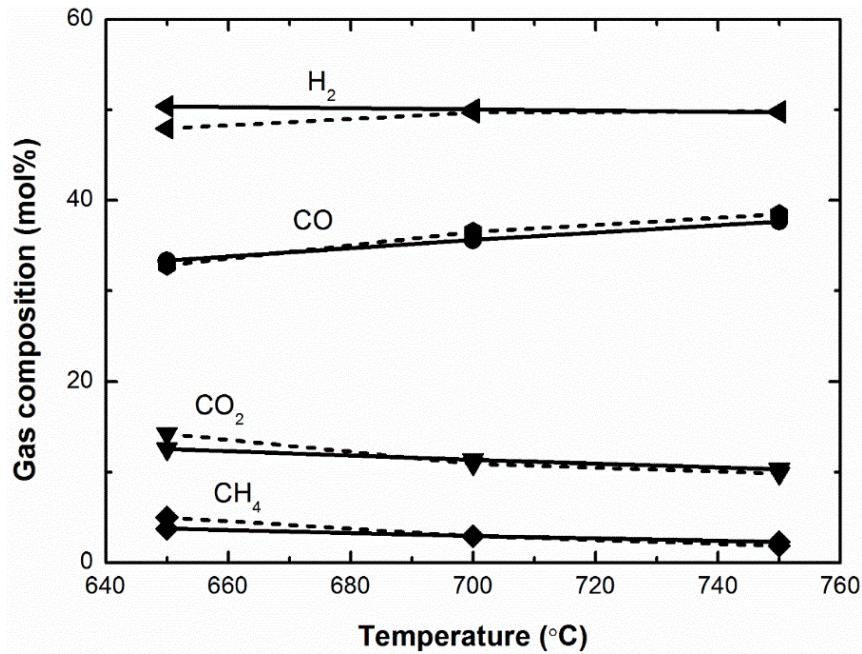


Figure 6.3: Dependence of composition of the product gas (dry and argon free basis) on operating temperature for Case 1: dotted lines represent experimental data and the solid lines are modelling results

The molar composition profile of the reactants and products along the catalytic bed length is shown in Figure 6.4. The mole fraction of the methane decreased gradually throughout the catalytic bed length. These trends are comparable with the work by De Smet et al. (2001) from autothermal reforming of methane.

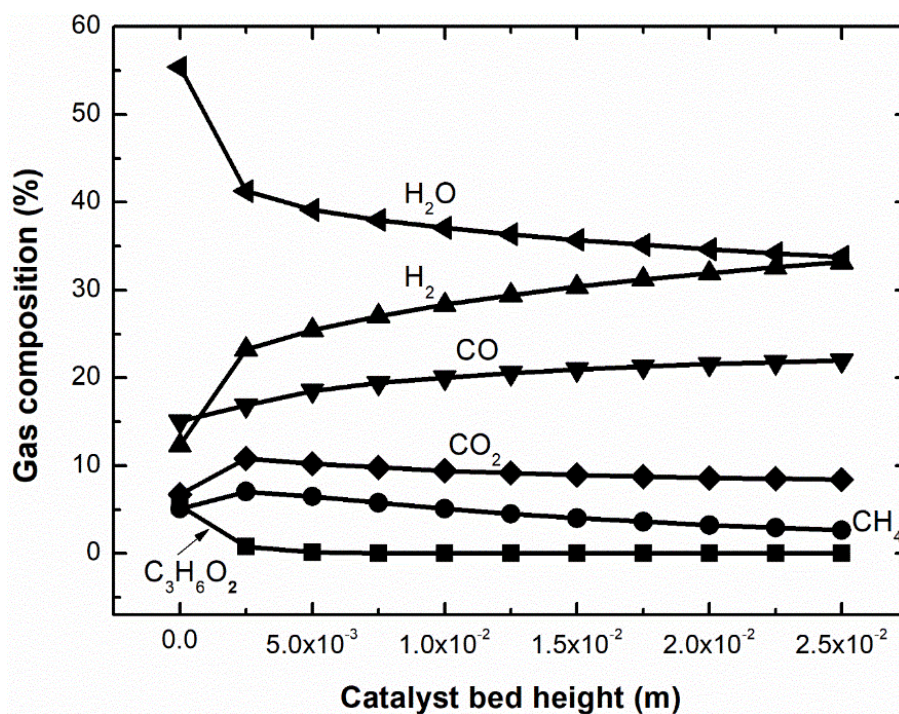


Figure 6.4: Mole fraction of the reactants and products along the catalytic bed length at operating temperature of 650°C on argon free basis

To check whether the unconverted carbon at the various reaction temperatures in the freeboard is in a form of unconverted acetol or intermediate compounds (such as acetaldehyde, acetic acid or formaldehyde), the simulation results were compared for these two cases. Both the final product composition and the temperature did not change in both cases. That said, however, the unconverted carbon in the form of intermediate compounds, which can easily be reformed catalytically, can potentially avoid carbon deposition on the catalyst bed as observed during the experiments.

Figure 6.5 shows a comparison of the gas composition between the kinetic and equilibrium conditions at 650°C. The product gas is rich in H₂ and CO₂ under the equilibrium whereas rich in H₂ and CO in the kinetic condition.

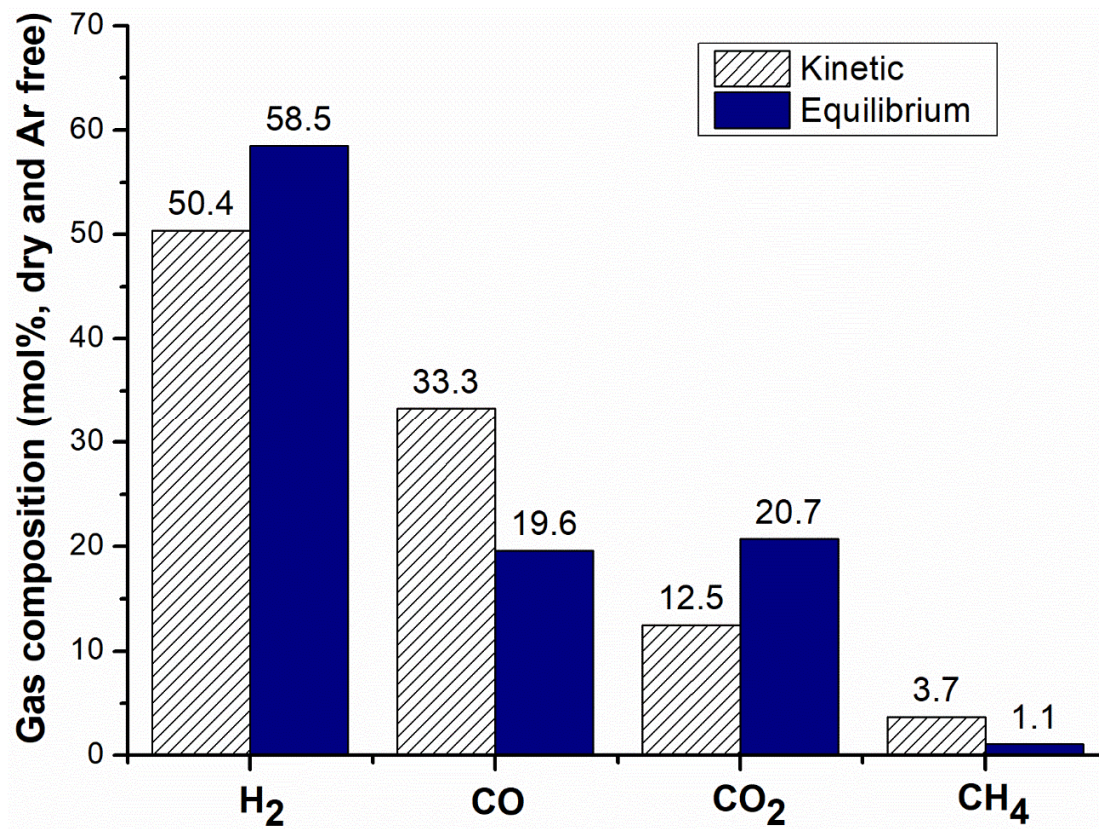


Figure 6.5: Comparison of the gas composition between kinetic and equilibrium conditions at 650°C

Under the adiabatic operation condition (Case 2), the syngas produced has lower CO content compared to Case 1 with H₂/CO-ratio of 2.6 at 650°C, Figure 6.6.

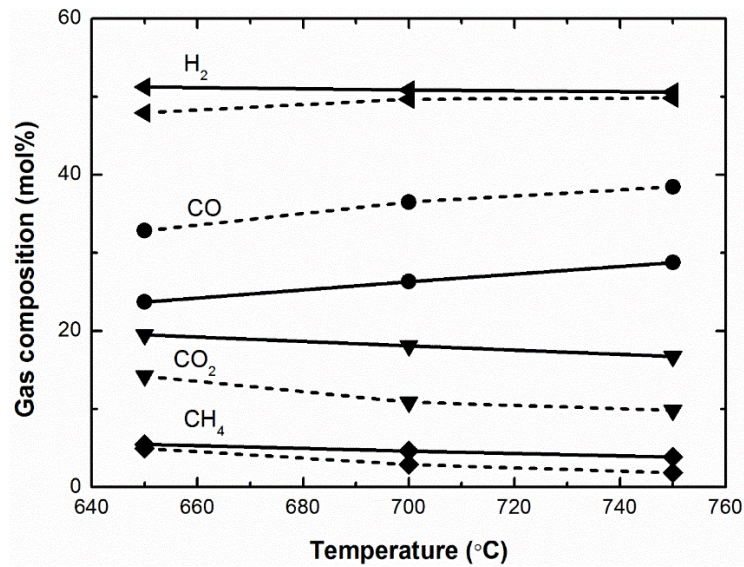


Figure 6.6: Dependence of composition of the product gas (dry and argon free basis) on operating temperature for Case 2: dotted lines represent experimental data and solid lines denote modelling results

The molar composition profile of the reactants and products along the catalytic bed length is shown in Figure 6.7. Because the catalytic bed temperature drops significantly (Figure 6.8) due to steam reforming of methane and unconverted acetol, the water-gas shift reaction does not proceed rapidly.

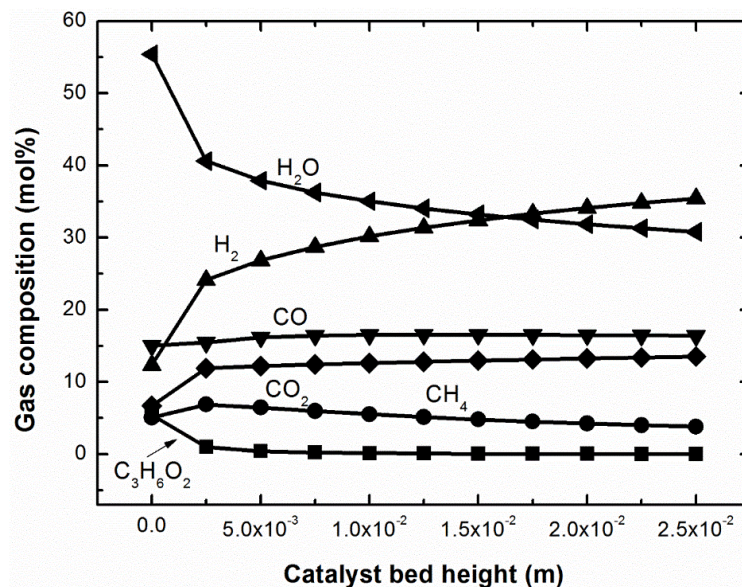


Figure 6.7: Mole fraction of the reactants and products along the catalytic bed length at 650°C on argon free basis

Figure 6.8 shows the bed temperature change for Case 1 and 2. The symbols for Case 1 represent measured values at the front and back face of the catalytic bed during experiments and the values in between were generated by Aspen Plus. The bed temperature drop in the adiabatic operation is significant (177°C) caused mainly by the endothermic reactions involving steam. The choice of operation between the two cases largely depends on the final application of the gas. The heat duty of the PFR for Case 1 is 0.23 MJ/kg of acetol.

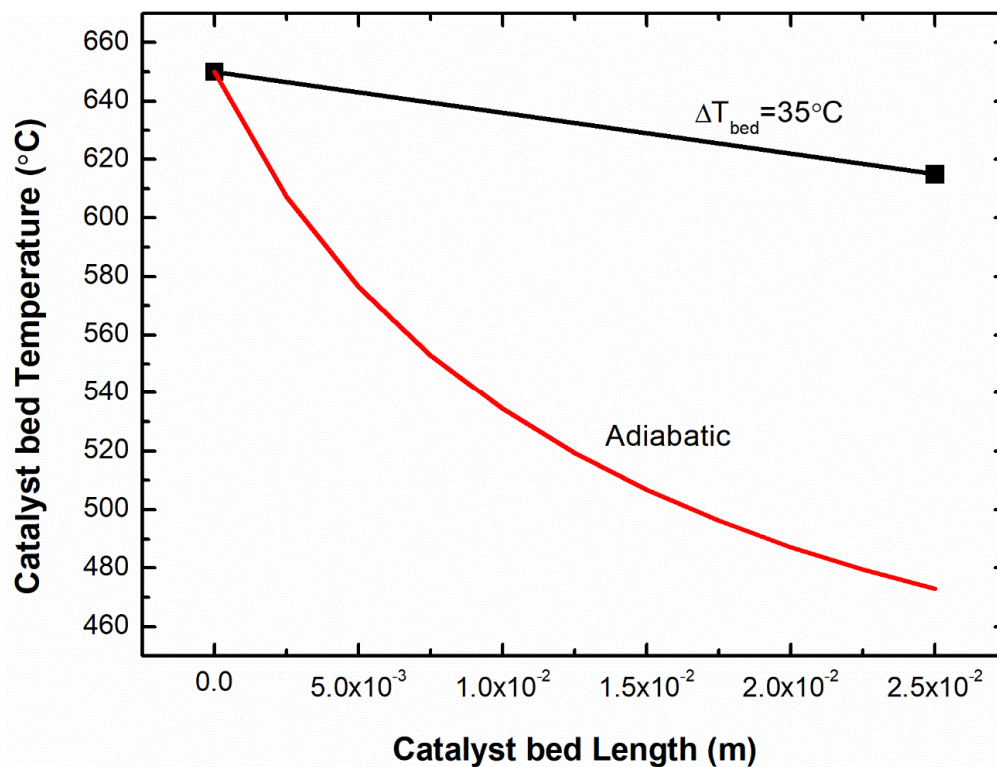


Figure 6.8: Catalytic bed temperature change for Case 1 and 2

6.4 Conclusions

Based on the modelling results it can be concluded that air-steam reforming of volatiles occurs in two parts: partial oxidation followed by steam reforming within the catalyst bed. Depending on the final application of the syngas, the mode of operation, volume of the freeboard, and the catalyst bed height can be varied. Overall, the developed Aspen Plus model provided insight into the nature of the autothermal reforming of acetol.

References

- Abdelouahed, L., Authier, O., Mauviel, G., Corriou, J. P., Verdier, G. & Dufour, A. 2012. Detailed modeling of biomass gasification in dual fluidized bed reactors under Aspen Plus. *Energy & Fuels*, 26, 3840-3855.
- Ai, M. & Ohdan, K. 1999. Formation of Pyruvaldehyde (2-Oxopropanal) by oxidative dehydrogenation of hydroxyacetone. *Bulletin of the Chemical Society of Japan*, 72, 2143-2148.
- Arregi, A., Lopez, G., Amutio, M., Barbarias, I., Santamaria, L., Bilbao, J. & Olazar, M. 2018. Kinetic study of the catalytic reforming of biomass pyrolysis volatiles over a commercial Ni/Al₂O₃ catalyst. *International Journal of Hydrogen Energy*.
- Bahmanpour, A. M., Hoadley, A. & Tanksale, A. 2015. Formaldehyde production via hydrogenation of carbon monoxide in the aqueous phase. *Green Chemistry*, 17, 3500-3507.
- Bustamante, F., Enick, R. M., Killmeyer, R. P., Howard, B. H., Rothenberger, K. S., Cugini, A. V., Morreale, B. D. & Ciocco, M. V. 2005. Uncatalyzed and wall-catalyzed forward water-gas shift reaction kinetics. *AIChE Journal*, 51, 1440-1454.
- De Smet, C. R. H., De Croon, M. H. J. M., Berger, R. J., Marin, G. B. & Schouten, J. C. 2001. Design of adiabatic fixed-bed reactors for the partial oxidation of methane to synthesis gas. Application to production of methanol and hydrogen-for-fuel-cells. *Chemical Engineering Science*, 56, 4849-4861.
- Gayubo, A. G., Valle, B., Aramburu, B., Montero, C. & Bilbao, J. 2018. Kinetic model considering catalyst deactivation for the steam reforming of bio-oil over Ni/La₂O₃- α -Al₂O₃. *Chemical Engineering Journal*, 332, 192-204.
- Hadman, G., Thompson, H. W. & Hinshelwood, C. N. 1932. The oxidation of carbon monoxide. *Proceedings of the Royal Society of London. Series A, Containing Papers of a Mathematical and Physical Character*, 137, 87-101.
- Lei, Y., Cant, N. W. & Trimm, D. L. 2005. Kinetics of the water-gas shift reaction over a rhodium-promoted iron-chromium oxide catalyst. *Chemical Engineering Journal*, 114, 81-85.
- Liang, X., Rahubadda, A., Haynes, B. S. & Montoya, A. 2015. Kinetic insights into the hydrothermal decomposition of dihydroxyacetone: A combined experimental and modeling study. *Industrial & Engineering Chemistry Research*, 54, 8437-8447.
- Liu, Y., Farrauto, R. & Lawal, A. 2013. Autothermal reforming of glycerol in a dual layer monolith catalyst. *Chemical Engineering Science*, 89, 31-39.

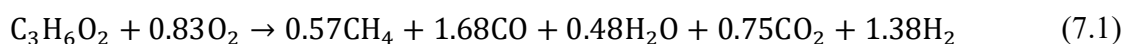
- Nguyen, M. T., Sengupta, D., Raspoet, G. & Vanquickenborne, L. G. 1995. Theoretical study of the thermal decomposition of acetic acid: decarboxylation versus dehydration. *The Journal of Physical Chemistry*, 99, 11883-11888.
- Saito, K., Kakumoto, T., Nakanishi, Y. & Imamura, A. 1985. Thermal decomposition of formaldehyde at high temperatures. *The Journal of Physical Chemistry*, 89, 3109-3113.
- Shafizadeh, F. & Lai, Y. Z. 1972. Thermal degradation of 1,6-anhydro-.beta.-D-glucopyranose. *The Journal of Organic Chemistry*, 37, 278-284.
- Winkler, C. A., Hinshelwood, C. N. & S., F. R. 1935. The thermal decomposition of acetaldehyde. *Proceedings of the Royal Society of London. Series A - Mathematical and Physical Sciences*, 149, 355-359.
- Zheng, J.-L., Zhu, Y.-H., Zhu, M.-Q., Wu, H.-T. & Sun, R.-C. 2018. Bio-oil gasification using air - Steam as gasifying agents in an entrained flow gasifier. *Energy*, 142, 426-435.

Chapter 7

Conclusions and Recommendations

7.1 Conclusions

Since the heating rate of a cellulose particle in the reactor freeboard is high (>800 K/sec), the pyrolysis of the particle on or above the catalytic bed will be fast (~ 75 ms). Hence, the kinetics of the reactive flash volatilization of biomass reduces to the reforming of the primary tar compounds (bio-oil) that makes up more than 60% of the pyrolysis products. The primary tar compounds are prone to polymerisation and condensation reactions that are responsible for secondary tars and carbon formation. Over the years a considerable research effort has been devoted to understanding the catalytic steam reforming of primary tars for hydrogen production with the emphasis on preventing the formation of carbon and secondary tars. Nevertheless, catalyst deactivation due to carbon deposition has still remained a big challenge in the reforming of bio-oil. Due to that reason, an *in-situ* primary tar conversion in the presence of oxygen and steam as that happens in the reactive flash volatilization of biomass is gaining popularity. The use of the oxygen as an additional oxidant in conjunction with an upstream freeboard design for the reactor have been reported to lessen carbon formation, but the detailed reaction mechanism and reactor kinetics are not well understood. This thesis contributes to the research gap in this area. Moreover, to date, acetol and guaiacol (the main products of cellulose and lignin pyrolysis, respectively) reforming under reactive flash volatilization conditions have not been reported in the literature. The findings of this thesis show that the primary tar compounds are converted into permanent gases (CO , CO_2 , H_2 , and CH_4) and reformable intermediate compounds through partial oxidation and thermal decomposition (oxidative pyrolysis), with the oxygen being completely consumed. Following that, the catalyst tunes the final composition of the gas via catalytic steam reforming and water-gas shift reactions avoiding carbon deposition on the catalyst surface. The overall stoichiometry of the oxidative pyrolysis of acetol is represented by reaction (7.1) and the experimentally-derived kinetic constants for the reaction are 239.4 s^{-1} and 56.4 kJ/mol .



$$\Delta H_r^\circ = -269.5 \text{ kJ/mol}$$

Since CO is a major product in the oxidative pyrolysis of the primary tar compounds, the water-gas shift reaction not achieving equilibrium within the catalytic bed leads to the production of syngas rich in CO and H₂. The reaction temperature, the partial pressure of steam, and the length of the catalytic bed significantly influence product distribution. To avoid secondary tar and carbon formation, a minimum reaction temperature of at least 500°C should be maintained for acetol reforming and 600°C for guaiacol. For acetol reforming, the optimal operating conditions were identified as C/O ratio of 1.7, S/C ratio of 1.2, and 650°C. Given that lignin-derived compounds are considerably difficult to reform, it is a major achievement to reform guaiacol without carbon deposition on the catalyst (1%Rh-10%Ni/ γ -Al₂O₃) at a moderate reaction temperature (700°C), relatively low steam partial pressure (S/C \leq 2.4), and C/O ratio of 0.85. The lower the S/C ratio, the smaller the reactor hence suitable for decentralized syngas production. During the acetol reforming no catalyst deactivation was observed for 10 h on stream, the maximum duration for the experiments. A kinetic model for reforming of acetol has been established by considering both the reactions in the freeboard and the heterogeneous reactions in the catalytic bed. The model allowed to evaluate the effect of process conditions such as the time-temperature history of the tar compound, the mode of reactor operation, and the influence of the catalytic reactions on the H₂/CO ratio in the product gas. By utilizing the excess energy of the exothermic oxidative pyrolysis reaction, autothermal reforming of the primary tar compound is demonstrated to be achievable. Overall, the findings from this work can help to improve direct processing of biomass in short contact time through the advancements in the understanding of the reactive flash volatilization process.

7.2 Contribution to Knowledge

The contribution to knowledge is as follows:

- To the best of our knowledge, this is one of the first few studies of the kinetics of the homogeneous gas phase reactions under reactive flash volatilisation conditions. The method that was developed allows the quantification of the amount of acetol converted

through the gas phase reactions, which in turn elucidates the possible global reaction schemes (Table 7.1) which was not well understood earlier.

Table 7.1: Possible major reactions in the reactor freeboard

Reaction	Chemical description
Acetol decomposition	$C_3H_6O_2 \rightarrow CH_3CHO + CH_2O$
Acetaldehyde decomposition	$CH_3CHO \rightarrow CH_4 + CO$
Formaldehyde decomposition	$CH_2O \rightarrow CO + H_2$
Partial oxidation of acetol	$C_3H_6O_2 + 1/2O_2 \rightarrow CH_3COOH + CH_2O$
Decarboxylation of acetic acid	$CH_3COOH \rightarrow CH_4 + CO_2$
Methane combustion	$CH_4 + 1/2O_2 \rightarrow 2H_2 + CO$
H ₂ combustion	$H_2 + 1/2O_2 \rightarrow H_2O$
CO combustion	$CO + 1/2O_2 \rightarrow CO_2$

- Determine the operating conditions for air-steam reforming of the primary tar compounds (acetol and guaiacol) to produce clean syngas free of tar and char. In the reaction, oxygen is consumed in the freeboard and steam conditions the gas composition in the catalyst bed.
- Develop kinetic model of the autothermal reforming of acetol that has been validated by experimental data, Figure 7.1. The effects of the time-temperature history of the tar compound, the mode of reactor operation, and the influence of the catalytic reactions on H₂/CO ratio can be assessed using this model, which is useful for future reactor design and optimization.

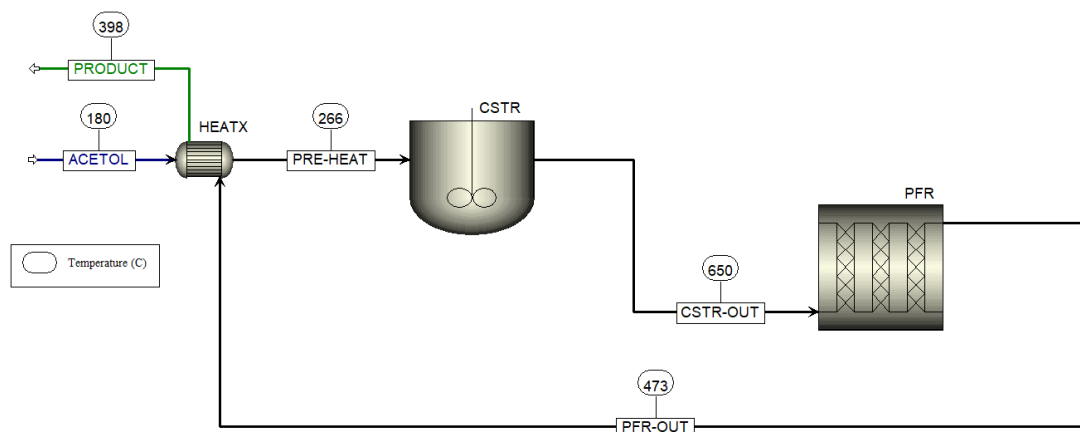


Figure 7.1: Aspen Plus simulation setup for autothermal reforming of acetol

7.3 Recommendations

Since some of the intermediates from the homogeneous gas phase conversion of acetol and guaiacol in the freeboard are likely to be condensable, the use of advanced analysis techniques such as a high-temperature *in-situ* FTIR or a pyrolysis-gas chromatography/mass spectrometry (Py-GC/MS) instrumental method will enable an *in-situ* analysis. Condensation was a major problem during sample collection for the *ex-situ* analysis in the current work, which caused considerable variation in signal strength. Hence, if intermediates are detected by this approach, the kinetics of their catalytic reforming can be included in future kinetic models, considering possible catalyst deactivation reactions as well. It is also proposed to study the conversion behaviour of the mixture of acetol and guaiacol, and the crude bio-oil as well. On a broader context, the identification of intermediates in the freeboard using the Py-GC/MS method could also pave a way to evaluate the possibility of recovering valuable chemicals, if any.

The stability of the Rh-Ni/ γ -Al₂O₃ catalyst needs to be checked for a longer time on stream and the effectiveness of catalyst regeneration by a low temperature oxidation should be assessed. To further reduce the cost of the catalyst other type of promoters such as platinum and palladium can be studied as well. For an industrial scale application, pellets of the catalyst with different shapes can be tested to help avoid pressure drop issues.

Appendices

Appendix 3A

A One-Dimensional Two-Phase Flow Model

In the lab-scale gasifier an electric furnace is used for heating the reactor to a desired temperature. Under this condition, temperature profile of a single particle in the non-reactive two-phase flow can be determined applying the energy conservation law. Thus, the rate of temperature change of the particle is proportional to the rate at which energy is being transferred to the particle as formulated in Equation (A.1). Generally, the effect of radiant heat transfer is dominant in furnaces. Prior to considering the inter-phase heat and momentum exchange between the two phases, analytical solutions were constructed for the particle phase with simplifying assumptions. The analytical solutions help to gain insights into the physics of the phenomenon before complexities are added.

$$c_p m_p \frac{dT_p}{dt} = \varepsilon \sigma A_p (T_{wall}^4 - T_p^4) \quad (A.1)$$

where A is the area of the particle (m^2), c_p the specific heat capacity of the particle ($J/g \cdot K$), T_p is the particle temperature (K), T_{wall} is the furnace wall temperature (K), ε is the emissivity of the particle surface, σ is the Stephen-Boltzmann constant ($5.67 \times 10^{-8} W/m^2 \cdot K^4$).

The following assumptions were considered in developing the model:

- The particle is spherical.
- The particle is free of moisture.
- The particle travels along the x -axis (axial direction) and any variation in the condition in the reactor are considered to occur in the axial direction.
- Constant wall temperature.
- Radiation is the major mode of heat transfer from the wall to the particle.
- Conductivity inside the particle is much faster.

The Biot number calculated considering maximum radiation at $\varepsilon = 1$ and $T_p = 700^\circ\text{C}$ was found to be 0.017 which is less than 0.1.

Using the radiation heat transfer coefficient (h_{rad} , $\text{W/m}^2 \cdot \text{K}$) Equation (A.1) can be rewritten as:

$$c_p m_p \frac{dT_p}{dt} = h_{rad} A_p (T_{wall} - T_p) \quad (\text{A.2})$$

where h_{rad} is calculated by:

$$h_{rad} = \varepsilon \sigma (T_{wall} + T_p)(T_{wall}^2 + T_p^2) \quad (\text{A.3})$$

The analytical and numerical solutions to Equation (A.2) are presented in Figure A.1. To compute the analytical solution, h_{rad} was considered to be independent of time. A built-in solver in Matlab known as 'fzero' was used to find root of the resulting nonlinear equation. The calculated value of h_{rad} at $t = 0$ is $74.6 \text{ W/m}^2 \cdot \text{K}$.

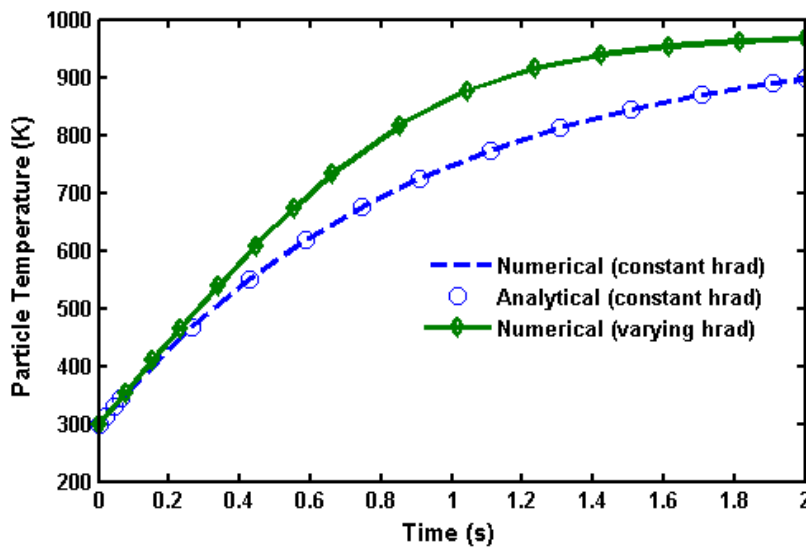


Figure A.1: The numerical and analytical solutions for particle temperature with constant and variable h_{rad}

From Figure A.1, the model formulation for finding numerical solutions is correct as the solution matches the analytical solution. Moreover, the numerical solution with the variable h_{rad} gave rise

to the increase in heating rate of the particle consistent with its temperature dependence as in Equation (A.3). Table A.1 includes the values of the parameters used in the model.

Table A.1: Values of the parameters used in the heat transfer model

Category	Properties	Numerical value	Reference
Operating conditions	Wall temperature (T_{wall} , °C)	700	(Dauenhauer et al., 2009)
	Initial particle temperature (T_p^0 , °C)	25	
	Particle diameter (d_p , µm)	315	(Dauenhauer et al., 2009)
	Number of particles	1	
Particle properties	Density (kg/m ³)	650	(Dauenhauer et al., 2009)
	Emissivity (ε)	1	Black body
	Thermal conductivity (k , W/m. K)	0.23	Wood
	Specific heat capacity (c_p , J/g. K)	2	

Assuming a constant fluid velocity, the effect of the fluid flow on the particle motion was modelled by Equation (A.4). Newton's second law of motion is applied to find the velocity profile of the particle (Ku et al., 2013). The vector sum of the forces being acted on the particle governs its translational motion, and the drag force is the dominant one as formulated in Equation (A.5) (Sommerfeld, 2000, Morsi and Alexander, 1972).

$$m_p \frac{du_p}{dt} = \sum_i F_i \quad (\text{A.4})$$

where F_i represents different forces being acted on the particle in the fluid-particle system (Morsi and Alexander, 1972).

$$m_p \frac{du_p}{dt} = \frac{1}{2} C_D \rho_f A_p (u_f - u_p)^2 \quad (\text{A.5})$$

The drag coefficient (C_D) was calculated by the combination of Stoke's correlation ($Re_p < 0.1$) and Schiller-Naumann's correlation ($Re_p > 0.1$):

$$C_D = \begin{cases} \frac{24}{Re_p} & Re_p < 0.1 \text{ (Viscous region)} \\ \frac{24}{Re_p} (1 + 0.15 Re_p^{0.687}) & 0.1 < Re_p < 1000 \text{ (Transition region)} \\ 0.44 & Re_p \geq 1000 \text{ (Inertial region)} \end{cases}$$

where Re_p is the particle Reynolds number which characterizes the relative flow between the particle and the fluid, and was calculated using Equation (A.6) (Papadikis et al., 2008):

$$Re_p = \frac{\rho_f d_p (u_f - u_p)}{\mu_f} \quad (\text{A.6})$$

The solution to the momentum conservation equation (Equation (A.5)) is shown in Figure A.2. From the figure, under the given reactor conditions, the particle attained its terminal velocity in about 0.2 seconds. The numerical solution was also validated by the corresponding analytical solution of the model equation. Table A.2 includes the values of the parameters used in the model.

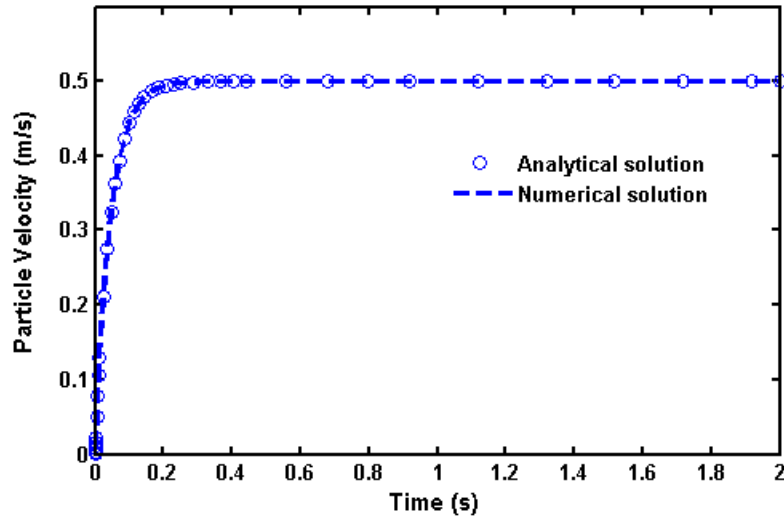


Figure A.2: Velocity profile of the particle

Table A.2: Values of the parameters used in the momentum transfer model

Category	Properties	Numerical Value
Operating conditions	Fluid density (air, g/m ³)	1.225×10 ³
	Fluid dynamic viscosity (air, g/m. s)	1.983×10 ⁻²
	Average fluid velocity (m/s)	0.5

Coupled Momentum and Energy Balance Equations

In the momentum and energy balance equations solved above, the average fluid velocity was assumed to be constant. In addition, the heat exchange between the two phases has not been included yet. Hence, to calculate the one-dimensional velocity profile of the fluid, the fundamental mass conservation equation (Equation (A.7)) was solved for a steady flow. Considering the fluid behaves as an ideal gas mixture its velocity at any point in the axial direction was calculated by Equation (A.8).

$$\frac{\partial}{\partial t}(\rho_f) + \frac{\partial}{\partial x}(\rho_f u_f) = 0 \quad (\text{A.7})$$

$$u_f(x) = u_f^0 \frac{T_f(x)}{T_f^0} \quad (\text{A.8})$$

where u_f^0 and T_f^0 denote the initial velocity and temperature of the gas, respectively.

The interphase convective heat transfer between the gas and particulate phases was included in the energy equation (Equation (A.9)) to account the energy exchange between the two phases:

$$c_p m_p u_p \frac{dT_p}{dx} = \varepsilon \sigma A_p (T_{wall}^4 - T_p^4) + h_{cov} A_p (T_f - T_p) \quad (\text{A.9})$$

where h_{cov} is the convective heat transfer coefficient and depends on the type of fluid, the flow properties such as velocity and viscosity as given in Equation (A.10).

$$h_{cov} = \frac{k_f N_u}{d_p} \quad (\text{A.10})$$

where N_u is the Nusselt number: a dimensionless parameter characterizing the convective heat transfer coefficient and k_f is the thermal conductivity of the fluid at the average fluid temperature. The Ranz and Marshall correlation was used to calculate the Nusselt number as in Equation (A.11) (Di Blasi, 2004).

$$N_u = (2 + 0.6Re_p^{1/2}Pr^{1/3}) \quad (\text{A.11})$$

where Pr is the Prandtl number, a dimensionless parameter representing the ratio of diffusion of momentum to heat in the fluid.

The mean fluid temperature variation with position along the reactor length is modelled applying energy balance on a differential control volume which yields the following model equation (Di Blasi, 2004):

$$\frac{dT_f}{dx} = \frac{P}{\dot{m}_f c_{p,f}} h_{cov,f} (T_{wall} - T_f) \quad (\text{A.12})$$

where $h_{cov,f}$ is the convective heat transfer coefficient between the gas and the reactor wall and P is the perimeter of the reactor tube. For the fluid flow with constant wall temperature, the Nusselt number is taken as 3.66 (Di Blasi, 2004).

Hence, the following coupled system of equations was solved to explore the effect of the two-phase flow on the heating rate of the particle. The values of the parameters used in the model are given in Table A.3.

$$u_f(x) = u_f^0 \frac{T_f(x)}{T_f^0} \quad (\text{A.13})$$

$$m_p u_p \frac{du_p}{dx} = \frac{1}{2} c_d \rho_f A_P (u_f - u_p)^2 \quad (\text{A.14})$$

$$c_p m_p u_p \frac{dT_p}{dx} = \varepsilon \sigma A_p (T_{wall}^4 - T_p^4) + h_{cov} A_p (T_f - T_p) \quad (A.15)$$

$$\frac{dT_f}{dx} = \frac{P}{\dot{m} c_p} h_{cov,f} (T_{wall} - T_f) \quad (A.16)$$

Table A.3: Values of the parameters used in the coupled model

Category	Properties	Numerical value
Operating conditions	Thermal conductivity of air	0.024
	Specific heat capacity of air	1.006

The temperature of the particle determined by the temperature of the fluid and the radiant walls. Figures A.3 and A.4 show temperature profiles of the particle and the fluid along the reactor length with the constant and variable fluid velocities, respectively. Heat is transferred from the fluid to the particle by convection which led to the increase in the particle temperature with the inclusion of the convective heat transfer term. Under the constant fluid velocity, the particle heats up rapidly within 0.3 m of the reactor before it reached in thermal equilibrium with the fluid temperature. On the other hand, with the variable velocity the particle took longer (0.5m) due to the density effect of the fluid. Based on these results the particle heating is fast. Hence, heat transfer at this stage of the reactor model will not be a rate limiting step.

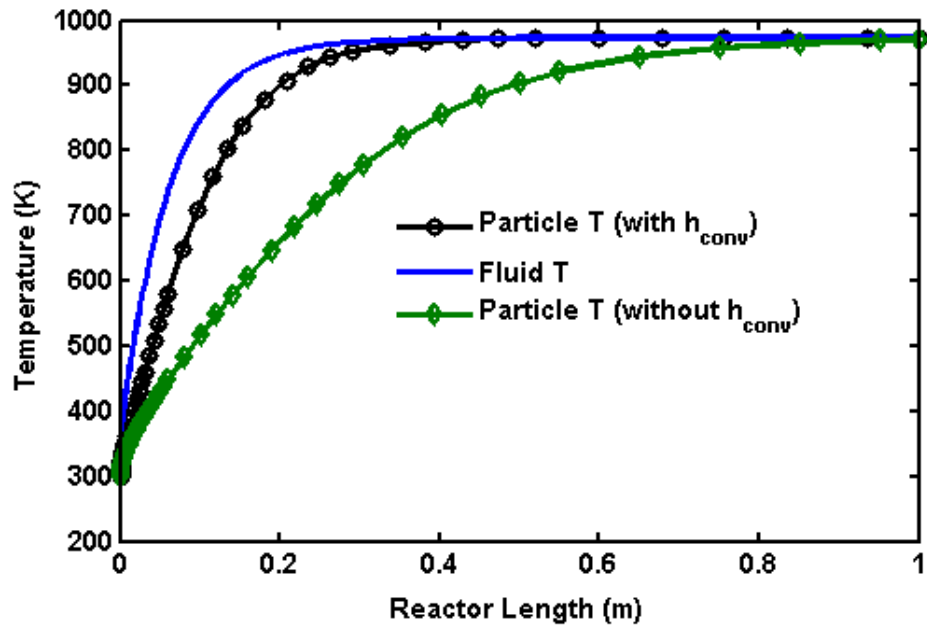


Figure A.3: Temperature of the fluid and the particle over the reactor length with the constant fluid velocity

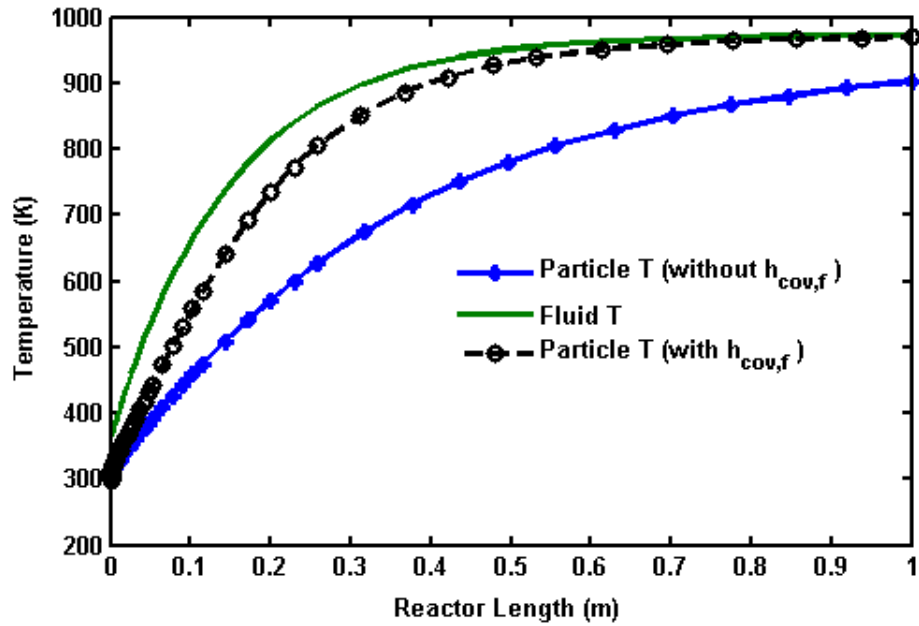


Figure A.4: Temperature of the fluid and the particle over the reactor length with variable fluid velocity

Pyrolysis Sub-model

Figure A.5 shows the kinetic scheme chosen to represent pyrolysis of cellulose (Koufopoulos et al., 1991). The important feature of this kinetic scheme is the variation in the percentage of tar, char and gases can be predicted under varying operating conditions (Di Blasi and Russo, 1993). The kinetic parameters for the primary reactions (1-3) are taken from (Chan et al., 1985) and are given in Table A.4.

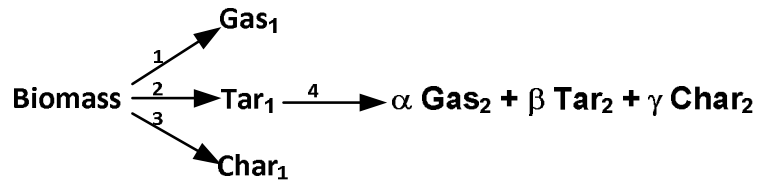


Figure A.5: A two-stage semi-global reaction scheme (Koufopoulos et al., 1991)

Table A.4: Pyrolysis kinetic parameters used for in the kinetic model

Reaction	$k_i (s^{-1})$	$E_i (kJ.mol^{-1})$	Comment and Reference
1	1.3×10^8	140	Gas ₁ : primary gases, e.g. CO ₂ , CO, CH ₄ (Chan et al., 1985)
2	2.0×10^8	133	Tar ₁ : primary tar, e.g. Acetol, phenols (Chan et al., 1985)
3	1.08×10^7	121	(Chan et al., 1985)

A first order kinetic with the Arrhenius temperature dependence is then applied to model the pyrolysis process as follows:

$$\frac{dw_B}{dt} = -(k_1 + k_2 + k_3)w_B \quad (\text{A.17})$$

$$\frac{dw_B}{dt} = -(k_1 + k_2 + k_3)w_B \quad (\text{A.18})$$

$$\frac{dw_G}{dt} = k_1 w_B \quad (\text{A.19})$$

$$\frac{dw_T}{dt} = k_2 w_B \quad (\text{A.20})$$

$$\frac{dw_C}{dt} = k_3 w_B \quad (\text{A.21})$$

Figure A.6 shows the pyrolysis product distribution at the temperature of 973K. At high pyrolysis temperatures the percentage of primary tar (Tar_1) is expected to be high (Balat et al., 2009), thus the simulation results are consistent with this observation.

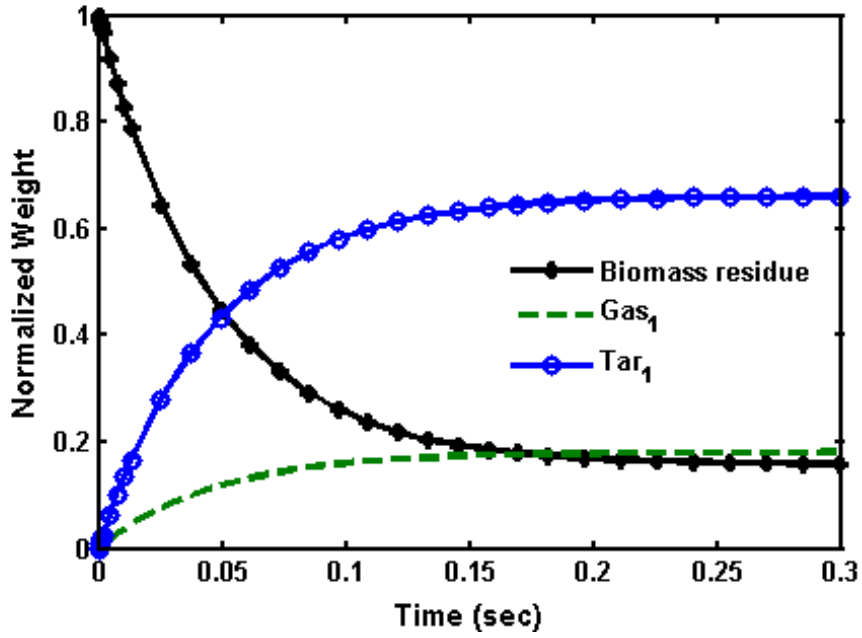


Figure A.6: Pyrolysis products distribution at temperature of 700°C

References

- Balat, M., Balat, M., Kirtay, E. & Balat, H. 2009. Main routes for the thermo-conversion of biomass into fuels and chemicals. Part 1: Pyrolysis systems. *Energy Conversion and Management*, 50, 3147-3157.
- Chan, W.R., Kelbon, M. & Krieger, B. B. 1985. Modelling and experimental verification of physical and chemical processes during pyrolysis of a large biomass particle. *Fuel*, 64, 1505-1513.
- Di Blasi, C. 2004. Modeling wood gasification in a countercurrent fixed-bed reactor. *AIChE Journal*, 50, 2306-2319.
- Koufopanosi, C.A., Maschio, G. & Lucchesit, A. 1989. Kinetic modelling of the pyrolysis of biomass and biomass components. *The Canadian Journal of Chemical Engineering*, 67, 75-84.
- Ku X., Li, T. & Løvås, T. 2015. CFD-DEM simulation of biomass gasification with steam in a fluidized bed reactor. *Chemical Engineering Science*, 122, 270-283.
- Morsi, S.A. & Alexander, A.J. 1972. An investigation of particle trajectories in two-phase flow systems. *Journal of Fluid Mechanics*, 55, 193-208.
- Papadikis, K., Bridgwater, A.V. & Gu, S. 2008. CFD modelling of the fast pyrolysis of biomass in fluidised bed reactors, Part A: Eulerian computation of momentum transport in bubbling fluidised beds. *Chemical Engineering Science*, 63, 4218-4227.
- Sommerfeld, M. Theoretical and experimental modelling of particulate flows. 2000. Institut für Verfahrenstechnik.

Appendix 3B

Catalyst Bed Temperature from Reactive Flash Volatilization of Cellulose by Colby et al. (2008)

Figure B.1 shows the catalyst bed temperature from reactive flash volatilization of cellulose as reported by Colby et al. (2008). The value at 10 mm downstream of the front face was used for the simulation model developed in the present study.

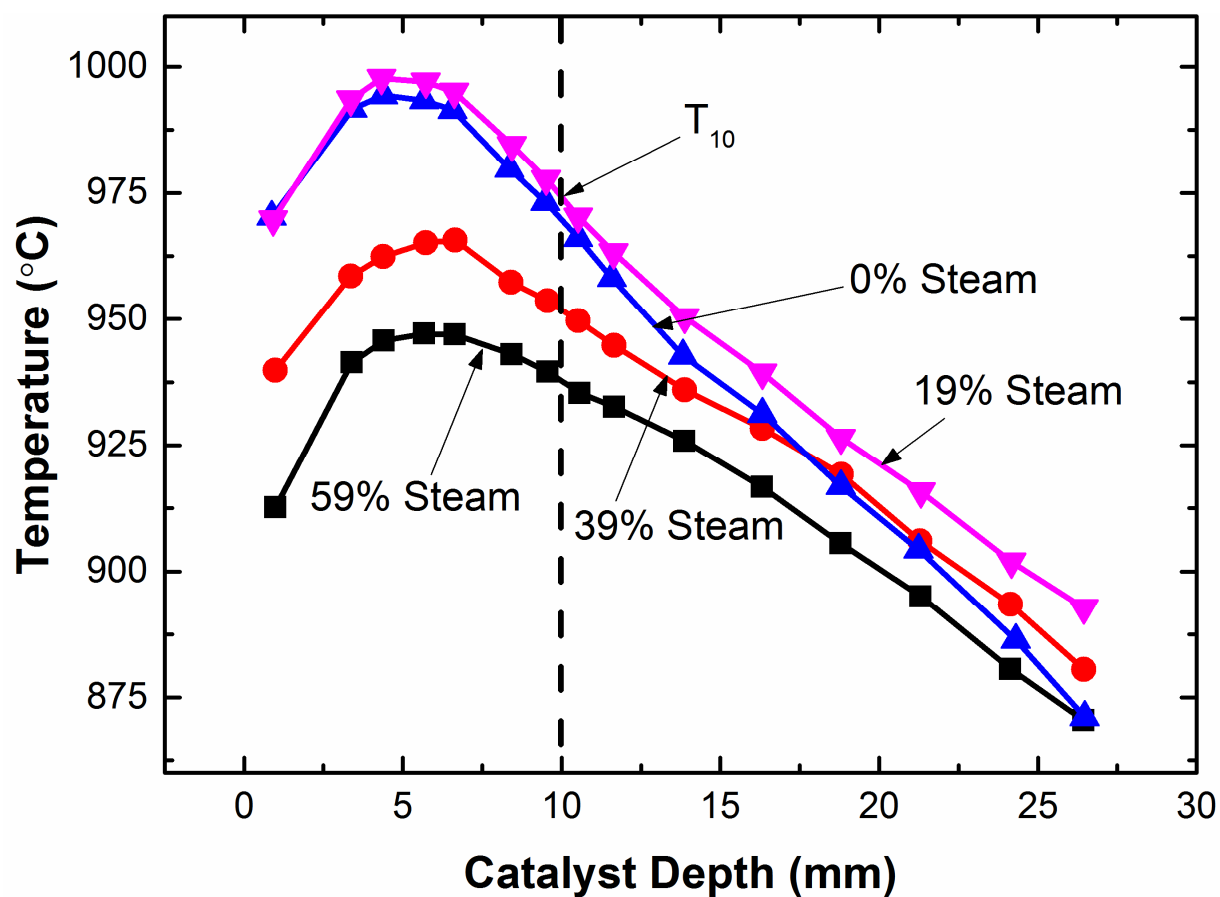


Figure B.1: Catalyst bed temperature adapted from Colby et al. (2008)

Appendix 4A

Sample Calibration Plots for Mass Flow Controllers

The mass flow controllers were calibrated every time before experiments in the range of flows required for the reactions. The tables and figures included in the appendix are sample calibration curves for nitrogen and oxygen flow rates.

Table A.1: Measured Ar flow rate from the mass flow controller for different set-points

Setpoint flow rate of Ar (mL/min)	Actual flow rate (mL/min)
80	54.99
150	111.72
300	244.53
400	356.08

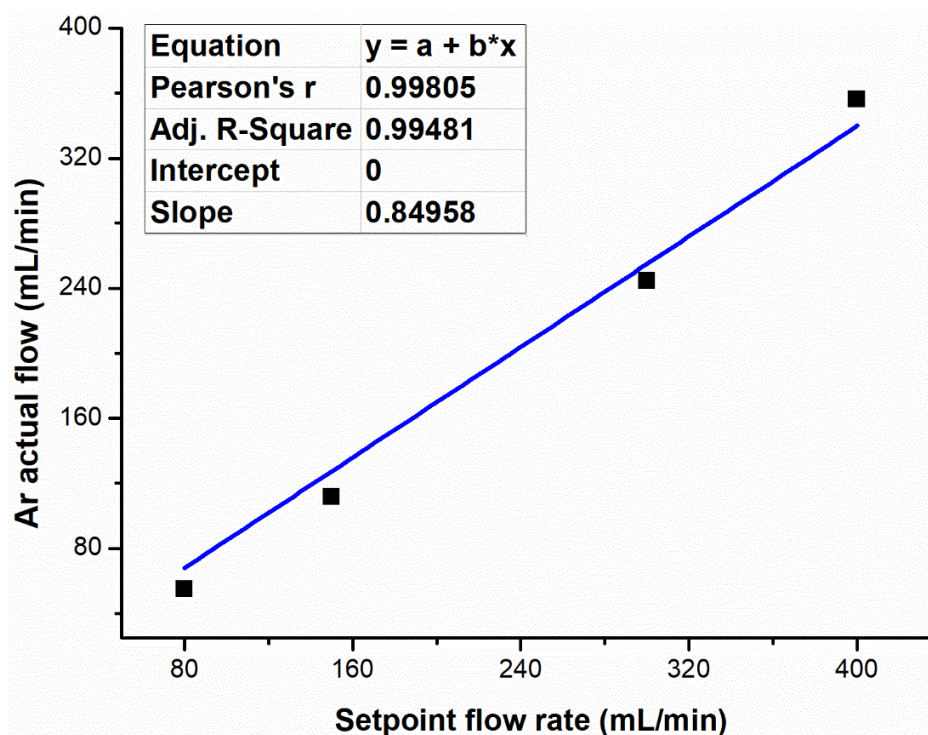


Figure A.1: Calibration curve for Ar feed rate

Table A.2: Measured O₂ outlet flow rates from the mass flow controller for different set-points

Setpoint flow rate of Acetol (mL/min)	Actual flow rate (mL/min)
38	17.58
80	38.53
150	87.54
250	146.64

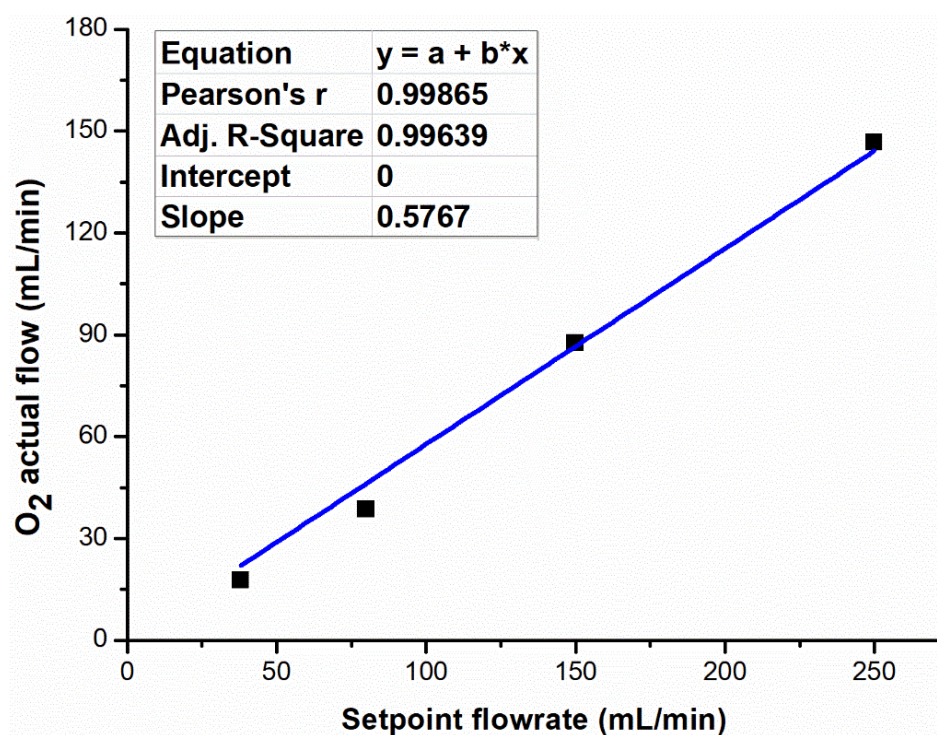


Figure A.2: Calibration curve for O₂ feed rate

Appendix 4B

Calibration Curve for Syringe Pump

This appendix includes calibration plots for acetol and guaiacol feed rates using the Syringe pump.

Table B.1: Measured acetol feed rate using the syringe pump for different set-points

Setpoint flow rate of Acetol (mL/min)	Actual flow rate (mL/min)
0.05	0.048
0.1	0.097
0.15	0.014
0.3	0.287

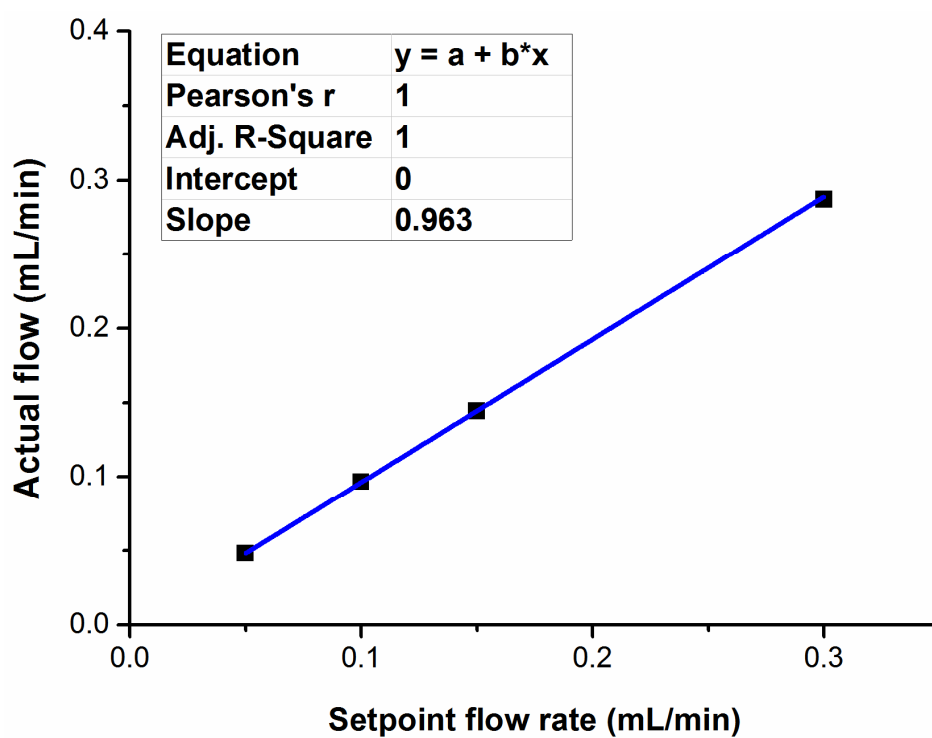


Figure B.1: Calibration curve for acetol feed rate using the syringe pump

Table B.2: Measured guaiacol feed rates using the syringe pump

Setpoint flow rate of Guaiacol (mL/min)	Actual flow rate (mL/min)
0.033	0.031
0.05	0.045
0.067	0.063
0.083	0.078
0.1	0.097
0.13	0.129
0.25	0.245

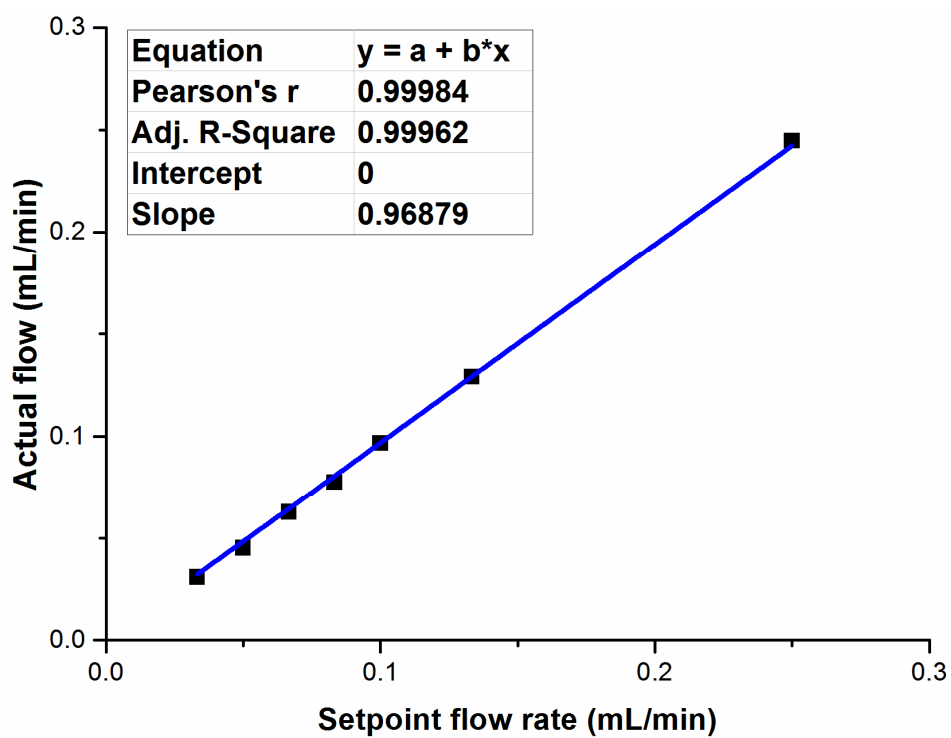


Figure B.2: Calibration curve for the guaiacol feed rate using the syringe pump

Appendix 4C

Calibration Curve for HPLC Metering Pump

Table C.1 and Figure C.1 show the data and calibration plot for water outlet flows using the HPLC pump.

Table C.1: Measured water outlet flow rate from the for HPLC pump for different set-points

Setpoint flow rate of water (mL/min)	Actual flow rate (mL/min)
0.05	0.047
0.1	0.097
0.2	0.193
0.3	0.292
0.4	0.372

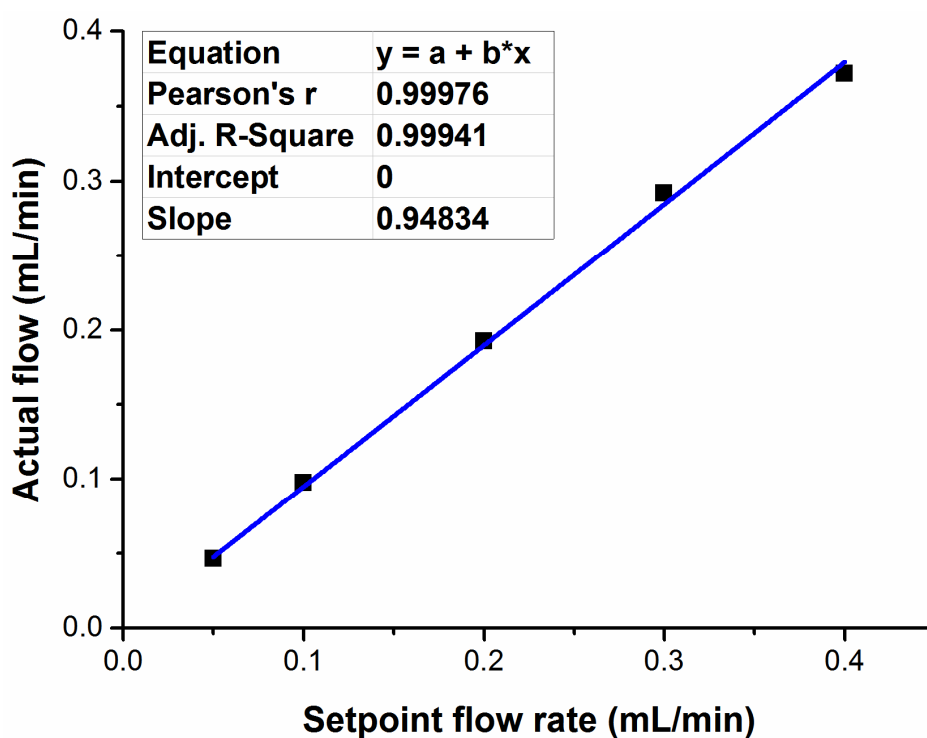


Figure C.1: Calibration curve for the water feed rate using the HPLC pump

Appendix 4D

Calibration Plots for GC

This appendix includes the calibration plots for H₂, CO, CO₂, CH₄, O₂, and N₂. The reported mean areas are average values of at least three different measured values.

Table D.1: GC peak areas for known concentrations of H₂

H ₂ concentration (mol %)	Mean area (mol %)
0.1	5933
1	52978
2	96457
6	307748
8.11	506185
20.43	1229389
42.5	2066432
100	5232441

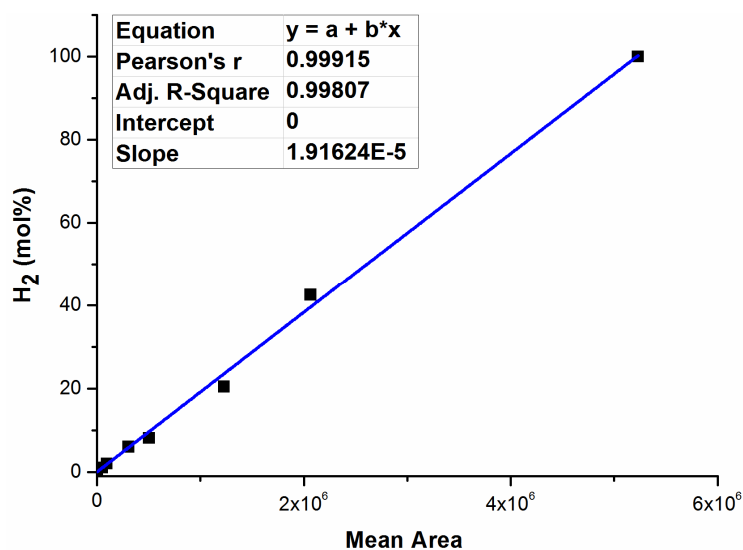


Figure D.1: Calibration plot for H₂ analysis using GC

Table D.2: GC peak areas for known concentrations of CO

CO concentration (mol %)	Mean area
1	661411
4.98	7581670
20.2	30118604
100	143620975

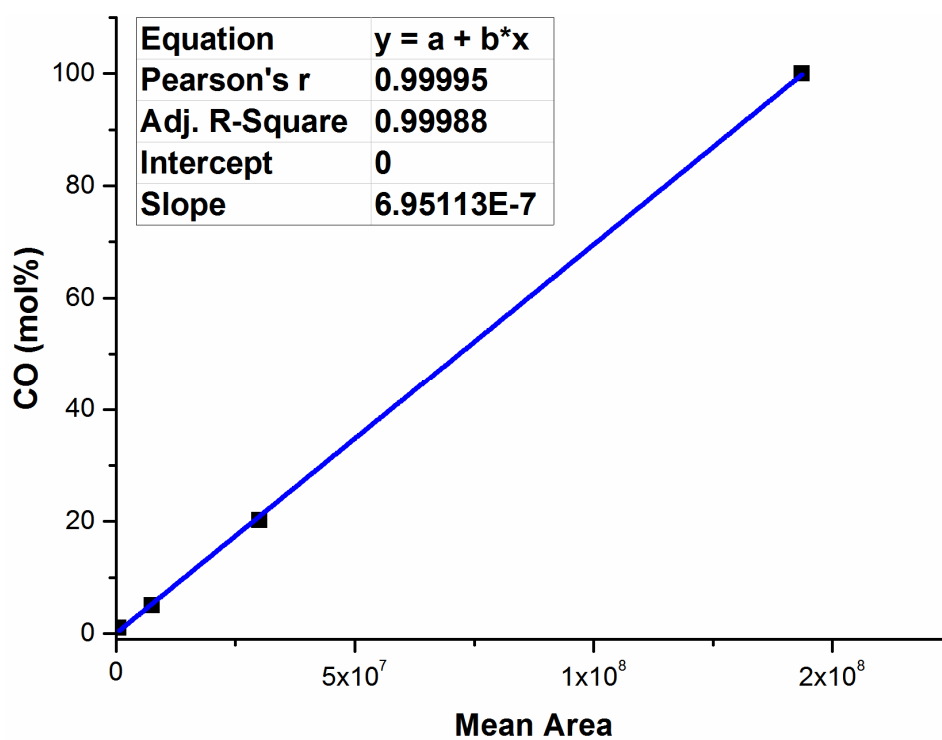


Figure D.2: Calibration curve for CO analysis using GC

Table D.3: GC peak areas for known concentrations of CO₂

CO ₂ concentration (mol%)	Mean area
1	1321987
10.09	15338559
25	38222915
100	152063487

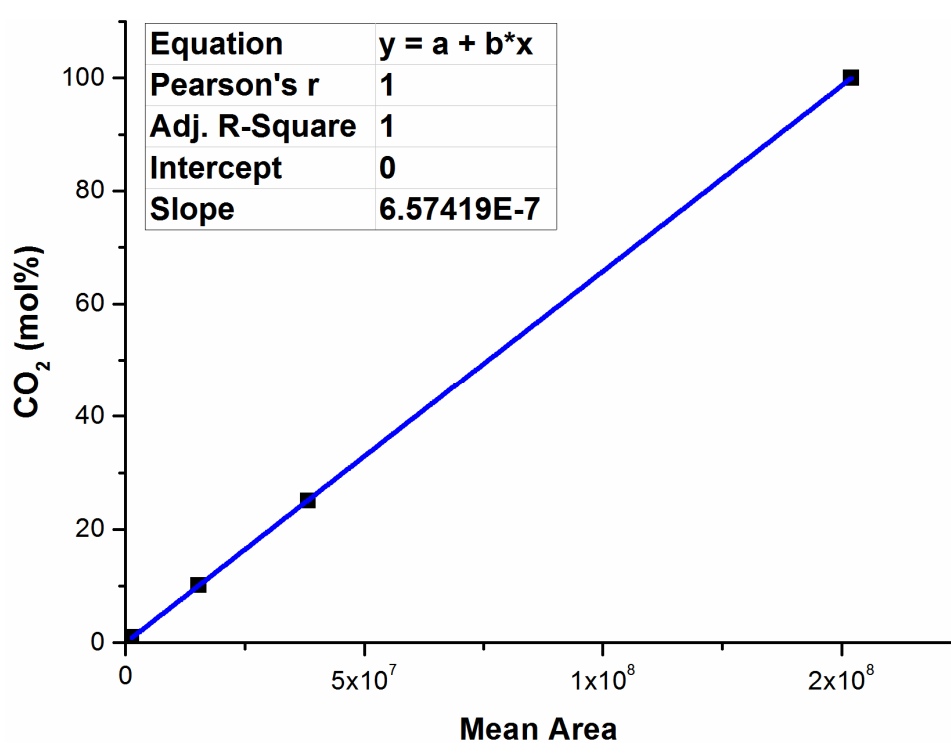


Figure D.3: Calibration curve for CO₂ analysis using GC

Table D.4: GC peak areas for known concentrations of CH₄

CH ₄ concentration (mol%)	Mean area
1	657291
8.24	12531172
10.08	15915598
20	31943750
100	147982677

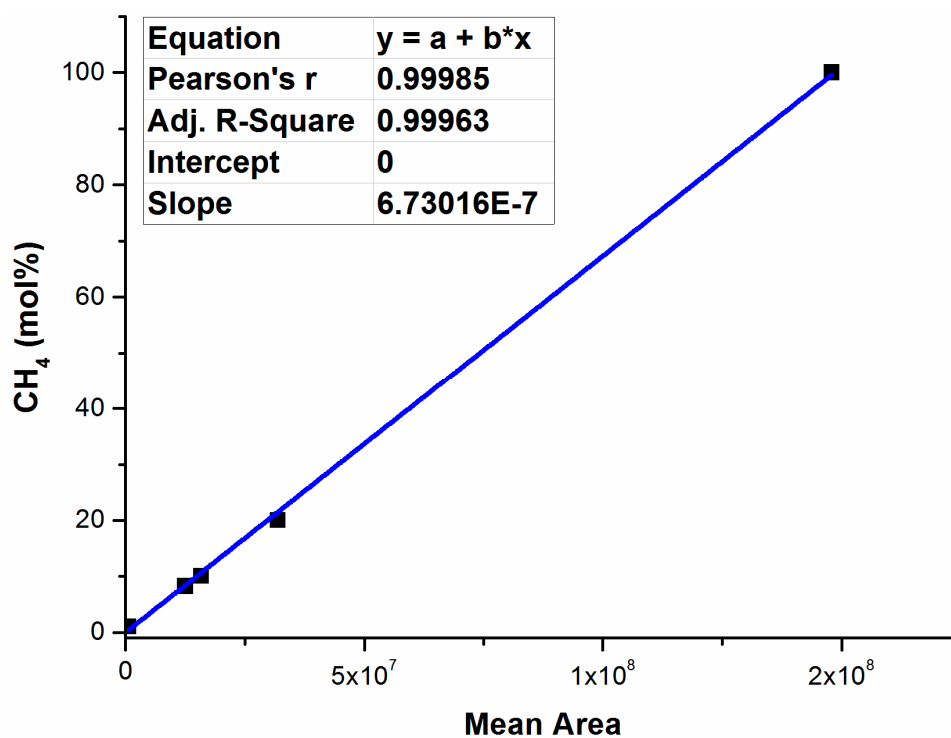


Figure D.4: Calibration plot for CH₄ analysis using GC

Table D.5: GC peak areas for known concentrations of N₂

N ₂ concentration (mol %)	Mean area
1	16161
39.2	202206
48.67	248158
100	437306

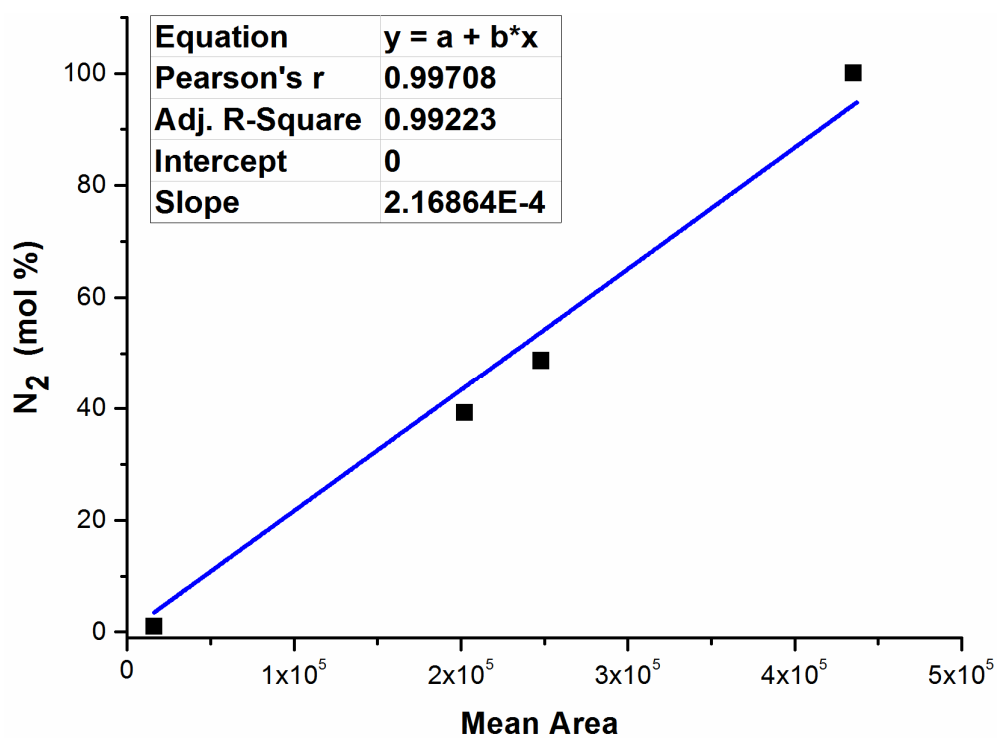


Figure D.5: Calibration curve for N₂ analysis using GC

Table D.6: GC peak areas for O₂ analysis using GC

O ₂ concentration (mol %)	Mean area
2	13424.3
15	95902.55
32.5	172757.2
50	279546.9
75	404365.5
100	539610.6

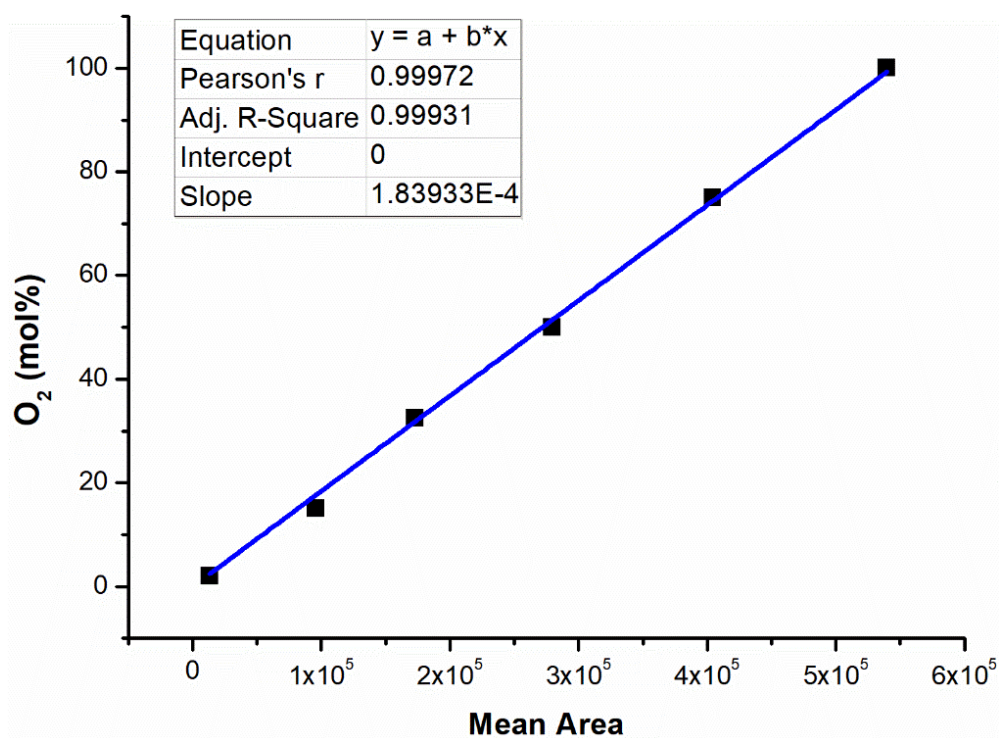


Figure D.6: Calibration curve for O₂ analysis using GC

Appendix 4E

Calibration Curve for HPLC

Table E.1 and Figure E.1 show the calibration data and curve for quantifying acetol concentration in the liquid samples from the condenser using HPLC.

Table E.1: HPLC peak areas for known concentration of acetol

Concentration (vol%)	Area (from DAD1)
6.24E-03	230.52
0.0125	502.75
0.025	1000.7
0.05	1994.705
0.125	5346.815
0.25	1.02×10^4
0.5	2.01×10^4
1	3.83×10^4
2	7.06×10^4

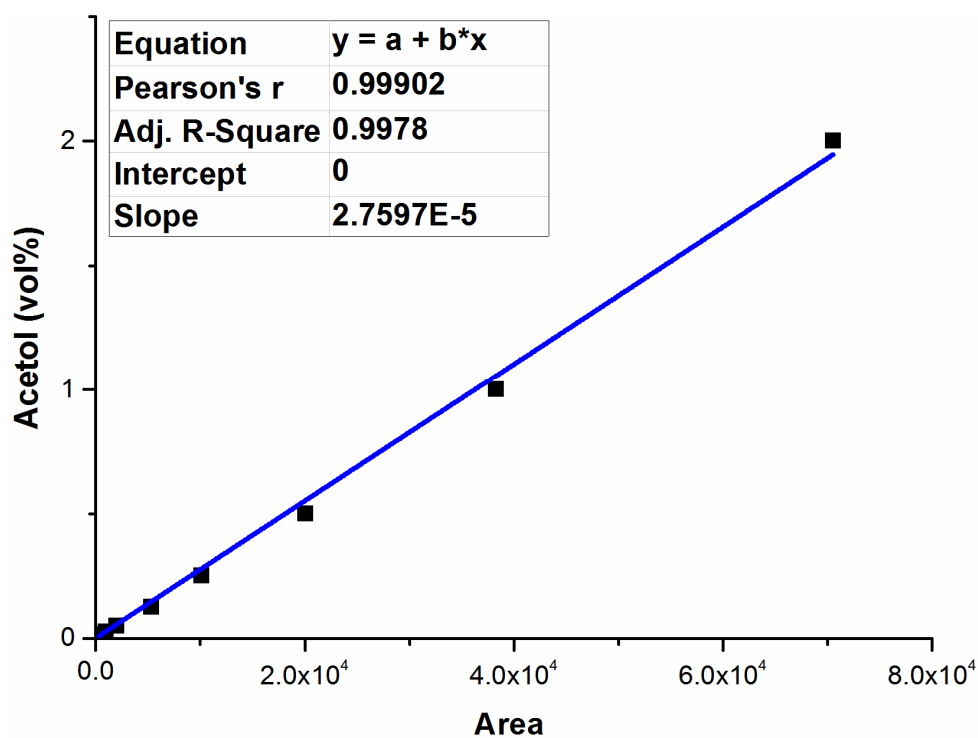


Figure E.1: Calibration curve for acetol concentration in liquid samples using HPLC

Appendix 4F

A Sample Experimental Result using 1%Ru-10%Ni/Al₂O₃ Catalyst

Figure F.1 shows a sample result from acetol reforming using Ru-Ni/Al₂O₃ catalyst. A high content of CO₂ was present in the product gas.

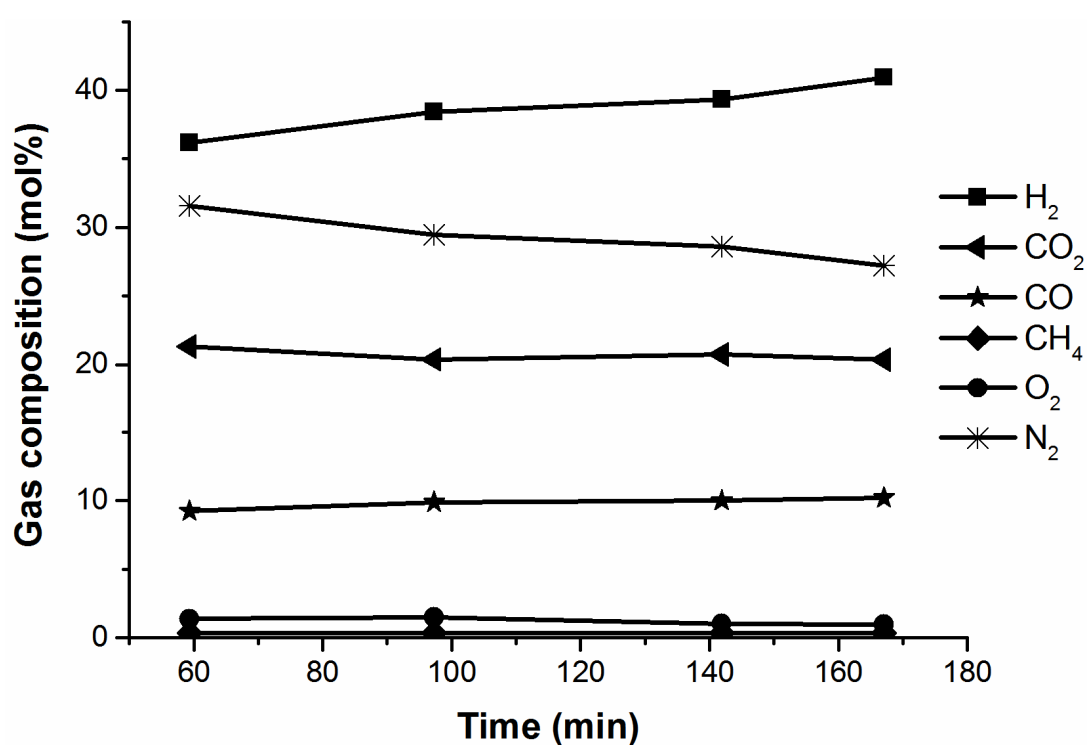


Figure F.1: Sample result from acetol conversion using 1%Ru-10%Ni/Al₂O₃ (T=700°C, S/C=1.2, C/O=1.13)

Appendix 4G

Elemental Mass Balance (C, H, and O)

Table G.1 shows the sample mass balance for C, H and O for the tail gas. The mass balance closes within $\pm 5\%$.

Table G.1: An element mass balance for the tail gas

Feed						
	Nitrogen-in	Water-in	Acetol-in	Oxygen-in		
Flowrate (mol/min)	0.012860998	0.004444444	0.001294111	0.002009657		
Total flow (mol/min)	0.02060921					
mol%	62.40412902	21.56533132	6.279283591	9.751256074		
Total moles of gas produced						
Nitrogen-in	Total number of moles					
0.012860998	0.022789679					
Product gas composition						
Component	CH ₄	H ₂	CO ₂	CO	O ₂	N ₂
Composition (mol%)	0	25.58517487	9.695997919	7.534351412	0.751044181	56.43343
Moles	0	0.005830779	0.002209687	0.001717055	0.000171161	
C, H and O Atom balance						
Component	H-in	O-in	C-in			
H2O	0.008888889	0.002222222				
Acetol	0.007764664	0.002588221	0.003882332			
O2	0	0.004019314				
Total	0.016653553	0.008829757	0.003882332			
Component	H-out	O-out	C-out			
CO	0	0.001717055	0.001717055			
CO2	0	0.004419374	0.002209687			
H2	0.011661559	0	0			
CH4	0	0	0			
O2	0	0.000342321	0			
H2O	0.004991995	0.002495997	0			
Total	0.016653553	0.008974747	0.003926741			
Yield (%)	100	101.6420527	101.143877			

Appendix 4H

Calibration Curves for RGA

This appendix includes the calibration curves constructed for known concentrations of the compounds (H₂, CO, CO₂, CH₄, O₂, acetol, H₂O, Ar, and He) against the corresponding areas under the peaks.

Table H.1: Calibration data for H₂ analysis using RGA

Area (Torr.s)	H ₂ (vol%)
5.15×10 ⁻⁶	3.636364
1.47×10 ⁻⁵	13.63636
3.26×10 ⁻⁵	27.27273
6.96×10 ⁻⁵	59.09091
1.15×10 ⁻⁴	100

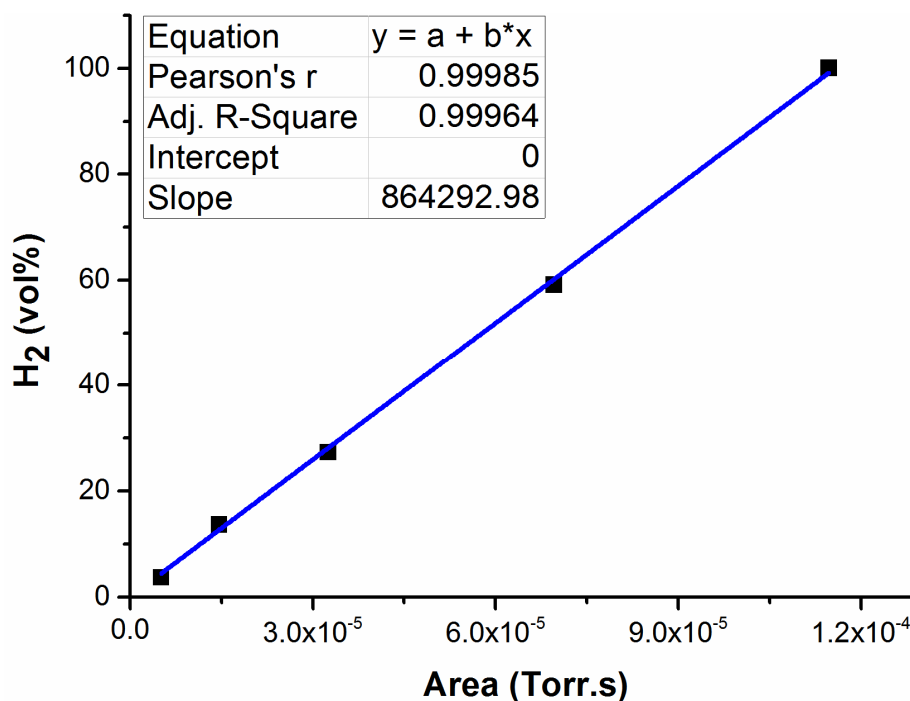


Figure H.1: Calibration curve for H₂ analysis using RGA

Table H.2: Calibration data for CO analysis using RGA

Area (Torr.s)	H ₂ (vol%)
1.31×10 ⁻⁶	3
1.22×10 ⁻⁵	15
2.56×10 ⁻⁵	30
4.97×10 ⁻⁵	60
8.86×10 ⁻⁵	100

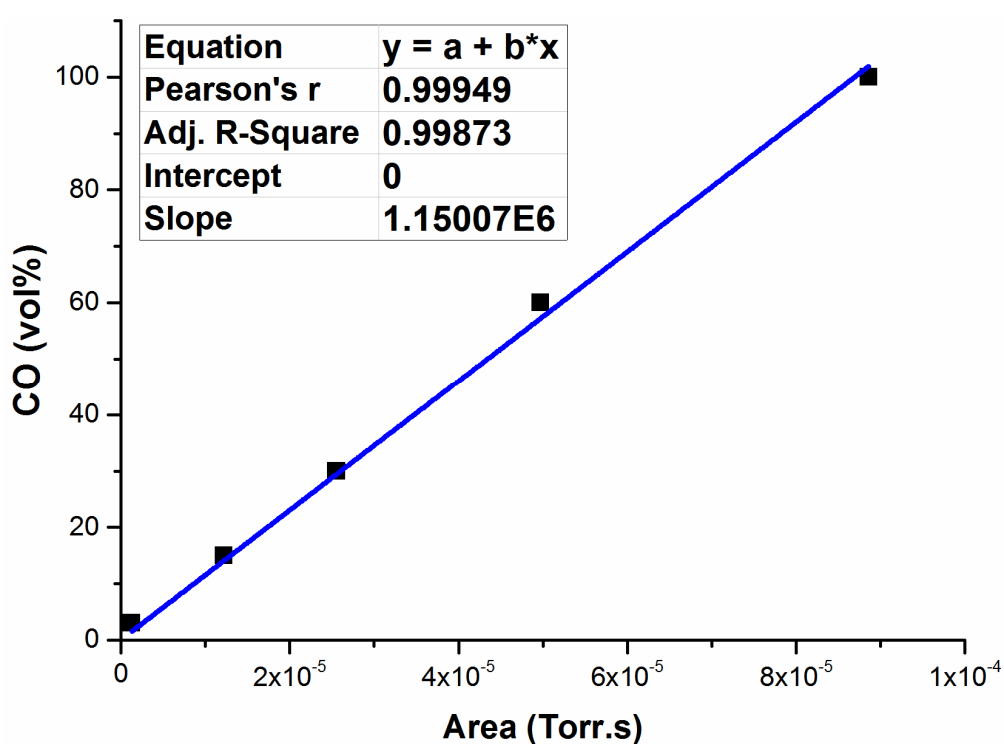


Figure H.2: Calibration curve for CO analysis using RGA

Table H.3: Calibration data for CO₂ analysis using RGA

Area (Torr.s)	CO ₂ (vol%)
1.42×10 ⁻⁶	2.17
8.37×10 ⁻⁶	10
4.62×10 ⁻⁵	42.55
6.69×10 ⁻⁵	60.87
1.09×10 ⁻⁴	100

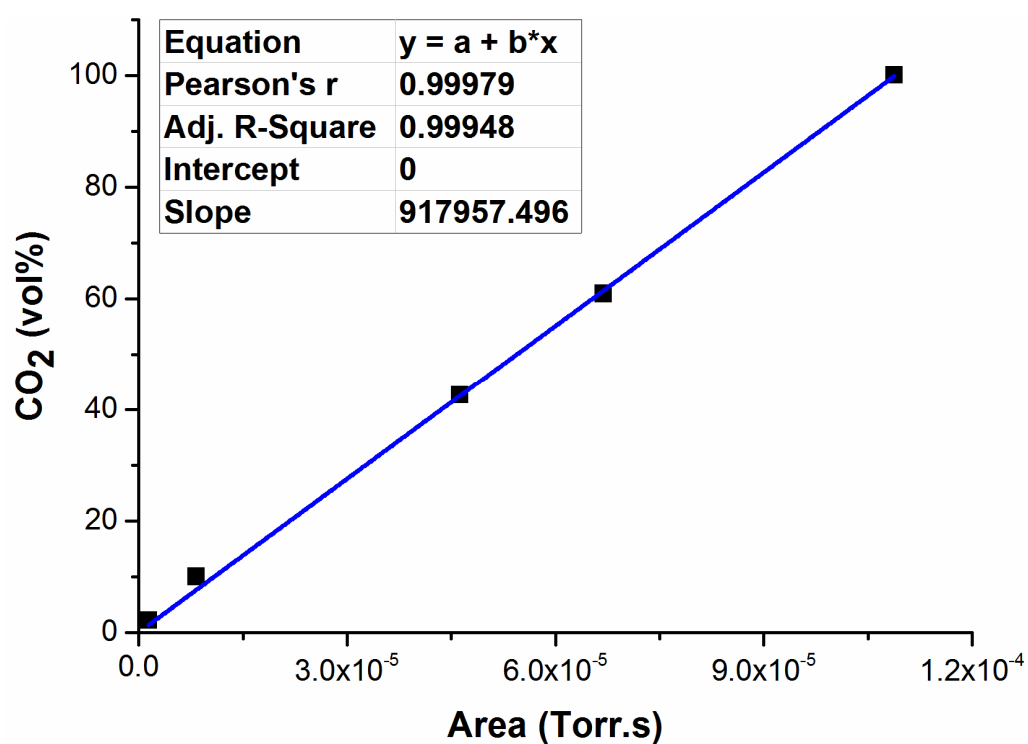


Figure H.3: Calibration plot for CO₂ analysis using RGA

Table H.4: Calibration data for CH₄ analysis using RGA

Area (Torr.s)	CH ₄ (vol%)
1.26×10 ⁻⁶	2.73
9×10 ⁻⁶	13.64
2.25×10 ⁻⁵	36.36

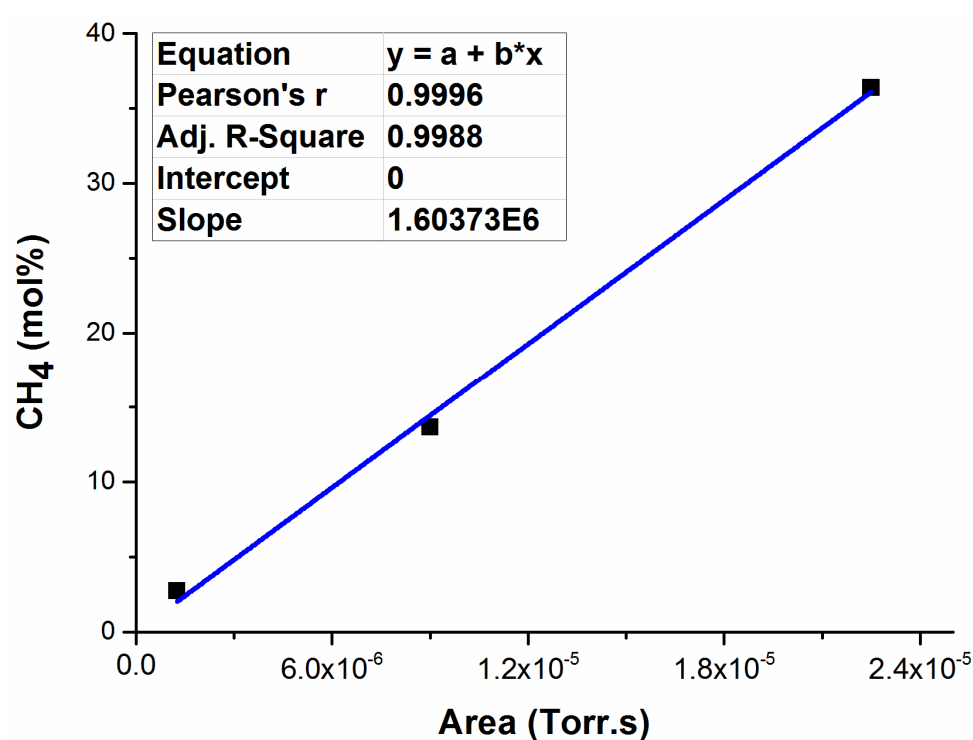


Figure H.4: Calibration curve CH₄ analysis using RGA

Table H.5: Calibration data for Ar analysis using RGA

Area (Torr.s)	Ar (vol%)
2.54×10^{-6}	3.64
1.77×10^{-5}	13.64
7.43×10^{-5}	45.45
1.24×10^{-4}	72.73
1.68×10^{-4}	100

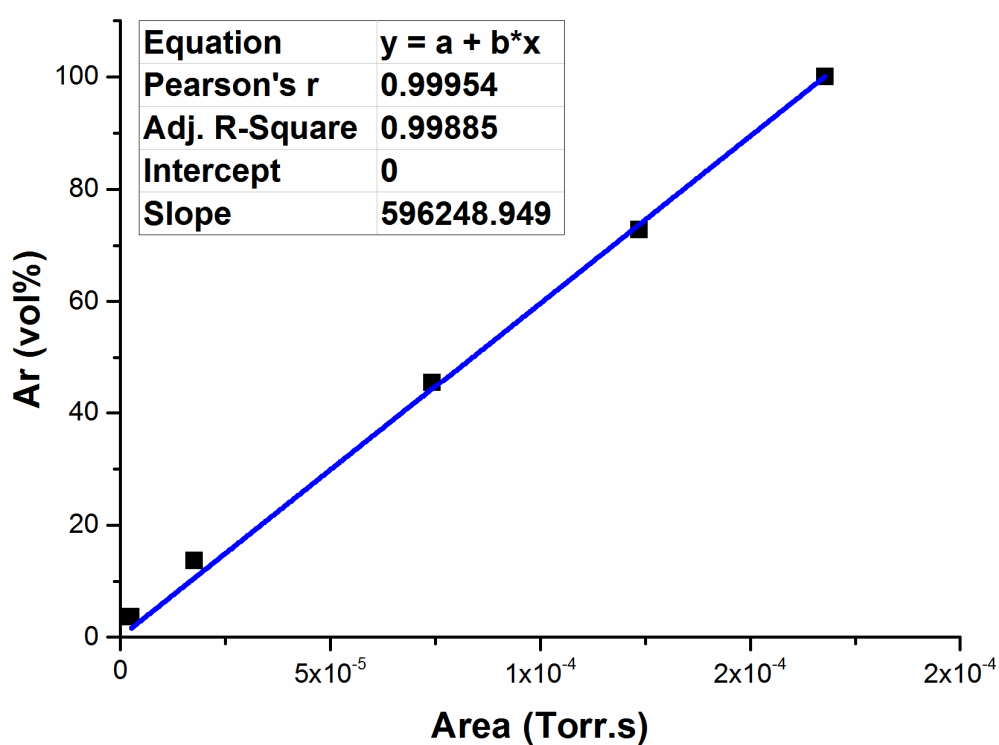


Figure H.5: Calibration curve Ar analysis using RGA

Appendix 5A

Oxygen and Acetol Ion Spectra in the Reactor Freeboard

The oxygen added to the reactant stream was consumed completely in the freeboard as seen in the ion spectra in Figure A.1. For C₂ compounds (C₂H₂, C₂H₄, and C₂H₆) an ion fragment at m/z 24 is expected, however, its signal intensity is zero suggesting that no C₂ compounds are being formed in the reaction.

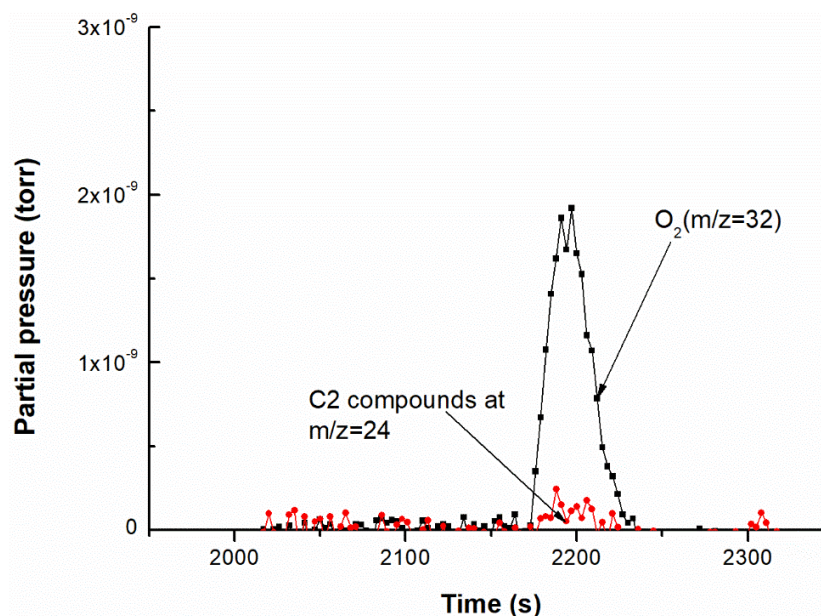


Figure A.1: Ion spectra for gas sample taken from the reactor freeboard at 650°C

Appendix 5B

Mass Balance for the Gas Analysis from the Freeboard

This appendix includes the elemental balance calculations for all the reaction temperatures tested.

Table B.1: Moles of compounds in the feed

Parameter	Inlet flow			
	Acetol_in	Ar_in	H ₂ O_in	O ₂ _in
MW (g/mol)	74.08	39.9	18.01	32
Molar flow (mol/min)	0.0013	0.0078	0.0047	0.0011

Table B.2: Total molar flow rate of the gas in the freeboard (dry basis)

Temperature (°C)	Ar_in (mol/min)	y_Ar (out)	Total moles of the gas (mol/min)
650°C	0.00781	0.686	0.0114
700°C	0.00781	0.654	0.0119
750°C	0.00781	0.627	0.0124
850°C	0.00781	0.555	0.0141

Table B.3: Composition and molar flow rate of the gases in the freeboard (dry basis)

Temperature (°C)	CH₄ (mol%)	H₂ (mol%)	CO₂ (mol%)	CO (mol%)	Ar (mol%)
650	4.11	9.89	5.37	12.02	68.61
700	4.69	11.25	6.06	12.60	65.39
750	5.23	12.98	6.61	12.46	62.72
850	6.49	15.93	6.35	15.72	55.52
Temperature (°C)	CH₄ (mol/min)	H₂ (mol/min)	CO₂ (mol/min)	CO (mol/min)	Ar (mol/min)
650	0.00047	0.00113	0.00061	0.00137	0.00781
700	0.00056	0.00134	0.00072	0.00151	0.00781
750	0.00065	0.00162	0.00082	0.00155	0.00781
850	0.00091	0.00224	0.00089	0.00221	0.00781

Table B.4: Mass balance for the reaction temperature of 650°C

Compound	Inlet		
	H_in	O_in	C_in
H ₂ O	0	0	0
C ₃ H ₆ O ₂	0.00778	0.00260	0.00389
O ₂	0	0.00226	0
Total	0.01712	0.00487	0.00389

Compound	Outlet			
	H_out	O_out	C_out	Unconverted Compound
H ₂	0.00225	0	0	
CO	0	0.00137	0.00137	
CO ₂	0	0.00122	0.00061	
CH ₄	0.00187	0	0.00047	
O ₂	0	0	0	
H ₂ O	0.00121	0.0006	0	0.0006
C ₃ H ₆ O ₂	0.00126	0.00042	0.00063	0.00021
CH ₂ O	0.00165	0.00083	0.00083	0.00083
Total	0.00823	0.00444	0.00390	
Percent (%)	105.4	91.2	100	

Table B.5: Mass balance for the reaction temperature of 700°C

Compound	Inlet			
	H_in	O_in	C_in	
H ₂ O	0	0	0	
C ₃ H ₆ O ₂	0.00778	0.00260	0.00389	
O ₂	0	0.00226	0	
Total	0.01712	0.00487	0.00389	
Compound	Outlet			Unconverted Compound
	H_out	O_out	C_out	
H ₂	0.00269	0	0	
CO	0	0.00151	0.00151	
CO ₂	0	0.00145	0.00072	
CH ₄	0.00224	0	0.00056	
O ₂	0	0	0	
H ₂ O	0.001	0.0005	0	0.0005
C ₃ H ₆ O ₂	0.001	0.00033	0.0005	0.00017
CH ₂ O	0.00123	0.00061	0.00061	0.00061
Total	0.00816	0.00440	0.0039	
Percent (%)	104.5	90.4	100	

Table B.6: Mass balance for the reaction temperature of 750°C

Compound	Inlet		
	H_in	O_in	C_in
H ₂ O	0	0	0
C ₃ H ₆ O ₂	0.00778	0.00260	0.00389
O ₂	0	0.00226	0
Total	0.01712	0.00487	0.00389

Compound	Outlet			Unconverted Compound
	H_out	O_out	C_out	
H ₂	0.00323	0	0	
CO	0	0.00155	0.00155	
CO ₂	0	0.00164	0.00082	
CH ₄	0.00261	0	0.00065	
O ₂	0	0	0	
H ₂ O	0.0008	0.0004	0	0.0004
CH ₃ COOH	0.00079	0.00026	0.00039	0.00013
CH ₂ O	0.00096	0.00048	0.00048	0.00048
Total	0.00839	0.00434	0.00390	
Percent (%)	107.5	89.2	100	

Table B.7: Mass balance for the reaction temperature of 850°C

Compound	Inlet			
	H_in	O_in	C_in	
H ₂ O	0	0	0	
C ₃ H ₆ O ₂	0.00778	0.00260	0.00389	
O ₂	0	0.00226	0	
Total	0.01712	0.00487	0.00389	
Compound	Outlet			Unconverted Compound
	H_out	O_out	C_out	
H ₂	0.00448	0	0	
CO	0	0.00221	0.00221	
CO ₂	0	0.00179	0.00089	
CH ₄	0.00365	0	0.00091	
O ₂	0	0	0	
H ₂ O	0.00906	0.00453	0	0.0003
Total	0.00873	0.00429	0.00402	
Percent (%)	111.8	88.3	102.9	

Appendix 5C

Chromatogram from GC Analysis

Figure C.1 and C.2 show the sample chromatograms from the experiments with the total analysis time 20 min.

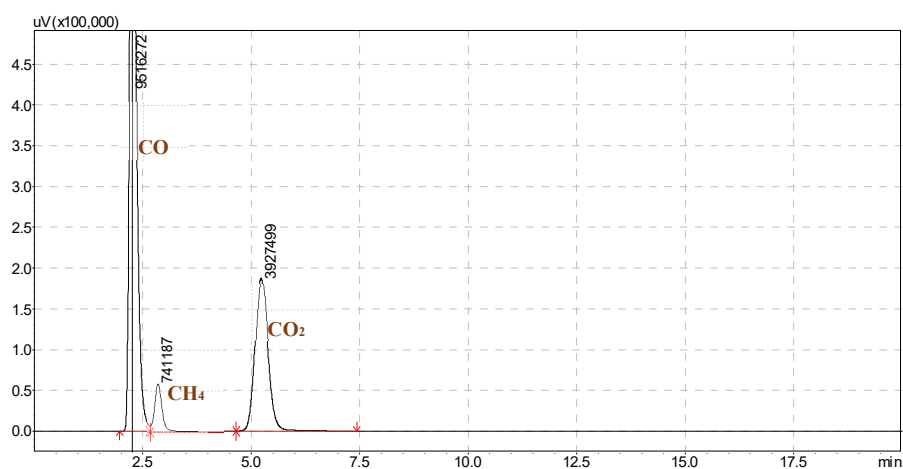


Figure C.1: A sample chromatogram from the flame ionization detector (FID)

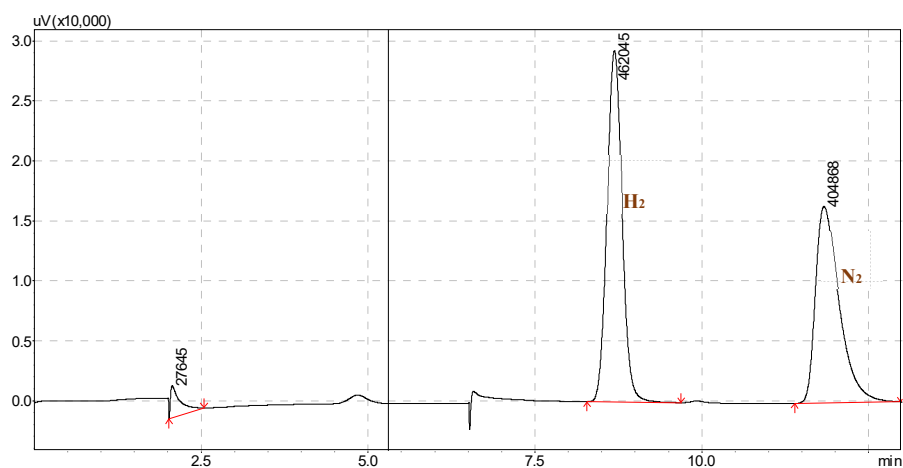


Figure C.2: A sample chromatogram from the thermal conductivity detector (TCD)

Appendix 5D

Experimental Design: ANOVA Analysis for the Acetol Conversion

The tables in this appendix contain the results from the analysis of variance for the included factors for the acetol conversion. The model variables which correspond to the factors in the experimental design are: A (Temperature), B (S/C ratio), C (C/O ratio), D (GHSV), and E (Catalyst mass)

Response: H₂ (mol %)

Table D.1: Summary of analysis of variance for H₂ (mol%) for acetol conversion

Source	Sum of Squares	DF	Mean Square	F Value	Prob > F	
Model	124.48	5	24.9	35.83	0.0274	significant
A	14.24	1	14.24	20.5	0.0455	
B	67.02	1	67.02	96.45	0.0102	
D	25.4	1	25.4	36.55	0.0263	
E	12.05	1	12.05	17.34	0.0531	
BC	5.77	1	5.77	8.3	0.1023	
Residual	1.39	2	0.69			
Cor Total	125.87	7				

- The Model F-value of 35.83 implies the model is significant. There is only a 2.74% chance that a "Model F-Value" this large could occur due to noise.
- Values of "Prob > F" less than 0.0500 indicate model terms are significant. In this case A, B, D are significant model terms.
- Values greater than 0.1000 indicate the model terms are not significant.

Response: CO (mol %)

Table D.2: Summary of analysis of variance for CO (mol%)

Source	Sum of Squares	DF	Mean Square	F Value	Prob > F	
Model	127.9	5	25.58	68.68	0.0144	significant
A	21.31	1	21.31	57.2	0.017	
B	93.56	1	93.56	251.19	0.004	
C	7.29	1	7.29	19.57	0.0475	
E	3.51	1	3.51	9.42	0.0918	
DE	2.24	1	2.24	6.01	0.1337	
Residual	0.74	2	0.37			
Cor Total	128.65	7				

- The Model F-value of 68.68 implies the model is significant. There is only a 1.44% chance that a "Model F-Value" this large could occur due to noise.
- Values of "Prob > F" less than 0.0500 indicate model terms are significant. In this case A, B, C are significant model terms.
- Values greater than 0.1000 indicate the model terms are not significant.

Response: CH₄ (mol %)Table D.3: Summary of analysis of variance for CH₄ (mol%)

Source	Sum of Squares	DF	Mean Square	F Value	Prob > F	
Model	1.86	5	0.37	281.26	0.0035	significant
A	1.32	1	1.32	1000.11	0.001	
B	0.4	1	0.4	302.03	0.0033	
D	0.11	1	0.11	85.96	0.0114	
E	0.021	1	0.021	16	0.0572	
BE	2.88E-03	1	2.88E-03	2.18	0.2777	
Residual	2.64E-03	2	1.32E-03			
Cor Total	1.86	7				

- The Model F-value of 281.26 implies the model is significant. There is only a 0.35% chance that a "Model F-Value" this large could occur due to noise.
- Values of "Prob > F" less than 0.0500 indicate model terms are significant. In this case A, B, and D are significant model terms.
- Values greater than 0.1000 indicate the model terms are not significant.

Response: CO₂ (mol %)Table D.4: Summary of analysis of variance for CO₂ (mol%)

Source	Sum of Squares	DF	Mean Square	F Value	Prob > F	
Model	88.38	5	17.68	43.29	0.0227	significant
A	49.75	1	49.75	121.86	0.0081	
B	7.21	1	7.21	17.66	0.0522	
C	2.22	1	2.22	5.43	0.1452	
D	27.7	1	27.7	67.86	0.0144	
E	1.49	1	1.49	3.66	0.1959	
Residual	0.82	2	0.41			
Cor Total	89.19	7				

- The Model F-value of 43.29 implies the model is significant. There is only a 2.27% chance that a "Model F-Value" this large could occur due to noise.
- Values of "Prob > F" less than 0.0500 indicate model terms are significant. In this case A and D are significant model terms.
- Values greater than 0.1000 indicate the model terms are not significant.

Response: H₂/CO (mol %)Table D.5: Summary of analysis of H₂/CO (mol%)

Source	Sum of Squares	DF	Mean Square	F Value	Prob > F	
Model	3.39	4	0.85	18.9	0.0182	significant
A	0.25	1	0.25	5.48	0.1012	
B	2.77	1	2.77	61.84	0.0043	
C	0.15	1	0.15	3.43	0.161	
E	0.22	1	0.22	4.84	0.1153	
Residual	0.13	3	0.045			
Cor Total	3.52	7				

- The Model F-value of 18.90 implies the model is significant. There is only a 1.82% chance that a "Model F-Value" this large could occur due to noise
- Values of "Prob > F" less than 0.0500 indicate model terms are significant. In this case B are significant model terms
- Values greater than 0.1000 indicate the model terms are not significant.

Response: CO/CO₂ (mol %)

Table D.6: Summary of analysis of variance for CO/CO₂ (mol%)

Source	Sum of Squares	DF	Mean Square	F Value	Prob > F	
Model	2.53	4	0.63	104.96	0.0015	significant
A	1.05	1	1.05	174.24	0.0009	
B	0.92	1	0.92	153.28	0.0011	
C	0.11	1	0.11	17.54	0.0248	
D	0.45	1	0.45	74.79	0.0033	
Residual	0.018	3	6.03E-03			
Cor Total	2.55	7				

- The Model F-value of 104.96 implies the model is significant. There is only a 0.15% chance that a "Model F-Value" this large could occur due to noise.
- Values of "Prob > F" less than 0.0500 indicate model terms are significant. In this case A, B, C, D are significant model terms.
- Values greater than 0.1000 indicate the model terms are not significant.

Appendix 5E

Experimental Design: ANOVA Analysis for the Guaiacol Conversion

The tables in this appendix includes the analysis of variance for the responses which correspond to the concentration of each gases. The model terms are: A (S/C ratio), B (C/O ratio), C (Temperature), and D (GHSV).

Response: H₂ (mol %)

Table E.1: Summary of analysis of variance for H₂ (mol%)

Source	Sum of Squares	DF	Mean Square	F Value	Prob > F	
Model	124.48	5	24.9	35.83	0.0274	significant
A	14.24	1	14.24	20.5	0.0455	
B	67.02	1	67.02	96.45	0.0102	
D	25.4	1	25.4	36.55	0.0263	
E	12.05	1	12.05	17.34	0.0531	
DE	5.77	1	5.77	8.3	0.1023	
Residual	1.39	2	0.69			
Cor Total	125.87	7				

- The Model F-value of 35.83 implies the model is significant. There is only a 2.74% chance that a "Model F-Value" this large could occur due to noise.
- Values of "Prob > F" less than 0.0500 indicate model terms are significant. In this case A, B, D are significant model terms.
- Values greater than 0.1000 indicate the model terms are not significant.

Response: CO (mol %)

Table E.2: Summary of analysis of variance for CO (mol%)

Source	Sum of squares	DF	Mean Squares	F value	Prob >F	
Model	424.35	4	106.09	45.07	0.0052	Significant
A	387.78	1	387.78	164.73	0.0010	
C	19.07	1	19.07	8.10	0.0653	
D	13.03	1	13.03	5.53	0.1001	
AC	4.48	1	4.48	1.90	0.2617	
Residual	7.06	3	2.35			
Cor Total	431.41	7				

- The model F-value of 45.07 implies the model is significant. There is only a 0.52% chance that a “Model F-Value” this large could occur due to noise.
- Values of “Prob>F” less than 0.0500 indicate model terms are significant. In this case A is a significant model term.
- Values greater than 0.1000 indicate the model terms are not significant.

Response: CH₄ (mol %)Table E.3: Summary of analysis of variance for CH₄ (mol%)

Source	Sum of squares	DF	Mean Squares	F value	Prob >F	
Model	1.85	4	0.30	28.88	0.0338	Significant
A	0.72	1	0.72	68.15	0.0144	
B	0.0016	1	0.016	1.50	0.3457	
C	0.22	1	0.22	20.94	0.0446	
AC	0.53	1	0.53	49.84	0.0195	
AD	0.042	1	0.042	3.99	0.1839	
Residual	0.021	2	1.84×10 ⁻³			
Cor Total	1.55	7				

- The model F-value of 28.88 implies the model is significant. There is only a 3.38% chance that a “Model F-Value” this large could occur due to noise.
- Values of “Prob>F” less than 0.0500 indicate model terms are significant. In this case A, C, and AC are significant model terms.
- Values greater than 0.1000 indicate the model terms are not significant.

Response: CO₂ (mol %)Table E.4: Summary of analysis of variance for CO₂ (mol%)

Source	Sum of squares	DF	Mean Squares	F value	Prob >F	
Model	123.10	2	61.55	7.67	0.0299	Significant
A	75.74	1	75.74	9.44	0.0277	
D	47.37	1	47.37	5.91	0.0594	
Residual	40.10	5	8.02			
Cor Total	163.20	7				

- The model F-value of 7.67 implies the model is significant. There is only a 2.99% chance that a “Model F-Value” this large could occur due to noise.
- Values of “Prob>F” less than 0.0500 indicate model terms are significant. In this case A is significant model term.
- Values greater than 0.1000 indicate the model terms are not significant.

Appendix 6A

Ion Spectra for Gas Sample taken from the Freeboard

Figure A.1 shows the acetol/formaldehyde/acetic acid spectra at $m/z=27$, 29, and 30.

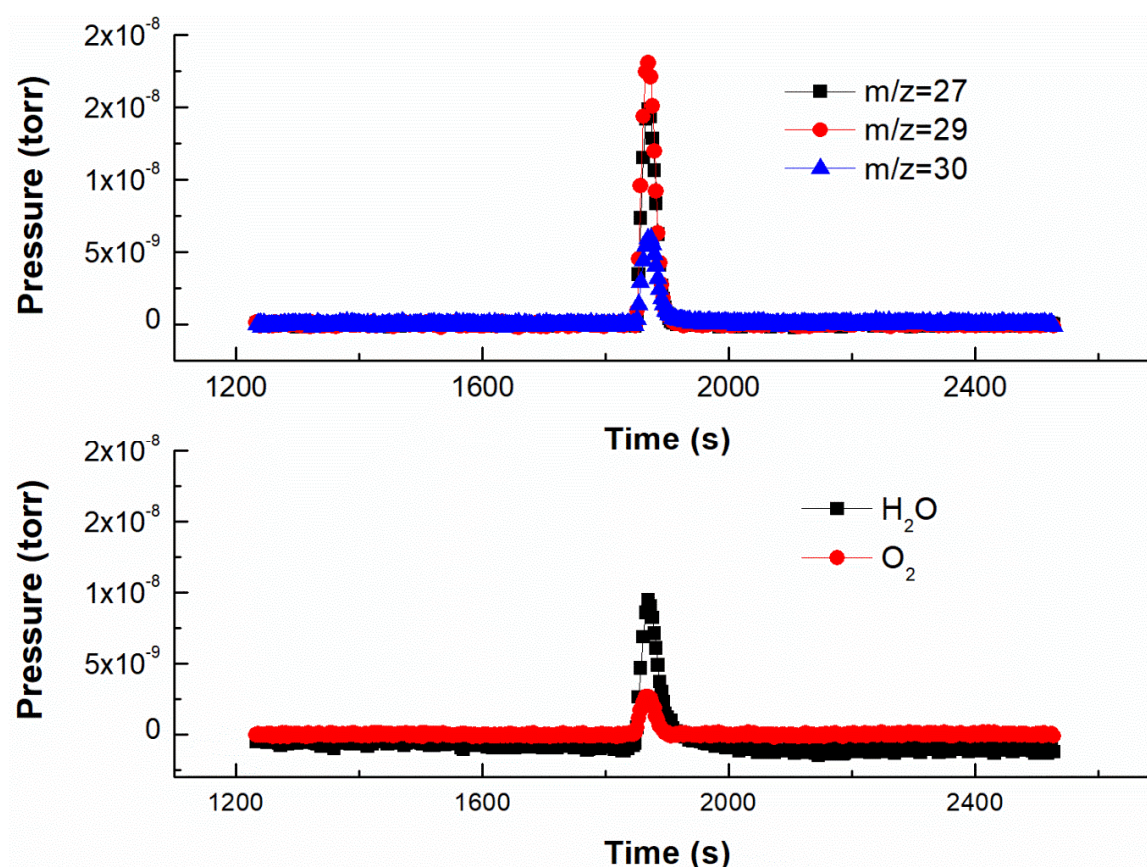


Figure A.1: Mass spectra from acetol conversion in the freeboard: $T=650^{\circ}\text{C}$, $C/O=1.7$, and $S/C=1.2$